Sensorless Commissioning and Control of High Anisotropy Synchronous Motor Drives


Doctoral Dissertation
Doctoral Program in Electrical Enginering (31^{st} cycle)

Sensorless Commissioning and Control of High Anisotropy Synchronous Motor Drives

Paolo Pescetto

* * * * * *

Supervisor
Prof. Gianmario Pellegrino

Doctoral Examination Committee:
Prof. Mauro Zigliotto, Referee, Università di Padova
Prof. Marco Tursini, Referee, Università degli Studi dell'Aquila
Prof. Roberto Petrella, Università di Udine
Prof. Aldo Boglietti, Politecnico di Torino
Prof. Giovanni Griva, Politecnico di Torino

Politecnico di Torino
April 1^{st}, 2019

I hereby declare that, the contents and organization of this dissertation constitute my own original work and does not compromise in any way the rights of third parties, including those relating to the security of personal data.

. . . . . .

Paolo Pescetto

Turin, April 1st, 2019

Summary

In the last decade, synchronous motor drives became an attractive solution for replacing traditional Induction Motors (IMs) in a growing number of variable speed applications, mostly because of their generally higher efficiency and competitive torque per volume ratio. Among the synchronous machines, the ones presenting high anisotropy, i.e. Synchronous Reluctance (SyR) and PM assisted SyR (PM-SyR) motors present the most interesting features.

One key factor limiting the adoption of SyR and PM-SyR machines is the highly non-linear current-to-flux relationship, also called magnetic model. Moreover, in order to properly replace the IMs in variable speed applications the machine should be controlled without using position transducers, e.g. encoders or resolvers.

The main research topic during these years have been automatic parameters identification, namely self-commissioning, and investigation of reliable encoderless control strategies for high anisotropy synchronous motor drives. Particular focus is given to the magnetic model self-identification. Several sensorless control solutions are proposed. All the presented techniques have been experimentally tested.

Finally, both the self-commissioning and sensorless control were validated on a high current SyR prototype designed for on-board electric power generation in avionic applications. Following this experience, an innovative technology named "Dual Winding", expected to reduce the size of the power electronic converter, is investigated.

For better clarity, the papers authored or co-authored by me are report at the beginning of the bibliography [1-15].

Acknowledgements

These three years of PhD program have been so intense that it seems impossible to acknowledge every person who contributed to this achievement. I will try to do my best in this difficult task.

First of all, I will be always grateful to my loved Alice for providing me with unfailing encouragement throughout the most difficult moments of these years, to Rachele who was able to make me smile even in the darkest days and to our baby not born yet, but already loved. Extremely important have been my loving parents and sisters, in blood or in law, who never denied me their priceless support. This accomplishment would not have been possible without them.

Special acknowledge is deserved for my supervisor, Prof. Gianmario Pellegrino, for his patience and guidance extended well beyond the research environment. I would like to expand my gratitude to the other researchers of DENERG department and PEIC center with whom I've been pleased to collaborate and learn, in particular the professors Eric Armando, Radu Bojoi, Paolo Guglielmi, Aldo Boglietti, Enrico Carpaneto and Mario Chiampi.

The PhD program gave me the opportunity to work with Prof. Marko Hinkkanen and the other researchers from Aalto university. I've been always glad for this fruitful cooperation, not only for the scientific achievements but mostly for the human relationship we could establish.

An important acknowledge is given to GE-Aviation System, and in particular to Dr. Davide Ronchetto, for the significant support to our research.

Last but not least, I would especially like to thank the colleagues and friends Fausto, Sandro, Simone and Riccardo who shared this PhD adventure with me, Arzhang and Anantaram for the productive cooperation during these years which helped improving my research and all the other students, older or younger, who contributed making the department a nicer environment to work and live in.

Contents

List of Figures

List of Tables

Chapter 1

Introduction

This manuscript contains the research developments achieved during three years of PhD program at Politecnico di Torino. As described in the title, the main research topics during these years have been automatic parameters identification, namely self-commissioning, and investigation of reliable encoderless control strategies for high anisotropy synchronous motor drives. For better clarity, the papers authored or co-authored by me are report at the beginning of the bibliography [1–15].

Synchronous motor drives are an attractive solution for replacing traditional Induction Motors (IMs) in a growing number of variable speed applications. This trend is pushed by the generally higher efficiency and competitive torque per volume ratio of the synchronous machines compared with the IMs. Generally, IMs are still preferred in such applications where the electrical motor is directly connected to the grid, eliminating the need of a power electronic converter at the cost of a reduced or null control capability. However, the reliability of power electronic converters is considerably grown in recent years, while their cost is progressively reducing, making the grid connected applications less appealing.

A wide variety of synchronous machines is available in the market. In general, torque can be produced either thanks to the flux linkage given by Permanent Magnets (PM) or exploiting rotor anisotropy. The PM can be either ferrite or rare earth (NdFeB or SmCo). The ferrite magnets are relatively cheap, but with low remanent magnetization (e.g. 0.4 T) and relevant risk of demagnetization when medium-high current is applied to the motor. Conversely, rare earth magnets present considerably higher remanence (typically 0.8-1.1 T for SmCo and 1-1.25 for NdFeB) and moderate risk of demagnetization even in overload conditions. Anyway, the price of the rare earth materials is at least highly uncertain. Moreover, if the torque contribution due to PM is high in percentage respect to the reluctance torque, the

risk of Uncontrolled Generation Operation (UGO) occurs in case of inverter failure.

For these reasons, the interest in high anisotropy motor drives is considerably grown in the last decade. In Synchronous Reluctance Motors (SyRM), PMs are not adopted, and salient rotor structure is obtained with proper machine design, aiming to achieve the highest possible anisotropy and reduced torque ripple [16]. It is a cheap and robust solution for low cost applications, but thanks to its generally high efficiency it can be adopted also in high performance drives. At the same time, the manufacturing process is relatively easy, making these machines particularly appealing. Moreover, thanks to the absence of PM, high transient overload capability can be usually achieved.

Another interesting feature of the SyRM is that the losses in the rotor are almost null. Similarly to most of the synchronous machines, there are no rotor windings and so no rotor copper losses, while the rotor iron losses are very low since in normal circumstances the shaft rotates synchronous with the excitation field. In addition, any other synchronous machine would present additional losses due to eddy currents on the PM, which are not present here. Therefore, the main machine losses are only copper and iron losses in the stator, leading to a commonly high efficiency. Moreover, the stator has a better positioning from a thermal point of view respect to the rotor, with easier access to the cooling system.

On the other hand, pure synchronous reluctance motors usually present low power factor (typically $0.5 \div 0.8$), especially if high overload capability is required. Therefore, the power electronic converter must be oversized respect to the rated power of the machine. Moreover, under inverter voltage limitation, large constant power speed range cannot be achieved because the motor incurs the Maximum Torque Per Voltage (MTPV) locus.

These drawbacks can be overcome using PM-assisted Synchronous Reluctance Motors (PM-SyRM). The stator and rotor structures are almost equal to the SyR machine, except for second order design optimization, but small amount of PM are insert into the flux barriers. In this way, the power factor of the machine is considerably improved, and under proper machine design the MTPV trajectory is virtually reached at infinite speed [16]. Therefore, a very large constant power speed range is reached. Finally, thanks to the PM, the torque capability is also increased. For optimal motor design, roughly 80% of the torque is generated thanks to the anisotropy while the remaining 20% comes from the PM.

Advanced motor control of ac drives requires the knowledge of rotor position. Anyway, the use of position transducers such as encoders or resolvers brings additional cost to the drive. In home appliances such as washing machines, an encoder may cost twice the price of the motor, which is not

reasonable. Moreover, more cables are necessary, increasing the complexity of the system. For these reasons, most of the low cost variable speed applications, e.g. pumps, fans, home appliances, etc. require a sensorless control algorithm, where the rotor position is observed based on the electrical quantities. In other cases, e.g. electrical traction and critical industrial application, despite a position transducer is commonly adopted, the safety constrains often require a sensorless strategy which has to be ready to work in case of fault conditions.

If sensorless techniques have been widely studied for IMs, the use of synchronous motors and in particular of SyRM and PM-SyRM introduces relevant challenges and possible improvements, which will be discussed in this manuscript. Proper dedicated encoderless strategies must be developed to allow a proper replacement of IMs in variable speed applications.

Sensorless control is often affected by parameters uncertainty. In any motor control algorithm the stator voltage is not measured, but evaluated relying on the inverter commands and measured DC-link voltage v_{dc}. Anyway, for a proper estimation the voltage drop across the inverter, which depends on the phase currents, must be taken into account. Moreover, the stator resistance R_{s} is often necessary, e.g. to evaluate the electromotive forces. Finally, the current-to-flux relationship is highly non-linear for SyRM and PM-SyRM, and it has to be accurately evaluated to be adopted in flux observers and motor control. It should be noted that both the stator resistance and the PM flux are temperature dependent.

All these parameters can be estimated in several ways. The most accurate solution is to offline test the machine in dedicated test rigs, which commonly imply high human intervention and laboratory equipment such as driving machines, oscilloscopes or data recorders, signal generators, torque meters and so on. This solution is applicable only for small number of machines; in a large industrial series production is commonly not feasible to test every single motor.

If the motors of a production line are reasonably similar, the manufacturer may decide to accurately test only few sample machines, randomly selected, and extend the results to every produced motor. However, in most of the low cost applications the tolerances of the manufacturing process introduce relevant parameters discrepancy between the motors, despite they are nominally equal. For this reason, automatic parameters identification test, commonly called self-commissioning, are often preferred. These tests should be able to identify all the machine parameters necessary for motor control without need of additional hardware and without perturbing the motor, which may be already connected to the load or not. Self-commissioning tests are adopted also in case the motor control is not designed by the final user, so very limited

knowledge of motor parameters is available at the control calibration stage.

The scientific literature presents a wide variety of self-commissioning techniques, but most of them require a position transducer. It is worth noticing that a full sensorless approach requires also the self commissioning technique to be encoderless.

1.1 Thesis Content and Personal Contributions

This manuscript is organized as follow. Chapter 2 gives the definition of several quantities and notations and a summary of theoretical background principles useful to better understand the rest of the thesis. Then, the two main topics, i.e. self-commissioning and sensorless control, are treated in Chapter 3 and Chapter 4 respectively. In both cases, the chapter contains a deep literature review of the already existing techniques, followed by personal achievements and contributions. Finally, Chapter 5 validates the sensorless and self-identification techniques discussing the possible application of SyR and PM-SyR motors for aerospace applications. In particular, Section 5.1 reports the experience with a high power SyRM prototype. The main drawback of this machine, limiting its applicability, is the very high current rating of the power electronic converter. Section 5.2 presents an innovative technology, called Dual Winding (DW) which is capable of reducing the converter size.

The main innovative contributions included in this manuscript are briefly summarized here:

Chapter 3 - Self-commissioning of SyR and PM-SyR machines:

- A feasible magnetic model self-identification test sequence was adopted and tested on several SyRM, demonstrating to be able to accurately evaluate the flux maps in the most demanding conditions (i.e. standstill and free shaft).

- The test sequence was augmented for the first time with high frequency signal injection for online position tracking, considerably improving the measurement domain in the current plane and so the accuracy of the obtained flux maps.

- Accurate automatic calibration procedure was defined to make the algorithm self-tuned with negligible human intervention.

- Several post-processing methods for extracting the flux maps are proposed. An accurate algebraic magnetic model resulted well-suited for every tested machine, and a proper data manipulation sequence is given for retrieving its parameters. Other solutions are also discussed.

- The self-commissioning test sequence was extended to PM-SyR machines at free shaft. Two novel methods for retrieving the flux linkage contribution at standstill are proposed, with promising results.

Chapter 4 - Sensorless control of SyR machines:

- The peculiarities and critical issues of SyRM were extensively analyzed, discussing benefits and drawbacks of different sensorless techniques.

- An appropriate saliency based low speed position estimation technique was adopted, resulting immune from position error due to cross-saturation effect.

- The low speed sensorless algorithm was merged with two different model based position observers at high speed, thus covering a wide speed range from stand-still to flux weakening.

- At best of Author knowledge, MTPA trajectory was adopted for the first time for sensorless control of SyRM.

- Fine analysis of local saliency characteristic of SyRM in the dq plane was conducted addressing the critical aspects of saliency tracking via HF injection and demodulation. This analysis demonstrates that a modified MTPA law is recommendable also for the sake of stability of saliency-based sensorless methods.

- Automatic tuning criteria are proposed for control self-calibration. Combined with the automatic tuning of the self-commissioning technique, a completely plug-in control is reached.

- Novel low speed injectionless position estimation algorithm is presented and discussed.

Chapter 5 - SyR and PM-SyR for more electric aircrafts:

- A 250 kW SyRM was tested in laboratory environment. The self-commissioning test sequence was successfully applied, and based on the obtained flux maps a feasible sensorless algorithm was calibrated and successfully tested.

- Then, the machine flux maps were accurately evaluated using state of the art methods, showing good consistency with the self-commissioning results. Altogether, it is proved that the magnetic model identification method works properly independently by the size of the machine.
- A novel topology for reducing the converter size of on-board generators for aeronautic applications is discussed. A reduced size motor prototype was designed and successfully tested.
- Several solutions are proposed for its motor control and efficiency optimization.
- The designed prototype highlighted a relevant unbalance in the windings temperature distribution. Proper thermal model to analyze this effect is proposed, together with a test sequence able to accurately retrieve its parameters. This thermal model can be adopted both for optimized machine design and for online temperature monitoring.

Chapter 2

Theoretical Background

Synchronous electrical machines commonly present higher efficiency and lower volume and weight compared to Induction Motors (IMs). Anyway, in steady state conditions and rotating at constant speed, they are inherently capable of generating average torque only when the excitation frequency is synchronous with the electrical rotating frequency[1]. For this reason, the synchronous motors usually require to be supplied by a power electronic converter instead of being directly connected to the grid, as can be often done for the IMs. The aggregate of the electrical motor and its converter is commonly called electrical drive.

In this preliminary Chapter, a brief summary of the machine modeling for synchronous electrical machines is given in Section 2.1. The main goal of this Section is to define the adopted terminology and machine equations, which will be used in the rest of the manuscript. Then, a review of some of the most common control strategies is given in Section 2.2, in particular highlighting the dependency of each of them from the knowledge of rotor position and the effects of eventual inaccurate machine model. Several flux observer structures are presented in Section 2.3, while Section 2.4 provides three sensorless model based flux and position observer.

2.1 Synchronous Motor Drives: Machine Model

This Section briefly summarizes the main equations related to the mathematical model of synchronous machines, which will be adopted for the rest of the manuscript, with the aim of defining the notations and symbols. In the entire thesis, vector quantities will be written as bold lowercase letters, the

[1]Few exceptions to this assumption can be found for special machines, such as line starters, which will not be treated here.

matrices as bold uppercase and the scalar quantities as non-bold symbols.

2.1.1 Classification of Synchronous Machines

First of all, it must be mentioned that a wide variety of synchronous machine types can be designed, as defined for example in [16]. In particular, in [16] a PM flux versus saliency plane ($\lambda_{\text{pm}} - \xi$) was determined, where ξ is the machine saliency defined as the ratio between inductances in maximum and minimum permeance direction and λ_{pm} is the flux linkage contribution given by the (eventual) permanent magnets in per unit value. This ($\lambda_{\text{pm}} - \xi$) plane is report in Figure 2.1. Every synchronous machine can be located at a precise position of this plane. Surface-mounted Permanent Magnet(SPM) motors with distributed windings are placed on the horizontal axis ($\lambda_{\text{pm}} = 1, \xi = 0$), while pure Synchronous Reluctance Machines (SyRM)[2] fall into the vertical axis, with $\lambda_{\text{pm}} = 0$ and $\xi \gg 1$. Between these two extreme cases, every Permanent Magnet Synchronous Machine (PMSM) is placed in an optimal design locus, having $\lambda_{\text{pm}} > 0$ and various levels of anisotropy. In particular, in this work the machines presenting $\xi > 1$ and $\lambda_{\text{pm}} > 0$ will be referred to as Internal Permanent Magnets (IPM) motors if the torque is mainly given by the PMs, while machines where the torque is mainly obtained from their high anisotropy ratio will be called PM-SyR machines.

It should be reminded that the $\lambda_{\text{pm}} - \xi$ plane also gives an idea of the non-linear behavior of the machine magnetic model. Indeed, the saturation characteristic tends to be more linear for low saliency, high λ_{pm} machines, thus getting close to the SPMs, while high anisotropy motors such as SyRM and PM-SyRM present strong nonlinear magnetic model.

2.1.2 Machine Equations

In this first part of the Section, linear magnetic model and so constant inductances are considered, thus neglecting saturation effects.

The machine model can be expressed in different reference frames. The basic notation is written in three-phase coordinates abc, where the electrical and magnetic equations can be expressed as:

$$\begin{cases} \boldsymbol{v}_{\text{abc}} &= R_{\text{s}} \boldsymbol{i}_{\text{abc}} + \frac{\partial}{\partial t} \boldsymbol{\lambda}_{\text{abc}} \\ \boldsymbol{\lambda}_{\text{abc}} &= (L_\sigma \mathbf{I}_3 + \boldsymbol{M}_{\text{abc}})\, \boldsymbol{i}_{\text{abc}} + \boldsymbol{m}_\theta^{abc} \lambda_{\text{pm}} \end{cases} \tag{2.1}$$

where $\boldsymbol{v}_{\text{abc}}$, $\boldsymbol{i}_{\text{abc}}$ and $\boldsymbol{\lambda}_{\text{abc}}$ are the voltage, current and flux linkage vectors in 3-phase reference frame, L_σ is the leakage inductance, $\mathbf{I}_3$ is the $3x3$ identity

[2] In this manuscript, the acronyms SyR and SyRM stand for Synchronous Reluctance and Synchronous Reluctance Motor respectively.

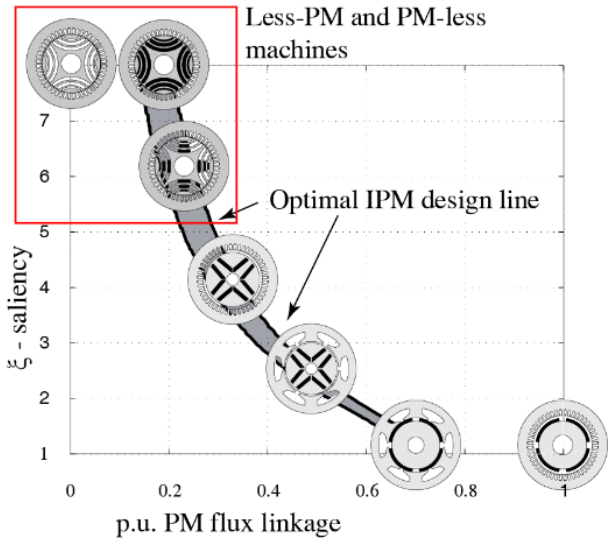

Figure 2.1: Definition of $(\lambda_{\text{pm}} - \xi)$ plane for synchronous machines. Image taken from [16] under permission.

matrix, $\boldsymbol{M}_{\text{abc}}$ the matrix of mutual coupling between the phases and $\boldsymbol{m}_{\theta}^{abc}$ a vector defining the projection of the PM flux λ_{pm} on each stator phase. Since the rotor structure is not isotropic, the coefficients of $\boldsymbol{M}_{\text{abc}}$ and $\boldsymbol{m}_{\theta}^{abc}$ depend on the rotor position. Assuming the angle θ as the direction of the λ_{pm} vector respect to the a phase, the analytical expression of the coefficients of $\boldsymbol{M}_{\text{abc}}$ and $\boldsymbol{m}_{\theta}^{abc}$ are given as:

$$\boldsymbol{M}_{\text{abc}} = \frac{L_{\text{d}} + L_{\text{q}}}{2} \cdot \boldsymbol{M}_{\text{abc}}^{CM} + \frac{L_{\text{d}} - L_{\text{q}}}{2} \cdot \boldsymbol{M}_{\text{abc}}^{CM} \tag{2.2}$$

$$\boldsymbol{M}_{\text{abc}}^{DM} = \begin{bmatrix} 1 & -\frac{1}{2} & -\frac{1}{2} \\ -\frac{1}{2} & 1 & -\frac{1}{2} \\ -\frac{1}{2} & -\frac{1}{2} & 1 \end{bmatrix}$$

$$\boldsymbol{M}_{\text{abc}}^{CM} = \begin{bmatrix} \cos(2\theta) & \cos(2\theta - \frac{2\pi}{3}) & \cos(2\theta - \frac{4\pi}{3}) \\ \cos(2\theta - \frac{2\pi}{3}) & \cos(2\theta - \frac{4\pi}{3}) & \cos(2\theta) \\ \cos(2\theta - \frac{4\pi}{3}) & \cos(2\theta) & \cos(2\theta - \frac{2\pi}{3}) \end{bmatrix}$$

$$\boldsymbol{m}_{\theta}^{abc} = \begin{bmatrix} cos(\theta) \\ cos(\theta - \frac{2\pi}{3}) \\ cos(\theta - \frac{4\pi}{3}) \end{bmatrix} \tag{2.3}$$

where L_{d} and L_{q} are the machine inductances in direct and quadrature axes. The orientation of dq direction depends on the machine type, as will be described in Section 2.1.2.2.

2.1.2.1 Stator Coordinates $\alpha\beta$

The Clarke transformation (2.4) allows to re-write (2.1) in stator coordinates $(\alpha, \beta, 0)$, where 0 indicates the homopolar component:

$$\boldsymbol{T}_{\mathrm{c}} = \begin{bmatrix} 1 & -\frac{1}{2} & -\frac{1}{2} \\ 0 & \frac{\sqrt{3}}{2} & -\frac{\sqrt{3}}{2} \\ \frac{1}{\sqrt{2}} & \frac{1}{\sqrt{2}} & \frac{1}{\sqrt{2}} \end{bmatrix} \quad ; \quad \boldsymbol{X}_{\alpha\beta 0} = \boldsymbol{T}_{\mathrm{c}} \boldsymbol{X}_{\mathrm{abc}} \tag{2.4}$$

where $\boldsymbol{X}_{\mathrm{abc}} = [x_a, x_b, x_c]^T$ and $\boldsymbol{X}_{\alpha\beta 0} = [x_\alpha, x_\beta, x_0]^T$ stand for generic vector in 3-phase and stator coordinates, respectively. The zero-sequence current is usually negligible and does not contribute to the machine torque. Therefore, it can be omitted, leading to a model in two components $\alpha\beta$:

$$\begin{cases} \boldsymbol{v}_{\alpha\beta} &= R_{\mathrm{s}} \boldsymbol{i}_{\alpha\beta} + \frac{\mathrm{d}\boldsymbol{\lambda}_{\alpha\beta}}{\mathrm{d}t} \\ \boldsymbol{\lambda}_{\alpha\beta} &= (L_\sigma + \boldsymbol{L}_{\alpha\beta})\, \boldsymbol{i}_{\alpha\beta} + \boldsymbol{m}_\theta^{\alpha\beta} \lambda_{\mathrm{pm}} \end{cases} \tag{2.5}$$

Considering a linear magnetic model having constant inductances:

$$\boldsymbol{L}_{\alpha\beta} = \frac{L_{\mathrm{d}} + L_{\mathrm{q}}}{2} \mathbf{I} + \frac{L_{\mathrm{d}} - L_{\mathrm{q}}}{2} \begin{bmatrix} \cos(2\theta) & \sin(2\theta) \\ \sin(2\theta) & -\cos(2\theta) \end{bmatrix} \quad ; \quad \boldsymbol{m}_\theta^{\alpha\beta} = \begin{Bmatrix} \cos(\theta) \\ \sin(\theta) \end{Bmatrix} \tag{2.6}$$

where $\mathbf{I} = \begin{bmatrix} 1 & 0 \\ 0 & 1 \end{bmatrix}$ is the $2x2$ identity matrix. In this formulation, λ_{pm} is considered to be along the d axis. As well-known from the theory of electrical machine modelling, the electro-mechanical torque equation can be obtained from the balance between input and output power, resulting as:

$$T = \frac{3}{2} p \left(\lambda_\alpha i_\beta - \lambda_\beta i_\alpha \right) \tag{2.7}$$

2.1.2.2 Rotor Coordinates dq

For motor control, it is convenient to rotate the model by the electrical rotor angle θ using the rotation matrix (2.8), obtaining the machine model in rotor coordinates dq:

$$\boldsymbol{X}_{\mathrm{dq}} = \begin{bmatrix} \cos(\theta) & \sin(\theta) \\ -\sin(\theta) & \cos(\theta) \end{bmatrix} \boldsymbol{X}_{\alpha\beta} = e^{-j\theta} \boldsymbol{X}_{\alpha\beta} \tag{2.8}$$

$$\begin{cases} \boldsymbol{v}_{\mathrm{dq}} &= R_{\mathrm{s}} \boldsymbol{i}_{\mathrm{dq}} + \frac{\partial \boldsymbol{\lambda}_{\mathrm{dq}}}{\partial t} + \omega \mathbf{J} \boldsymbol{\lambda}_{\mathrm{dq}} \\ \boldsymbol{\lambda}_{\mathrm{dq}} &= \boldsymbol{L}_{\mathrm{dq}} \boldsymbol{i}_{\mathrm{dq}} + \boldsymbol{m}_\theta^{dq} \lambda_{\mathrm{pm}} \end{cases} \tag{2.9}$$

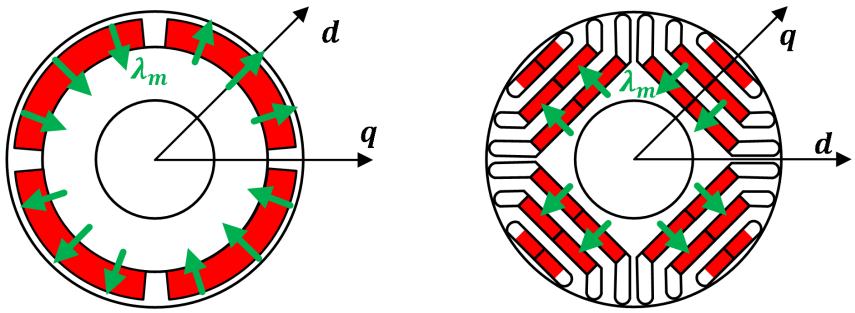

(a) (b)

Figure 2.2: Schematic representation of (a) SPM and (b) PM-SyR machines, defining d and q axis for (a) SPM and IPM; (b) PM-SyR and SyR. The red area represent permanent magnets and green arrows their orientation.

Where $\mathbf{J} = \begin{bmatrix} 0 & -1 \\ 1 & 0 \end{bmatrix}$ is the imaginary unit expressed in matrix form, $\boldsymbol{X}_{\mathrm{dq}} = [x_d, x_q]^T$ is a generic vector in dq coordinates and $\boldsymbol{L}_{\mathrm{dq}}$ is the inductance matrix, later defined.

It must be noted that, looking at the complete spectrum of the synchronous machines, a discrepancy is found in the definition of d and q axes. For SPM and IPM machines, the d axis corresponds to the direction where the permanent magnets are oriented, therefore $\boldsymbol{m}_\theta^{dq} = \{1, 0\}^T$ and, for IPMs, it corresponds to the minimum inductance ($L_\mathrm{d} < L_\mathrm{q}$). Conversely, for SyR and PM-SyR machines it results convenient to define the d axis in the direction of maximum inductance ($L_\mathrm{d} > L_\mathrm{q}$), since the main component of the flux is given by the magnetizing current in such direction. In this way, the small amount of magnets in PM-SyR motors is oriented in negative q axis, so $\boldsymbol{m}_\theta^{dq} = \{0, -1\}^T$. Figure 2.2 helps describing the definition of θ for the two types of machines. Also, Figure 2.3(a) defines $\alpha\beta$, dq and $d_\mathrm{s}q_\mathrm{s}$ (later defined) coordinates.

After straightforward analytical manipulation, the torque equation in qd reference frame can be obtained:

$$T = \frac{3}{2} p \left(\lambda_\mathrm{d} i_\mathrm{q} - \lambda_\mathrm{q} i_\mathrm{d}\right) \tag{2.10}$$

As can be seen, in this formulation the dependence of the electrical quantities from the rotor position is eliminated. The stator voltage, current and flux can be represented in vectorial form as in Figure 2.3(b), where the angles γ and δ are defined.

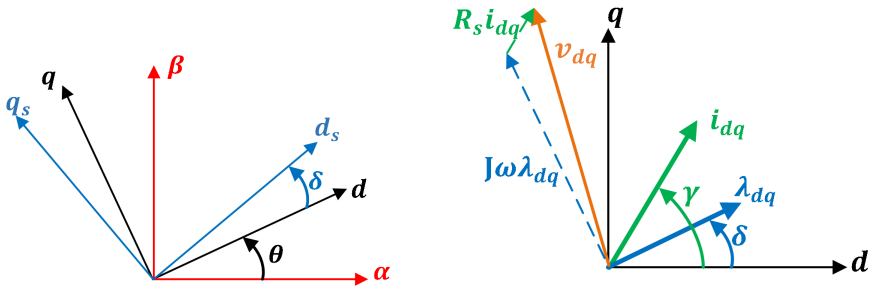

(a) (b)

Figure 2.3: (a) definition of $\alpha\beta$, dq and $d_s q_s$ coordinates. (b) Steady state vector diagram in dq reference frame for synchronous motors.

2.1.2.3 Flux Coordinates $d_s q_s$

The machine model in stator flux coordinates is obtained by rotating (2.9) by the stator flux angle δ:

$$\boldsymbol{X}_{\mathrm{ds,qs}} = \begin{bmatrix} \cos(\delta) & \sin(\delta) \\ -\sin(\delta) & \cos(\delta) \end{bmatrix} \boldsymbol{X}_{\mathrm{dq}} = e^{-j\delta} \boldsymbol{X}_{\mathrm{dq}} \tag{2.11}$$

$$\begin{cases} v_{\mathrm{ds}} &= R_{\mathrm{s}} i_{\mathrm{ds}} + \frac{\partial \lambda}{\partial t} \\ v_{\mathrm{qs}} &= R_{\mathrm{s}} i_{\mathrm{qs}} + \lambda \left(\omega + \frac{\mathrm{d}\delta}{\mathrm{d}t}\right) \end{cases} \tag{2.12}$$

Where $\boldsymbol{X}_{\mathrm{ds,qs}} = [x_{ds}, x_{qs}]^T$ is a generic vector in $d_s q_s$ coordinates and λ is the amplitude of the flux vector. Such model is aligned with the d_s axis along the stator flux vector, so $\lambda_{\mathrm{ds}} = \lambda$ and $\lambda_{\mathrm{qs}} = 0$ by definition. Therefore, the electromagnetic torque can be expressed as:

$$T = \frac{3}{2} p \lambda i_{\mathrm{qs}} \tag{2.13}$$

Alternatively, the torque equation can be written as a function of the machine inductances and the flux amplitude and phase:

$$T = \frac{3}{2} p \frac{L_{\mathrm{d}} - L_{\mathrm{q}}}{2 L_{\mathrm{d}} L_{\mathrm{q}}} \lambda^2 \sin(2\delta) \tag{2.14}$$

2.1.2.4 Flux Linkage Maps

Up to now, a linear magnetic model has been adopted. Anyway, especially for high anisotropy motors, the magnetic saturation has to be taken into account, so that the flux linkages become a non-linear function of the current:

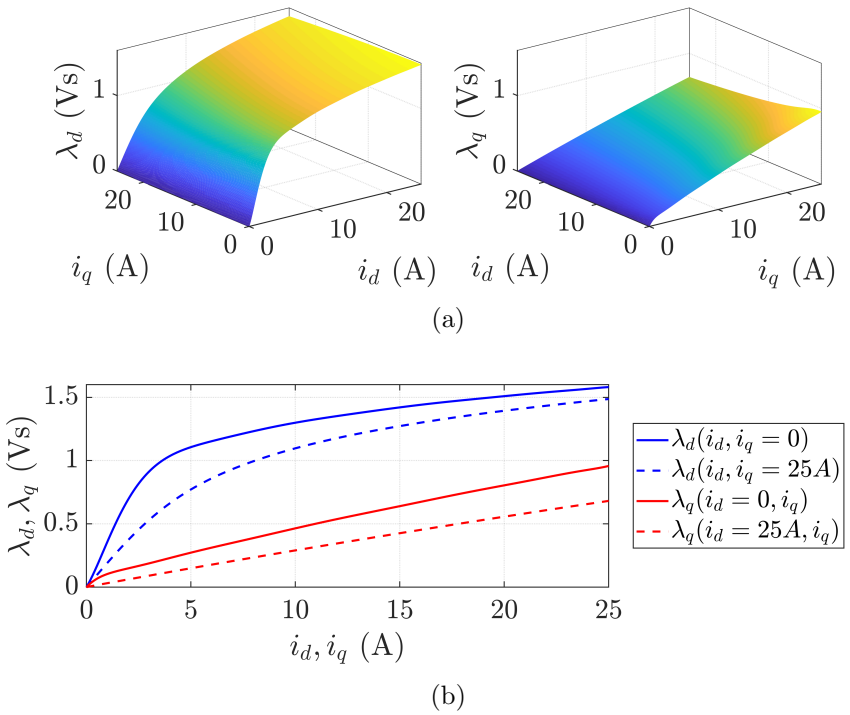

Figure 2.4: Self-saturation characteristic of the SyR motor SR2kW2. (a) 3D surfaces; (b) extreme curves.

$$\begin{cases} \lambda_\mathrm{d} &= \lambda_\mathrm{d}\left(i_\mathrm{d}, i_\mathrm{q}\right) \\ \lambda_\mathrm{q} &= \lambda_\mathrm{q}\left(i_\mathrm{d}, i_\mathrm{q}\right) \end{cases} \tag{2.15}$$

From there on, such non-linear characteristic will be called flux maps. In each axis, the saturation of the core is due to both the current component in its direction (self-saturation) and to the current in the other axis (cross-saturation or cross-coupling). Figure 2.4 represents the typical flux maps of a SyR motor in d and q axes, both when the current in the other axis is null and in presence of strong cross-coupling.

2.1.2.5 Apparent and Incremental Inductances

Exploiting the first order Taylor series expansion, the flux maps can be linearized around a specific working point $(i_{\mathrm{d}0}, i_{\mathrm{q}0})$ as:

$$\begin{cases} \lambda_\mathrm{d}\left(i_\mathrm{d}, i_\mathrm{q}\right) &= \lambda_\mathrm{d}\left(i_{\mathrm{d}0}, i_{\mathrm{q}0}\right) + \frac{\partial \lambda_\mathrm{d}}{\partial i_\mathrm{d}} \mathrm{d}i_\mathrm{d} + \frac{\partial \lambda_\mathrm{d}}{\partial i_\mathrm{q}} \mathrm{d}i_\mathrm{q} \\ \lambda_\mathrm{q}\left(i_\mathrm{d}, i_\mathrm{q}\right) &= \lambda_\mathrm{q}\left(i_{\mathrm{d}0}, i_{\mathrm{q}0}\right) + \frac{\partial \lambda_\mathrm{q}}{\partial i_\mathrm{d}} \mathrm{d}i_\mathrm{d} + \frac{\partial \lambda_\mathrm{q}}{\partial i_\mathrm{q}} \mathrm{d}i_\mathrm{q} \end{cases} \tag{2.16}$$

The first term of the right-hand side of the equation is predominant when the flux is slowly varying, therefore it is related to the fundamental component, while the two terms containing flux derivatives become important in case of High Frequency (HF) oscillations. The two aspects can be decoupled, identifying the low frequency and high frequency magnetic models. In this concern, it is useful to define the following quantities:

$$\begin{bmatrix} \lambda_{\mathrm{d}0} \\ \lambda_{\mathrm{q}0} \end{bmatrix} = \begin{bmatrix} L_{\mathrm{d}} & L_{\mathrm{dq}} \\ L_{\mathrm{dq}} & L_{\mathrm{q}} \end{bmatrix} \begin{bmatrix} i_{\mathrm{d}} \\ i_{\mathrm{q}} \end{bmatrix} = \boldsymbol{L}_{\mathrm{dq}} \boldsymbol{i}_{\mathrm{dq}} \tag{2.17}$$

$$\boldsymbol{l}_{\mathrm{dq}} = \begin{bmatrix} l_{\mathrm{d}} & l_{\mathrm{dq}} \\ l_{\mathrm{qd}} & l_{\mathrm{q}} \end{bmatrix} = \begin{bmatrix} \frac{\partial \lambda_{\mathrm{d}}}{\partial i_{\mathrm{d}}} & \frac{\partial \lambda_{\mathrm{d}}}{\partial i_{\mathrm{q}}} \\ \frac{\partial \lambda_{\mathrm{q}}}{\partial i_{\mathrm{d}}} & \frac{\partial \lambda_{\mathrm{q}}}{\partial i_{\mathrm{q}}} \end{bmatrix} \tag{2.18}$$

where L_{d} and L_{q} are called apparent inductances in d and q axis direction, respectively, L_{dq} is the cross-saturation term, l_{d}, l_{q}, l_{dq}, l_{qd} are called incremental (or differential) inductances. Figure 2.5 helps describing the physical meaning of apparent and differential inductances, taking the example of d axis when $i_{\mathrm{q}} = 0$. In particular, it can be useful to define these quantities as:

$$L_{\mathrm{d}}(i_{\mathrm{d}}, i_{\mathrm{q}}) = \left.\frac{\lambda_{\mathrm{d}}}{i_{\mathrm{d}}}\right|_{i_{\mathrm{q}}=0} \quad ; \quad L_{\mathrm{dq}}(i_{\mathrm{d}}, i_{\mathrm{q}}) = \left.\frac{\lambda_{\mathrm{d}} - L_{\mathrm{d}} i_{\mathrm{d}}}{i_{\mathrm{q}}}\right|_{i_{\mathrm{q}}\neq 0} \tag{2.19}$$

$$l_{\mathrm{d}}(i_{\mathrm{d}}, i_{\mathrm{q}}) = \frac{\partial \lambda_{\mathrm{d}}}{\partial i_{\mathrm{d}}} \quad ; \quad l_{\mathrm{dq}}(i_{\mathrm{d}}, i_{\mathrm{q}}) = \frac{\partial \lambda_{\mathrm{d}}}{\partial i_{\mathrm{q}}} \tag{2.20}$$

The other terms of (2.17) and (2.18) can be easily retrieved in the same way. From this definition, the apparent inductances $L_{\mathrm{d}}, L_{\mathrm{q}}$ are given by the ratio between flux and current in absence of cross-coupling, while the differential inductances are retrieved from the local slope of the flux maps.

Considering the principle of energy conservation, the reciprocity conditions [17] holds:

$$\frac{\partial \lambda_{\mathrm{d}}}{\partial i_{\mathrm{q}}} = \frac{\partial \lambda_{\mathrm{q}}}{\partial i_{\mathrm{d}}} \quad \rightarrow \quad l_{\mathrm{dq}} = l_{\mathrm{qd}} \tag{2.21}$$

It must be remarked that the literature presents also other method to analytically describe the magnetic saturation. As an example, the iron losses are taken into account in [17, 18], considering both transient losses and eddy currents.

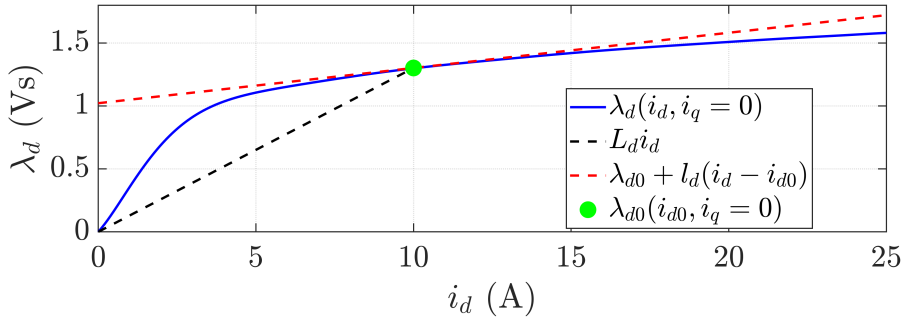

Figure 2.5: Definition of apparent and incremental inductance in d axis.

2.1.2.6 Mechanical Model

The mechanical dynamic is given by the balance between electromagnetic and load torque T_l, and the mechanical speed ω_r is the derivative of rotor position:

$$T - T_\mathrm{l} = J\frac{\mathrm{d}\omega_\mathrm{r}}{\mathrm{d}t} \tag{2.22}$$

$$\omega_\mathrm{r} = \frac{w}{p} = \frac{1}{p}\frac{\mathrm{d}\theta}{\mathrm{d}t} \tag{2.23}$$

where J is the mechanical inertia. The load torque may be constant, dependent on the rotor speed (e.g. pumps or fans), given by external conditions (e.g. for traction) or a combination of different contributions.

2.2 Control Strategies

In this Section, some of the most common algorithms adopted for motor control are briefly described. Being the present work a manuscript about sensorless commissioning and control, for each of the selected control strategies particular focus will be given to identifying which blocks of the control scheme require the knowledge of rotor position and the effect of eventual position error or inaccuracy in determining the magnetic model of the machine.

The block diagram of every considered strategy is report. The quantities dependent on observed position will be highlighted in red, while the blocks requiring the knowledge of machine parameters will present a green outline. Accordingly, the blocks dependent on both rotor position and machine model, such as flux observers, are drawn in red with green outline. Also, in each case the reference torque T^* is given by the speed loop (speed control). Every

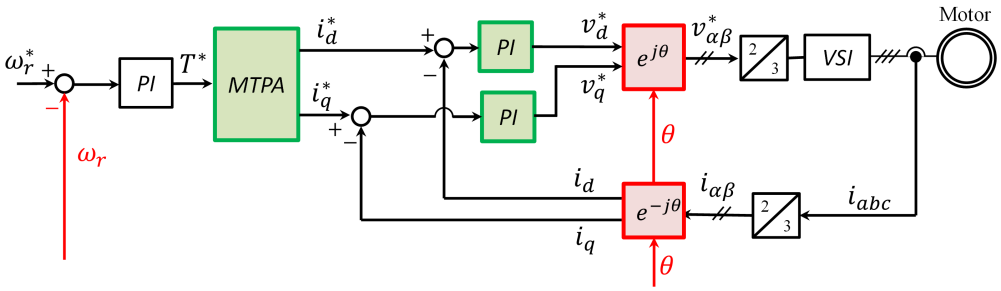

Figure 2.6: Basic block diagram for dq current control.

presented scheme applies also for torque control when T^* is given by the user, thus canceling the speed loop.

Some general considerations, which apply to any control strategy, are report here. First, in case the motor is sensorless speed controlled the performance of the speed loop depends on the goodness of speed estimation. Eventual noise or inaccuracy in determining the observed speed would limit the speed loop bandwidth and precision, respectively. A second consideration, which applies both in case of torque or speed control, is that in case of relevant position error the working point in the dq plane may move considerably far from the reference, with possible instability and loss of control. Finally, dealing with parameters identification, it must be considered that in case of inaccurate knowledge of the machine flux maps the MTPA trajectory is not properly evaluated, so the imposed working point does not fall into the minimum copper losses locus.

2.2.1 *dq* Current Vector Control

The qd current control, often called Field Oriented Control (FOC) in the literature, is one of the most common strategies adopted in many applications. It is based on the motor model in dq reference frame, as expressed in (2.9). The basic block diagram of such algorithm is represented in Figure 2.6.

The two control variables are the currents $i_\mathrm{d}, i_\mathrm{q}$, forced to be equal to the reference values through the PI regulators, whose calibration requires at least a rough estimation of the machine inductances. The reference torque command T^* is transformed to the references $i_\mathrm{d}^*, i_\mathrm{q}^*$ according to the MTPA trajectory, usually computed offline. In case of sensorless control of SyRM, a minimum i_d is forced to ensure the convergence of the position observer. A minimum i_d is sometimes adopted also when a position transducer is available to increase the torque dynamic, at the cost of lower efficiency at low load. In flux weakening and MTPV region the references $i_\mathrm{d}^*, i_\mathrm{q}^*$ are modified to follow

the maximum torque trajectory under voltage limitation. It should be noted that the definition of these trajectories is strongly dependent on the motor parameters, which may vary with the operating conditions (e.g. lower λ_{pm} at higher temperature), often resulting in imprecise motor control.

The main effect of eventual inaccurate flux maps is that the reference torque will not corresponds to the real one, since inaccurate i_d^*, i_q^* would be set. This effect is mitigated in case the motor is speed controlled, since the speed loop adapts the reference T^* to correct the speed error. In addition, the maximum torque trajectories imposed in flux weakening and MTPV regions will be inaccurate, therefore it is necessary to adopt a safety voltage margin and it is not possible to exploit the maximum theoretical voltage.

In case of position estimation error, the observed dq coordinates would not correspond to the real ones. Therefore, even if accurate magnetic model is assumed, the working point will not lie on the correct MTPA trajectory and the obtained torque will be again different from T^*. The eventual position error becomes particularly critical in flux weakening and MTPV operation, since the reference current may fall into unstable regions.

2.2.2 Model Based Predictive Control

Model Predictive Control (MPC) schemes include a wide number of different control strategies. The basic idea is to exploit all the available information to predict the future behavior of the machine relying on a machine model, in order to define the most appropriate reference voltage. Considering the discrete time nature of digital control, the number of future sampling periods at which the machine states are predicted is called prediction horizon. Due to the reduced available computational power and time, the prediction horizon is usually limited to a few sampling periods.

The choice of the reference voltage for the time step $k + 1$ is based on the minimization of a cost function also called decision function. Thanks to this approach, non-linear systems (eventually constrained) can usually be better handled respect to PI-based closed loop controls. Many different cost functions have been proposed in the literature [19–24] to include efficiency maximization, rapid torque and speed dynamic, control stability, fulfillment of inverter and mechanical constrains and so on.

One of the main drawbacks is that the states prediction and evaluation of the cost function can be quite time consuming, especially for low cost applications with limited computational power. The literature distinguishes linear MPC, where the optimization problem is solved online, and explicit MPC, where the optimization is solved offline and the reference voltage is chosen based on look-up-tables or tree diagrams. The reference voltage, i.e.

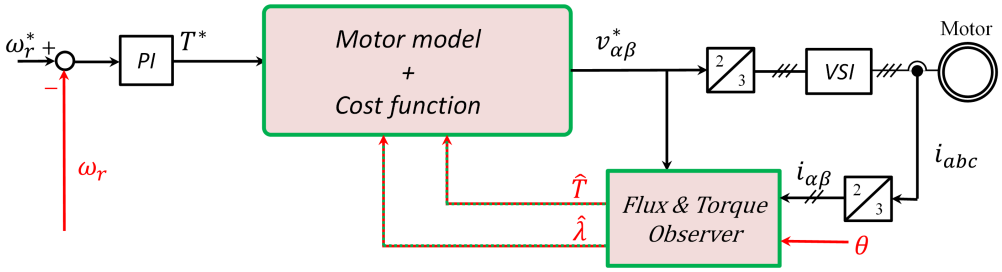

Figure 2.7: Basic block diagram for MPC.

the solution of the optimization, can be a linearized voltage to be managed by a PWM modulator or it can take into account the discrete nature of the inverter directly choosing the optimal voltage vector between the eight reference vectors. The two approaches are called Continuous Control Set (CCS) and Finite Control Set (FCS) MPC. Because of the high variability of the control techniques falling into the MPC category, a very generic scheme is given in Figure 2.7. More details will be given in Section 4.2.5.

In any MPC schemes, both the rotor position and accurate knowledge of the flux maps are necessary mostly to correctly evaluate the motor model for a reliable prediction of the future machine states. The MPC concept has been merged with sensorless control, as an example, in [20, 21].

2.2.3 Direct Flux Vector Control

The Direct Flux Vector Control (DFVC) method, based on the model (2.12) expressed in stator flux synchronous frame $d_s q_s$, was presented in [25] and followed, as an example, in [26–29]. It combines several features of Direct Torque Control (DTC), such as imposing the flux amplitude and torque, with the features of vector control methods like fixed switching frequency and straightforward limitation of the current vector amplitude. In DFVC, the two controlled variables, closed loop imposed by dedicated PI controllers, are the amplitude of the observed flux λ and the quadrature current i_{qs}. The basic motor control is represented in the block diagram of Figure 2.8. Also in this case, it is possible to switch between speed and torque control by enabling/disabling the speed loop. A more complete scheme for DFVC of SyRMs will be presented later in Figure 4.18.

Also for DFVC, in case of sensorless control of pure SyR machines a minimum magnetic excitation must always be guaranteed, obtained by imposing a minimum reference flux $\lambda^* \geq \lambda_{\min}$. Thanks to the direct control of the stator flux linkage, voltage utilization in the flux weakening speed operating region is straightforward. Similarly, the inverter current limit is explicitly

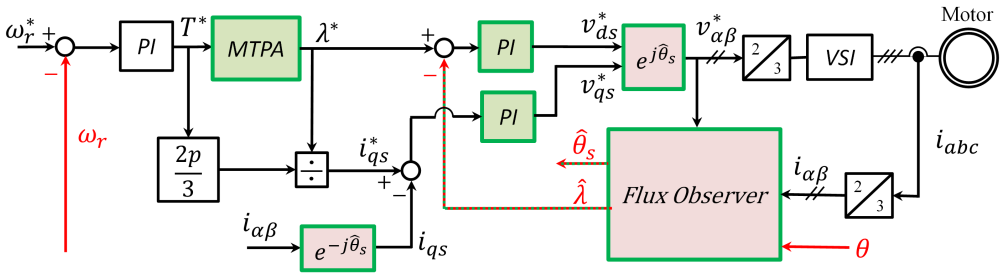

Figure 2.8: Basic block diagram for DFVC.

handled via direct saturation of the reference i_{qs}. Both voltage and current limit blocks are parameter independent. Moreover, the calibration of the PI flux regulator depends only by the switching frequency and the inverter accuracy, but it is independent from the motor.

Similarly to DTC, the DFVC does not exploit rotor dq reference frame, therefore it may be considered independent from rotor position. Moreover, the motor control itself is almost independent by machine parameters, except for the calibration of the i_{qs} PI regulator, where a rough estimation of the motor inductance is normally sufficient. In this concern, DFVC scheme can be considered inherently sensorless. Anyway, both rotor position and accurate magnetic model are necessary for the flux observer at least at low speed, where the flux estimation is based on the current model, as will be described in the next Section.

In turn, when torque control is required at standstill [30], inaccurate flux maps or position estimation error result in wrong flux estimation and therefore inaccurate determination of the $d_{\mathrm{s}}q_{\mathrm{s}}$ directions, thus affecting the control performances. Moreover, particularly critical both in low and high speed is the determination of the appropriate flux amplitude, according to the MTPA concept, since the determination of the locus of minimum copper losses is based on the magnetic model.

2.3 Flux Observers

Generally, in most of the electric drives the currents are measured by current transducers and the voltages are estimated by reference inverter commands, but measuring the flux linkage is unfeasible. If the knowledge of the flux vector is necessary for the machine control, as for DTC, MPC and DFVC, it is necessary to estimate it using a flux observer.

A generic Multiple Input Multiple Output (MIMO) system can be described in canonical form:

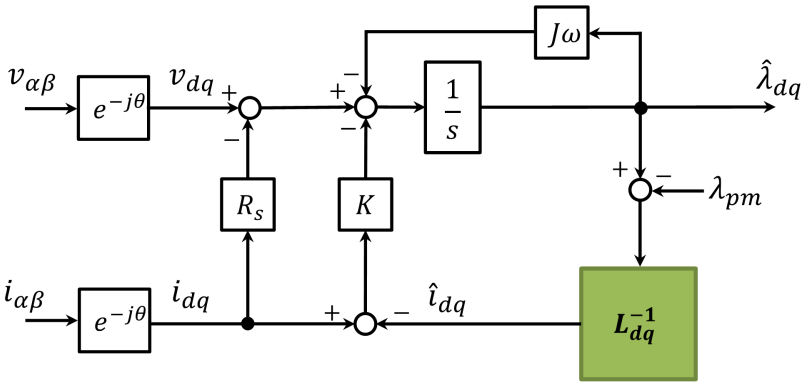

Figure 2.9: Block diagram for flux observer with current error feedback in rotor coordinates.

$$\begin{cases} \frac{\mathrm{d}}{\mathrm{d}t}\boldsymbol{x} &= \boldsymbol{A}\boldsymbol{x} + \boldsymbol{B}\boldsymbol{u} \\ \boldsymbol{y} &= \boldsymbol{C}\boldsymbol{x} + \boldsymbol{D}\boldsymbol{u} \end{cases} \tag{2.24}$$

where the vectors $\boldsymbol{x}$, $\boldsymbol{y}$ and $\boldsymbol{u}$ are the system states, outputs and inputs. The canonical equations defining a state observer can be written as:

$$\begin{cases} \frac{\mathrm{d}}{\mathrm{d}t}\hat{\boldsymbol{x}} &= \hat{\boldsymbol{A}}\hat{\boldsymbol{x}} + \hat{\boldsymbol{B}}\boldsymbol{u} + \boldsymbol{K}\left(\boldsymbol{y} - \hat{\boldsymbol{y}}\right) \\ \hat{\boldsymbol{y}} &= \hat{\boldsymbol{C}}\hat{\boldsymbol{x}} + \hat{\boldsymbol{D}}\boldsymbol{u} \end{cases} \tag{2.25}$$

where $\boldsymbol{K}$ is the matrix of the observer gains. As can be seen, the feedback signal is the difference between measured and estimated output $(\boldsymbol{y} - \hat{\boldsymbol{y}})$. If correct motor model and parameters is assumed, i.e. $\hat{\boldsymbol{A}} = \boldsymbol{A}$, $\hat{\boldsymbol{B}} = \boldsymbol{B}$, $\hat{\boldsymbol{C}} = \boldsymbol{C}$, $\hat{\boldsymbol{D}} = \boldsymbol{D}$, the dynamic of the convergence of the estimated states to the real ones is regulated by the following equation:

$$\frac{\mathrm{d}\boldsymbol{\Delta x}}{\mathrm{d}t} = \left(\boldsymbol{A} - \boldsymbol{K}\boldsymbol{C}\right)\boldsymbol{\Delta x} \tag{2.26}$$

where $\boldsymbol{\Delta x} = \boldsymbol{x} - \hat{\boldsymbol{x}}$ is the discrepancy between observed and real system states. In case of flux observer for electrical drives, $\boldsymbol{x} = \boldsymbol{\lambda}$, $\boldsymbol{y} = \boldsymbol{i}$ and $\boldsymbol{u} = \boldsymbol{v}$.

2.3.1 Observer in dq Coordinates

Considering the machine equations in rotor reference frame (2.9) and the rotor position measured with encoder, the observer matrices can be retrieved:

$$\frac{\mathrm{d}\hat{\boldsymbol{\lambda}}_{\mathrm{dq}}}{\mathrm{d}t} = \boldsymbol{v}_{\mathrm{dq}} - R_{\mathrm{s}}\boldsymbol{i}_{\mathrm{dq}} - \omega\mathbf{J}\boldsymbol{i}_{\mathrm{dq}} + \boldsymbol{K}\left(\boldsymbol{i}_{\mathrm{dq}} + \boldsymbol{L}_{\mathrm{dq}}^{-1}\left(\hat{\boldsymbol{\lambda}}_{\mathrm{dq}} - \boldsymbol{m}_{\theta}^{dq}\lambda_{\mathrm{pm}}\right)\right) \tag{2.27}$$

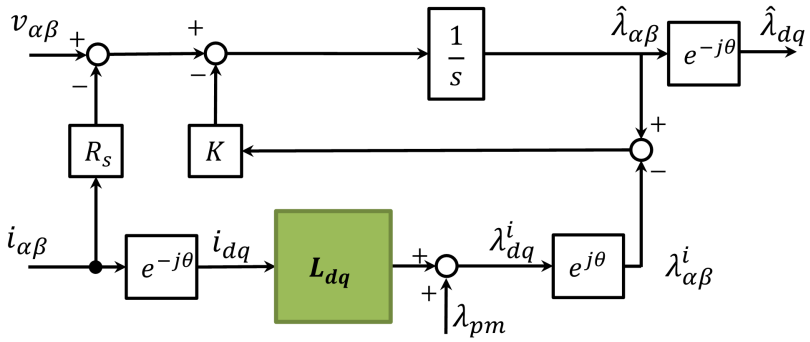

Figure 2.10: Block diagram for flux observer with flux error feedback in stator coordinates.

Such observer corresponds to the block diagram structure reported in Figure 2.9. The observer feedback is the difference between measured and estimated current $\left(\boldsymbol{i}_{\mathrm{dq}} - \hat{\boldsymbol{i}}_{\mathrm{dq}}\right)$, where $\hat{\boldsymbol{i}}_{\mathrm{dq}}$ is obtained from the inverse magnetic model.

2.3.2 Observer in $\alpha\beta$ Coordinates

Many works in the literature, including [9–11, 13, 15, 31–34], preferred to transfer the flux observer to $\alpha\beta$ reference frame, obtaining the scheme report in Figure 2.10. With proper selection of the observer gains, the two observer schemes are equivalent if correct position is assumed and magnetic saturation is omitted, as demonstrated in [35]. In this scheme, the feedback signal is the discrepancy between the observed flux $\hat{\boldsymbol{\lambda}}_{\alpha\beta}$ and the flux estimation based on the current model $\boldsymbol{\lambda}^i_{\alpha\beta}$. This structure will be adopted in all the sensorless control techniques presented in Chapter 4.

The gain matrix can be chosen to be diagonal:

$$\boldsymbol{K} = g\mathbf{I} \tag{2.28}$$

where g is a real positive number. With this assumption, the flux observation dynamic is governed by the following expression:

$$\hat{\boldsymbol{\lambda}}_{\alpha\beta} = \frac{s}{s+g}\left(\frac{\boldsymbol{v}_{\alpha\beta} - R_{\mathrm{s}}\boldsymbol{i}_{\alpha\beta}}{s}\right) + \frac{g}{s+g}\boldsymbol{\lambda}^i_{\alpha\beta} \tag{2.29}$$

It can be noted that the observed flux is the aggregate of two contributions: the first is given by the integral of the electromotive force, while the second comes from the magnetic (or current) model. According to (2.29), the voltage integration contribution is high-pass-filtered, meaning that it is

predominant during fast transients and in steady state condition when the rotor speed is sufficiently higher than g. Conversely, the term $\boldsymbol{\lambda}^i_{\alpha\beta}$ is low-pass-filtered, therefore it is relevant only in low speed steady state.

This is particularly useful for industrial drives applications, where the estimated voltage, based on the inverter commands, is unreliable at low speed where the inverter non-linear effects become more significant. Conversely, the flux estimate $\boldsymbol{\lambda}^i_{\alpha\beta}$ is based on the current measurement, which is unavoidably sampled with one switching cycle delay. This time delay is usually not significant at low speed, but it can result in inaccurate flux observation when the speed increases. In other words, both the contributions are exploited in the speed region where they are more reliable.

2.4 Model Based Flux and Position Observer

Up to now, the rotor position was assumed to be measured, and therefore correct. In case of encoderless drives, the rotor position and speed become part of the machine states that have to be estimated, affecting the observer dynamic. The flux observers report in Figure 2.9 and 2.10 are modified adopting $\hat{\omega}$ and $\hat{\theta}$ for coordinate rotations.

In sensorless control scheme, the estimation of flux linkage and rotor position are often merged into a unique observer structure. In this case, the dynamics of the two estimations are necessarily linked. Three examples of combined flux and position observers are report in the following, and will be extensively discussed in Section 4.3.

2.4.1 Sensorless Speed Adaptive Observer

One of the possible methods to extract rotor position and speed is to modify the flux observer by adding a speed adaptation law, as represented in Figure 2.11. This method has been used, as an example, in [36, 37].

The speed adaptation law combines the measured current and observed flux to obtain an error signal ϵ:

$$\epsilon = G_\omega \left(\boldsymbol{i}_{\hat{\mathrm{d}}\hat{\mathrm{q}}}, \hat{\boldsymbol{\lambda}}_{\mathrm{dq}} \right) = - \left(\boldsymbol{L}_{\mathrm{dq}} \boldsymbol{i}_{\hat{\mathrm{d}}\hat{\mathrm{q}}} + \lambda_{\mathrm{pm}} - \hat{\boldsymbol{\lambda}}_{\mathrm{dq}} \right)^T \mathbf{J} \boldsymbol{K}_{\boldsymbol{\omega}} \tag{2.30}$$

where $\boldsymbol{K}_{\boldsymbol{\omega}}$ is a projection vector, which may be constant or adapted with the working point. As can be seen, ϵ is basically a manipulation of the discrepancy between the flux estimates coming from voltage and current model. This error signal is driven to zero my means of a PI regulator, obtaining the estimated speed $\hat{\omega}$. Finally, the integral of $\hat{\omega}$ gives the observed position $\hat{\theta}$,

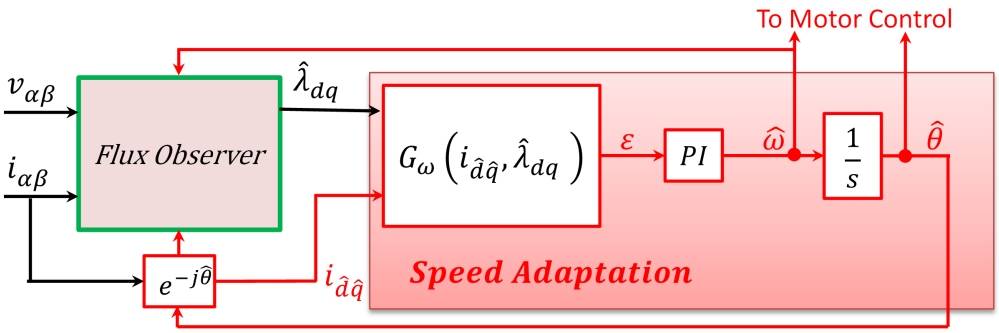

Figure 2.11: Block diagram for sensorless flux and position observer with speed adaptation law.

which is driven back to the motor control and flux observer, where is used for coordinates transformations.

2.4.2 Sensorless Observer in $\alpha\beta$ Coordinates

Considering the observer in Figure 2.10, eventual inaccuracy in rotor position estimation affects in different ways the current and voltage based branches of the observer. An error in $\boldsymbol{\lambda}^{i}_{\alpha\beta}$ arises because the magnetic model is applied in wrong reference frame. Conversely, the voltage model in $\alpha\beta$ frame does not contain any position or speed dependent term, therefore it is inherently immune from position or speed estimation error. In other words, the $\hat{\boldsymbol{\lambda}}_{\alpha\beta}$ flux is independent from the accuracy of position estimation when the rotor speed is sufficiently high. This is particularly useful for example in case of DFVC, where the $\hat{\boldsymbol{\lambda}}_{\alpha\beta}$ vector is adopted for definition of $d_{\mathrm{s}}q_{\mathrm{s}}$ direction. Anyway, in presence of position error also the back-EMF integration is transferred to deviated coordinates when written in dq frame $\hat{\boldsymbol{\lambda}}_{\mathrm{dq}}$.

A feasible alternative to the speed adaptive observer is to combine the two flux estimates to directly retrieve the rotor position. This solution was adopted in [10, 31, 32, 38]. By manipulating the equations of the rotation transformation, the observed flux $\hat{\boldsymbol{\lambda}}_{\alpha\beta}$ and the flux estimate coming from the current model $\boldsymbol{\lambda}^{i}_{\hat{\mathrm{d}}\hat{\mathrm{q}}\mathrm{h}}$ are adopted:

$$\begin{cases} \sin\hat{\theta}^{\mathrm{HS}} &= \dfrac{\lambda^{i}_{\hat{\mathrm{d}}}\hat{\lambda}_{\beta} - \lambda^{i}_{\hat{\mathrm{q}}}\hat{\lambda}_{\alpha}}{\left|\boldsymbol{\lambda}^{i}_{\hat{\mathrm{d}}\hat{\mathrm{q}}}\right|\left|\hat{\boldsymbol{\lambda}}_{\alpha\beta}\right|} \\ \cos\hat{\theta}^{\mathrm{HS}} &= \dfrac{\lambda^{i}_{\hat{\mathrm{d}}}\hat{\lambda}_{\alpha} + \lambda^{i}_{\hat{\mathrm{q}}}\hat{\lambda}_{\beta}}{\left|\boldsymbol{\lambda}^{i}_{\hat{\mathrm{d}}\hat{\mathrm{q}}}\right|\left|\hat{\boldsymbol{\lambda}}_{\alpha\beta}\right|} \end{cases} \tag{2.31}$$

Differently from (2.30), an estimate of rotor position is directly obtained. The speed can be retrieved from the discrete derivative of $\hat{\theta}^{\mathrm{HS}}$. Anyway, both

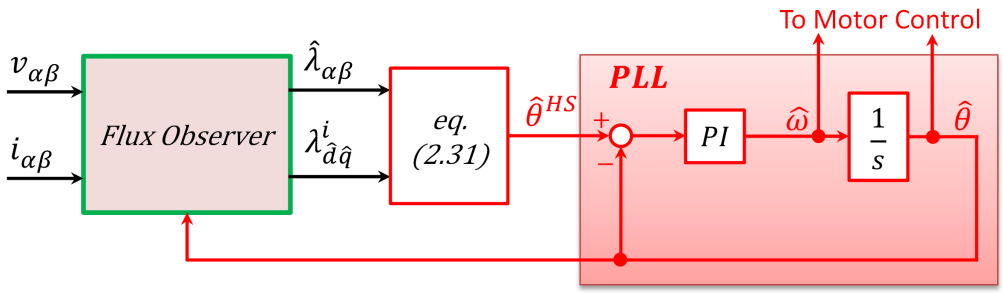

Figure 2.12: Block diagram of flux and position observer according to (2.31).

these position and speed estimates are highly sensitive to several sources of noise, such as in current measurement. For obtaining more reliable and smoother $\hat{\theta}$ and $\hat{\omega}$, a Phase Locked Loop (PLL) structure is usually added in cascade to the flux observer. The resulting flux and position observer is report in Figure 2.12.

This observer structure was demonstrated to be equivalent to the one described in Section 2.4.1 under proper choice of observer gains [35].

2.4.3 Active Flux Concept

The Active Flux (AF) concept was proposed for the first time in [33] and exploited in [9] for sensorless control of SyRM. The idea behind it is to turn an anisotropic ac machines into an equivalent non-salient one. To explain this concept, the magnetic model of the machine must be written in terms of apparent inductances as in (2.9). The AF is a vector defined as:

$$\boldsymbol{\lambda}^{\mathrm{AF}} = \boldsymbol{\lambda}_{\mathrm{s}} - L_{\mathrm{q}}\boldsymbol{i}_{\mathrm{s}} \tag{2.32}$$

where the stator flux vector $\boldsymbol{\lambda}_{\mathrm{s}}$ and current $\boldsymbol{i}_{\mathrm{s}}$ can be expressed either in stator or rotor reference frame. For a SyR machine, where λ_{pm}=0, if dq coordinates are adopted, neglecting cross-saturation effects and exploiting complex representation of the vector quantities, (2.32) turns to be:

$$\begin{aligned}\boldsymbol{\lambda}^{\mathrm{AF}} &= \lambda_{\mathrm{d}} + j\lambda_{\mathrm{q}} - L_{\mathrm{q}}\left(i_{\mathrm{d}} + ji_{\mathrm{q}}\right)\\ &= L_{\mathrm{d}}i_{\mathrm{d}} + jL_{\mathrm{q}}i_{\mathrm{q}} - L_{\mathrm{q}}\left(i_{\mathrm{d}} + ji_{\mathrm{q}}\right)\\ &= \left(L_{\mathrm{d}} - L_{\mathrm{q}}\right)i_{\mathrm{d}}\end{aligned} \tag{2.33}$$

Therefore, the q component of the vector $\boldsymbol{\lambda}^{\mathrm{AF}}$ is null, i.e. $\boldsymbol{\lambda}^{\mathrm{AF}}$ is aligned with the d axis. So, $\boldsymbol{\lambda}^{\mathrm{AF}}$ can be conveniently calculated in $\alpha\beta$ reference frame, and its phase corresponds to the rotor position, as illustrated in Figure 2.13.

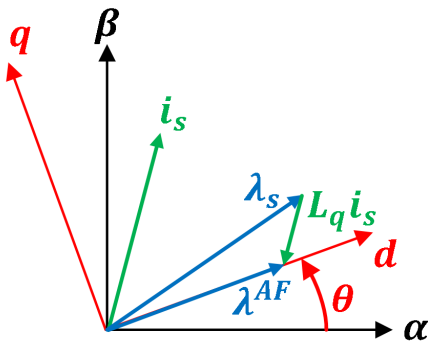

Figure 2.13: Visual representation of active flux concept in vectorial form.

$$\begin{cases} \sin\hat{\theta}^{\mathrm{HS}} & = \dfrac{\lambda_\beta^{\mathrm{AF}}}{\left|\boldsymbol{\lambda}^{\mathrm{AF}}\right|} & = \dfrac{\hat{\lambda}_\beta - L_\mathrm{q} i_\beta}{\left|\boldsymbol{\lambda}^{\mathrm{AF}}\right|} \\ \cos\hat{\theta}^{\mathrm{HS}} & = \dfrac{\lambda_\alpha^{\mathrm{AF}}}{\left|\boldsymbol{\lambda}^{\mathrm{AF}}\right|} & = \dfrac{\hat{\lambda}_\alpha - L_\mathrm{q} i_\alpha}{\left|\boldsymbol{\lambda}^{\mathrm{AF}}\right|} \end{cases} \tag{2.34}$$

Similarly to Section 2.4.2, this position estimation can be either directly used for dq axes definition or sent to a PLL for more robust position and speed extraction, at the cost of limiting the bandwidth of position tracking. Figure 2.14 illustrates the resulting active flux observer. Normally, a fixed L_q is used. In [9], the value of L_q was online varied, improving the reliability of the estimated position as detailed in Section 4.3.

The vector $\boldsymbol{\lambda}^{\mathrm{AF}}$ can also be seen as the total torque producing flux, while i_q becomes the torque producing current. Indeed, if the torque equation is written in terms of inductances:

$$T = \frac{3}{2} p \left(L_\mathrm{d} i_\mathrm{d} i_\mathrm{q} - L_\mathrm{q} i_\mathrm{d} i_\mathrm{q}\right) = \frac{3}{2} p \, \boldsymbol{\lambda}^{\mathrm{AF}} \, i_\mathrm{q} \tag{2.35}$$

It should be noted that, in the original formulation of [33], the AF concept was written for IPM machines, therefore the convention of the dq coordinates were reversed respect to the one adopted for SyRM (see Figure 2.2). With the IPM convention, i.e. d axis on the minimum inductance direction, despite the different meaning of the terms, the vector $\boldsymbol{\lambda}^{\mathrm{AF}}$ still drops on the d axis:

$$\begin{aligned} \boldsymbol{\lambda}^{\mathrm{AF}} &= \lambda_\mathrm{d} + j\lambda_\mathrm{q} - L_\mathrm{q}\left(i_\mathrm{d} + j i_\mathrm{q}\right) \\ &= L_\mathrm{d} i_\mathrm{d} + \lambda_\mathrm{pm} + j L_\mathrm{q} i_\mathrm{q} - L_\mathrm{q}\left(i_\mathrm{d} + j i_\mathrm{q}\right) \\ &= \left(L_\mathrm{d} - L_\mathrm{q}\right) i_\mathrm{d} + \lambda_\mathrm{pm} \end{aligned} \tag{2.36}$$

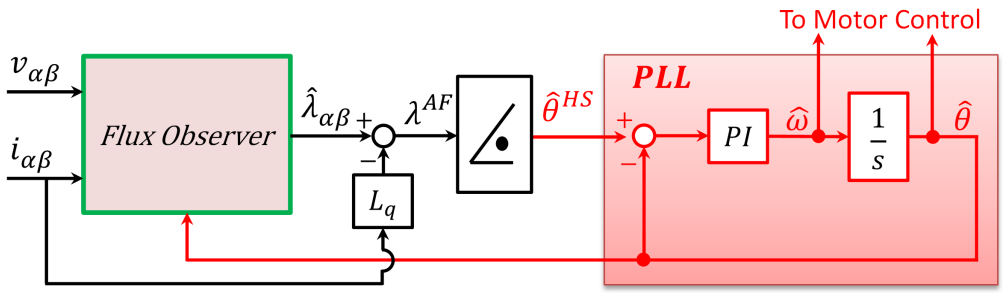

Figure 2.14: Block diagram of flux and position observer based on active flux concept.

2.4.4 Conclusion

In both the techniques of Sections 2.4.1 and 2.4.2, the rotor position information is obtained from the discrepancy between the flux estimates coming from the current model and voltage model. Both these formulations are reliable only when the speed is sufficiently high so that the observed flux $\hat{\boldsymbol{\lambda}}_{\alpha\beta}$ is based on EMF integration, i.e. above the cross-over frequency g. Below this speed, both $\hat{\boldsymbol{\lambda}}_{\alpha\beta}$ and $\boldsymbol{\lambda}^{i}_{\hat{\mathrm{dqh}}}$ are based on current model, therefore the error $\epsilon = G_{\omega}\left(\boldsymbol{i}_{\hat{\mathrm{dq}}}, \hat{\boldsymbol{\lambda}}_{\mathrm{dq}}\right)$ computed in (2.30) is almost zero independently by the position error. Similarly, (2.31) cannot converge to the rotor position.

Considering the active flux concept, (2.32) gives a reliable $\hat{\theta}$ only if $\hat{\boldsymbol{\lambda}}_{\alpha\beta}$ is based on the back-EMF integration. If the term $L_{\mathrm{q}}\boldsymbol{i}_{\mathrm{s}}$ is subtracted from $\boldsymbol{\lambda}^{i}_{\hat{\mathrm{dq}}}$, any correlation with the real θ is lost. Therefore, also in this case $\hat{\theta}$ can be observed only when the speed overcomes g.

In turn, any model based technique is able to observe the $\hat{\theta}$ only at sufficiently high speed, while the position information is not reliable at low speed and completely vanishes at standstill. For this reason, saliency based position tracking algorithms are adopted for low speed sensorless control, aiming to detect the dq directions based on rotor anisotropy. The literature provides a wide variety of these techniques, which will be extensively discussed in Section 4.1. The method adopted in [9] and [10] will be analyzed in Section 4.2.

Chapter 3

Self-Commissioning of SyRM and PM-SyRM at Standstill

Part of the work described in this Chapter has been previously published in [4–8, 11, 12, 14].

The knowledge of motor parameters is mandatory for most of the advanced control techniques present in the literature. In particular, the current-to-flux relationship must be accurately known for valid flux estimation based on the measured current, adopted in most of the flux observers.

In case of SPM machines, the isotropic nature of the rotor usually allows to adopt a constant inductance model with only one parameter L_s, which may slightly vary depending on the applied current due to saturation effects. In case of IPM machines, and even more for PM-SyR and SyR motors, the salient rotor structure requires at least two parameters $L_\mathrm{d}, L_\mathrm{q}$ to be estimated. As discussed in Section 2.1, the constant inductance model often fails with high anisotropy motors such as SyR and PM-SyR. Therefore, the use of those machines impose the knowledge of the machine flux map $\boldsymbol{\lambda}_\mathrm{dq}(\boldsymbol{i}_\mathrm{dq})$.

For several practical reasons, the characteristics of non-linear PMSM are usually not provided by the motor manufacturer, which often declares only a few rated values in the nameplate, such as nominal torque, speed, current, voltage and efficiency. Modern PMSMs do not even have a reference standard for testing and determination of key parameters, with the exception of the IEEE guidelines [39]. One of the main reasons is the wide variety of different synchronous machine types that can be designed [16].

Several methods for accurate measurement of all the mentioned motor parameters have been presented [40]. All such methods require dedicated testing hardware, such as torque meter, voltage probes, oscilloscopes and so on. In turn, a dedicated test bench must be equipped. For this reason, such

approaches are feasible for those motors designed for a specific application, but way less for general purpose, industrial drives. Examples of the former case are high power applications, more electric aircraft and electric vehicles. For applications such as pumps, fans and home appliances, it is not cost efficient to singularly test every motor in a dedicated laboratory. It is possible to test random samples of a large production and then extend the data to all the other motors of the same chain. However, such low cost applications often present manufacturing variability and parameters deviation, which might affect the motor characteristics and the control accuracy.

For all these cases, self-commissioning techniques (also called self identification) are preferred. With such methods, it is assumed that the knowledge of machine parameters is initially limited to the nameplate data. Specific automatic tests are included in the start-up routine of the motor. The results of these tests must give sufficient information to extract all the necessary motor parameters, including stator resistance, inverter non-linear effect characteristic and flux maps. These data are used to properly tune the control strategy. The self commissioning tests are usually performed only the first time the motor is connected to the inverter; the obtained results can be stored in the control memory for subsequent usage. A review of the self-commissioning methods is given in [12, 41].

3.1 Definition of Self-Commissioning

Different applications may impose several constrains to the self commissioning test sequence:

- The self-commissioning test must provide all the necessary motor parameters with sufficient accuracy for proper tuning of the control.
- Limited or null knowledge of the motor characteristics is assumed before the identification stage, so the commissioning tests must require limited or automatic tuning and minimal intervention from the final user.
- The control and post-processing algorithms should be enough computationally simple to be executed in low cost micro-controllers.
- The self-identification must not imply extra hardware respect to the drive itself, i.e. the inverter, measurement of the phase currents and DC-link voltage.
- Despite many techniques found in the literature require a position transducer, the self-commissioning is often needed in encoderless drives, so also the self-identification tests must be performed sensorless.

- A load may be already connected to the motor, therefore it is imposed that movement is unnecessary during the commissioning stage (standstill constraint).
- In other cases, the shaft is free or torque is negligible around standstill, e.g. with pumps or fans. This excludes those identification methods requiring to lock the rotor (no rotor locking constraint).
- Many applications, e.g. washing machines, require the self-identification stage to be performed as fast as possible, e.g. in few seconds or less.

In this dissertation, specific focus will be given to the self-identification of the flux maps. Self-commissioning algorithms also include the evaluation of inverter voltage drop as a function of the phase current and measurement of the stator resistance, adopted as an example to compute the back-emf in any flux observer. Interesting works about these two issues, not treated here, can be found in [42–47].

3.2 State of the Art of Synchronous Motor Commissioning

As detailed in Section 2.2, most of the motor control strategies present in the literature are sensitive to parameter mismatch, especially the magnetic model. Analysis of this sensitivity is given in [48–53]. Moreover, it was demonstrated in [54–58] that parameter uncertainty is even more critical in case of sensorless control.

Several solutions for parameter identification of IMs are well defined by the IEEE standard [59] and self-commissioning tests [12, 60], but will not be further investigated here. Conversely, the identification procedure for synchronous machines is still not completely defined, mostly due to the wide variety of motor types present on the market. This Section provides a deep literature review of the existing magnetic model identification techniques for synchronous machines [12].

3.2.1 Finite Element Analysis

If a Finite Element Analysis (FEA) model of the machine is available, i.e. at the machine design stage, a universal computation method for defining the inductances of multiphase PM machines is given in [61], while different methods are used in [62,63]. Moreover, in [64,65] the magnetic characteristic is computed considering the winding function theory. Despite the analytical

methods like [61–65] can provide interesting initial information on the machine behavior, an experimental test is often needed to prove their accuracy.

3.2.2 With Linear Power Supply

Several techniques have been proposed in the scientific literature for identifying the magnetic model of synchronous machines requiring sinusoidal power supplies or signal generators [66–70]. Some of these techniques result very accurate, but since they require dedicated supply and equipment they are usually not compatible with industrial constrains, so their application is restricted to laboratory environment. Several of these techniques have been reviewed in [71], while a comparison with identification methods supplied by power converters is given in [72].

3.2.3 With the Power Converter

A wide number of Authors proposed offline magnetic model identification techniques only requiring the power converter of the drive. The works [40, 73–79] imply a closed loop current control imposing an appropriate current vector of variable magnitude along a predetermined direction with respect to rotor d axis and observe the machine response. These methods require a position transducer, therefore they are not suitable for a full sensorless approach. Moreover, in all those papers torque is inherently produced, either because the current is not parallel to the magnets in PMSMs or because the cross-saturation has to be evaluated in SyRMs, so both d and q axes are excited. For this reason, [40,74,76–78] also imply that the rotor must be free to rotate, while [73] requires the rotor to be mechanically locked. Therefore, these methods are not strictly considered self-commissioning techniques.

If a prime mover is available, the method described in [40] is often considered one of the most accurate for determining the machine magnetic model. The prime mover maintains a constant rotor speed, while the current vector is moved in a grid of points along the entire dq plane, obtaining the complete saturation and cross-coupling characteristics. Appropriate combination of positive and negative current is applied in order to accurately compensate eventual mismatch in stator resistance estimation and inaccuracies in inverter compensation. In addition, the method is almost immune from iron loss effects, since the (constant) test speed is relatively low. Similar strategy was adopted in [73], but with the necessity of mechanically locking the rotor, and in [79] implying a quantum genetic algorithm. Another method exploring the full dq plane is presented in [76] without the necessity of a

Table 3.1: Classification of identification methods.

	Numerical	Dyno	Standstill/Locked	Free shaft
PMSM	[61–63, 80]	[40, 66, 67, 77–79]	[68–70, 73, 75]	[74]
PMSM s.c.			[8, 81–84]	[76, 85]
SyRM	[64, 65]	[40]		
SyRM s.c.			[4–7, 14, 86–89]	

prime mover, where the Authors apply a sequence of current vectors similar to [40], obtaining a series of accelerations and decelerations. The same equations [40] are used to estimate the flux in the speed range where the back-emf are sufficiently higher than the resistive and inverter voltage drops, while the goodness of the acquired flux maps is determined by estimating the inertia at every sampling point. Despite this method is accurate, it may result in too high acceleration and runaway condition for high torque, low inertia machines.

3.2.4 Self Commissioning

The above mentioned flux identification methods require that the motor must be disconnected from the load, therefore, strictly speaking, they are not considered self-commissioning methods. Despite the techniques in [80–85] satisfy some of the self-commissioning constrains defined in the introduction of Chapter 3, their universal applicability and accuracy is still not proved. Moreover, most of these methods require a position transducer. As an example, [85] identifies the inductances and mechanical parameters of PMSMs, but neglecting magnetic saturation and requiring shaft rotation. Conversely, [80] takes into account the effects of inductance saturation and nonlinear inverter voltage drop, but it is based on open-loop voltage injection that may trigger overcurrent protection in case of low-impedance machines. The d axis inductance was well measured in [82], without exploring the full dq plane.

In [81], the complete flux maps of IPM and SPM were obtained. The self-axis saturation curves are retrieved by injecting a closed loop controlled HF sinusoidal current with variable amplitude in d and q axes separately, while the flux is estimated by integrating the back-EMF. Then, cross-saturation is evaluated by injecting a DC current in one axis and HF current in the other one. Similarly, in [83] the differential inductances are estimated in

the full *dq* plane by injecting a HF sinusoidal current superimposed to a DC fundamental current vector. The HF component is used for inductance estimation, while the DC component defines the working point. A different method is presented in [86], where a square-wave current is injected in the two axes separately and the fluxes are computed from the transient response. Differently from [81, 83], iron losses are also taken into account in [86].

3.2.5 Proposed Method: Bipolar Voltage Pulses

Several authors, e.g. [73, 87] for IPM and [5, 14, 86, 88, 90] for SyRM, identified the flux maps exciting the machine with bipolar voltage pulses. The methods [73, 86, 87] reach the steady state condition by applying low voltage steps, so they are sensitive to inaccurate compensation of inverter and resistive voltage drops. Moreover, the rotor must be locked. Conversely, [5, 88, 90] explored the full *dq* plane applying voltage pulses in the order of magnitude of the rated voltage, thus resulting almost insensitive to parameters deviation. Instead of reaching the steady state, the flux is estimated from the transient response. The analytical model proposed in [88] resulted accurate for extracting the self-axis saturation characteristic, but requires a wide number of parameters to be estimated and describes the cross-saturation effect with moderate accuracy. The method was combined with a different magnetic model in [90], where the model parameters are retrieved using a genetic algorithm. The work in [5] adopted a complete algebraic magnetic model [89] with only five parameters which resulted accurate in several tested SyRM. The parameters are obtained with separate post-processing based on analytical solution. The obtained flux maps, compared with the reference ones measured according to [40], resulted very accurate also in the high cross-saturation region. Also, in [14] the identification procedure was augmented with HF injection for online position tracking, considerably extending the measurement range, while in [8] the identification was extended to PM-SyR machines. The method is completely encoderless and performed at free-shaft without rotor movement, thus fulfilling the self-commissioning constrains.

3.2.6 Evaluation of PM Flux Linkage

In case of PMSM, the estimation of flux linkage contribution given by the permanent magnets has to be included in the self-commissioning. The most common technique is to rotate the machine at sufficiently high speed and evaluate the back-emf when the stator current is null. This can be done either using an oscilloscope to measure the stator voltage at open windings or relying on the reference voltages when the current is closed loop forced to zero.

However, this method does not fulfill the constrains of self-commissioning procedure, since the shaft rotation may not be allowed in some applications. The magnet flux was estimated in [83], but requiring a position transducer and a closed loop speed control. Accurate quasi stand still method was proposed in [8], while [91] exploited limited shaft rotation, e.g. 180°.

3.2.7 Online Parameters Adaptation

Several authors also proposed dedicated techniques for online estimation of the machine parameters during operation. As a few examples, [58, 92] developed a technique for online adaptation of the stator resistance, to take into account its variation with windings temperature. In [22, 93] the motor inductances are online estimated. Also, MTPA trajectory is online computed or updated in [93–96].

Finally, it should be remarked that offline parameter identification or self-commissioning can also be used as a diagnosis tool, identifying eventual asymmetries in the machine caused by fault conditions [97].

3.3 Commissioning of SyR Motors

The high anisotropy of SyRM makes them appealing for sensorless control. As known, SyRM magnetic model presents highly non-linear characteristic. Moreover, the cross-coupling between d and q axes is in average more pronounced than in PMSMs, so the flux linkage saturation depends on both current components. If not properly taken into account, this phenomenon affects sensorless control at low speed leading to steady state position error, as will be better detailed in Section 4.2. For these reasons, the self commissioning of SyRMs must provide the complete flux maps $\boldsymbol{\lambda}_{\mathrm{dq}}(\boldsymbol{i}_{\mathrm{dq}})$.

This section is organized as follow. Section 3.3.1 describes the proposed square wave magnetic model self-identification test sequence and flux computation. In Section 3.3.2 the test is augmented with high frequency injection for online position tracking, increasing the test stability and reliability and considerably extending the measurement domain in q axis direction. Section 3.3.3 analyzes all the phenomena that may produce an error in flux computation, proving the substantial robustness of the method against inaccurate parameter estimation. In Section 3.3.4 a complete and automatic tuning procedure is proposed, both in the case the test is executed with or without being augmented with HF injection. All these Sections include experimental results based on a reference motor, called SR2kW2. The commissioning test sequence was also validated on several other SyR motors,

whose nameplates are report in Table 3.3. The tests on these motors are report in the dedicated Section 3.3.5. The magnetic model self-identification was also implemented in a high current motor prototype (SR250kW), which will be treated separately in Section 5.1 for sake of clarity.

3.3.1 Bi-polar High Voltage Steps at Standstill

In this section, the square wave voltage injection technique for magnetic model self-identification is analyzed and experimentally validated on a reference SyRM.

This test can be performed at free-shaft, despite an eventual connected load would increase the mechanical inertia and friction, further improving its robustness. Anyway, even if the rotor is free to rotate, it does not move during the test sequence. In this way, both stand-still and free-shaft conditions are respected. Moreover, no mechanical transducer is required, so the test also fulfills the sensorless constrain. Therefore, this self-identification method works in the most demanding conditions. Obviously, the eventual presence of an encoder and/or the possibility to lock the rotor would make the identification even more reliable.

This section describes the test sequence in case of encoderless drives. At first, the initial rotor position θ_0 is evaluated. This can be done aligning the rotor along a predefined position by injecting a DC current (parking), if slight rotor movement is permitted. Otherwise, one of the many methods present in the literature for determining θ_0 by injecting a high frequency signal can be used [98–101]. The various techniques mainly differ for the type of injected signal, which can be voltage or current, pulsating or rotating, and for the demodulation process. In any case, θ_0 is evaluated without requiring a position transducer. Once θ_0 is determined, it is assumed that the rotor does not move, therefore θ_0 is used for dq reference frame determination through the complete identification session. It must be noted that eventual uncontrolled rotor movement may cause a test failure. The test sequence is divided in three steps, called test #1, test #2 and test #3.

3.3.1.1 Test #1: *d* Axis

A square-wave voltage is injected along the estimated $\hat{d}$ axis, according to the scheme report in Figure 3.1(a). The amplitude of the injected voltage is defined as V_{sc}. The polarity of the applied voltage is reversed whenever the magnitude of $|i_{\mathrm{d}}|$ overcomes a defined threshold value $I_{\mathrm{d,max}}$, according to a hysteresis mechanism. The q axis can either be controlled with null reference voltage ($v_{\mathrm{q}}^{*} = 0$) or by imposing zero current through a PI current

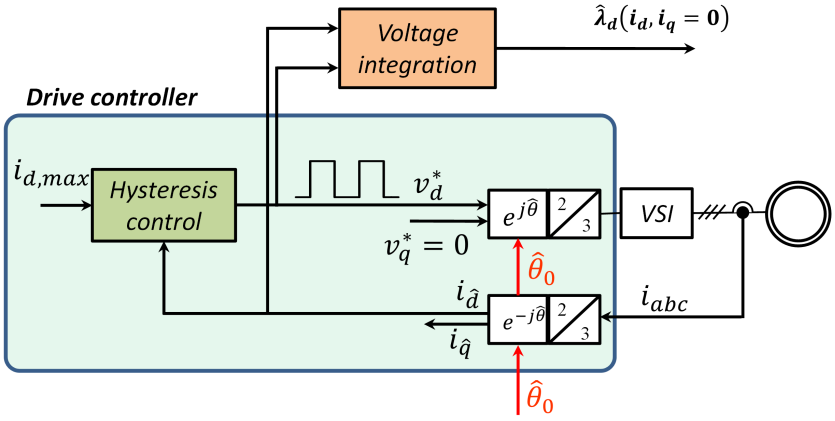

(a)

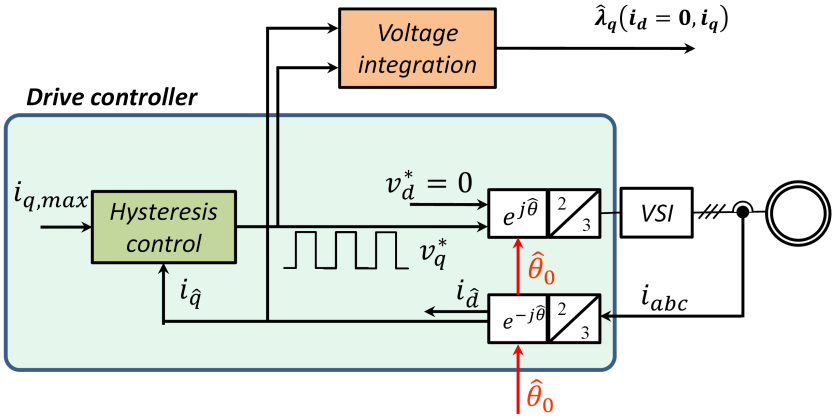

(b)

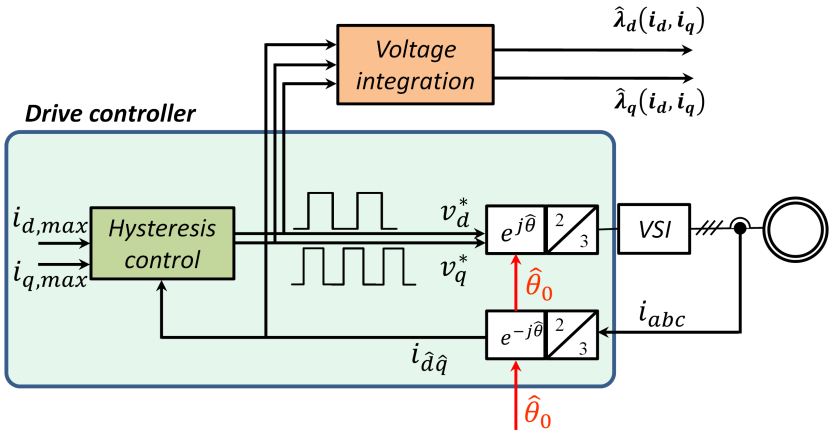

(c)

Figure 3.1: Block scheme for motor control during (a) test #1, (b) test #2 and (c) test #3. In every test, the initial position estimation is adopted for defining dq axes coordinates.

loop ($i_{\mathrm{q}}^{*} = 0$). The first option is easier for implementation, the latter is slightly more robust. Anyway, no relevant differences were experimentally observed in any tested motor, except SR250kW.

During this test, naming $\hat{V}_{\mathrm{th}}$ the estimated amplitude of the inverter voltage distortion term [102], the d axis self-characteristic is evaluated:

$$\hat{\lambda}_{\mathrm{d}}(i_{\mathrm{d}}, i_{\mathrm{q}} = 0) = \int v_{\mathrm{d}}^{*} - \hat{R}_{\mathrm{s}} i_{\mathrm{d}} - \hat{V}_{\mathrm{th}} sign(i_{\mathrm{d}}) dt \tag{3.1}$$

3.3.1.2 Test #2: *q* Axis

A similar test sequence is adopted for evaluating the q axis self-characteristic. In this case, the control scheme is modified as in Figure 3.1(b), where v_{q}^{*} is a square wave defined by a hysteresis mechanism on q axis current. Also in this case, v_{q}^{*} is reversed whenever $|i_{\mathrm{q}}|$ overcomes a defined threshold value $I_{\mathrm{q,max}}$ while the d axis can either be voltage or current controlled ($v_{\mathrm{d}}^{*} = 0$ or $i_{\mathrm{d}}^{*} = 0$). The q axis self-saturation curve is evaluated as:

$$\hat{\lambda}_{\mathrm{q}}(i_{\mathrm{d}} = 0, i_{\mathrm{q}}) = \int v_{\mathrm{q}}^{*} - \hat{R}_{\mathrm{s}} i_{\mathrm{q}} - \hat{V}_{\mathrm{th}} sign(i_{\mathrm{q}}) dt \tag{3.2}$$

3.3.1.3 Test #3: *dq* Cross-saturation

The hysteresis controllers of both the axes are activated, so both d and q axes are excited with square wave voltage reversed when the correspondent current overcome a threshold value (Figure 3.1(c)). In this way, the current follows a random path in the dq plane in the area limited by $I_{\mathrm{d,max}}$ and $I_{\mathrm{q,max}}$. This test completes the exploration of the flux saturation characteristic in the dq plane, evaluating the cross-coupling effect:

$$\hat{\lambda}_{\mathrm{d}}(i_{\mathrm{d}}, i_{\mathrm{q}}) = \int v_{\mathrm{d}}^{*} - \hat{R}_{\mathrm{s}} i_{\mathrm{d}} - \hat{V}_{\mathrm{th}} sign(i_{\mathrm{d}}) dt \tag{3.3}$$

$$\hat{\lambda}_{\mathrm{q}}(i_{\mathrm{d}}, i_{\mathrm{q}}) = \int v_{\mathrm{q}}^{*} - \hat{R}_{\mathrm{s}} i_{\mathrm{q}} - \hat{V}_{\mathrm{th}} sign(i_{\mathrm{q}}) dt \tag{3.4}$$

A clarification on the adopted terminology is necessary at this point. The same voltage magnitude can be adopted in the two axes, so the amplitude of the square wave voltage is called V_{sc}. Conversely, if different voltage amplitudes are adopted the correspondent values will be called $V_{\mathrm{d,sc}}$ and $V_{\mathrm{q,sc}}$.

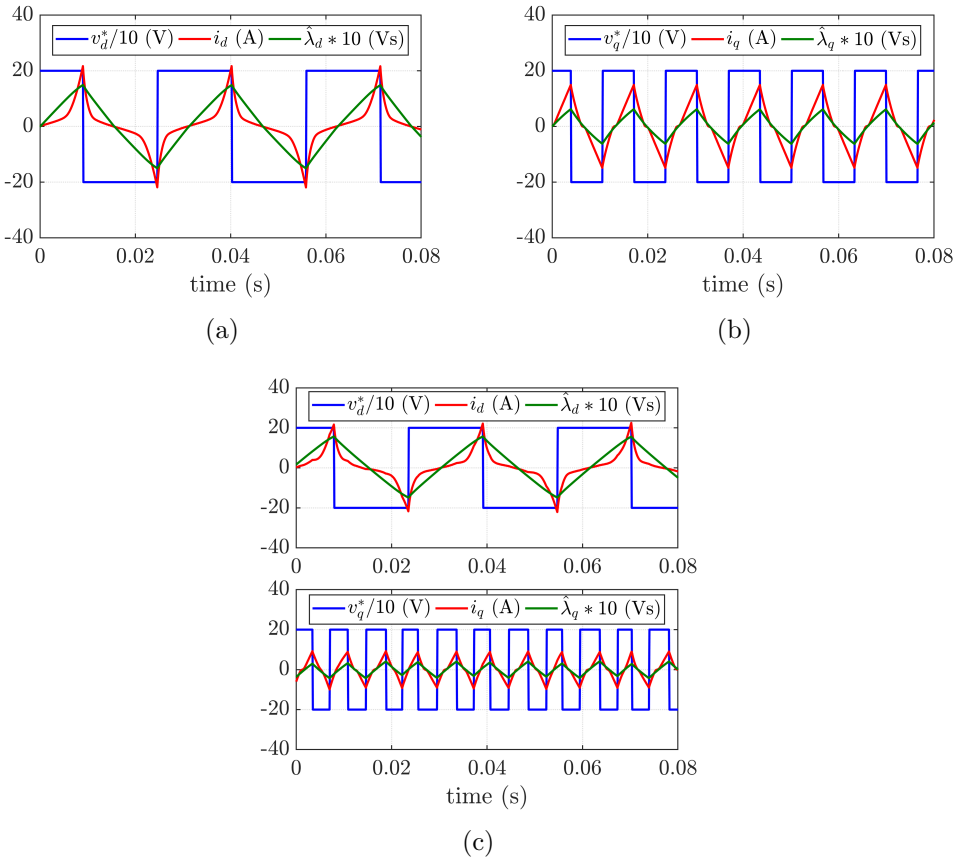

Figure 3.2: Experimental: time waveforms of reference voltage, current and estimated flux. (a) test #1 ($v_\mathrm{q} = 0; i_\mathrm{q} \approx 0$); (b) test #2 ($v_\mathrm{d} = 0; i_\mathrm{d} \approx 0$); (c) test #3. Motor: SR2kW2. Rated current: 5.08 A.

3.3.1.4 Features of the Identification Method

During test #1, only the d axis is excited, therefore torque is not produced and there is no risk of test failure because of rotor movement. This test is self-aligning, meaning that in case of a small inaccuracy in evaluating the initial position θ_0 the current along $\hat{d}$ axis tends to align the real d axis to the estimated $\hat{d}$, thus correcting the position error. Theoretically, also during test #2 torque is not produced, since only q axis is involved. Anyway, in this case in presence of an eventual initial misalignment a torque would be produced with such a polarity that tends to increase the position error (see Figure 3.10). Therefore, for a sufficiently high $I_{\mathrm{q,max}}$ the produced torque would overcome the mechanical friction, so the rotor may drift and start to rotate. In this case, the test would fail. In test #3 both axes are excited, so

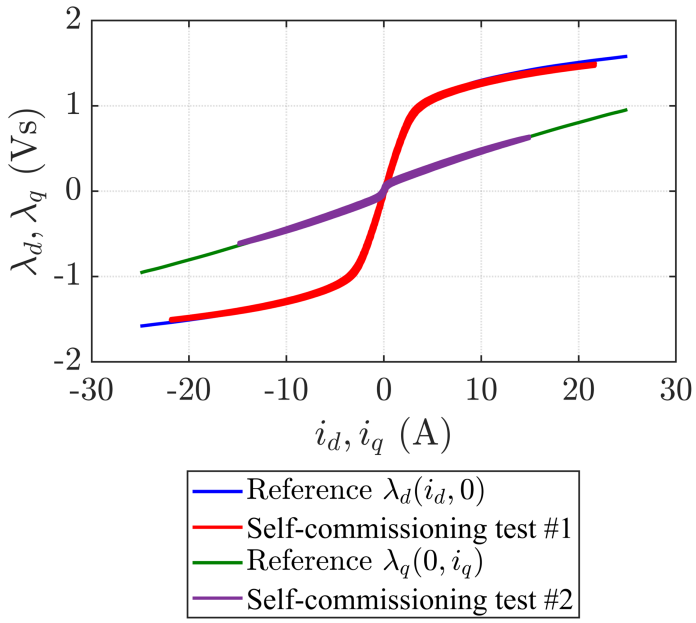

Figure 3.3: Experimental: comparison between self-axis reference flux maps and characteristics obtained in self-commissioning from test #1 and test #2. Motor: SR2kW2.

torque is necessarily produced. Anyway, its polarity is reversed every time i_d or i_q changes its sign, and its average value is null. If the torque is reversed at sufficiently high frequency, only small vibrations are produced without significant drift from the initial position. Therefore, the standstill condition is respected. The torque reversal frequency is defined by the applied voltage V_sc, the thresholds $I_\mathrm{d,max}$ and $I_\mathrm{q,max}$ and the motor inductances $L_\mathrm{d}, L_\mathrm{q}$.

This is the major shortcoming of the method, which limits the measurement range in q axis direction for test #2 and test #3. In any case, at least the rated current has been reached for every tested motor, as can be seen from the results. For some of the motors, the current measurement range in q axis was extended up to three times the nominal value. Appropriate method to exploit maximum measurement area will be described in Section 3.3.4. Moreover, the measurement range in q direction can be increased by adopting online position estimation, as will be described in Section 3.3.2.

The experimental results on the reference motor SR2kW2 are presented in the following. Extended validation of the self-commissioning method on several other motors is report in Section 3.3.5.

Figure 3.2 highlights the reference voltage and measured current during

the three tests of the self-commissioning stage, together with the real time estimated flux characteristic. It can be highlighted that, due to the digital delay introduced by the discrete time controller, the reference voltage of the time instant k is applied at $k+1$, therefore the sign of the current slope changes one sample after the correspondent reference voltage is reversed. In test #3, the d axis self-saturation characteristic was explored up to $i_\mathrm{d} = 22\ A$, while in test #2 the curve $\lambda_\mathrm{q}(0, i_\mathrm{q})$ was evaluated up to $i_\mathrm{q} = 14\ A$. In test #3, the saturation characteristic was explored up to $(i_\mathrm{d} = 22\ A; i_\mathrm{q} = 9\ A)$. Considering that the rated current of this motor is 5.08 A, we can assert that the test explored the magnetic model up to strong overload conditions. It can also be noted that the test sequence is very fast, since each test lasts only tens of milliseconds. Obviously, the test #2 is the fastest because $l_\mathrm{q} < l_\mathrm{d}$, so the current rising and falling transients are faster.

Figure 3.3 compares the reference flux characteristic in d and q axes with the measurement data obtained from test #1 and #2. The reference flux maps were measured according to [40]. As can be seen, the self-commissioning curves are well in accordance with the reference flux maps. Also, the two curves obtained in self-commissioning present almost the same slope close to zero current, due to local saturation of the structural ribs, as will be better detailed in Section 4.2.7. It must be noted that most of the techniques present in the literature are not accurate enough to observe this effect.

Figure 3.4 presents the surface of the reference flux maps and the measured points during test #3. Evaluating the accuracy of this test is less trivial. Anyway, it can be observed that the measurement points are partially above and partially below the reference surface. Therefore, with appropriate data manipulation it is possible to extract an average characteristic which is very close to the reference, as will be described in Section 3.4.

3.3.2 Bi-polar High Voltage Steps Augmented with HF Injection

In this section, the square wave voltage injection self-identification technique is modified in order to extend as far as possible the measurement area in the dq plane. It must be remarked that this implies additional tuning effort, so it is adopted only in case the test performed at open loop did not reach the desired measurement range in the current domain.

This is not an issue for test #1. Since, as said, this test is self-aligning, the measurement range can be extended as far as desired by increasing $I_\mathrm{d,max}$. Conversely, if $I_\mathrm{q,max}$ is set too high the tests #2 and #3 may fail, since the rotor may start to drift from its initial position starting to rotate.

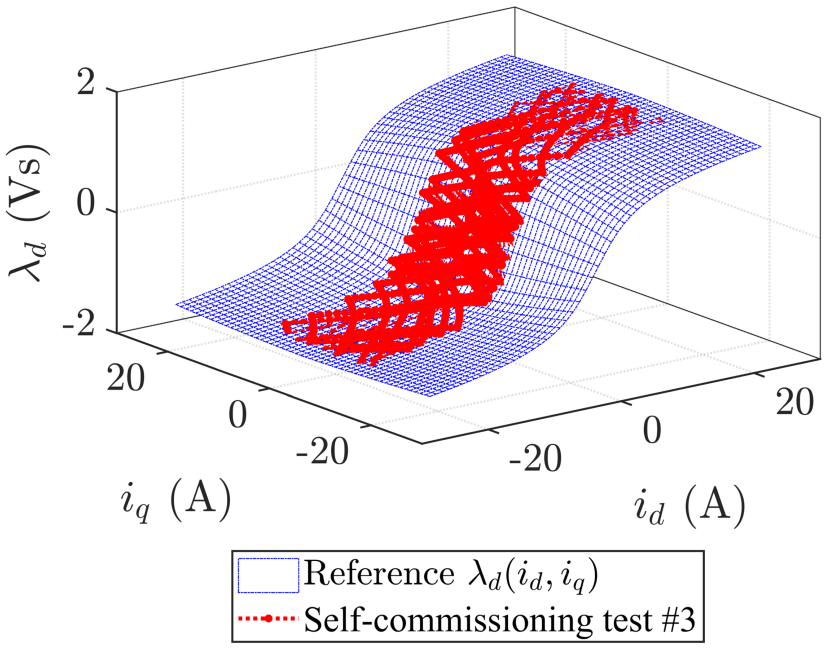

(a)

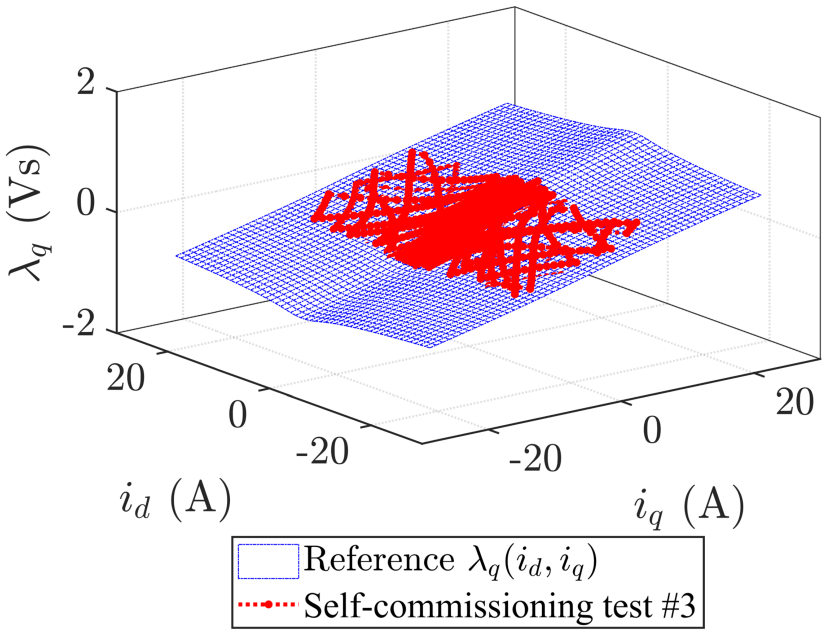

(b)

Figure 3.4: Experimental: comparison between self-axis reference flux maps and characteristics obtained in self-commissioning from test #3. (a) d axis; (b) q axis. Motor: SR2kW2.

To avoid such unwanted shaft rotation, the rotor position can be online estimated during the tests #2 and #3. The commissioning is performed without rotor movement, therefore model based sensorless techniques cannot be adopted, since they rely on back-EMF, which are proportional to the speed (see Section 4.3). A saliency based position tracking loop can be used instead, where a HF disturbance is deliberately injected into the motor and the machine response is demodulated, extracting the position information. Such techniques are largely adopted in both literature and industrial applications for low speed sensorless control [103]. The various techniques differ one from the other mainly because of the type of injected signal and the demodulation algorithms. A comprehensive description of such methods will be detailed in Section 4.2.

Unfortunately, the tuning of most of the saliency based sensorless techniques requires the knowledge of the flux maps, which is not available before the self-identification stage. Moreover, it is essential that the frequency of the injected signal must be much higher than the frequency of the square wave voltage injected for the self-identification test, in order to guarantee a good decoupling between test voltage and position observation.

The method presented in [104] was modified to satisfy both these requirements. In this position tracking technique, an HF voltage at half of the switching frequency $f_c = f_{sw}/2$ is injected in the estimated d axis, superimposed to the test fundamental voltage. Being at $f_{sw}/2$, and since its average value must be zero, also the injected HF signal is necessarily a symmetrical square wave, reversing its sign at every sampling time. In order to distinguish between the fundamental square wave voltage injected for flux maps identification and the HF injection applied for position tracking, the amplitude of the latter one will be called u_c. The choice of injecting at $f_{sw}/2$ permits the maximum possible decoupling between fundamental and HF signal.

The control scheme for test #2 and #3 are shown in Figure 3.5. The HF current response i_{qh} in estimated q axis is extracted through a band-pass filter. An approximated expression for i_{qh} can be retrieved as:

$$i_{qh} = \frac{u_c \left(l_d - l_q\right)}{2\omega_c l_d l_q} \sin\left(\omega_c t\right) \sin\left(2\Delta\theta\right) \tag{3.5}$$

where $\omega_c = 2\pi f_c$. Then, as shown in Figure 4.3, the demodulation algorithm consists of multiplying i_{qh} by $\sin\left(\omega_c t\right)$ and then low-pass filtering the obtained signal with a cut-off frequency ω_f. It must be noted that, being the injection at half of the switching frequency, at every sampling time we have $\sin\left(\omega_c t\right) = \pm 1$. The amplitude of the demodulated signal can be approximated as:

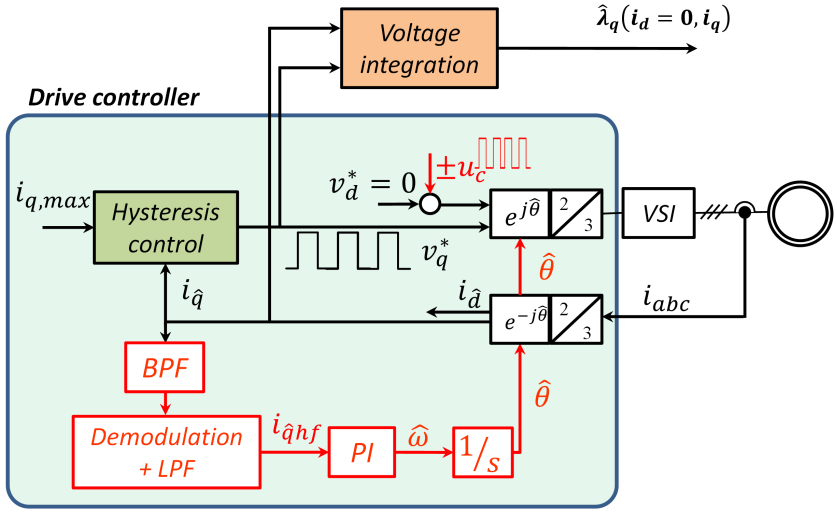

(a)

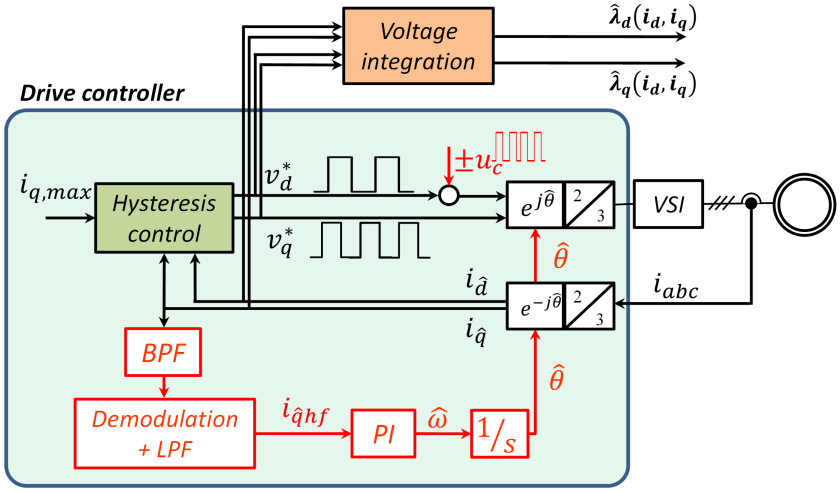

(b)

Figure 3.5: Block scheme for motor control during (a) test #2 and (b) test #3. In both cases, the test is augmented with HF voltage injection in d axis for online position estimation.

$$|i_{\mathrm{qh}}| = \frac{u_{\mathrm{c}}\,(l_{\mathrm{d}} - l_{\mathrm{q}})}{4\omega_{\mathrm{c}} l_{\mathrm{d}} l_{\mathrm{q}}} \sin(2\Delta\theta) \tag{3.6}$$

Therefore, considering $\Delta\theta \approx 0$, the amplitude of i_{qh} is almost proportional to the position error:

$$|i_{\mathrm{qh}}| \approx k_\epsilon \Delta\theta \tag{3.7}$$

where

$$k_\epsilon\left(i_{\mathrm{d}}, i_{\mathrm{q}}\right) = \frac{u_{\mathrm{c}}\left(l_{\mathrm{d}} - l_{\mathrm{q}}\right)}{2\omega_{\mathrm{c}} l_{\mathrm{d}} l_{\mathrm{q}}} \tag{3.8}$$

k_ϵ is a function of the working point in the dq current plane due to magnetic saturation. The derivation of (3.5) will be detailed in Section 4.2. By forcing i_{qh} to zero through a PLL, the observed position $\hat{\theta}$ converges to the real one θ. The PLL scheme is highlighted in red in Figure 3.5, while its dynamic, bandwidth and tuning will be discussed in Section 3.3.4. For now, it is sufficient to underline that a high bandwidth of the position tracking loop is not necessary. Indeed, the undesired rotor movement during test #2 and #3 can be decomposed into fast vibrations superimposed to a drift from the initial position. The real time position observer is designed only to follow the drift, which is relatively slow.

The injection at half of the injected frequency also simplify the demodulation of i_{qh}. Indeed, the HF square wave can be rectified by simply reversing one sample every two, with no need of evaluating any trigonometric function.

It must be remarked that (3.5) was obtained considering constant inductances and neglecting the cross-saturation. Therefore, this encoderless position tracking technique is inherently affected by position error due to cross-saturation effect [32], as analyzed in Section 4.2. The scientific literature provides several methods to get rid of such position error [32, 37, 105], but all of them require the knowledge of the flux maps, not available before the self commissioning stage.

Another important consideration is that if HF injection is adopted the test does not diverge and can be successfully completed even in case the shaft drifts from its initial state. Anyway, in this case, the standstill constrain is not strictly satisfied.

The self-commissioning test augmented with HF injection was experimentally tested on the motor SR2kW2. In every test, the automatic tuning procedure and stop criteria described in Section 3.3.4 were adopted for achieving the maximum measurement area. In this experiment, test #2 was performed using $V_{\mathrm{q,sc}} = 200\ V$ and, in Figure 3.11(a), $u_{\mathrm{c}} = 50\ V$ and $\omega_{\mathrm{f}} = 2\pi \cdot 150\ rad/s$. Figure 3.6 compares the measurement area in the dq plane for the three tests performed with and without online sensorless position tracking. It can be seen that test #2 executed at open loop reached a maximum $I_{\mathrm{q,max}}$ of 7.9 A, while this limit was considerably increased up

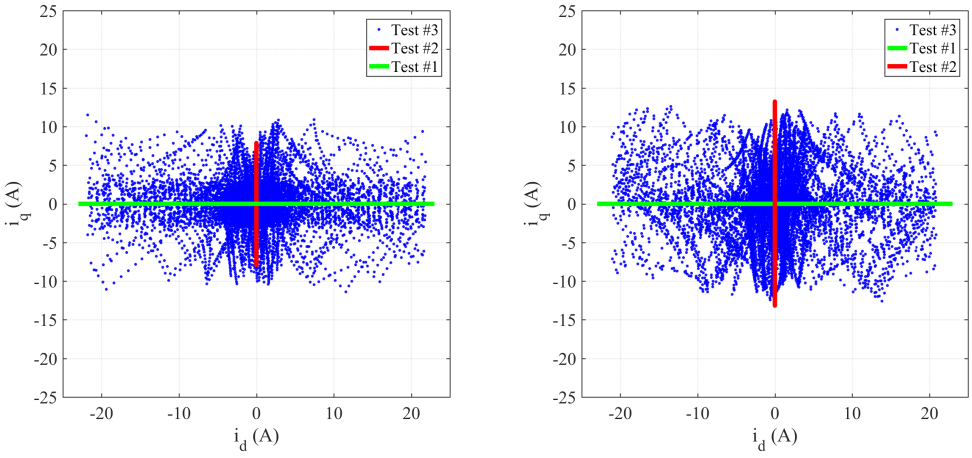

(a) (b)

Figure 3.6: Measurement domain in the dq current plane. Green: test #1; red: test #2; blue: test #3. (a) test #2 and #3 performed with open loop position estimation; (b) test #2 and #3 augmented with online position tracking.

to 13.2 A peak when online position tracking was adopted, enhancing the measurement range by 67 %.

A much more moderate improvement was obtained for test #3, where the HF injection only permitted to increase the maximum $I_{\mathrm{q,max}}$ from 11.5 A to 12.6 A, while $I_{\mathrm{d,max}} = 20\ A$. This can be explained considering that the instability problems of test #3 are due to the high transient torque arising during the test more than position inaccuracy. Moreover, in order to be able to inject a relevant HF signal the test voltage had to be decreased, thus affecting the stability of the test. In this implementation, $V_{\mathrm{d,sc}} = V_{\mathrm{q,sc}} = 200\ V$ in case on open loop position estimation while $V_{\mathrm{d,sc}} = V_{\mathrm{q,sc}} = 150\ V$, $u_{\mathrm{c}} = 100\ V$ and $\omega_{\mathrm{f}} = 2\pi \cdot 50\ rad/s$. Figure 3.11 and 3.12 compare the time waveforms of voltage and currents during test #2 and test #3 respectively, comparing the case with and without adopting online position tracking.

The flux maps obtained from the self-commissioning test augmented with online position tracking are compared with the open loop case and the reference flux maps in Figure 3.7. The measurement data were manipulated using the technique presented in Section 3.4.4, which allows extrapolating the flux characteristic out of the measurement range relying on an analytical inverse model. The curve $\lambda_{\mathrm{d}}(i_{\mathrm{d}}, i_{\mathrm{q}} = 0)$ was based on test #1 at open loop

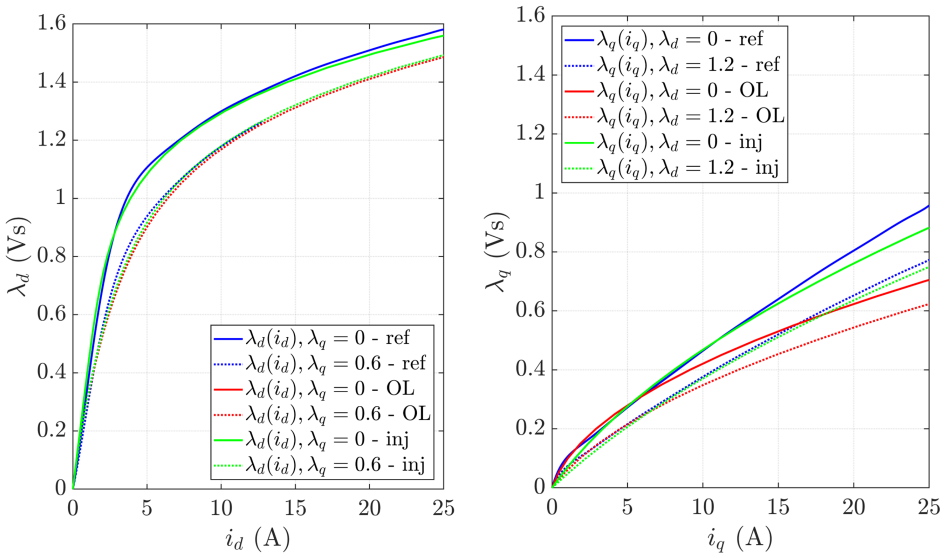

(a) (b)

Figure 3.7: Comparison between reference flux maps (blue), extrapolated characteristic using self-commissioning and Open Loop (OL) position estimation (red) and self-commissioning with online position tracking (green, inj). (a) solid lines refer to $\lambda_{\mathrm{q}} = 0\ Vs$, dotted lines refer to $\lambda_{\mathrm{q}} = 0.6\ Vs$ (strong cross-saturation). (b) solid lines refer to $\lambda_{\mathrm{d}} = 0\ Vs$, dotted lines refer to $\lambda_{\mathrm{d}} = 1.2\ Vs$ (strong cross-saturation). Curves based on the model (3.35).

in any case, so the solid red and green lines in the left figure are perfectly overlapped. The most evident result is that in the test augmented with HF injection the q axis characteristic results accurate up to considerably higher current (around 15 A), while relevant discrepancy is observed for the open loop test for $i_{\mathrm{q}} > 8\ A$. The accuracy at higher current is due to the extended measurement range, which allows basing the Linear Least Square (LLS) optimization in a wider current domain. From the Figure it is also evident that the cross-saturation effect can be evaluated from test #3 either with or without HF injection with negligible discrepancy, being limited the improvement in the measurement domain.

3.3.3 Parameter Sensitivity Analysis

In this section, the accuracy of the proposed method is analyzed, considering the possible error sources that may influence the flux estimation. As will be

demonstrated, all of them are either not relevant or easily compensated.

As can be seen in (3.1)-(3.4), the fluxes are obtained as the integral of the estimated electromotive forces. The applied voltage is estimated from the inverter commands after compensation of nonlinear effects. So, inaccurate inverter compensation may reflect on flux inaccuracy. Similarly, the back-EMF is obtained considering the voltage drop on the estimated stator resistance, so eventual error in evaluating $\hat{R}_\mathrm{s}$ would produce a flux estimation error. Moreover, the iron losses are not taken into account in the machine model, possibly causing a flux estimation error. Since the integration is performed at open loop, the risk of drifting is relevant and has to be solved. Finally, the estimated position may not correspond to the real one, and the position error may produce an error in the flux computation.

3.3.3.1 Inverter Error and Stator Resistance

Most of the papers published in the literature [73] are based on the injection of low pu voltage or current signals. Conversely, the test voltage V_sc applied here is relatively high, in the order of magnitude of the rated voltage. For this reason, the resistive and inverter voltage drops are small in percentage. This is the main reason why the method results almost insensitive to mismatch in parameters estimation, as will be demonstrated in this Section.

For this analysis, only the test #1 is considered for simplicity. The same considerations apply for test #2 and test #3. The flux estimation in ideal conditions, i.e. immune from R_s and V_th inaccuracies, is computed as:

$$\lambda_\mathrm{d} = \int v_\mathrm{d}^* - R_\mathrm{s} i_\mathrm{d} - V_\mathrm{th} sign(i_\mathrm{d}) dt \tag{3.9}$$

Therefore, the flux estimation error is

$$\begin{aligned} \epsilon_\mathrm{d} &= \lambda_\mathrm{d} - \hat{\lambda}_\mathrm{d} \\ &= \int v_\mathrm{d}^* - R_\mathrm{s} i_\mathrm{d} - V_\mathrm{th} sign(i_\mathrm{d}) dt - \int v_\mathrm{d}^* - \hat{R}_\mathrm{s} i_\mathrm{d} - \hat{V}_\mathrm{th} sign(i_\mathrm{d}) dt \end{aligned} \tag{3.10}$$

The effects of inaccurate inverter compensation and stator resistance estimation are decomposed in two terms. Assuming $\hat{R}_\mathrm{s} = R_\mathrm{s}$, the flux error only due to imprecise $\hat{V}_\mathrm{th}$, i.e. $\epsilon_\mathrm{d,Vth}$, is extracted from (3.10):

$$\epsilon_\mathrm{d,Vth} = \int (\hat{V}_\mathrm{th} - V_\mathrm{th}) sign(i_\mathrm{d}) dt \tag{3.11}$$

Similarly, assuming perfect inverter compensation ($\hat{V}_\mathrm{th} = V_\mathrm{th}$), the flux error only due to stator resistance inaccuracy $\epsilon_\mathrm{d,Rs}$ is obtained as:

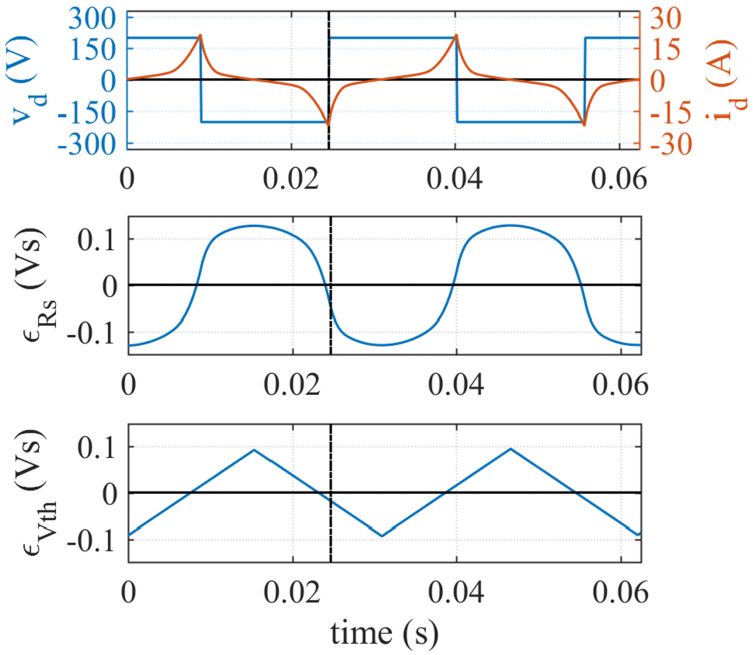

Figure 3.8: Time waveforms during test #1. From top to bottom: voltage and current in d axis, $\epsilon_{\mathrm{d,Rs}}$ and $\epsilon_{\mathrm{d,Vth}}$.

$$\epsilon_{\mathrm{d,Rs}} = (\hat{R}_{\mathrm{s}} - R_{\mathrm{s}}) \int i_{\mathrm{d}} dt \tag{3.12}$$

Figure 3.8 reports the time waveforms of $\epsilon_{\mathrm{d,Vth}}$ and $\epsilon_{\mathrm{d,Rs}}$ for test #1 performed on the motor SR2kW2 without online position detection. In these plots, the extreme detuning case was considered, imposing $\hat{R}_{\mathrm{s}} = 0$ and $\hat{V}_{\mathrm{th}} = 0$ respectively. As can be seen, assuming that $\hat{V}_{\mathrm{th}} - V_{\mathrm{th}}$ is constant, $\epsilon_{\mathrm{d,Vth}}$ follows a triangular shape with the peak in correspondence of the zero crossing of i_{d}. If constant inductance is assumed, the waveform of $\epsilon_{\mathrm{d,Rs}}$ would follow a series of exponential transients. Anyway, its shape is deviated into a highly nonlinear function because of the strong magnetic saturation. Both waveforms were obtained from open loop integration; the initial condition was set so that the average error within the first complete test cycle is null.

An interesting phenomenon is observed in the shape of $\epsilon_{\mathrm{d,Rs}}$ and $\epsilon_{\mathrm{d,Vth}}$. From the motor model (2.9), the back-EMF during the rising transient is:

$$e_{\mathrm{d}} = V_{\mathrm{sc}} - R_{\mathrm{s}} i_{\mathrm{d}} \tag{3.13}$$

while during the falling transient:

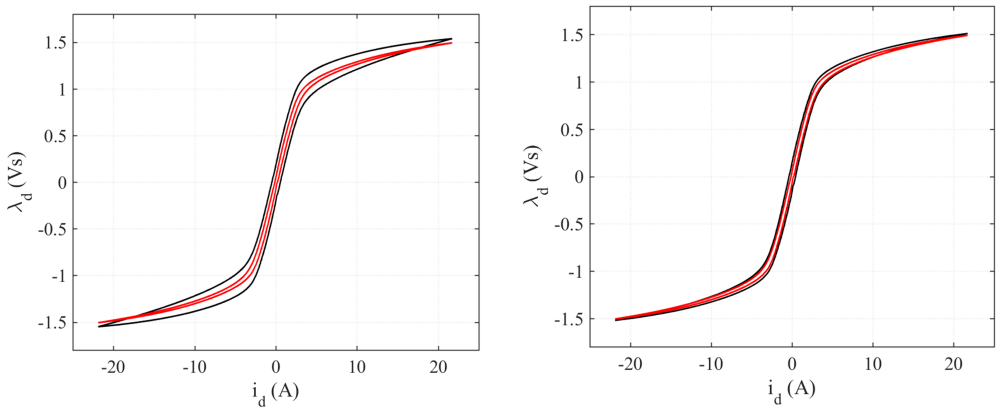

Figure 3.9: Obtained flux linkage characteristic based on test #1 ($i_\mathrm{q} = 0$). Black lines: flux estimated with accurate compensation of resistive and inverter voltage drops. Red lines: flux estimated considering (a) $\hat{R}_\mathrm{s} = 0$ and accurate inverter compensation; (b) accurate $\hat{R}_\mathrm{s}$ and $\hat{V}_\mathrm{th} = 0$.

$$e_\mathrm{d} = -V_\mathrm{sc} - R_\mathrm{s} i_\mathrm{d} \tag{3.14}$$

The amplitude of e_d is lower when the sign of i_d is in accordance with the sign of the applied voltage, e.g. rising transient for positive i_d. Therefore, the current takes more time to reach the threshold value $I_\mathrm{d,max}$ and, in case of inaccurate $\hat{R}_\mathrm{s}$, the error calculated in (3.12) becomes asymmetric for rising and falling transient, since it is obtained from a time integral. Due to this asymmetry, the time instant when i_d reaches its peak does not correspond to the zero crossing of $\epsilon_\mathrm{d,Rs}$. Similarly, $\epsilon_\mathrm{d,Vth}$ is a triangular waveform with constant rising and falling slope, it reaches its peak at the current zero crossing and it is forced to have zero average value. Since, for $i_\mathrm{d} > 0$, the current rising time is larger than the falling one, also the zero crossing of $\epsilon_\mathrm{d,Vth}$ does not match with the maximum current.

Figure 3.9 compares the flux characteristics obtained during the test with proper V_th and R_s compensation (red lines) with the ones computed without any compensation of resistive voltage drop ($\hat{R}_\mathrm{s} = 0$) or without compensating inverter non-linear effects ($\hat{V}_\mathrm{th} = 0$). As can be seen, the main effect of inaccurate compensation is that the estimated flux characteristic becomes a thicker loop instead of a single line. A second order effect is that, due to the above described asymmetry, the error is not null at the maximum current peak, causing a shift at high current of the badly tuned characteristics. Anyway, even in those extreme cases the average curve of the loop is well in

accordance with the reference.

The evaluation of which term, between $\epsilon_{\mathrm{d,Vth}}$ and $\epsilon_{\mathrm{d,Rs}}$, is more significant in practical implementation is not trivial. As said, the two signals present different shape and the estimation of R_{s} and V_{th} is linked to different factors, so various scenarios are possible depending on the accuracy of $\hat{R}_{\mathrm{s}}$ and $\hat{V}_{\mathrm{th}}$. With the analyzed motor and the adopted inverter, the two error sources present similar peak value (around 0.1 Vs, as in Figure 3.8), but according to Figure 3.9 the effect of $\epsilon_{\mathrm{d,Rs}}$ is more evident, both for the loop thickness and for the shift at high current. This effect is mostly related to the shape of $\epsilon_{\mathrm{d,Rs}}$, presenting a high flux error for a longer time respect to $\epsilon_{\mathrm{d,Vth}}$.

It must be considered that the analyzed case with 100 % detuning is a hyper worst case scenario. R_{s} can be easily estimated through DC current injection tests and in many cases a reference value is given in the machine nameplate, so it is improbable that it is completely unknown. It can happen that R_{s} is badly known, e.g. it is known at a different temperature, but in this case the error in flux estimation would be much smaller than the case presented in this Section. The evaluation of V_{th} is less trivial, but still can be done in several ways [43, 45]. Therefore, also in this case a lower error than the signal presented in Figure 3.8 is expected.

It should also be highlighted that, even if the error was big, the average of the loop described by the estimated flux well corresponds to the reference saturation characteristic. So, a precise flux map can be obtained through the method later described in Section 3.4.

In conclusion, the parameter sensitivity respect to $\hat{R}_{\mathrm{s}}$ and $\hat{V}_{\mathrm{th}}$ is very low thanks to the high test voltage. Therefore, V_{sc} should be set as high as possible, as will be analyzed in Section 3.3.4.

3.3.3.2 Iron Loss

During the test, the motor is excited with a relatively high frequency, therefore hysteresis losses and parasitic currents are surely present. In principle, these phenomena may affect the flux estimation, since iron losses are not taken into account in the adopted machine model (2.9). The reference method for flux maps identification [40] is considered immune from iron loss effects since the motor is rotated at constant and low speed. The good agreement between the flux characteristic obtained in self commissioning and the flux maps measured by [40] for all the tested motors demonstrates the good immunity of the square wave injection self-identification technique respect to iron loss effects.

It should be considered that SyR machines are usually adopted in applications requiring relatively high efficiency, e.g. IE4 standards. Therefore,

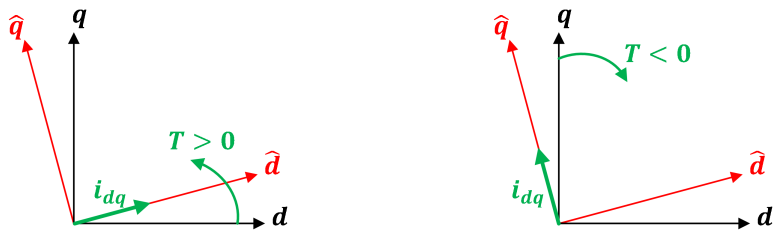

(a) (b)

Figure 3.10: Polarity of the torque produced in presence of eventual position error. (a) Test #1: the current vector is along $\hat{d}$, the torque tends to align the rotor along the estimated position. (b) Test #2: the current vector is along $\hat{q}$, the torque tends to increase the position error and making the test to diverge.

these machines commonly adopt high performance iron with low power loss rate [106]. Still, some information about the entity of iron losses can be extracted from this test, as will be discussed in Section 3.4.6.

3.3.3.3 Alignment Error

The square wave test relies on estimated rotor position. A position estimation error $\Delta\theta = \hat{\theta} - \theta$ is possible for different causes in the three tests. Test #1 is self-aligning, as said, since the torque produced in presence of eventual $\Delta\theta$ tends to align the rotor to the estimated position, as explained in Figure 3.10. Anyway, in some applications the motor may be already connected to a load that locks the rotor. In this case, the initial position error would not be corrected, and the current would not be controlled in the real d axis. So, a wrong saturation characteristic would be measured. Similarly, test #2 can be successfully performed in slightly wrong estimated coordinates in case the rotor is locked. Position error may also be produced during test #3 in free-shaft conditions, since the alternate produced torque yields to small rotor oscillations around the initial estimated position.

In order to analyze the effect of $\Delta\theta$ on the flux estimation error, a general case where both axes are excited must be considered. In this analysis, accurate resistance estimation and compensation of inverter non-linear effects is assumed. The reference voltages are applied in estimated reference frame $\hat{d}\hat{q}$, that differ from the real one by $\Delta\theta$. So, the applied voltage and currents in estimated reference frame are

$$\begin{cases} v_{\hat{\mathrm{d}}} &= v_{\mathrm{d}} \cos(\Delta\theta) + v_{\mathrm{q}} \sin(\Delta\theta) \\ v_{\hat{\mathrm{q}}} &= -v_{\mathrm{d}} \sin(\Delta\theta) + v_{\mathrm{q}} \cos(\Delta\theta) \end{cases} \tag{3.15}$$

$$\begin{cases} i_{\hat{\mathrm{d}}} &= i_{\mathrm{d}} \cos(\Delta\theta) + i_{\mathrm{q}} \sin(\Delta\theta) \\ i_{\hat{\mathrm{q}}} &= -i_{\mathrm{d}} \sin(\Delta\theta) + i_{\mathrm{q}} \cos(\Delta\theta) \end{cases} \tag{3.16}$$

Therefore, the estimated flux in observed reference frame can be written as a function of the real physical quantities:

$$\begin{cases} \hat{\lambda}_{\mathrm{d}} &= \int v_{\hat{\mathrm{d}}} - R_{\mathrm{s}} i_{\hat{\mathrm{d}}} dt \\ \hat{\lambda}_{\mathrm{q}} &= \int v_{\hat{\mathrm{q}}} - R_{\mathrm{s}} i_{\hat{\mathrm{q}}} dt \end{cases}$$

$$\begin{cases} \hat{\lambda}_{\mathrm{d}} &= \int v_{\mathrm{d}} \cos(\Delta\theta) + v_{\mathrm{q}} \sin(\Delta\theta) - R_{\mathrm{s}} \left[i_{\mathrm{d}} \cos(\Delta\theta) + i_{\mathrm{q}} \sin(\Delta\theta) \right] dt \\ \hat{\lambda}_{\mathrm{q}} &= \int -v_{\mathrm{d}} \sin(\Delta\theta) + v_{\mathrm{q}} \cos(\Delta\theta) - R_{\mathrm{s}} \left[-i_{\mathrm{d}} \sin(\Delta\theta) + i_{\mathrm{q}} \cos(\Delta\theta) \right] dt \end{cases} \tag{3.17}$$

while the correct fluxes can be computed as

$$\begin{cases} \lambda_{\mathrm{d}} &= \int v_{\mathrm{d}} - R_{\mathrm{s}} i_{\mathrm{d}} dt \\ \lambda_{\mathrm{q}} &= \int v_{\mathrm{q}} - R_{\mathrm{s}} i_{\mathrm{q}} dt \end{cases} \tag{3.18}$$

After straightforward manipulation, the flux estimation error due to inaccurate observed position can be written as:

$$\begin{cases} \epsilon_{\mathrm{d},\theta} &= \int (v_{\mathrm{d}} - R_{\mathrm{s}} i_{\mathrm{d}}) (1 - \cos(\Delta\theta)) - (v_{\mathrm{q}} - R_{\mathrm{s}} i_{\mathrm{q}}) \sin(\Delta\theta)\, dt \\ \epsilon_{\mathrm{q},\theta} &= \int (v_{\mathrm{q}} - R_{\mathrm{s}} i_{\mathrm{q}}) (1 - \cos(\Delta\theta)) + (v_{\mathrm{d}} - R_{\mathrm{s}} i_{\mathrm{d}}) \sin(\Delta\theta)\, dt \end{cases} \tag{3.19}$$

By substituting (3.18), the following relationship is obtained:

$$\begin{cases} \epsilon_{\mathrm{d},\theta} &= \lambda_{\mathrm{d}} (1 - \cos(\Delta\theta)) - \lambda_{\mathrm{q}} \sin(\Delta\theta) \\ \epsilon_{\mathrm{q},\theta} &= \lambda_{\mathrm{q}} (1 - \cos(\Delta\theta)) + \lambda_{\mathrm{d}} \sin(\Delta\theta) \end{cases} \tag{3.20}$$

Finally, if small position error is assumed ($\Delta\theta \approx 0$), the flux error due to position mismatch can be simplified as

$$\begin{cases} \epsilon_{\mathrm{d},\theta} &\approx -\lambda_{\mathrm{q}} \Delta\theta \\ \epsilon_{\mathrm{q},\theta} &\approx \lambda_{\mathrm{d}} \Delta\theta \end{cases} \tag{3.21}$$

During test #1, the q axis is not excited, therefore λ_{q} is almost null and $\epsilon_{\mathrm{d},\theta}$ is negligible. Conversely, $\epsilon_{\mathrm{q},\theta}$ would be much more relevant since λ_{d} goes up to the rated value. Anyway, this is not a problem since during test #1 λ_{q} is not evaluated. Similar consideration apply for test #2, with $\lambda_{\mathrm{d}} \approx 0$ and $\epsilon_{\mathrm{d},\theta}$ not important. Therefore, an eventual position estimation error would not affect the evaluation of $\lambda_{\mathrm{d}}(i_{\mathrm{d}}, 0)$ and $\lambda_{\mathrm{q}}(0, i_{\mathrm{q}})$.

The test #3 is more critical, since both axes are excited and position vibrations are possible. Anyway, for the success of the test the real position is supposed to oscillate around the initial position, so $\Delta\theta$ is alternatively positive and negative, as well as λ_d and λ_q. Therefore, if sufficient measurement points are acquired and appropriately averaged, the flux estimation error due to $\Delta\theta$ is at least partially compensated.

3.3.4 Automatic Tuning and Stop Criteria

In this section, an automatic procedure is suggested to tune the main control parameters for the self-identification and for the position tracking loop. In particular, it is necessary to properly set the current thresholds in the hysteresis control $I_{\mathrm{d,max}}$ and $I_{\mathrm{q,max}}$ and the amplitude of the fundamental square wave voltage $V_{\mathrm{d,sc}}$ and $V_{\mathrm{q,sc}}$. Moreover, dedicated automatic stop criteria are proposed, able to detect undesired rotor movements and consequently stopping the test. Finally, in case test #2 and test #3 are augmented by HF injection for online position tracking, the amplitude of the injected voltage u_c and the tracking loop gains have to be tuned.

3.3.4.1 Setting of the Current Limits

The values of $I_{\mathrm{d,max}}$ and $I_{\mathrm{q,max}}$ define the measurement area in the dq plane where the magnetic characteristic is measured. For control purposes, it is usually preferred if the flux maps are available in a wide current range, covering the overload conditions. Anyway, by setting too high thresholds the stability of the self-commissioning may not be guaranteed.

As already said in Section 3.3.3, test #1 is inherently stable, so the flux maps identification can be extended along d axis as far as necessary by increasing $I_{\mathrm{d,max}}$ up to the maximum inverter current capability.

Test #2 is only marginally stable, since position deviations produce torque and further misalignment. If the produced torque is high enough to overcome the mechanical friction and it is applied for sufficiently long time, the rotor drifts from its initial state and starts to rotate. In this case, the test fails. For equal position error, the torque amplitude is directly dependent on the threshold $I_{\mathrm{q,max}}$. Also, for equal applied $V_{\mathrm{q,sc}}$ by increasing $I_{\mathrm{q,max}}$ the current i_q takes more time to reach $I_{\mathrm{q,max}}$, so the torque subsists for longer time.

Evaluating a priori the maximum allowed $I_{\mathrm{q,max}}$ is not trivial. An automatic solution is proposed in [6, 14]. The identification starts with a low $I_{\mathrm{q,max}}$, which is then linearly increased at every voltage cycle. The test is automatically stopped when a movement is detected, according to the stop method described later. In this way, the maximum possible $I_{\mathrm{q,max}}$ is reached.

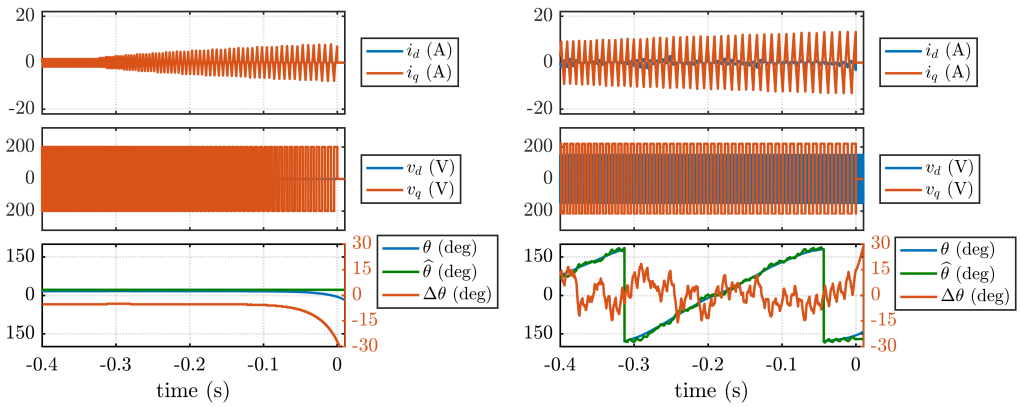

Figure 3.11: Test #2 executed (a) with open loop position estimation and (b) augmented with online position tracking. from top to bottom: dq currents, dq voltages, real and observed position and position error.

In test #3, both axes are excited and so torque is inherently produced. It has to be noted that the current follows a random trajectory in the dq plane, so it is rare that $I_{\mathrm{d,max}}$ and $I_{\mathrm{q,max}}$ are reached contemporary. Anyway, the two thresholds give an idea of the maximum torque magnitude. Similarly to the previous tests, i_{d} tends to stabilize the test, aligning the rotor to the estimated angle, while the current in q axis is destabilizing. For this reason, [6,14] also proposes to adopt constant $I_{\mathrm{d,max}}$ threshold and linearly increase it at every cycle on q axis. The test is stopped as soon as a relevant movement is detected. Also in this case, a reliable movement detection technique is necessary, and detailed in the next Section. This technique allows extending the measurement range to cover the complete stable operating area.

3.3.4.2 Stop Criterion for Test #2

In test #2, if the position estimation is correct the q axis only is excited. Therefore, insignificant $i_{\hat{\mathrm{d}}}$ should be measured. Nevertheless, in presence of rotor misalignment the d axis is slightly excited and a current in observed coordinates $i_{\hat{\mathrm{d}}}$ can be measured, hence, $i_{\hat{\mathrm{d}}}$ can be adopted as error feedback signal. Therefore, test #2 is stopped whenever relevant $i_{\hat{\mathrm{d}}}$ is detected.

A case not treated in [6] is when $i_{\hat{\mathrm{d}}}$ is forced to zero through a PI control, thus $i_{\hat{\mathrm{d}}} = 0$ instead of simply $v_{\hat{\mathrm{d}}} = 0$. In this case, dual to the previous one, $v_{\hat{\mathrm{d}}}$ can be used as position error signal.

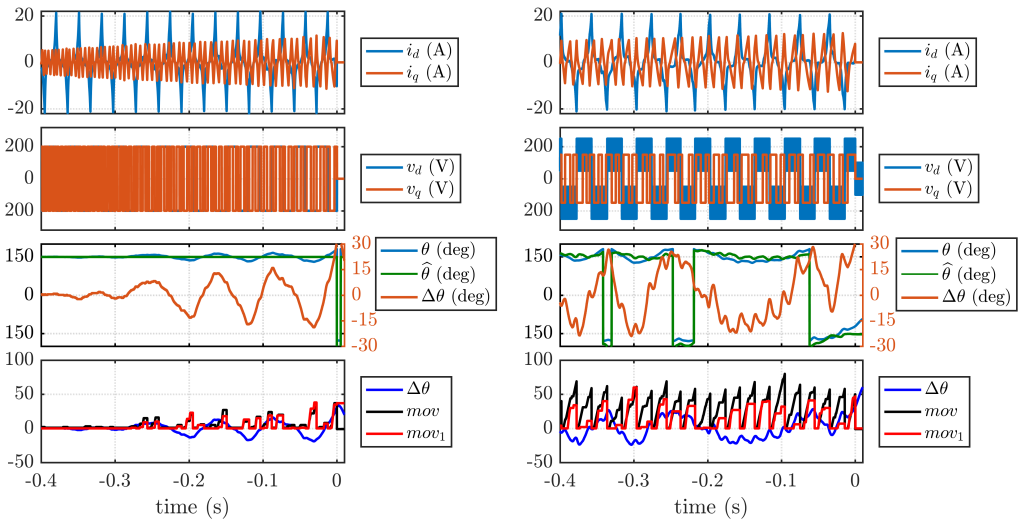

Figure 3.12: Test #3 executed (a) with open loop position estimation and (b) augmented with online position tracking. from top to bottom: dq currents, dq voltages, real and observed position and position error.

3.3.4.3 Stop Criteria for Test #3

Detecting a rotor movement during test #3 is less straightforward. In [6] it was proposed to rely on the sign of the current derivative in d axis. For correct position estimation, $i_{\hat{\mathrm{d}}}$ is monotonic according to $v_{\hat{\mathrm{d}}}$. Anyway in presence of relevant misalignment $i_{\hat{\mathrm{d}}}$ is distorted and its derivative may temporarily be not coherent with $v_{\hat{\mathrm{d}}}$. A movement detection signal can be obtained, preventing excessive rotor movement. At every sampling time, this signal is artificially increased by one if the $i_{\hat{\mathrm{d}}}$ derivative is not in accordance with $v_{\hat{\mathrm{d}}}$, and it is reset to zero whenever the voltage $V_{\mathrm{d,sc}}$ is reversed, that is at every half cycle. In this way, the amplitude of the movement detection feedback at the end of every half cycle of $v_{\hat{\mathrm{d}}}$ tells for how many samples the current has been distorted, representing an approximation of the integral of the position error within that half cycle, i.e. during one sweep of i_{d}. The self-identification test is stopped if the feedback signal overcomes an appropriate threshold value. Figure 3.13 presents a zoom of the $i_{\mathrm{d}}, i_{\mathrm{q}}$ waveforms in presence of relevant position error, where a significant distortion of i_{d} is visible.

Different solutions were proposed in the case the test is performed with open loop position estimation [6] or if it is augmented by HF injection [14]. In the first case, the sign of the derivative of $i_{\hat{\mathrm{d}}}$ is computed as the sign of the difference between the measured current in two consecutive sampling times:

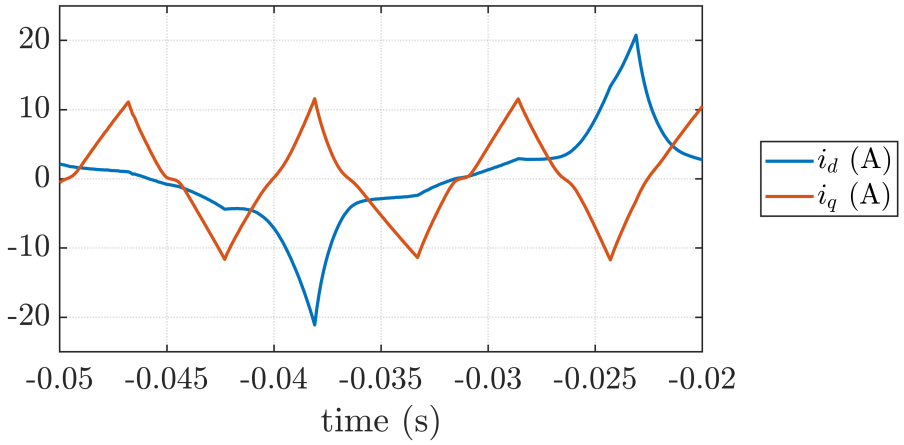

Figure 3.13: Zoom of Figure 3.12(a): current distortion of i_d in presence of relevant position error.

$$mov_k = mov_{k-1} + \frac{1 - sign\left[\left(i_{\hat{\mathrm{d}},\mathrm{k}} - i_{\hat{\mathrm{d}},\mathrm{k}-1}\right) \cdot v_{\hat{\mathrm{d}},\mathrm{k}}\right]}{2} \tag{3.22}$$

where the subscripts k and $k-1$ refer to the voltage and current at the present and at the previous sampling time, respectively, and mov is the movement detection feedback. This formulation resulted accurate enough when the test was based on the initial position estimation. Conversely, if the test is augmented for online position tracking, the injected HF voltage naturally produces an HF oscillation in $i_{\hat{\mathrm{d}}}$, thus affecting its derivative. Therefore, the movement detection (3.22) fails. Considering that u_c is injected at half of the switching frequency, (3.22) can be conveniently modified as:

$$mov^1_\mathrm{k} = mov^1_{\mathrm{k}-1} + \frac{1 - sign\left[\left(i_{\hat{\mathrm{d}},\mathrm{k}} - i_{\hat{\mathrm{d}},\mathrm{k}-2}\right) \cdot v_{\hat{\mathrm{d}},\mathrm{k}}\right]}{2} \tag{3.23}$$

where mov^1 is the new computed movement detection feedback. In this way, the sign of current derivative is computed from the difference between two sampling times, thus removing the HF component. This formulation is equivalent to (3.22) applied to a band-stop filtered current.

The bottom plots of Figure 3.12 compare the movement detection signals computed during test #3 using (3.22) and (3.23). It can be seen that in Figure 3.12(a), where the rotor position was open loop estimated, the two signals are almost equivalent and the value they reach at every voltage reversal is almost proportional to the position error. Conversely, in Figure 3.12(b) the signal mov grows at almost the same level at every half cycle of i_d, whatever

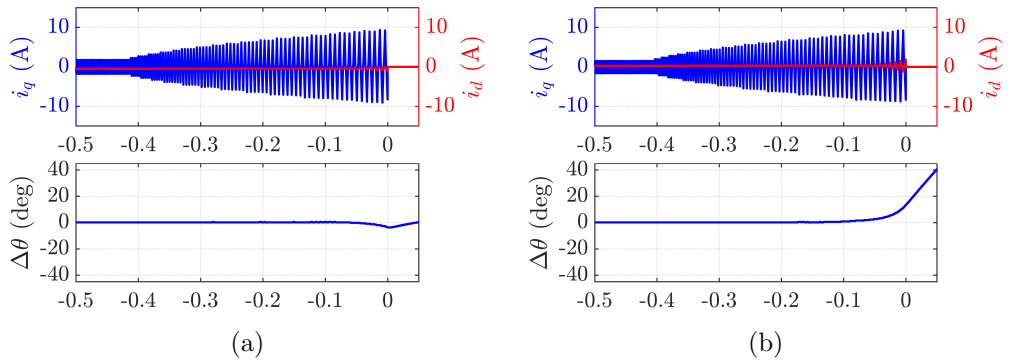

Figure 3.14: Tuning of the movement detection for test #2. (a) test stopped at $i_\mathrm{d} > 1\ A$; (b) test stopped at $i_\mathrm{d} > 2\ A$.

is the position error, while the signal mov^1 results much more reliable, being almost proportional to the position error during a current sweep.

3.3.4.4 Calibration of Test #2 stop

Unfortunately, the adoption of automatic movement detection techniques leads to the necessity of tuning the threshold value at which the test has to be stopped. Appropriate maximum i_d must be set for test #2. This is easily done considering that as soon as a misalignment occurs i_d suddenly rises and is easily detected whatever is the selected threshold. This consideration was experimentally validated in Figure 3.14, where test #2 was executed two times with open loop position estimation. In Figure 3.14(a), the test was stopped at $i_\mathrm{d} = 1\ A$, while in Figure 3.14(b) the threshold was increased to $i_\mathrm{d} = 2\ A$. As can be seen, in both cases a rotor movement is immediately detected and almost the same $I_\mathrm{q,max}$ was reached. Therefore, the test demonstrated to be robust towards the choice of the i_d threshold.

3.3.4.5 Calibration of Test #3 stop

Dealing with the cross-saturation, the relationship between the selected $I_\mathrm{d,max}$ and the achievable $I_\mathrm{q,max}$ has to be found, as well as the relationship between the threshold of mov (or mov^1) and the maximum position error, which is strongly non-linear. To do that test #3 was executed several times on varying $I_\mathrm{d,max}$ and the mov threshold aiming at maximizing the feasible $I_\mathrm{q,max}$, while the position error was monitored with an encoder for analysis purposes only. The results of this test campaign are summarized in Table 3.2, while some examples of obtained waveforms during some of the tests are report in

Figure 3.15. In particular, in Figure 3.15(a) and Figure 3.15(b) the test was stopped at $mov = 10$ with a current limit of $I_{\mathrm{d,max}} = 10\ A$ and $I_{\mathrm{d,max}} = 20\ A$, respectively. In these two tests, the maximum position displacement has been between 6 and 8 mechanical degree. In Figure 3.15(c) and Figure 3.15(d) the movement threshold was increased at $mov = 20$, still with $I_{\mathrm{d,max}} = 10\ A$ and $I_{\mathrm{d,max}} = 20\ A$, respectively. Also in this case similar maximum position oscillation (between 16 and 20 mechanical degree) was reached.

As can be seen, by rising $I_{\mathrm{d,max}}$ the achievable $I_{\mathrm{q,max}}$ is slightly increased. This phenomenon can be explained considering that higher i_{d} helps to align the rotor with the estimated position, thus diminishing the risk of drifting. However, in every executed test the most unstable situation, correctly detected with highest current distortion, resulted to be when i_{q} is reaching $I_{\mathrm{q,max}}$ while i_{d} close to the zero crossing. This is the most critical condition, and it can randomly occur during the test. This effect reduces the sensitivity of the maximum achievable $I_{\mathrm{q,max}}$ respect to the chosen $I_{\mathrm{d,max}}$. In real-world implementation, if one test is prematurely stopped without covering the desired current domain this will be executed again, until aleatory unfavorable conditions are not met.

About the threshold of mov, a good consistency is observed respect to the maximum position oscillation, as can be seen in Table 3.2. This threshold also slightly influenced the maximum achieved $I_{\mathrm{q,max}}$. Therefore, considering the relationship between position and flux estimation error detailed in Section 3.3.3, the tuning of mov threshold has to be found as a tradeoff between the desired current domain and the required flux accuracy. Anyway, except for few randomly favorable or unfavorable cases, the variation of the reached $I_{\mathrm{q,max}}$ is very limited, being around 11 A. Thus, this test campaign proves the substantial insensitivity of the test respect to parameter tuning.

3.3.4.6 Calibration of the Voltage Amplitude

The accuracy analysis detailed in Section 3.3.3 demonstrated that the sensitivity of the flux estimation respect to eventual inaccuracies in stator resistance estimation or compensation of inverter voltage drop is low thanks to the amplitude of the applied test voltage V_{sc}. In turn, the higher is V_{sc}, the lower are the voltage drops on inverter and R_{s} in percentage.

Furthermore, the voltage is regulated by hysteresis controllers, so higher V_{sc} also increases the frequency of the square wave voltage. As a consequence, the polarity of the torque produced in test #3 is reversed with higher frequency, thus limiting the mechanical vibrations. Also, in test #2 the torque due to eventual position error stands for lower time. In both cases, the test turns out to be more stable and accurate, limiting the risk of rotor movement.

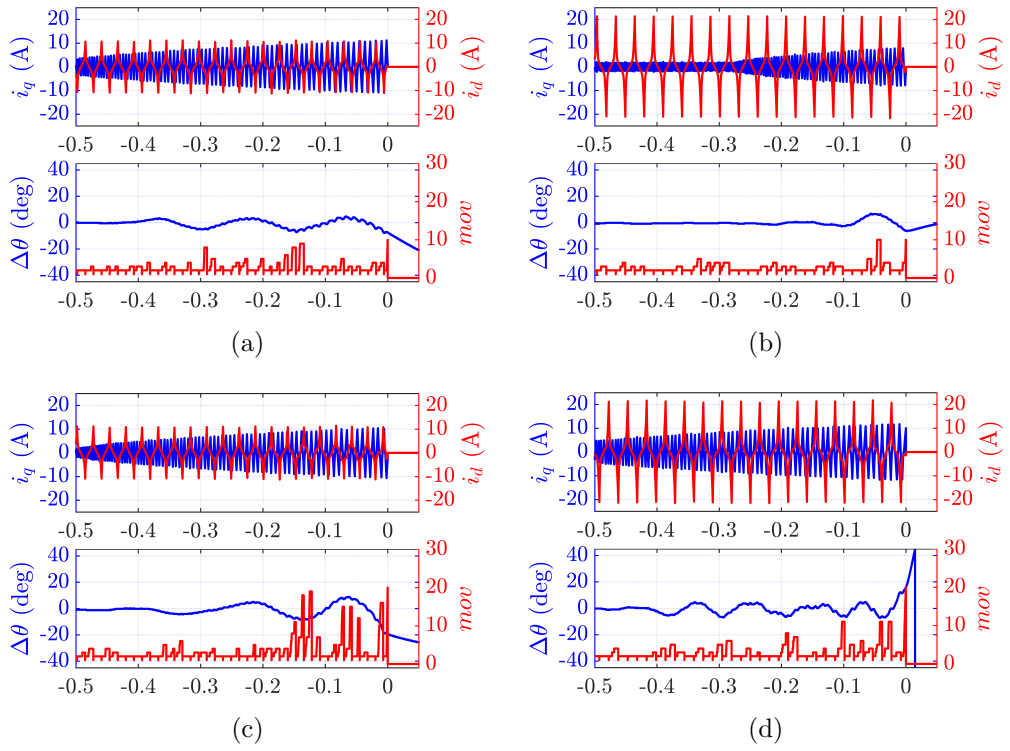

Figure 3.15: Tuning of the movement detection for test #3. (a) test stopped at $mov > 10$ using $I_{\mathrm{d,max}} = 10$; (b) test stopped at $mov > 10$ using $I_{\mathrm{d,max}} = 20$; (c) test stopped at $mov > 20$ using $I_{\mathrm{d,max}} = 10$; (d) test stopped at $mov > 20$ using $I_{\mathrm{d,max}} = 20$;

To prove the effect of the amplitude of V_{sc} on the test stability and accuracy, the test #1 was performed using $V_{\mathrm{sc}} = 100\ V$ and $V_{\mathrm{sc}} = 200\ V$. The current and voltage waveforms are compared in Figure 3.16, together with the position oscillation around θ_0. From the comparison it is clear that the test executed at $V_{\mathrm{sc}} = 200\ V$ is much more stable, with very limited position oscillations and negligible current on the not excited axis, while relevant i_{q} is present in the test at $V_{\mathrm{sc}} = 100\ V$. Therefore, in this latter case the flux estimation would be compromised, and the flux estimation error due to inaccurate $\hat{R}_{\mathrm{s}}$ or $\hat{V}_{\mathrm{th}}$ becomes more significant.

The comparison is repeated for test #2 in Figure 3.17, again with $V_{\mathrm{sc}} = 100\ V$ and $V_{\mathrm{sc}} = 200\ V$. In both cases, the test was not augmented by HF injection for comparison purposes. As can be seen, this test is even more critical since the test performed at $V_{\mathrm{sc}} = 200\ V$ was perfectly working, with negligible position error and $i_{\mathrm{d}} \approx 0$, while the test executed with $V_{\mathrm{sc}} = 100\ V$ failed. In this case, the test was so unstable that the rotor drifted from its

initial position, so the control was lost.

The main constrain limiting the affordable V_{sc} is that if it is set very high the transient may be too fast, resulting in an inadequate number of measurement samples per current sweep. Therefore, it was proposed in [6] to execute the self-identification using the maximum voltage allowed by the inverter limitation v_{max} and check if the number of current (and flux) samples per period

Table 3.2: Performances of movement detection during test #3.

mov **threshold**	$I_{d,max}$ **[A]**	$I_{q,max}$ **[A]**	$\Delta\theta$ **[mec. deg.]**
10	5	8.56	11.08
	10	11.18	7.55
	15	10.51	6.16
	20	8.33	6.14
15	5	9.08	12.12
	10	12.21	8.97
	15	9.35	9.03
	20	11.99	13.89
20	5	10.45	17.76
	10	10.43	19.15
	15	11.01	12.83
	20	11.74	16.12
25	5	8.35	15.30
	10	11.06	18.11
	15	11.80	21.63
	20	11.78	24.43
30	5	9.49	18.11
	10	11.74	17.04
	15	11.96	14.23
	20	11.53	24.08

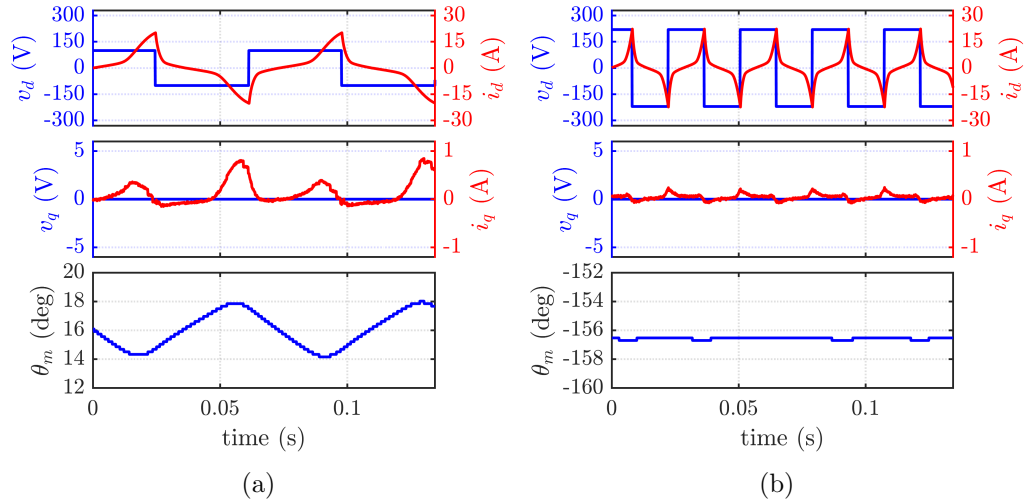

Figure 3.16: Effect of the test amplitude on stability and accuracy of test #1. (a) V_{sc} =100 V. (b) V_{sc} =200 V.

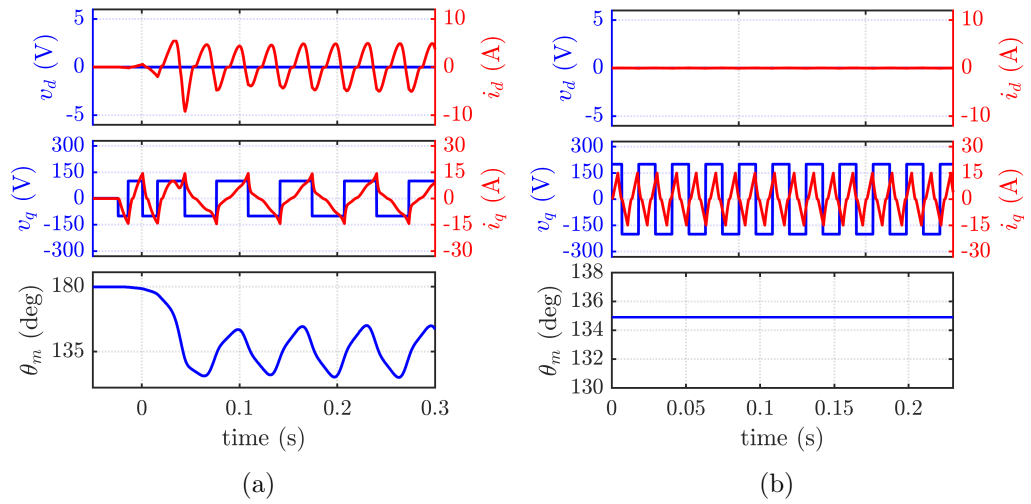

Figure 3.17: Effect of the test amplitude on stability and accuracy of test #2. (a) V_{sc} =100 V. (b) V_{sc} =200 V. The test (a) failed since the rotor drifted from its initial position, so the control was lost.

N_{s} is sufficient. If N_{s} is not adequate, the test can be iteratively repeated, progressively reducing V_{sc} until the desired N_{s} is reached. Figure 3.20 shows the calibration sequence for determining V_{sc}.

The choice of the test voltage is slightly complicated in case the test is augmented by HF signal injection. In this case, a high u_{c} is desired, since

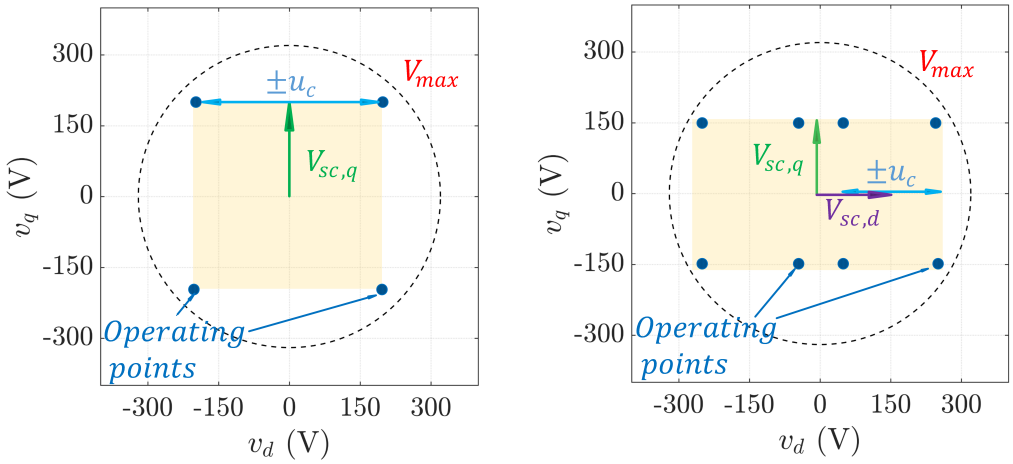

Figure 3.18: Movement of the voltage vector in the dq plane for (a) test #2 and (b) test #3.

it leads to a higher HF current and so a more reliable demodulated signal. Therefore, the position estimation becomes more robust, with higher signal-to-noise ratio. This is in contrast with the requirement of having a high V_{sc}, since the total voltage is limited by the inverter DC-link. For this reason, the tuning of V_{sc} and u_{c} are strictly connected and require a trade-off solution.

The voltage vector moves along fixed positions in the voltage plane. In test #2, the d axis is only excited by the HF signal injected for position tracking, while v_{q} is determined by the fundamental excitation $V_{\mathrm{q,sc}}$. Since both signals are of the square wave type, the vector $\boldsymbol{v}_{\mathrm{dq}}$ is always in one of the vectors of a rectangle, with $v_{\mathrm{d}} = \pm u_{\mathrm{c}}$ and $v_{\mathrm{q}} = \pm V_{\mathrm{q,sc}}$. In test #3, in d axis the HF excitation is superimposed to $V_{\mathrm{d,sc}}$, therefore $\boldsymbol{v}_{\mathrm{dq}}$ moves in eight possible points, being $v_{\mathrm{d}} = \pm V_{\mathrm{d,sc}} \pm u_{\mathrm{c}}$ and $v_{\mathrm{q}} = \pm V_{\mathrm{q,sc}}$.

The allowed positions for $\boldsymbol{v}_{\mathrm{dq}}$ are report in Figure 3.18, together with the inverter voltage limitation. From this Figure it is easy to retrieve the maximum allowed u_{c} for given $V_{\mathrm{d,sc}}$ and $V_{\mathrm{q,sc}}$:

$$u_{\mathrm{c}} < \begin{cases} \sqrt{v_{\mathrm{max}}^2 - V_{\mathrm{q,sc}}^2} & \text{test \#2} \\ \sqrt{v_{\mathrm{max}}^2 - V_{\mathrm{q,sc}}^2} - V_{\mathrm{d,sc}} & \text{test \#3} \end{cases} \tag{3.24}$$

So, this equation can be used to tune u_{c}.

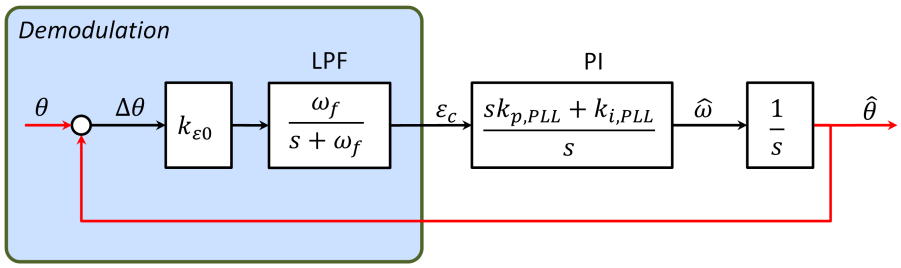

Figure 3.19: Equivalent transfer function of the position tracking loop.

3.3.4.7 Calibration of Position Tracking Loop

The adoption of position tracking loop increases the stability of the self-identification, but it also introduces additional tuning effort. For this reason, the method was simplified respect to [104], reducing the order of the position observer at the cost of lower dynamic response. Precise tuning of the PLL requires the knowledge of the flux maps, which is not available at the self-commissioning stage. Nevertheless, this section provides a tuning strategy based only on a rough estimation of the machine parameters.

In sensorless motor control, it is often required to extend the bandwidth of the position tracking loop ω_b as much as possible, permitting a faster convergence in transient conditions without risk of losing the control.

This is not necessary in the proposed self-identification technique. Indeed, the rotor movement during test #2 and #3 can be seen as a fast vibration at the fundamental frequency of V_sc, due to the reversing of torque polarity, and a drift, which tends to move the rotor from its position with subsequent loss of control. The tracking loop and PLL are designed only to follow the drift, which is reasonably slow, thus correcting the firing angle for V_sc, but neglecting the fast vibrations. So, a low ω_b is enough to guarantee the convergence of the PLL (e.g. $\omega_\mathrm{b} = 10 \div 20\, rad/s$).

First of all, the term k_ϵ is estimated in (3.8), which requires u_c, determined as in (3.24), and the machine inductances. l_d can be easily retreated from test #1, which is always performed without online position tracking. Evaluating l_q is trickier. Anyway, as previously said, the tests #2 and #3 are augmented with HF injection only in the case they did not cover the desired current range when executed with open loop position estimation, so even in this case the test #2 performed at open loop can give at least a rough estimation of l_q, sufficient to evaluate k_ϵ.

The variability of k_ϵ with the current will be temporary neglected. Figure 3.19 shows the equivalent transfer function linking the real and observed position. In this scheme, the shaded area is fictitious, equivalent to the de-

modulation process if cross-saturation effect is neglected. ω_{f} is the cut-off frequency of the LPF used in the demodulation, as shown in Figure 3.5.

From Figure 3.19, the open loop transfer function between $\hat{\theta}$ and θ is:

$$H = k_{\epsilon}\frac{\omega_{\mathrm{f}}}{s+\omega_{\mathrm{f}}} \cdot \frac{sk_{\mathrm{p,PLL}} + k_{\mathrm{i,PLL}}}{s} \cdot \frac{1}{s} \tag{3.25}$$

The approximate bandwidth $\omega_{\mathrm{b},\theta}$ of the PLL can be conveniently obtained from (3.25) by neglecting the integrative gain:

$$\omega_{\mathrm{b},\theta} = k_{\epsilon}k_{\mathrm{p,PLL}} \tag{3.26}$$

This equation can be exploited to properly calibrate the proportional gain $k_{\mathrm{p,PLL}}$ to reach the desired $\omega_{\mathrm{b},\theta}$. At this point, the integral gain $k_{\mathrm{i,PLL}}$ can be tuned keeping in mind that the zero introduced by the PI regulator has to be lower than $\omega_{\mathrm{b},\theta}$ in order to guarantee a phase margin of at least 45°:

$$k_{\mathrm{i,PLL}} < k_{\mathrm{p,PLL}}\omega_{\mathrm{b},\theta} \tag{3.27}$$

The last parameter to be calibrated is the cut-off frequency ω_{f} of the demodulation LPF. This frequency must be considerably higher than $\omega_{\mathrm{b},\theta}$, in order to not affect the phase margin of the PLL, but sufficiently lower than ω_{c} to effectively filter the noise introduced by the HF injection. The adopted choice of $f_{\mathrm{c}} = f_{\mathrm{sw}}/2$ allows the maximum possible decoupling between injection and fundamental frequency, and so the widest frequency range for choosing $\omega_{\mathrm{b},\theta}$ and ω_{f}, thus facilitating the calibration procedure even without flux maps:

$$\omega_{\mathrm{b},\theta} \ll \omega_{\mathrm{f}} \ll 2\pi f_{\mathrm{sw}} \tag{3.28}$$

In this implementation, the selected values are $\omega_{\mathrm{b},\theta} = 20\ rad/s$, $\omega_{\mathrm{f}} = 940\ rad/s$ and the switching frequency is $f_{\mathrm{sw}} = 10\ kHz$.

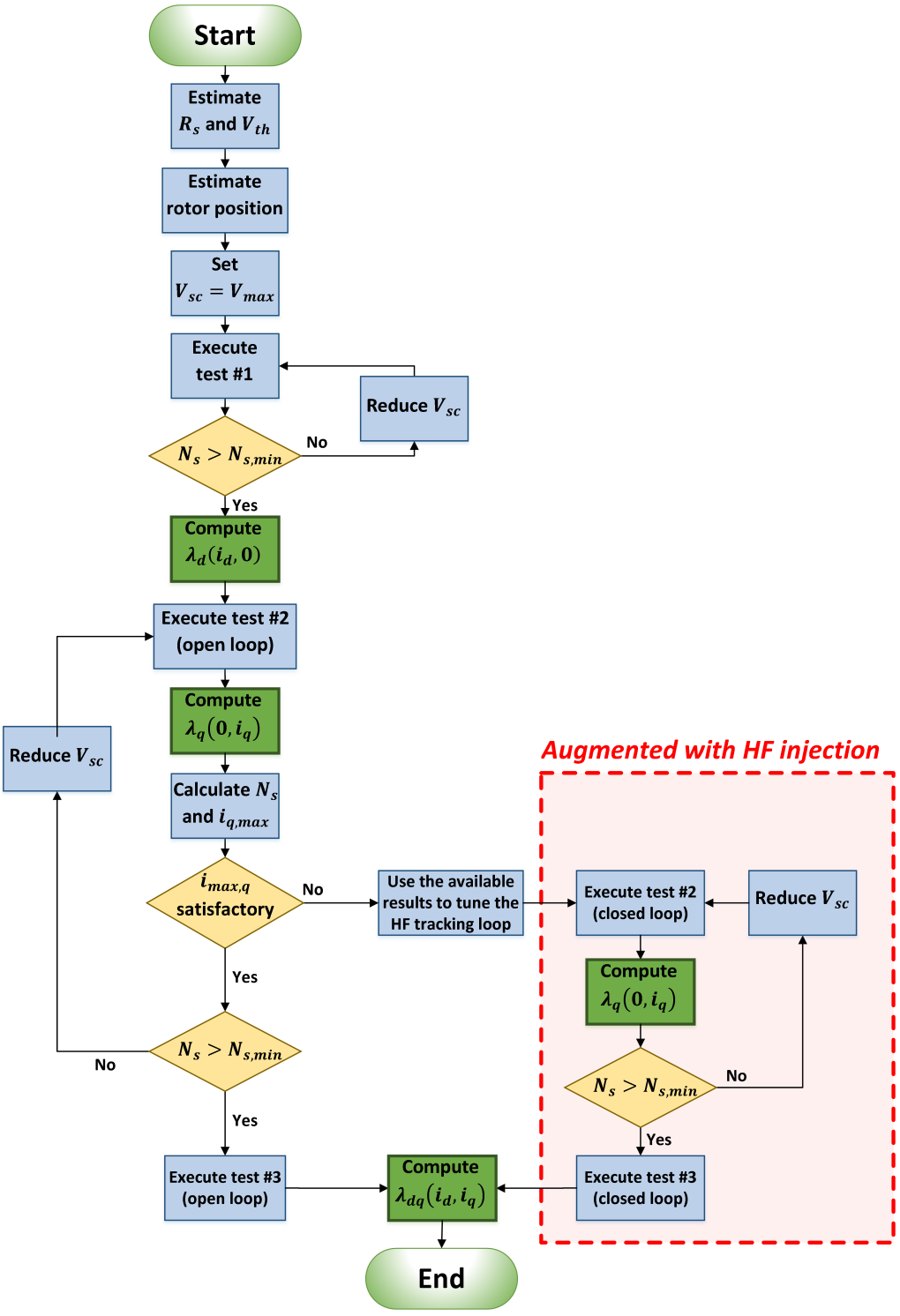

Figure 3.20: Automatic test sequence for the commissioning of SyR motors.

3.3.5 Experimental Results

The proposed magnetic model identification technique was experimentally validated on several SyRMs. Table 3.3 summarizes the main machine parameters [1], while Figure 3.21 shows the picture of three of them. Every test was implemented using a dSpace 1103 PPc controller board. The adopted DC bus voltage was $v_{dc} = 560\ V$ with a maximum inverter current of 40 A.

Table 3.3: Ratings of the SyR motors under test.

	SR1kW1	**SR2kW2**	**SR4kW**	**DOL7kW5**
Rated current [A]	2.8	5.08	17.5	17.6
Rated voltage [V]	408	400	400	365
Pole pairs	2	2	3	2
Rated torque [Nm]	7.1	15	37.5	47.8
Rated speed [rpm]	1479	1400	1000	1500
Rated power [kW]	1.1	2.2	4	7.5
Phase resistance [Ω]	4.63	3.58	0.4175	0.33
Switching frequency [kHz]	10	10	10	10

The results obtained from the motor SR2kW2 were already derailed in the previous sections. Figure 3.22 shows the time waveforms of voltages and currents while testing the motor SR1kW1. In this case, the current limit was pushed up to $i_d = 11\ A$ in test #1 and $i_q = 9.5\ A$ in test #2, using $V_{sc} = 220\ V$ in both cases. During test #3, a maximum swing of ($i_d = 13.2\ A, i_q = 8.3\ A$) was reached with $V_{d,sc} = V_{q,sc} = 260\ V$. As can be seen in Figure 3.22.d, the correspondence between the reference flux maps and the self-commissioning characteristic is almost perfect up to strong overload conditions, being the rated current of 2.8 A.

Similar considerations can be applied for the motor SR4kW, whose test results are report in Figure 3.23. This motor was tested up to $i_d = 30\ A$ in test #1 and $i_q = 28\ A$ in test #2, with $V_{sc} = 200\ V$. During test #3, the measurement domain was extended up to ($i_d = 33\ A, i_q = 20\ A$) adopting

[1] The motors SR1kW1, SR2kW2 and SR4kW are pure transverse laminated SyR machines, while the DOL7kW5 motor is a line starter, so it is basically a SyRM but it also has a squirrel cage for self-starting if connected directly to the grid.

Figure 3.21: Picture of three tested SyR motors. From left to right: SR4kW, SR2kW2 and SR1kW1.

$V_{\mathrm{d,sc}} = V_{\mathrm{q,sc}} = 140\ V$. Also in this case, the computed flux maps are well in accordance with the reference characteristic even in overload. Further exploration of the characteristic was not possible because of the inverter current limitation.

Finally, self commissioning was tested on the motor DOL7kW5 (see Figure 3.24). In this test, the maximum achieved currents have been $i_{\mathrm{d}} = 25\ A$ in test #1 with $V_{\mathrm{sc}} = 230\ V$ and $i_{\mathrm{q}} = 16.5\ A$ in test #2 using $V_{\mathrm{sc}} = 200\ V$. Test #3 was not executed in this motor because for this application it was not required to evaluate the cross-saturation effect. In this case, the $\lambda_{\mathrm{q}}(i_{\mathrm{q}})$ curve obtained in self-commissioning matches very well with the reference flux maps, but a relevant deviation is observed for the d axis. This effect can be explained considering that the reference method [40] evaluates the machine response at the fundamental frequency. Conversely, during self-commissioning the motor is excited with a square wave voltage, thus implying the presence of high order harmonics. Such high harmonics give negligible effects in case of pure SyR motors, such as SR1kW1, SR2kW2 and SR4kW, but excite the squirrel cage present in the DOL7kW5 machine, thus increas-

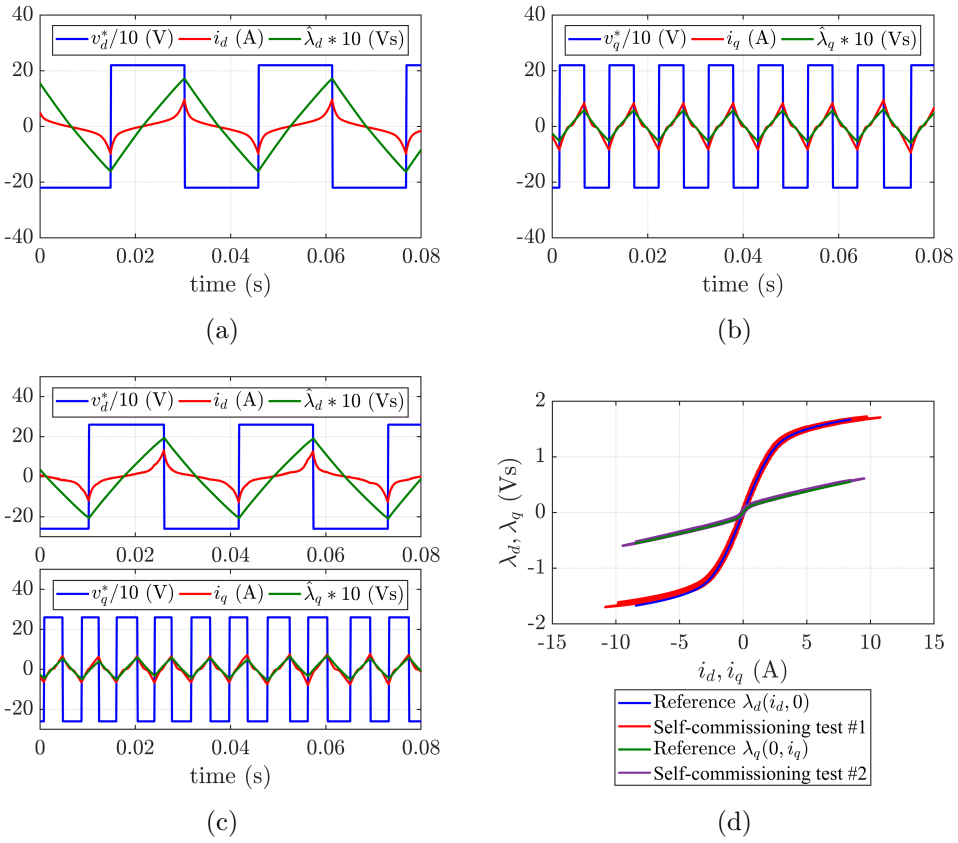

Figure 3.22: Experimental: time waveforms of reference voltage, current and estimated flux and comparison with the reference flux maps. (a) test #1 ($v_\mathrm{q} = 0; i_\mathrm{q} \approx 0$); (b) test #2 ($v_\mathrm{d} = 0; i_\mathrm{d} \approx 0$); (c) test #3; (d) computed flux characteristics. Motor: SR1kW1. Rated current: 2.8 A.

ing the equivalent inductance in d axis. Anyway, it should be noted that this kind of motors are made for grid-connected applications and they are rarely adopted in drives. Moreover, for low speed sensorless control, the motor is often excited with HF signal injection, thus the additional l_d due to the cage should be taken into account. Therefore, the self-commissioning maps may be more effective than the reference ones.

The square wave voltage injection magnetic model identification was also tested with different hardware on a very high current prototype of SyR machine for aerospace applications (SR250kW). For sake of better organizing the work, these results are discussed in a dedicated Section 5.1.3.

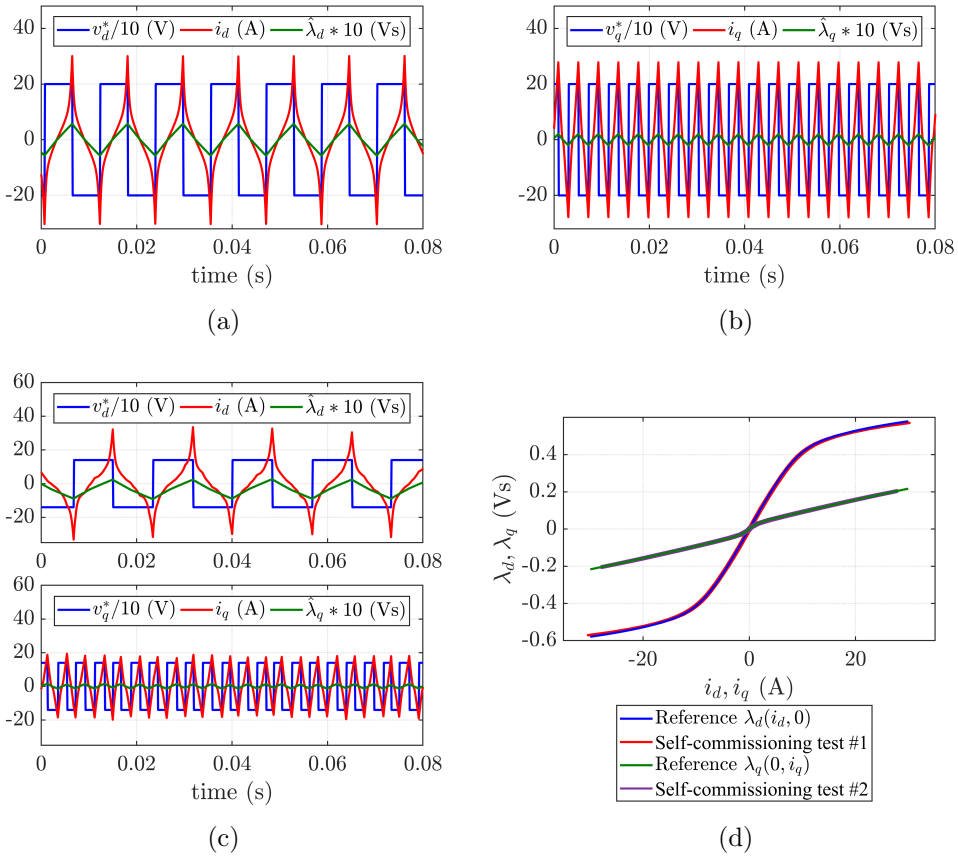

Figure 3.23: Experimental: time waveforms of reference voltage, current and estimated flux and comparison with the reference flux maps. (a) test #1 ($v_\mathrm{q} = 0; i_\mathrm{q} \approx 0$); (b) test #2 ($v_\mathrm{d} = 0; i_\mathrm{d} \approx 0$); (c) test #3; (d) computed flux characteristics. Motor: SR4kW. Rated current: 17.5 A.

3.4 Data Manipulation

In this section, the techniques adopted for manipulating the rough data measured during the self-commissioning stage for obtaining the flux maps are described. The section is organized as follow: Section 3.4.1 describes the problems related to the back-EMF open loop integration; Section 3.4.2, Section 3.4.3 and Section 3.4.4 present three alternative methods to extract the average flux characteristic from the measured data. In particular, the first two give the direct flux maps in form of look-up-tables, while the third describes a polynomial inverse magnetic model, together with the methods adopted to determine the required model parameters and a novel method for computing MTPA trajectory from this inverse magnetic model. Sec-

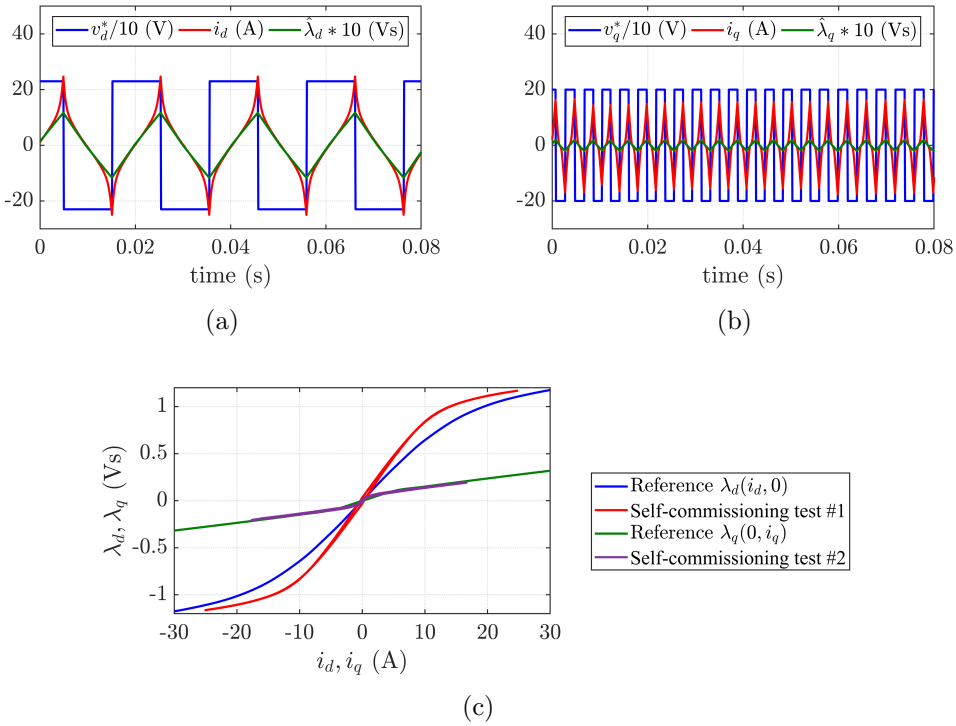

Figure 3.24: Experimental: time waveforms of reference voltage, current and estimated flux and comparison with the reference flux maps. (a) test #1 ($v_\mathrm{q} = 0; i_\mathrm{q} \approx 0$); (b) test #2 ($v_\mathrm{d} = 0; i_\mathrm{d} \approx 0$); (c) computed flux characteristics. Motor: DOL7kW5. Rated current: 17.6 A.

tion 3.4.5 describes the effects on the computed flux characteristic due to the HF voltage injection eventually adopted for online position tracking. Finally, Section 3.4.6 discusses a possible method to retrieve information about iron losses based on the same data used for flux maps identification.

3.4.1 Flux Integration Drift

The flux characteristics are estimated from open loop integration of the back-EMF, thus it requires an appropriate initial value. Moreover, in presence of small inaccuracies in determining the electromotive forces, e.g. due to inaccurate resistance estimation or inverter compensation, the flux estimation tends to diverge, drifting from the real saturation characteristic.

There are several options to get rid of this problem. An easy solution is to replace the pure integrators in (3.1)-(3.4) with low pass filters, which is equivalent to a high pass filter applied after the pure integrator. In this

way, the unavoidable offset in estimated EMF, which is a DC (or at least low frequency) component, is filtered out. For digital implementation, the equations (3.1)-(3.4) become:

$$\hat{\lambda}_{\mathrm{d}}(k) = \hat{\lambda}_{\mathrm{d}}(k-1) + T_{\mathrm{sw}}\left(v_{\mathrm{d}}^{*}(k-1) - \hat{R}_{\mathrm{s}} i_{\mathrm{d}} - \hat{V}_{\mathrm{th}} sign(i_{\mathrm{d}}) - \omega_{\mathrm{f}}\hat{\lambda}_{\mathrm{d}}(k-1)\right) \tag{3.29a}$$

$$\hat{\lambda}_{\mathrm{q}}(k) = \hat{\lambda}_{\mathrm{q}}(k-1) + T_{\mathrm{sw}}\left(v_{\mathrm{q}}^{*}(k-1) - \hat{R}_{\mathrm{s}} i_{\mathrm{q}} - \hat{V}_{\mathrm{th}} sign(i_{\mathrm{q}}) - \omega_{\mathrm{f}}\hat{\lambda}_{\mathrm{q}}(k-1)\right) \tag{3.29b}$$

where ω_{f} is the cut-off frequency of the applied filter, which must be chosen low enough to not influence the dynamic of flux estimation but sufficiently high to effectively eliminate the integration drift. With this solution, a random value can be adopted as initial state of the integrator, since after a few cycles it would converge to a loop with negligible average value. Reasonable values are $\omega_{\mathrm{f}} = 2\pi \cdot 2 \div 2\pi \cdot 5\ rad/s$.

A feasible alternative is to use only few current cycles (e.g. 2) for estimating the flux characteristic. In this way, the drift is very limited and its effects can be overcome by the other necessary post-processing techniques described in the following sections, e.g. Section 3.4.4. With this solution, the estimated saturation characteristic directly comes from voltage integration and it is not influenced by any filter. The (eventual) voltage offset is integrated for a reduced time and the flux drift is very limited and can be neglected. In this case, still there is the problem of defining the initial value of the integrator. It must be considered that the $\lambda_{\mathrm{d}}(i_{\mathrm{d}})$ and $\lambda_{\mathrm{q}}(i_{\mathrm{q}})$ curves (or λ_{q0} in case of PM-SyR) must be zero when the current is null. Therefore, a random initial value can be chosen and, after calculating the saturation characteristics, an offset is set to force the curves to pass through the origin of the plane.

3.4.2 Weighted Average

Once estimated the saturation characteristics, it is necessary to organize the data in appropriate look-up-tables suitable for being used in motor control. It is reasonable that the flux maps must be evaluated in form of vectors or matrices having regularly spaced current values, while the distribution of the measurement samples obtained from the self-commissioning depends on the applied voltage and differential machine inductance, so the samples are not equally spaced. Moreover, the measurement data describe a loop in the flux curve, so the average characteristic must be extracted.

To solve both these problems, a valid solution is to apply a weighted average of the measurement samples. As an example, the test #1 is considered.

The goal is to convert a set of measurement points $\boldsymbol{\lambda}_{\mathrm{d,meas}}(\boldsymbol{i}_{\mathrm{d,meas}})$ into a vector $\boldsymbol{i}_{\mathrm{d,tab}}$ and its correspondent flux estimate $\boldsymbol{\lambda}_{\mathrm{d,tab}}$. The values of the vector $\boldsymbol{i}_{\mathrm{d,tab}}$ are chosen equally spaced with an arbitrary step amplitude. Then, for each element of $\boldsymbol{i}_{\mathrm{d,tab}}$ the correspondent $\boldsymbol{\lambda}_{\mathrm{d,tab}}$ is obtained as the weighted sum of every flux estimate collected during the test, where the weight depends on the distance between the measured sample and the element of $\boldsymbol{i}_{\mathrm{d,tab}}$. So, the n^{th} element of $\boldsymbol{\lambda}_{\mathrm{d,tab}}$ is given by:

$$\boldsymbol{\lambda}_{\mathrm{d,tab}}(n) = \frac{\sum_{j=1}^{n_s} w(j)\boldsymbol{\lambda}_{\mathrm{d,meas}}(j)}{\sum_{j=1}^{n_s} w(j)} \tag{3.30}$$

where n_s is the number of measurement points, j is the index of the element of $\boldsymbol{i}_{\mathrm{d,meas}}$ (and therefore also $\boldsymbol{\lambda}_{\mathrm{d,meas}}$) and $w(j)$ is the weight of the j^{th} measurement sample:

$$w(j) = \frac{1}{\left[\ \boldsymbol{i}_{\mathrm{d,meas}}(j) - \boldsymbol{i}_{\mathrm{d,tab}}(n)\ \right]^4 + \frac{1}{w_{max}}} \tag{3.31}$$

The biquadratic function in (3.31) proved to be an effective weight function [8]. Anyway, other equations can be used instead. The term $w_{max} > 0$ limits the weight of a single measurement point and it was added to avoid eventual division by zero.

The equations (3.30) and (3.31) can be equivalently written for the q axis in case of test #2 and were adopted, as an example, to extract the average curve of $\lambda_{\mathrm{d}}(i_{\mathrm{d}})$ and $\lambda_{\mathrm{q0}}(i_{\mathrm{q}})$ report in Figure 3.34.

An alternative formulation must be adopted for test #3, since both axes are involved. In this case, the measured data must be converted into two matrices $\boldsymbol{\lambda}_{\mathrm{d,tab}}(\boldsymbol{i}_{\mathrm{d,tab}}, \boldsymbol{i}_{\mathrm{q,tab}})$ and $\boldsymbol{\lambda}_{\mathrm{q,tab}}(\boldsymbol{i}_{\mathrm{d,tab}}, \boldsymbol{i}_{\mathrm{q,tab}})$. In this case, the weighted average is modified as:

$$\boldsymbol{\lambda}_{\mathrm{d,tab}}(n, m) = \frac{\sum_{j=1}^{n_s} w(j)\boldsymbol{\lambda}_{\mathrm{d,meas}}(j)}{\sum_{j=1}^{n_s} w(j)} \tag{3.32}$$

where n and m are the indexes of the matrix $\boldsymbol{\lambda}_{\mathrm{d,tab}}$ in d and q direction and the weight is given by

$$w(j) = \frac{1}{\left[\ \left(\boldsymbol{i}_{\mathrm{d,meas}}(j) - \boldsymbol{i}_{\mathrm{d,tab}}(n,m)\right)\left(\boldsymbol{i}_{\mathrm{q,meas}}(j) - \boldsymbol{i}_{\mathrm{q,tab}}(n,m)\right)\ \right]^2 + \frac{1}{w_{max}}} \tag{3.33}$$

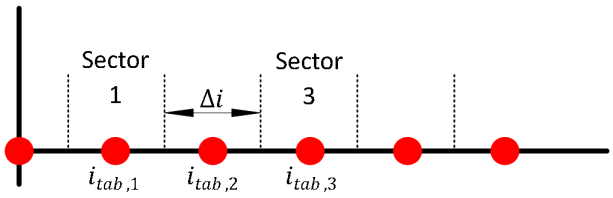

Figure 3.25: Division of the current domain for online filtering.

In this way, the Euclidean distance in the current plane between the measured samples and the points required for the look up tables is taken into account. It must be also considered that the weighted average limits the effects of drifting due to open loop integrator, described in Section 3.4.1.

3.4.3 Online Filter

A feasible alternative to the weighted average is to apply an online filter to the measured data. Basically, the current domain is divided into equally spaced sectors with an amplitude Δi, centered around the values of the vector $\boldsymbol{i}_{\mathrm{d,tab}}$. Therefore, the sectors are defined as $\boldsymbol{i}_{\mathrm{d,tab}} \pm \Delta i/2$, as shown in Figure 3.25. During the self-commissioning test, every measurement sample will belong to one of the sectors. If j is the index of the sector in which the measured current falls at the sampling time k, the value of $\boldsymbol{\lambda}_{\mathrm{d,tab}}(j)$ is updated according to the following relationship:

$$\boldsymbol{\lambda}_{\mathrm{d,tab}}(j) = p\boldsymbol{\lambda}_{\mathrm{d,tab}}(j) + (1-p)\boldsymbol{\lambda}_{\mathrm{d,meas}}(k) \tag{3.34}$$

Where $p < 1$ is arbitrary fixed. Whatever is the initialization of $\boldsymbol{\lambda}_{\mathrm{d,tab}}(j)$, after a reasonable number of iterations it will converge to an average value, which takes into account all the measured data falling in the j^{th} sector and can be conveniently adopted for motor control. The value of p defines the convergence speed. The advantage of this method is that it is computationally very efficient since it can be run online during the commissioning, therefore it does not require storing neither the rough measured data nor a post-processing data manipulation: the look-up tables are directly available at the end of the self-commissioning procedure. Moreover, the effects of open loop integration drift is inherently taken into account. A possible drawback is that, depending on the chosen p, it may require a high number of current sweeps.

3.4.4 Polynomial Fit of the Magnetic Model and MTPA Curve

A further way to post-process the measured data is to interpolate the samples with an analytical magnetic model. The advantage of this approach is that the saturation characteristic is represented with a much smaller number of parameters respect to Look-Up-Tables. Proper parameter set can be obtained by interpolating the flux waveforms measured during self-commissioning. Moreover, accurate analytical functions permit to extend the magnetic characteristic out of the measurement range.

The literature presents several algebraic models [88, 90, 107] to represent the magnetic characteristic, often requiring exponential or rational equations and therefore the fitting procedure aimed to evaluate the model parameters is usually complicated. Moreover, rational equations may present undesired vertical asymptotes and do not ensure monotonic behavior, so the fitting function may be not invertible.

For this reason, it was chosen to adopt an inverse magnetic model, presented in [89]. It means that the characteristic $\boldsymbol{i}_{\mathrm{dq}}(\boldsymbol{\lambda}_{\mathrm{dq}})$ is evaluated instead of the classical direct flux maps $\boldsymbol{\lambda}_{\mathrm{dq}}(\boldsymbol{i}_{\mathrm{dq}})$. If the direct characteristic is desired, it can be conveniently retrieved using several numerical methods. The advantage of this approach is that the inverse characteristic is well represented by polynomial functions, whose parameters can be easily retrieved.

The adopted algebraic magnetic model is given by the following equations, which were used, as an example, in Figure 3.7:

$$\hat{i}_{\mathrm{d}} = \lambda_{\mathrm{d}} \left(a_{\mathrm{d0}} + a_{\mathrm{dd}} |\lambda_{\mathrm{d}}|^{S} + \frac{a_{\mathrm{dq}}}{V+2} |\lambda_{\mathrm{d}}|^{U} |\lambda_{\mathrm{q}}|^{V+2} \right) \tag{3.35a}$$

$$\hat{i}_{\mathrm{q}} = \lambda_{\mathrm{q}} \left(a_{\mathrm{q0}} + a_{\mathrm{qq}} |\lambda_{\mathrm{q}}|^{T} + \frac{a_{\mathrm{dq}}}{U+2} |\lambda_{\mathrm{d}}|^{U+2} |\lambda_{\mathrm{q}}|^{V} \right) \tag{3.35b}$$

This model is physically reasonable, since, for example, for positive currents (and so fluxes), the cross-derivatives are both equal to $a_{\mathrm{dq}} \lambda_{\mathrm{d}}^{U+1} \lambda_{\mathrm{q}}^{V+1}$, so the reciprocity condition is respected:

$$\frac{\partial \hat{i}_{\mathrm{d}}}{\partial \lambda_{\mathrm{q}}} = \frac{\partial \hat{i}_{\mathrm{q}}}{\partial \lambda_{\mathrm{d}}} \tag{3.36}$$

Generally speaking, polynomial functions may not be able to extrapolate the model out of the measured range with optimal parameters computed in a limited domain, since the fitting polynomial may present undesired maximum or minimum out of the measurement domain. Anyway, in this case, the

Table 3.4: Best Fit Integer Exponents of (3.35) for Six SyRMs

Motor	Power (kW)	Speed (r/min)	S	T	U	V
CMP	0.9	3 600	6	1	1	0
SR2kW2	2.2	1 500	5	1	1	0
EA4	4.0	1 500	5	1	1	0
ABB	6.7	1 500	6	1	1	0
PMP	7.5	1 500	8	1	3	0
Sicme	250	1 000	5	1	1	0

monotonicity of the curves is ensured by forcing non-negative parameters of (3.35). Therefore, the flux maps can be conveniently extended far beyond the measurement area.

To test this polynomial model, the flux maps of six SyR motors of different size were studied and a proper parameters set was found for each of them (see Table 3.4). The model and the reference flux maps showed a good agreement, as can be seen from Figure 3.26, thus proving the validity of the model. The Figure compares the reference flux maps and the fitted surface using (3.35) for d and q axes, together with the discrepancy between the two expressed as current error.

The model presents five parameters a_{d0}, a_{q0}, a_{dd}, a_{qq} and a_{dq} and four exponents S, T, U, V. As can be noticed, (3.35) represents the complete magnetic model of the machine, including saturation and cross-saturation effects, but its complexity can be adapted to the application requirements by properly choosing the parameters. By choosing $a_{\mathrm{dq}} = 0$, the model represents the magnetic self-characteristic, thus neglecting the effects of cross-saturation. In addition, if the condition $a_{\mathrm{dd}} = a_{\mathrm{qq}} = a_{\mathrm{dq}} = 0$ is adopted, the equation (3.35) represents a linear magnetic model, with $a_{\mathrm{d0}} = 1/L_{\mathrm{d}}$ and $a_{\mathrm{q0}} = 1/L_{\mathrm{q}}$.

Several strategies are proposed to find optimal parameters set. Despite rational exponents could be adopted, integer exponents were conveniently used decreasing the computational complexity without considerably reducing the accuracy. In particular, optimal parameters set was retrieved for each motor and summarized in Table 3.4. As can be noticed, most of the motors were well represented by choosing $S = 5 \div 8$, $T = U = 1$ and $V = 0$. Moreover, the choice of S is not critical: a deviation of ± 1 from the optimal value does not considerably affects the mismatch between model and reference flux maps, as shown in Figure 3.27. Therefore, it is assumed that the exponents can be fixed a priori for every SyRM under test, or at least the number of possible exponents' combinations is limited to a few typical sets.

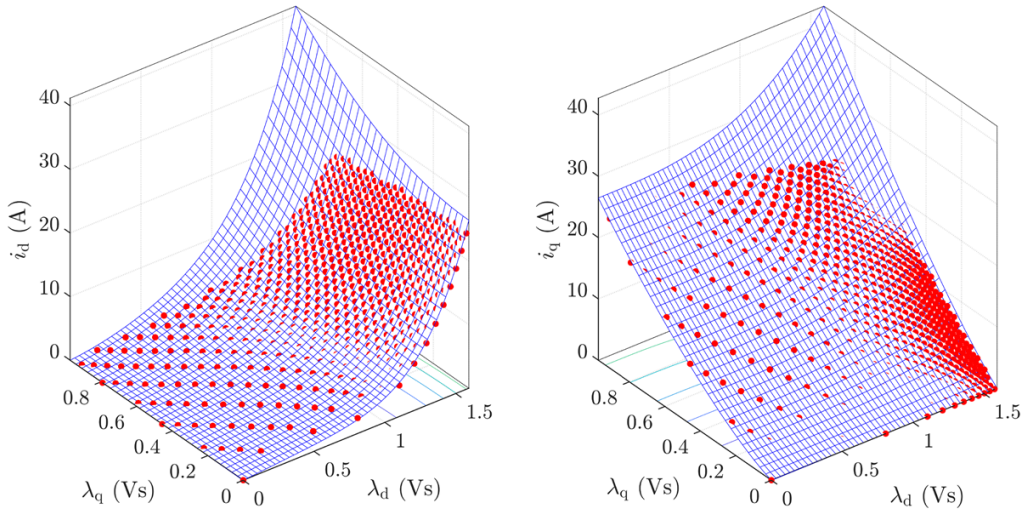

(a)

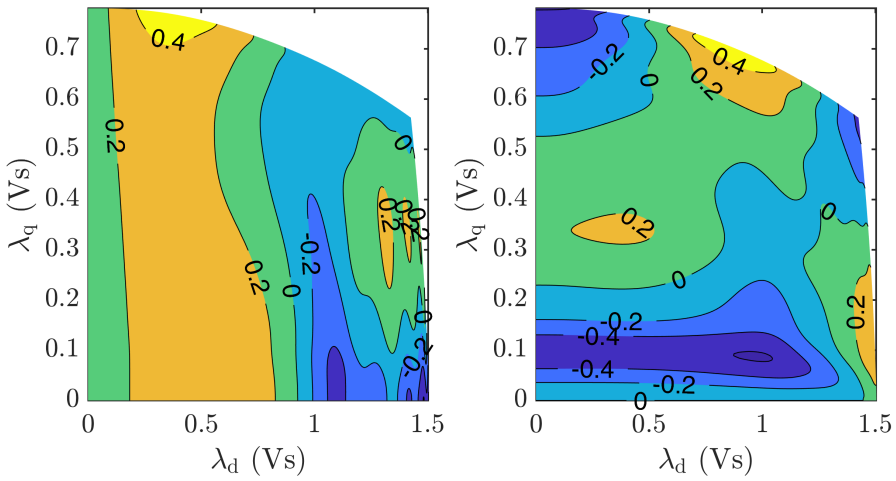

(b)

Figure 3.26: (a) Comparison between analytical model (blue grid) and reference flux maps (red dots) and (b) their current discrepancy (A) for the motor EA4. Left: d axis; right: q axis.

3.4.4.1 Analytical Solution Based on Few Measurement Points

To obtain a closed solution for identification of the model parameters, only positive currents and fluxes will be considered. The negative values can be conveniently reversed and averaged with the positive ones, if necessary. The

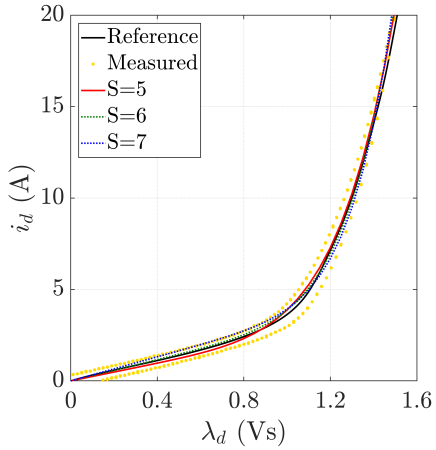

Figure 3.27: Black: reference flux maps. Yellow: measurement points for test #1. Red, green and blue: fitting function with (3.35) and $S = 5$, $S = 6$ and $S = 7$ respectively.

derivative of (3.35) can be exploited:

$$\frac{\partial \hat{i}_\mathrm{d}}{\partial \lambda_\mathrm{d}} = a_{\mathrm{d}0} + (S+1)\, a_{\mathrm{dd}} \lambda_\mathrm{d}^S + \frac{U+1}{V+2} a_{\mathrm{dq}} \lambda_\mathrm{d}^U \lambda_\mathrm{q}^{V+2} \tag{3.37a}$$

$$\frac{\partial \hat{i}_\mathrm{q}}{\partial \lambda_\mathrm{q}} = a_{\mathrm{q}0} + (T+1)\, a_{\mathrm{qq}} \lambda_\mathrm{q}^T + \frac{V+1}{U+2} a_{\mathrm{dq}} \lambda_\mathrm{d}^{U+2} \lambda_\mathrm{q}^V \tag{3.37b}$$

These derivatives calculated for $\lambda_\mathrm{d} \to 0$, $\lambda_\mathrm{q} \to 0$ permits to estimate the terms $a_{\mathrm{d}0}$ and $a_{\mathrm{q}0}$:

$$\left.\frac{\partial \hat{i}_\mathrm{d}}{\partial \lambda_\mathrm{d}}\right|_{\lambda_\mathrm{d} \to 0} = a_{\mathrm{d}0} \tag{3.38a}$$

$$\left.\frac{\partial \hat{i}_\mathrm{q}}{\partial \lambda_\mathrm{q}}\right|_{\lambda_\mathrm{q} \to 0} = a_{\mathrm{q}0} \tag{3.38b}$$

Therefore, $a_{\mathrm{d}0}$ can be conveniently obtained from test #1 and $a_{\mathrm{q}0}$ from test #2 relying on the samples acquired at low current. Once obtained these two parameters, the parameter a_{dd} and the exponent S of the curve passing for two points $i_{d1}(\lambda_{d1})$ and $i_{d2}(\lambda_{d2})$ measured during test #1 is analytically retrieved:

$$S = \frac{ln\frac{D_1}{D_2}}{ln\frac{\lambda_{d1}}{\lambda_{d2}}} - 1 \tag{3.39}$$

$$a_{\mathrm{dd}} = \frac{D_1}{\lambda_{d1}^{S+1}} = \frac{D_2}{\lambda_{d2}^{S+1}} \tag{3.40}$$

where D_1 and D_2 are known quantities:

$$D_1 = i_{d1} - a_{\mathrm{d0}}\lambda_{d1} = a_{\mathrm{dd}}\lambda_{d1}^{S+1}$$
$$D_2 = i_{d2} - a_{\mathrm{d0}}\lambda_{d2} = a_{\mathrm{dd}}\lambda_{d2}^{S+1}$$

Similarly, proper values of a_{qq} and T can be estimated from only two points $i_{q3}(\lambda_{q3})$ and $i_{q4}(\lambda_{q4})$ measured during test #2:

$$T = \frac{ln\frac{Q_3}{Q_4}}{ln\frac{\lambda_{q3}}{\lambda_{q4}}} - 1 \tag{3.41}$$

$$a_{\mathrm{dd}} = \frac{Q_3}{\lambda_{q3}^{T+1}} = \frac{Q_4}{\lambda_{q4}^{T+1}} \tag{3.42}$$

where

$$Q_3 = i_{q3} - a_{\mathrm{q0}}\lambda_{q3} = a_{\mathrm{qq}}\lambda_{q3}^{T+1}$$
$$Q_4 = i_{q4} - a_{\mathrm{q0}}\lambda_{q4} = a_{\mathrm{qq}}\lambda_{q4}^{T+1}$$

According to Table 3.4, we can assume $V = 0$. With this hypothesis, and using only one sample point $\lambda_{d5}(i_{d5}, i_{q5})$, $\lambda_{q5}(i_{d5}, i_{q5})$ measured during test #3, it is possible to retrieve the two missing parameters:

$$U = \frac{D_5}{Q_5}\lambda_{d5} - 2 \tag{3.43}$$

$$a_{\mathrm{dq}} = \frac{D_5}{\lambda_{d5}^{U+1}} = \frac{Q_5}{\lambda_{q5}^{U+2}}\,(U+2) \tag{3.44}$$

where

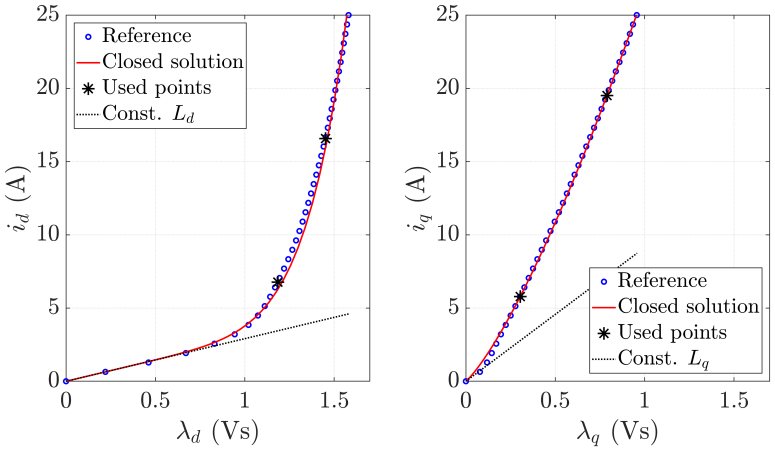

Figure 3.28: Reference flux maps of the motor EA3 (blue dots) interpolated with (3.35) (red line). The exponents and parameters were retrieved from the analytical solution based on the black points.

$$D_5 = 2\frac{i_{d5} - a_{\mathrm{d0}}\lambda_{d5} - a_{\mathrm{dd}}\lambda_{d5}^{S+1}}{\lambda_{q5}^2}$$
$$Q_5 = \frac{i_{q5} - a_{\mathrm{q0}}\lambda_{q5} - a_{\mathrm{qq}}\lambda_{q5}^{T+1}}{\lambda_{q5}}$$

So, optimal parameters set can be found considering only five measurement points and the initial slope of the flux curves. As shown in Figure 3.28, this method gave accurate results and it has the advantage of presenting a closed solution for all the model parameters and exponents. Anyway, it is quite sensitive to the choice of the five points adopted for the interpolation.

3.4.4.2 LLS Optimization

In alternative, the exponents can be chosen according to Table 3.4. For a given set of exponents, retrieving the fitting parameters becomes a linear problem, since it reduces to solving a set of linear equations that can be solved through Linear Least Square (LLS) techniques. The solution is unique and it does not require initial conditions nor cost functions. Several LLS recursive algorithms, e.g. [108], can be implemented in the drive micro-controller. Since the amount of feasible integer exponents is limited, the parameters can be solved for different typical sets of exponents, which

have been chosen in advance. Then, the set of exponents (and the corresponding fitted parameters) leading to the smallest root mean square error can be selected.

In principle, the data collected during test #1, #2 and #3 can be aggregate to find in an unique step the set of optimal parameters that minimize the global root mean square error between predicted and measured fluxes computed during the three tests. Anyway, it was found more accurate and less computationally heavy to split the optimization in three steps.

In the first stage, the data collected during test #1 are used to determine the parameters $a_{\mathrm{d}0}$ and a_{dd}. Since $i_{\mathrm{q}} = 0$ and $\lambda_{\mathrm{q}} = 0$, and considering for simplicity positive currents and fluxes, the model (3.35) reduces to:

$$i_{\mathrm{d}} = a_{\mathrm{d}0}\lambda_{\mathrm{d}} + a_{\mathrm{dd}}\lambda_{\mathrm{d}}^{S+1} \tag{3.45}$$

Since the exponent S is fixed (e.g. $S = 5$), this model is linear with respect to the two unknown parameters $a_{\mathrm{d}0}$ and a_{dd}. The LLS problem can be written in a vector form:

$$\underbrace{\begin{bmatrix} i_{\mathrm{d}}(1) \\ i_{\mathrm{d}}(2) \\ \vdots \\ i_{\mathrm{d}}(N_{\mathrm{d}}) \end{bmatrix}}_{y_d} = \underbrace{\begin{bmatrix} \lambda_{\mathrm{d}}(1) & \lambda_{\mathrm{d}}(1)^{S+1} \\ \lambda_{\mathrm{d}}(2) & \lambda_{\mathrm{d}}(2)^{S+1} \\ \vdots & \vdots \\ \lambda_{\mathrm{d}}(N_{\mathrm{d}}) & \lambda_{\mathrm{d}}(N_{\mathrm{d}})^{S+1} \end{bmatrix}}_{\boldsymbol{X}_{\mathrm{d}}} \underbrace{\begin{bmatrix} a_{\mathrm{d}0} \\ a_{\mathrm{dd}} \end{bmatrix}}_{\boldsymbol{\beta}_{\mathrm{d}}} + \underbrace{\begin{bmatrix} \varepsilon_{\mathrm{d}}(1) \\ \varepsilon_{\mathrm{d}}(2) \\ \vdots \\ \varepsilon_{\mathrm{d}}(N_{\mathrm{d}}) \end{bmatrix}}_{\boldsymbol{\varepsilon}_{\mathrm{d}}} \tag{3.46}$$

where $\boldsymbol{y}_{\mathrm{d}}$ is the vector of the current samples, $\boldsymbol{X}_{\mathrm{d}}$ is regressor matrix, $\boldsymbol{\beta}_{\mathrm{d}}$ is the parameter vector, $\boldsymbol{\varepsilon}_{\mathrm{d}}$ is the residual vector, and N_{d} is the number of samples acquired for test #1. The sum of the squared residuals is

$$J_{\mathrm{d}}(\boldsymbol{\beta}_{\mathrm{d}}) = \boldsymbol{\varepsilon}_{\mathrm{d}}^{\mathrm{T}}\boldsymbol{\varepsilon}_{\mathrm{d}} \tag{3.47}$$

The vector of parameters which minimize J_{d} is given by:

$$\boldsymbol{\beta}_{\mathrm{d}} = (\boldsymbol{X}_{\mathrm{d}}^{\mathrm{T}}\boldsymbol{X}_{\mathrm{d}})^{-1}\boldsymbol{X}_{\mathrm{d}}^{\mathrm{T}}\boldsymbol{y}_{\mathrm{d}} \tag{3.48}$$

Similarly, according to Table 3.4, $T = 1$ can be imposed, so optimal $a_{\mathrm{q}0}$ and a_{qq} can be retrieved from the data acquired during test #2. In this stage, the parameter vector becomes $\boldsymbol{\beta}_{\mathrm{q}} = [a_{\mathrm{q}0}, a_{\mathrm{qq}}]^{\mathrm{T}}$ while the number of samples is N_{q}. The only remaining parameter to be estimated is a_{dq}, which has to be

Table 3.5: Fitted Parameters Given in SI Units

S	T	U	V	a_{d0}	a_{dd}	a_{q0}	a_{qq}	a_{dq}
5	1	1	0	2.41	1.47	12.8	17.0	13.2

retrieved from test #3. For doing this, (3.35) is rewritten as

$$i_{\mathrm{d}} - a_{\mathrm{d0}}\lambda_{\mathrm{d}} - a_{\mathrm{dd}}\lambda_{\mathrm{d}}^{S+1} = \frac{a_{\mathrm{dq}}}{V+2}\lambda_{\mathrm{d}}^{U+1}\lambda_{\mathrm{q}}^{V+2} \tag{3.49a}$$

$$i_{\mathrm{q}} - a_{\mathrm{q0}}\lambda_{\mathrm{q}} - a_{\mathrm{qq}}\lambda_{\mathrm{q}}^{T+1} = \frac{a_{\mathrm{dq}}}{U+2}\lambda_{\mathrm{d}}^{U+2}\lambda_{\mathrm{q}}^{V+1} \tag{3.49b}$$

Adopting the previously computed a_{d0}, a_{dd}, a_{q0}, and a_{qq}, the left-hand term of this equation can be easily calculated, so the output vector becomes:

$$\boldsymbol{y}_{\mathrm{dq}} = \begin{bmatrix} i_{\mathrm{d}}(1) - a_{\mathrm{d0}}\lambda_{\mathrm{d}}(1) - a_{\mathrm{dd}}\lambda_{\mathrm{d}}(1)^{S+1} \\ i_{\mathrm{q}}(1) - a_{\mathrm{q0}}\lambda_{\mathrm{q}}(1) - a_{\mathrm{qq}}\lambda_{\mathrm{q}}(1)^{T+1} \\ \vdots \\ i_{\mathrm{d}}(N_{\mathrm{dq}}) - a_{\mathrm{d0}}\lambda_{\mathrm{d}}(N_{\mathrm{dq}}) - a_{\mathrm{dd}}\lambda_{\mathrm{d}}(N_{\mathrm{dq}})^{S+1} \\ i_{\mathrm{q}}(N_{\mathrm{dq}}) - a_{\mathrm{q0}}\lambda_{\mathrm{q}}(N_{\mathrm{dq}}) - a_{\mathrm{qq}}\lambda_{\mathrm{q}}(N_{\mathrm{dq}})^{T+1} \end{bmatrix} \tag{3.50}$$

where N_{dq} is the number of acquired points in test #3. The new regressor matrix becomes:

$$\boldsymbol{X}_{\mathrm{dq}} = \begin{bmatrix} \frac{1}{V+2}\lambda_{\mathrm{d}}(1)^{U+1}\lambda_{\mathrm{q}}(1)^{V+2} \\ \frac{1}{U+2}\lambda_{\mathrm{d}}(1)^{U+2}\lambda_{\mathrm{q}}(1)^{V+1} \\ \vdots \\ \frac{1}{V+2}\lambda_{\mathrm{d}}(N_{\mathrm{dq}})^{U+1}\lambda_{\mathrm{q}}(N_{\mathrm{dq}})^{V+2} \\ \frac{1}{U+2}\lambda_{\mathrm{d}}(N_{\mathrm{dq}})^{U+2}\lambda_{\mathrm{q}}(N_{\mathrm{dq}})^{V+1} \end{bmatrix} \tag{3.51}$$

Finally, the term a_{dq} representing the cross-coupling effect is given by

$$a_{\mathrm{dq}} = (\boldsymbol{X}_{\mathrm{dq}}^{\mathrm{T}}\boldsymbol{X}_{\mathrm{dq}})^{-1}\boldsymbol{X}_{\mathrm{dq}}^{\mathrm{T}}\boldsymbol{y}_{\mathrm{dq}} \tag{3.52}$$

Table 3.5 reports an example of optimal parameters set retrieved using LLS for the motor SR2kW2. The measurement points during the commissioning stage are compared with the fitting surface in Figure 3.4, while Figure 3.26 compares the analytical function with the reference flux maps for the motor EA4.

3.4.4.3 MTPA Calculation from Inverse Magnetic Model

The MTPA trajectory is easily retrieved from the direct flux maps $\boldsymbol{\lambda}_{\mathrm{dq}}(\boldsymbol{i}_{\mathrm{dq}})$. The traditional method consists of virtually moving offline the current vector along a circumference in the dq plane, thus in the locus of constant current amplitude, to find the angle γ corresponding to the maximum torque. This operation cannot be done using the inverse model (3.35), since current trajectories cannot be easily imposed. A feasible alternative is described here.

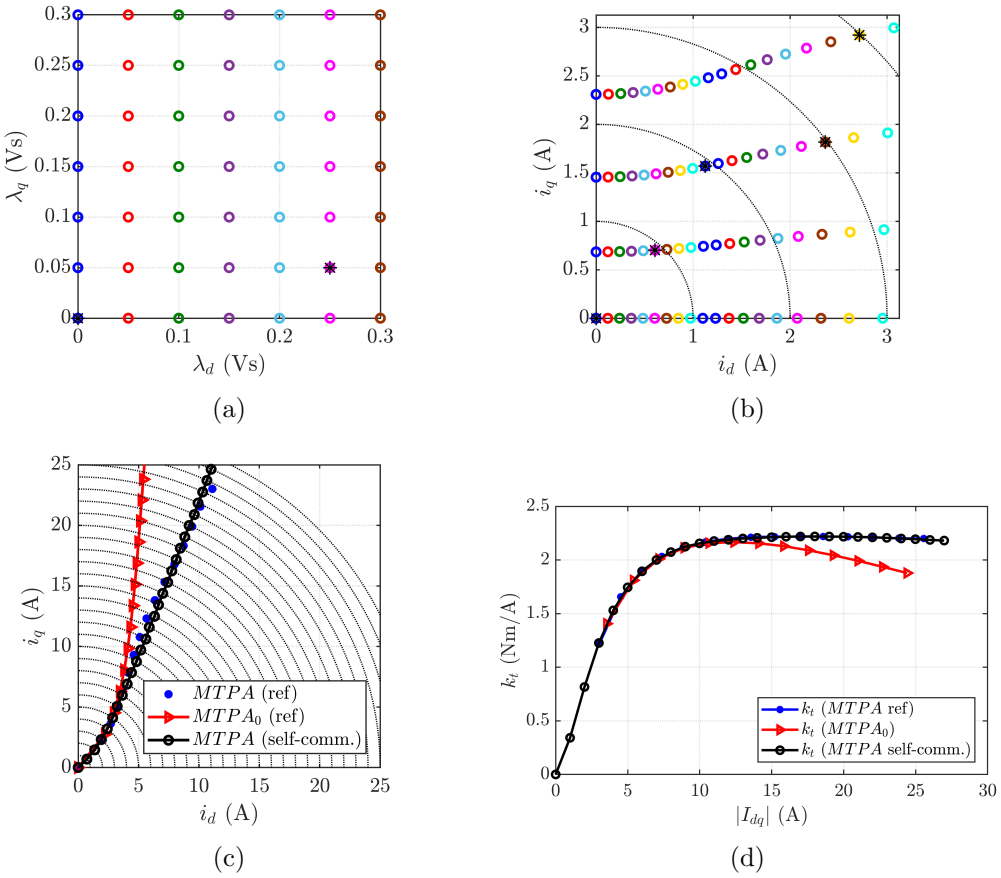

Figure 3.29: MTPA calculation based on inverse analytical magnetic model. (a) regular grid of reference points in the flux plane, detail at low current. (b) correspondent points on the current plane, detail at low current. (c) MTPA trajectory based on reference flux maps with (blue) and without (red) considering cross-saturation effect and MTPA curve obtained from the proposed method (black). (d) torque factor related to the three trajectories.

A regular grid is defined in the flux plane, with constant horizontal and vertical increment between consequent points, as in Figure 3.29(a). For each

of these reference points, the correspondent current is calculated using the inverse model (3.35), obtaining a set of points not equally spaced in the current plane (Figure 3.29(b)). Knowing the current and flux, for each point the torque and so the torque factor $k_t = T/|I|$ can be easily computed. Then, the current plane is divided into circular sectors, and for each of them, the point presenting the highest k_t is chosen as MTPA point, indicated with a black asterisk in Figure 3.29(b).

The accuracy of the MTPA trajectory depends on the step adopted when defining the regular grid in the flux plane, while the number of points on the trajectory is given by the number of sectors that divide the current plane. Figure 3.29(c) compares the MTPA trajectory calculated using the direct flux maps and the traditional method with the curve obtained from the inverse analytical model (3.35) and the proposed method. As can be seen, the two trajectories match very well, proving the validity of the proposed method. The same plot also presents the MTPA curve that would be estimated neglecting the cross-saturation (red line). Finally, Figure 3.29(d) compares the torque factor along those three trajectories.

3.4.5 Effects of HF Injection on Computed Flux Maps

In case the test #2 is augmented by HF signal injection for online position tracking, the flux estimation may be affected by the introduced HF oscillation. To overcome this issue, the reference voltage signals used for flux estimation are sampled before injection of the HF stimulus, as can be noticed in Figure 3.5, so the voltage integration does not see such component. Conversely, the measured current is directly used in (3.1)-(3.4) without any filtering and therefore it presents a HF component. This is reflected in two effects: on one side on the compensation of the resistive voltage drop, which contains the HF component, and on the other side the computed flux is referred to a current that is not monotonically increasing but presents an oscillation. Anyway, both these effects are minor if compared to other possible sources of error, such as inaccurate resistance estimation or compensation of inverter nonlinear effects, which are however well compensated as previously addressed. Moreover, the HF oscillation is canceled out once extracted the average curve from the measured cycle, as for example in Section 3.4.2-3.4.4.

In conclusion, it is not necessary to filter the HF component from the measured current used for flux estimation, which results almost immune from such disturbance. To prove this assert, Figure 3.30 plots the flux computed from test #2 augmented by voltage injection, comparing the flux directly estimated from (3.2) (blue line) with the saturation characteristic obtained when the current is preliminary filtered before voltage integration for the

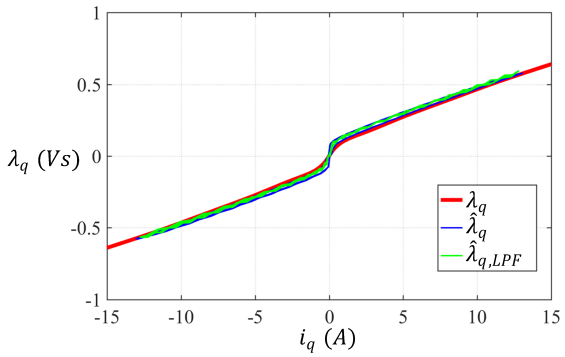

Figure 3.30: Effect of HF injection on the estimated flux. Red: reference flux maps. Blue: estimated without filtering the current. Green: estimated after filtering i_q.

motor SR2kW2. As can be seen, the two curves are overlapping.

3.4.6 Iron Loss

The square wave voltage identification resulted to be almost immune from iron losses effects. Anyway, a method to retrieve some information about the iron behavior was proposed in [6].

For this analysis, a simplified model is adopted to take into account iron behavior, as in Figure 3.31(a), where a resistance R_Fe is placed in parallel to the induced EMF. Although this model is quite rough and can be improved [17, 18], it can be conveniently used for this analysis. So, a resistive current $i_\mathrm{d,Fe}$ proportional to the induced voltage is superimposed to the inductive current $i_\mathrm{d,L}$. The resulting current waveform during magnetic model identification (test #1) was simulated in Figure 3.31(b).

$$i_\mathrm{d} = i_\mathrm{d,L} + i_\mathrm{d,Fe} \tag{3.53}$$

In particular, at the voltage reversal, i.e. when the current reaches the positive or negative peak, the current describes a small step as a consequence of iron losses. The amplitude of this step is manipulated to retrieve an approximated value of R_Fe. Considering a square wave excitation of the d axis as in test #1, and fixing k as the sampling time when the voltage polarity

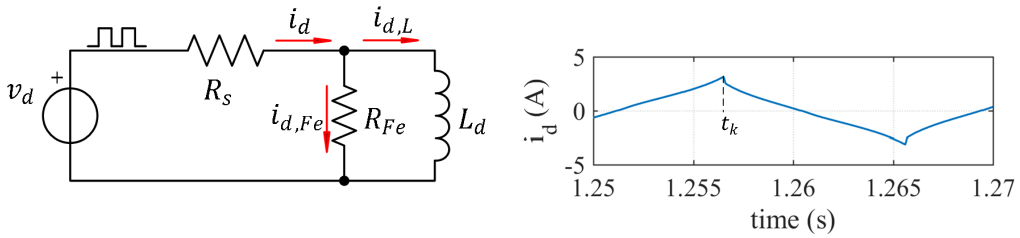

(a) (b)

Figure 3.31: (a) equivalent scheme of the motor in presence of iron losses. (b) effect of stator losses on the current i_d during test #1 (simulation).

is reversed, as in Figure 3.31(b), the following quantities are defined:

$$i_\mathrm{d}(k-0.5) = \frac{1}{2}\left(i_\mathrm{d}(k-1) + i_\mathrm{d}(k)\right) \tag{3.54a}$$

$$i_\mathrm{d}(k+0.5) = \frac{1}{2}\left(i_\mathrm{d}(k) + i_\mathrm{d}(k+1)\right) \tag{3.54b}$$

It is assumed that the current in the inductance $i_\mathrm{d,L}$ does not considerably change between the sampling instant $(k-1)$ and $(k+1)$, therefore the value of the apparent inductance L_d can be calculated before the voltage reversal and considered constant:

$$L_\mathrm{d} = \frac{V_\mathrm{sc} - R_\mathrm{s} i_\mathrm{d}(k-0.5) - V_\mathrm{th}}{i_\mathrm{d}(k) - i_\mathrm{d}(k-1)} T_\mathrm{sw} \tag{3.55}$$

The inductive and resistive current components at the sampling time $(k-1)$ can be respectively computed as:

$$i_\mathrm{d,L}(k-1) = i_\mathrm{d,L}(k) - \frac{V_\mathrm{sc} - R_\mathrm{s} i_\mathrm{d}(k-0.5) - V_\mathrm{th}}{L_\mathrm{d}} T_\mathrm{sw} \tag{3.56a}$$

$$i_\mathrm{d,Fe}(k-1) = \frac{V_\mathrm{sc} - R_\mathrm{s} i_\mathrm{d}(k-1) - V_\mathrm{th}}{R_\mathrm{Fe}} \tag{3.56b}$$

While, at the sampling time $(k+1)$:

$$i_\mathrm{d,L}(k+1) = i_\mathrm{d,L}(k) + \frac{-V_\mathrm{sc} - R_\mathrm{s} i_\mathrm{d}(k+0.5) - V_\mathrm{th}}{L_\mathrm{d}} T_\mathrm{sw} \tag{3.57a}$$

$$i_\mathrm{d,Fe}(k+1) = \frac{-V_\mathrm{sc} - R_\mathrm{s} i_\mathrm{d}(k+1) - V_\mathrm{th}}{R_\mathrm{Fe}} \tag{3.57b}$$

After a straightforward manipulation of (3.53)-(3.57), the value of R_{Fe} can be estimated as:

$$R_{\mathrm{Fe}} = \frac{2V_{\mathrm{sc}} - R_{\mathrm{s}}\left(i_{\mathrm{d}}(k-1) - i_{\mathrm{d}}(k+1)\right) - 2V_{\mathrm{th}}}{i_{\mathrm{d}}(k-1) - i_{\mathrm{d}}(k+1) - \frac{T_{\mathrm{sw}}}{L_{\mathrm{d}}}\left[R_{\mathrm{s}}\left(i_{\mathrm{d}}(k-0.5) + i_{\mathrm{d}}(k+0.5)\right) + 2V_{\mathrm{th}}\right]} \tag{3.58}$$

In turn, the iron loss circuital term R_{Fe} can be determined by manipulation of the current samples during the motor commissioning. This technique resulted accurate in simulations, as for example in Figure 3.31(b), where a constant R_{Fe} was used to represent the iron loss effect. Anyway, it must be considered that such model is a simplified representation made for steady state conditions, whereas the iron losses provoked by step voltage transients might behave differently. Still, the computed R_{Fe} can be adopted to have at least a general estimation of the relevancy of iron losses for a specific motor, or to compare different motors from the point of view of iron behavior. Unfortunately, at the moment of this manuscript it was not possible to experimentally validate the R_{Fe} estimation based on (3.58) due to hardware limitation. Such validation is still under investigation.

3.5 Commissioning of PM-SyR Motors

In this Section, the magnetic model self-identification is extended to PM-SyR motors. Possible extension to IPM and SPM machines is under investigation at the moment of this work and it will not be presented here.

The proposed flux maps identification of PM-SyR machines is similar to the case of SyR motors. Nevertheless, the presence of PM introduces several issues that must be taken into account. A valid sensorless test sequence is defined, able to accurately evaluate the complete magnetic model of PM-SyR machines at free-shaft and without rotating the motor.

The proposed self-commissioning techniques described in this Section have been experimentally validated on a reference PM-SyR machine. The main parameters of this motor, called PM10kW, are report in Table 3.6, while the reference flux maps measured at constant speed [40] are plotted in Figure 3.32. This motor was custom designed for light traction applications, and in particular for an electric scooter.

This Section is organized as follow. Section 3.5.1 describes the magnetic model adopted for the test. Section 3.5.2 details the implementation hurdles arising due to the presence of PM respect to the commissioning of SyRMs. In Section 3.5.3 a convenient expression for estimating the flux contribution

Table 3.6: Ratings of the PM-SyR motor under test (PM10kW).

Nominal current [A]	28
Nominal dc-link voltage [V]	360
Pole pairs	2
Nominal torque [Nm]	27
Nominal speed [rpm]	2500
Maximum speed [rpm]	10000
Nominal peak power [kW]	10
Phase resistance [Ω]	0.9
Switching frequency [kHz]	10

due to the PM is retrieved. This expression requires to evaluate the key current value i_{qT0} (later defined), so two alternative techniques to determine this value are detailed in Sections 3.5.4 and 3.5.5.

3.5.1 Extraction of the PM Flux Component

The same convention of SyR motors is adopted for PM-SyR machines, therefore the magnet flux contribution is pointing in negative q axis direction and the d axis stands for the orientation of minimum reluctance, according to

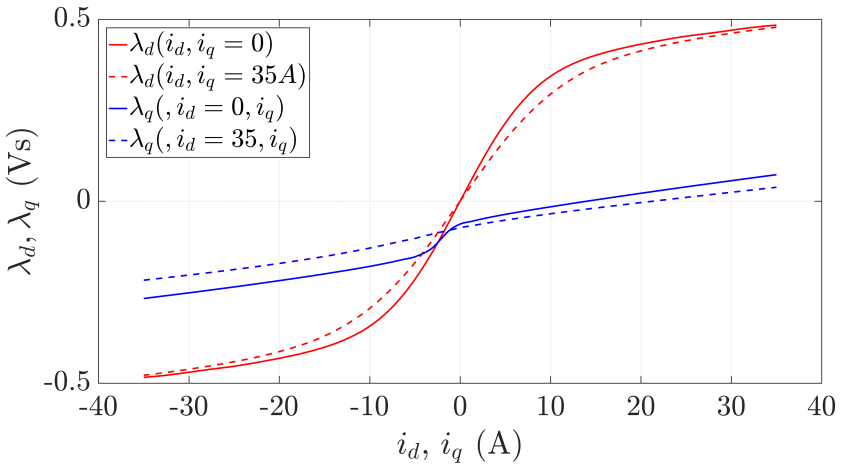

Figure 3.32: Reference flux maps of the PM-SyR motor under test.

Figure 2.2.

Therefore, the PM flux linkage contribution λ_{pm} is included in the λ_{q} flux. In this work it is convenient to separate the current dependent flux component in q axis λ_{q0} from λ_{pm}, treating this last term as a negative offset:

$$\lambda_{\mathrm{q}}(i_{\mathrm{d}}, i_{\mathrm{q}}) = \lambda_{\mathrm{q0}}(i_{\mathrm{d}}, i_{\mathrm{q}}) - \lambda_{\mathrm{pm}} \tag{3.59}$$

Figure 3.34(b) highlights the separation of the two flux contributions. In the proposed magnetic model self-identification, the term λ_{q0} will be identified through square wave voltage injection test (similar to the test #2 used for SyR motors), whereas determining λ_{pm} requires a dedicated set of tests.

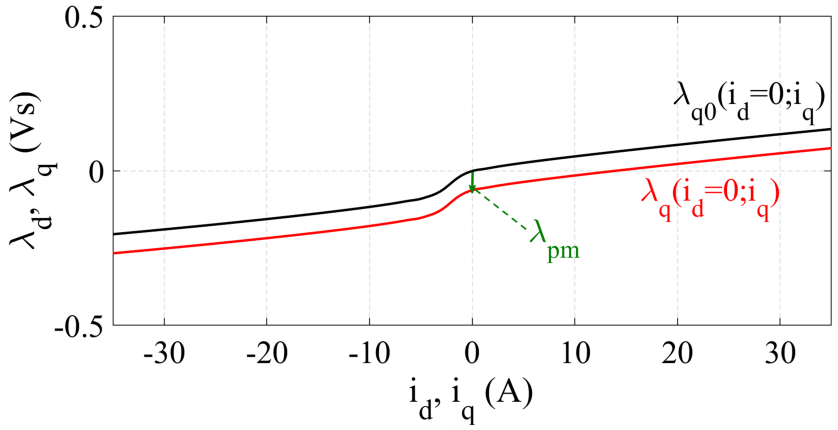

Figure 3.33: Separation of permanent magnet flux contribution λ_{pm} and current dependent component λ_{q0}.

3.5.2 Applicability of the Bipolar Voltage Pulse Method

The magnetic model identification through square wave voltage injection can be extended to PM-SyR machines, following the three steps procedure described for the SyRMs and the block schemes shown in Figure 3.1. The presence of permanent magnets adds several implementation issues that have to be taken into account.

3.5.2.1 Test #1: d Axis

Generally, the same procedure adopted for SyR machines can be applied, and the $\lambda_{\mathrm{d}}(i_{\mathrm{d}}, 0)$ characteristic can still be obtained using (3.1). Anyway, the d axis is not as stable as it is in case of SyR, since even exciting the

d axis only torque is produced, so the motor may start to rotate losing the initial position. In this case, the test would fail. Nevertheless, in case of PM-SyR machines the flux contribution given by the permanent magnets λ_{pm} is relatively low. Therefore, similarly to the test #3, also test #1 usually results in only small oscillations around the initial position if the current (and so the torque) is reversed at sufficiently high frequency.

3.5.2.2 Test #2: q Axis

Also test #2 can be executed according to Figure 3.1(b), but it becomes more unstable, since the q axis is not symmetrical anymore because of the λ_{pm} contribution. In this case, when the current is negative (and so in the direction of the magnets) it partially tends to stabilize the rotor, but when it is positive the risk of rotor movement is high, since i_{q} pushes against the PM and the equilibrium is unstable. Therefore, it may be possible that only a relatively low $I_{\mathrm{q,max}}$ can be explored. Still, the test resulted experimentally feasible for the motor under test at least up to 75 % of the rated current at free shaft. Considering that the $\lambda_{\mathrm{q}}(i_{\mathrm{q}})$ curve is almost linear for higher current, the obtained magnetic model can be easily extended and it resulted accurate enough for sensorless control. In any case, only the current dependent component λ_{q0} can be determined, so (3.2) is modified as:

$$\hat{\lambda}_{\mathrm{q0}}(i_{\mathrm{d}}=0,i_{\mathrm{q}}) = \int v_{\mathrm{q}}^{*} - \hat{R}_{\mathrm{s}} i_{\mathrm{q}} - \hat{V}_{\mathrm{th}} sign(i_{\mathrm{q}}) dt \tag{3.60}$$

3.5.2.3 Test #3: dq Cross-saturation

In test #3 the presence of the magnets does not relevantly complicate the procedure. Therefore, the same test described for SyR machines can be applied. Furthermore, in PM-SyR motors the cross-saturation effect is usually less important in percentage respect to SyR machines. For these reasons, test #3 will not be considered anymore in this Section.

3.5.2.4 Conclusions

From the above considerations it is clear that the test sequence becomes more sensitive to the choice of the amplitude of V_{sc} and the current limits. Therefore, the tuning considerations detailed in Section 3.3.4 are still valid and the sequence described in Figure 3.20 can still be followed, but the constrains on the test stability become more strict and may result in a reduced current measurement domain. Also in this case, the measurement area may be extended through online position tracking.

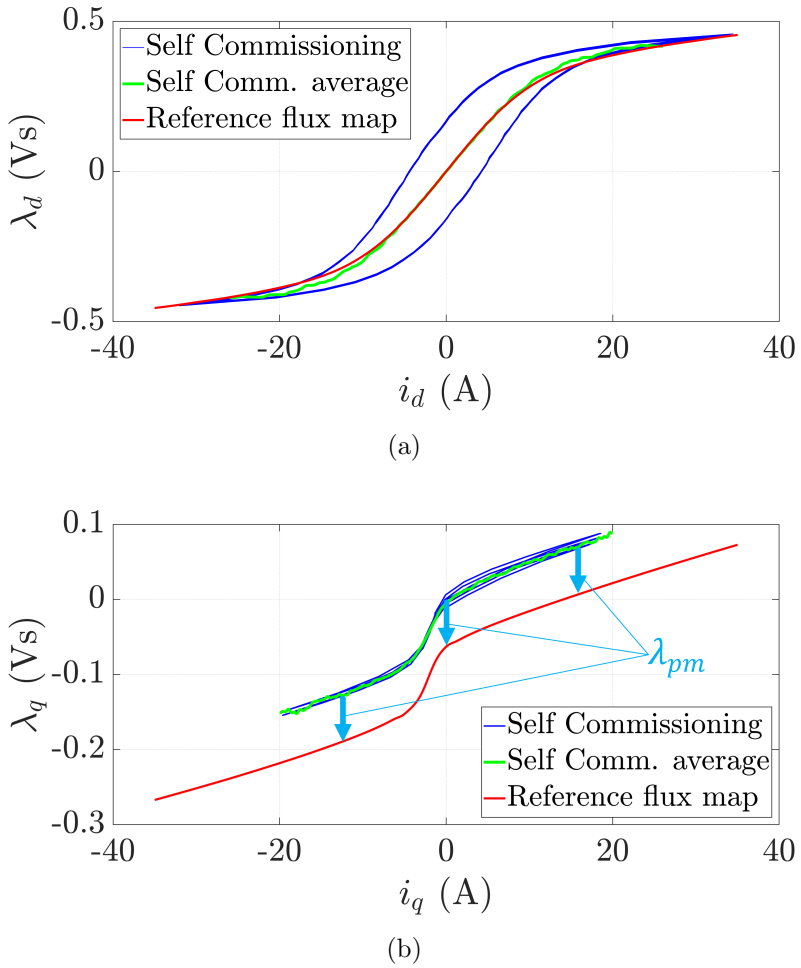

Figure 3.34: Results of the square wave voltage injection identification on the reference motor. (a) d axis, (b) q axis.

The flux identification was experimentally tested on the reference PM-SyR machine PM10kW. The results are shown in Figure 3.34. As can be seen, the average of the $\lambda_{\mathrm{d}}(i_{\mathrm{d}})$ characteristic in Figure 3.34(a) is very close to the reference flux map. Also, from Figure 3.34(b) it is evident that the computed characteristic $\lambda_{\mathrm{q0}}(i_{\mathrm{q}})$ is at approximately constant distance from the reference $\lambda_{\mathrm{q}}(i_{\mathrm{q}})$, in accordance with the adopted model. In both cases, the average curve was computed as described in Section 3.4.2.

Beside the slightly lower stability, the real challenge is to identify the λ_{pm} term at standstill, complying with the constrains of the self-commissioning, since it cannot be obtained from test #2. Indeed, λ_{pm} can be seen as an offset of the $\lambda_{\mathrm{q}}(i_{\mathrm{q}})$ curve, so it cannot be evaluated using open loop integrators as

in (3.60). A dedicated additional test is necessary, described in the next Sections.

3.5.3 PM Flux Identification at Standstill

The flux component λ_{pm} is traditionally evaluated from the back-EMF, while the motor is rotating at constant speed. Anyway, the self-commissioning requires the identification to be at standstill, so the back-EMF are null and cannot be exploited.

A feasible solution is to exploit the zero torque locus, defined as the trajectory in the dq plane where the torque is null[2]. Along this trajectory, highlighted in Figure 3.36, the torque contribution given by machine anisotropy is counteracted by the torque component due to the PM. It must be highlighted that this locus can be reached only for machines with sufficiently high anisotropy, such as PM-SyR machines and maybe IPM motors, but not for SPM machines, where the saliency is only given by local core saturation.

For every point of the locus, considering (2.10) we have:

$$\lambda_d i_q - \lambda_q i_d = 0 \tag{3.61}$$

therefore:

$$(\lambda_{q0} - \lambda_{pm})\, i_d = \lambda_d i_q \tag{3.62}$$

This equation presents two possible solutions. The first one, not useful for determining λ_{pm}, is $i_d = 0$ and so $\lambda_d = 0$, which means the current vector is aligned with the PM (q axis). The second solution, extracted for $i_d \neq 0$, is the zero torque locus, where PM and saliency effects are even:

$$\lambda_{pm} = \lambda_{q0} - \frac{\lambda_d i_q}{i_d} \tag{3.63}$$

This expression can be applied to any point of the zero torque locus to obtain an estimation of the λ_{pm}. However, the cross-saturation effect would require the knowledge of $\lambda_d(i_d, i_q)$ and $\lambda_{q0}(i_d, i_q)$ characteristics. A convenient alternative is to apply (3.63) to the singular point $(i_d = 0, i_q = i_{qT0})$, defined as the intercept between the zero torque locus and the q axis:

$$\lambda_{pm} = \lim_{i_d \to 0} \left(\lambda_{q0}(i_q) - \frac{\lambda_d i_q}{i_d} \right) = \lambda_{q0}(i_{qT0}) - L_d i_{qT0} \tag{3.64}$$

[2]For sake of precision, the torque is null also along the q axis. Anyway, in this thesis the zero torque locus refers to the trajectory where $T = 0$ out of the q axis, which lies in the third and fourth quadrant of the dq plane.

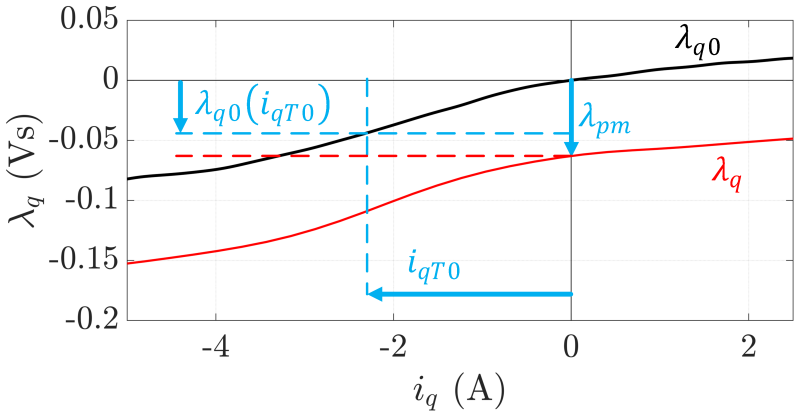

Figure 3.35: Zoom of q axis flux characteristic for visual representation of equation (3.64).

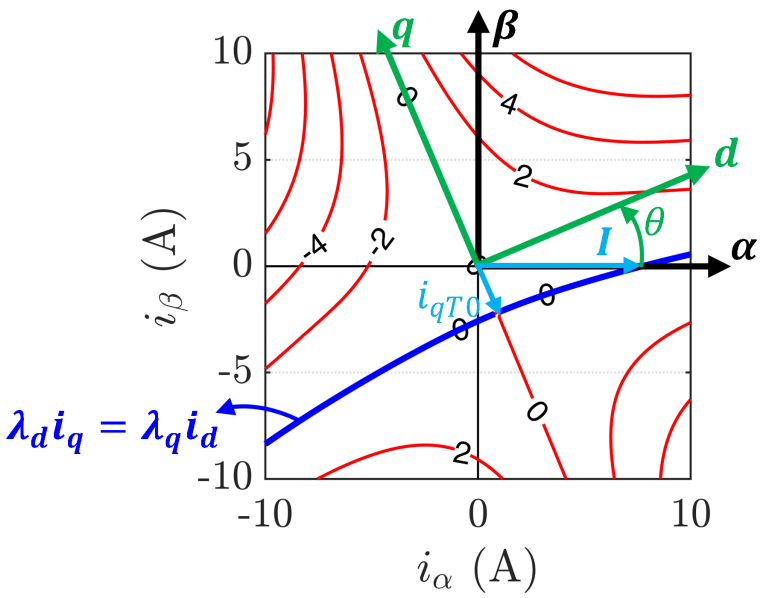

Figure 3.36: Rotor alignment on the zero torque contour with DC current excitation along α axis. Red: torque contour; blue: zero torque locus.

Figures 3.35 and 3.36 describe the application of (3.64). Considering that $i_\mathrm{d} \to 0$, in (3.64) L_d can be conveniently evaluated from test #1 in the linear region of d axis, while $\lambda_{\mathrm{q0}}(i_\mathrm{q})$ is given by test #2. So, at this point of the procedure the only missing parameter to evaluate λ_pm is the key current i_{qT0}.

Two methods are proposed to determine i_{qT0}: the first, performed at quasi standstill, is described in Section 3.5.4, while the second, described in

Section 3.5.5, is at standstill and relies on machine local saliency.

3.5.4 Determination of i_{qT0}: Method 1

This test, performed at free-shaft, aims at evaluating the value of i_{qT0} exploiting a series of rotor alignment. It is considered to be at quasi-standstill conditions because the motor is not rotating at relevant speed, but still limited shaft movement is required to align the rotor along a given position.

In particular, a PI based current loop in stationary $\alpha\beta$ reference frame is adopted to apply a DC current with given amplitude along the stator α axis, with $i^*_\beta = 0$ (rotor parking). Being in stator coordinates, the control does not require the knowledge of rotor position. Thanks to the free-shaft condition, the rotor slightly rotates until it reaches a stable position, so that the imposed current vector falls on the zero torque locus. In this condition, the rotor position corresponds to the current angle γ, as in Figure 3.36.

$$\theta = -\gamma \tag{3.65}$$

Therefore, by sensorless evaluating the rotor position it is possible to retrieve γ. From this angle and the amplitude of the imposed current, the dq coordinates of a point on the zero torque locus are obtained.

The test is repeated several times on varying the DC current amplitude, thus acquiring more points on the zero torque locus. Once enough data have been measured, the amplitude of i_{qT0} can be evaluated by approximating the zero torque locus with a fitting function and extrapolating the trajectory to intercept the vertical axis, and thus finding the required estimation of i_{qT0}. As an example, a bi-quadratic parabola having the maximum on the q axis can be adopted:

$$i_{\mathrm{q}}\left(T=0\right) = -a i_{\mathrm{d}}^4 + i_{\mathrm{qT0}} \tag{3.66}$$

The advantage of this fitting function is that the two parameters a and i_{qT0} can be easily retrieved using LLS algorithms. This solution is adopted here. At this point, the only open issue is how to sensorless determine the rotor position during the test, in order to retrieve the points on the zero Nm contour. Two methods are proposed and detailed in the following.

3.5.4.1 Method 1a: Online Position Tracking

Since the test is at stand-still, model based sensorless techniques cannot be adopted, so the position estimation must rely on saliency tracking. One feasible alternative is to augment the test with HF signal injection for online

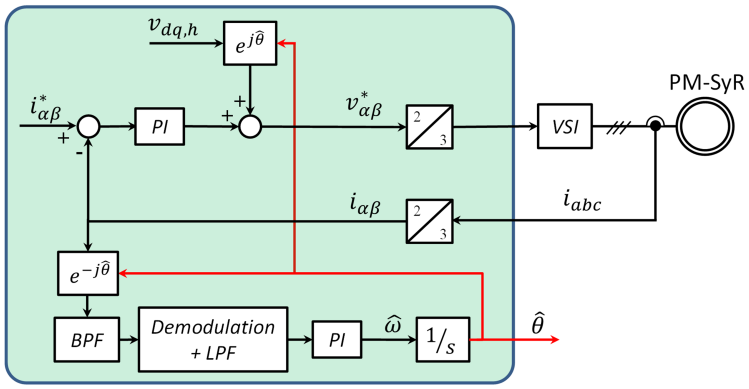

Figure 3.37: Control block scheme for aligning the rotor with a sequence of DC current vectors.

estimating the rotor position during the test. The evaluation of $\hat{\theta}$ is required only for determining i_{qT0} and so λ_{pm}, and not for control purposes. The same sensorless technique adopted in Section 3.3.2 for extending the measurement range in q axis can be used. Therefore, a HF square wave voltage is injected in $\hat{d}$ axis, while the current in $\hat{q}$ axis is demodulated. Thanks to the online position tracking, the reference i^*_α can be gradually increased, obtaining as many points as desired on the 0 Nm contour in the fourth quadrant. The resulting control scheme is shown in Figure 3.37.

The presence of PM does not affects the HF machine model and dynamic, therefore, equations (3.5)-(3.8) are still valid. Also, the same considerations for PLL tuning hold, since the motor is basically excited at stand-still, and so it requires only a very low bandwidth of the position tracking loop.

One important shortcoming occurring during this test is the position error due to cross-saturation, arising especially for high excitation currents:

$$\Delta\theta_{\mathrm{dq}}\left(i_{\mathrm{d}}, i_{\mathrm{q}}\right) = \frac{1}{2} \cdot \arctan\left(\frac{2l_{\mathrm{dq}}}{l_{\mathrm{d}} - l_{\mathrm{q}}}\right) \tag{3.67}$$

The derivation of his expression will be given in Section 4.2. The error $\Delta\theta_{\mathrm{dq}}$ depends on the working point in the current plane because of inductance variability due to magnetic saturation. All the techniques present in the literature to get rid of $\Delta\theta_{\mathrm{dq}}$ are not applicable without flux maps.

Figure 3.38(a) compares the measurement points obtained using the encoder (blue dots) and the sensorless position tracking (black dots). As can be seen, the position estimation is precise at low values of exciting current, so the sensorless points are close to the ones measured with the encoder, but the discrepancy increases at higher current, with a position error compatible with the value predicted through (3.67) and report in Figure 3.38(b).

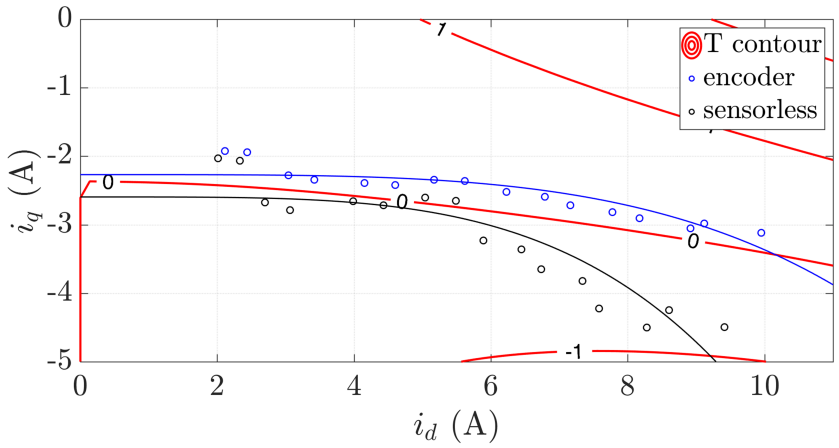

(a)

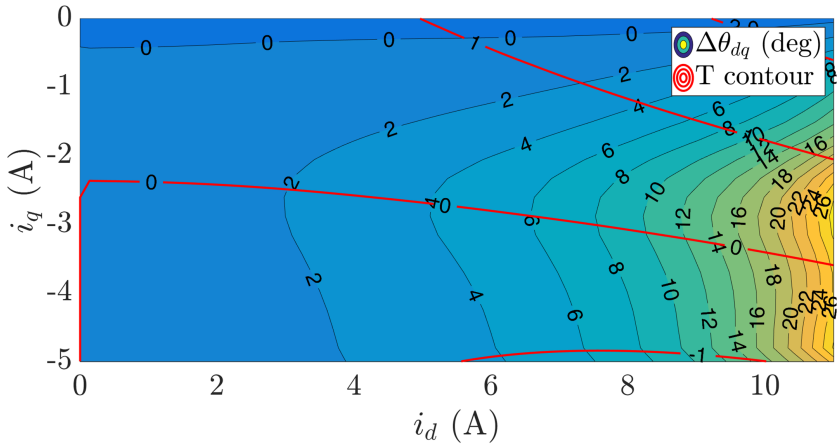

(b)

Figure 3.38: (a) Blue dots: measured points on the torque locus using the encoder. Black dots: measured points using sensorless position tracking loop with continuous current excitation. The correspondent solid lines are obtained through (3.66). (b) Expected position estimation error due to cross-saturation effect calculated with (3.67).

This phenomenon can be explained considering that during the test the current vector is forced to be on the zero torque locus, which lies in an area characterized by relevant $\Delta\theta_{\mathrm{dq}}$. Therefore, the estimation of i_{qT0} and so λ_{pm} may be compromised. Anyway it must be considered that the purpose of this test is only to evaluate i_{qT0}, while the rest of the 0 Nm characteristic is not interesting for control purposes. So, the most important points for a precise

estimation of i_{qT0} are the ones closer to the q axis, with low excitation current and low $\Delta\theta_{\mathrm{dq}}$. In other words, the weight of the black dots of Figure 3.38(a) measured at high i_α^* in the fitting function can be reduced, since the goal is to well approximate the zero torque locus at the intercept with the q axis. In this way, a precise estimation of i_{qT0} and λ_{pm} can be achieved.

3.5.4.2 Method 1b: On-Off Current Excitation

Alternatively, to avoid the effects of cross-saturation an on-off excitation of the fundamental current component can be adopted, according to the test sequence report in Figure 3.39.

Instead of continuously increase the current amplitude, the reference i_α^* is alternatively switched on and off. The excitation is switched on, aligning on the zero torque locus. Then, $i_\alpha^* = 0$ is rapidly forced. At this point, the rotor position is evaluated through one of the initial position sensorless methods described in the literature [98–101]. It is assumed that the rotor does not move when the excitation current is removed, so the position estimated at zero current corresponds to the required angle of the current vector on the zero Nm torque contour. Therefore, a point is obtained on the zero torque locus relying on this angle and the amplitude of i_α^*. Then, the procedure is repeated increasing the excitation current amplitude.

A relevant advantage of the on-off excitation method is that the rotor position is estimated at zero current, which is a safe and stable operating point immune from cross-saturation effects. Anyway, the main concern is the necessity of guaranteeing that the rotor does not move when the excitation is removed. During this operation a transient torque is produced, which may overcome the mechanical friction. Thus, the position estimated at zero

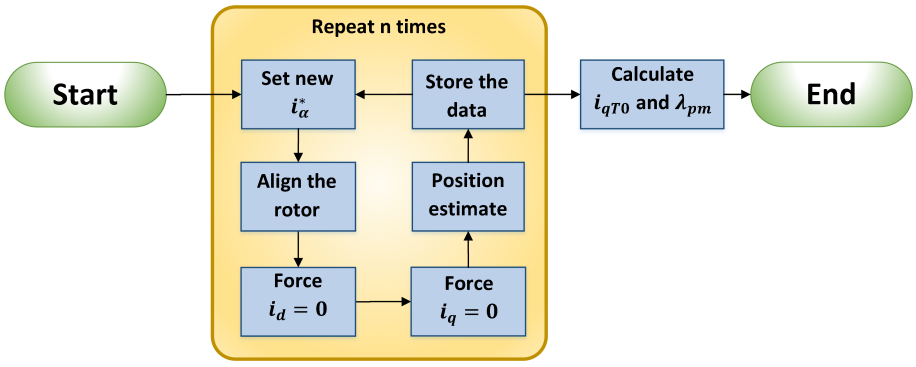

Figure 3.39: Test sequence for determining i_{qT0} with On-Off current excitation. A new value on the zero torque locus is acquired at every loop iteration.

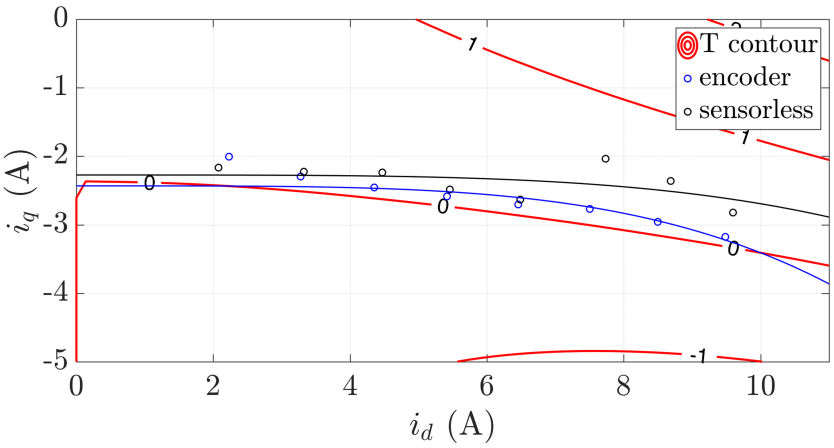

Figure 3.40: Blue dots: measured points on the torque locus using the encoder. Black dots: sensorless estimated points after de-excitation. The correspondent solid lines are obtained through (3.66).

current would not correspond anymore to the required load angle.

To limit the risk of rotor movement it is suggested to excite the machine with current controllers in $\alpha\beta$ coordinates, but switch to dq current control for de-excitation. In this way it is possible to decouple the d and q axes and to first force $i_{\mathrm{d}}^{*} = 0$ and then $i_{\mathrm{q}}^{*} = 0$. Therefore, the current vector is permanently close to the zero Nm torque contour and the transient torque is considerably reduced, avoiding shaft movements. Figure 3.39 better clarifies the steps of the procedure. It must be pointed out that the rotor position used for defining dq reference frame during de-excitation is the position estimated at zero current at the previous iteration.

In Figure 3.40, the current excitation amplitude was increased with steps of 1 A. For every tested current, the position at which the rotor was aligned was measured with the encoder, obtaining the blue dots. Then, the current was removed according to Figure 3.39 and the position was sensorless evaluated, obtaining the black points. As can be seen, the sensorless estimated position is accurate for currents lower than 7 A, while the last three dots present a relevant discrepancy between the data acquired with and without the encoder. The main reason is that for such high current the rotor slightly moved when the current was forced to zero. Also in this case, the solid line represents the fitting parabola obtained with (3.66).

Table 3.7: Estimated magnet flux linkage for the motor under test.

	i_{qT0} **(A)**	λ_{pm} **(mVs)**	**Relative error**
Reference	-2.35	62.0	-
Encoder	-2.43	60.3	2.82 %
Online position tracking	-2.59	64.4	-3.85 %
On-Off current excitation	-2.27	56.3	9.13 %
Online tracking + On-Off	-2.57	63.8	-2.92 %

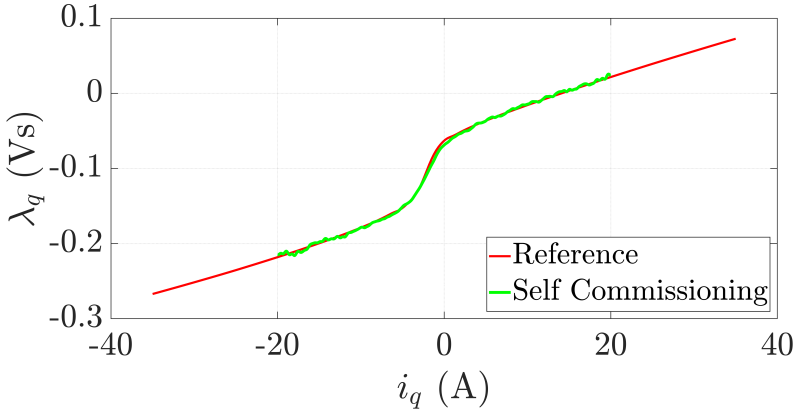

Figure 3.41: Comparison between q axis flux characteristic obtained in self commissioning and reference flux maps.

3.5.4.3 Summary

Different estimations of i_{qT0} were obtained using the points acquired with encoder, with the continuous excitation augmented with HF injection and with the on-off procedure. Moreover, a further estimation of i_{qT0} was obtained considering all the data sensorless acquired, aggregating the points from the continuous excitation and the ones measured with the on-off technique. For each of them, (3.64) was adopted to evaluate λ_{pm}. All the results are summarized in Table 3.7.

As can be seen, a good accuracy is reached using online position tracking, while the error is larger in case of on-off excitation. Anyway, both estimations result accurate enough for control purposes. An even more precise estimation is reached by combining the results of the two tests. This is explained

considering that the position error in the continuous excitation test, due to cross-saturation effect, tends to over-estimate the amplitude of i_{qT0}, while the eventual rotor movements in the on-off test leads to under-estimation. In the end, a relative error compatible with the "encoder" case is reached.

Figure 3.41 shows the total flux characteristic $\lambda_{\mathrm{q}}(i_{\mathrm{q}})$ obtained in self commissioning, and compared with the reference flux maps. As can be seen, the two curves are well in accordance with negligible discrepancy.

3.5.5 Determination of i_{qT0}: Method 2

This section presents an alternative to Method 1. This method 2 is completely at standstill, whatever the mechanical load.

Some preliminary considerations have to be done on the shape of the $\lambda_{\mathrm{q}}(i_{\mathrm{q}})$ curve. As can be seen in Figure 3.41, the curve is almost linear for every current value except a restricted area at negative i_{q}. This is because for null or positive current the structural ribs are saturated and the inductance l_{q} is mostly due to the leakage flux, so it is low dependent on the current amplitude. At negative current, the flux component in q axis due to i_{q} has the same direction of λ_{pm}, but their effects on local ribs saturation is opposite. Therefore, for a sufficiently high negative current, the two contributions are even and the local saturation is partially lost. In this condition the differential inductance l_{q} is almost equal to l_{d}, so the saliency drastically drops. If the negative i_{q} is further increased, the flux contribution due to the current overcomes λ_{pm}, thus saturating the ribs in the opposite direction. Beyond this point, the curve $\lambda_{\mathrm{q}}(i_{\mathrm{q}})$ becomes again linear with a slope similar to the l_{q} measured for positive current.

The basic assumption under this method is that the current i_{qT0}, which is the intercept between the zero torque locus and the q axis, coincides with the maximum l_{q} condition for $i_{\mathrm{d}} = 0$, which from here on will be called i'_{qT0}. In other words, the curve $\lambda_{\mathrm{q}}(i_{\mathrm{d}} = 0, i_{\mathrm{q}})$ presents its maximum slope approximately at $\lambda_{\mathrm{q}}(i_{\mathrm{qT0}})$. It must be noted that this condition also corresponds to the minimum local saliency along the q axis.

To demonstrate this assumption is rather critical analytically, since in that area the machine behavior is strongly non-linear and any assumption to simplify the analysis would fail. Anyway, the correspondence between i_{qT0} and i'_{qT0} was experimentally verified for several PM-SyR motors. All of them presented negligible discrepancy between the two current values.

If $i_{\mathrm{qT0}} \approx i'_{\mathrm{qT0}}$ is assumed, a new expression for evaluating λ_{pm} is obtained:

$$\lambda_{\mathrm{pm}} \approx \lambda_{\mathrm{q0}}\left(i'_{\mathrm{qT0}}\right) - L_{\mathrm{d}} i'_{\mathrm{qT0}} \tag{3.68}$$

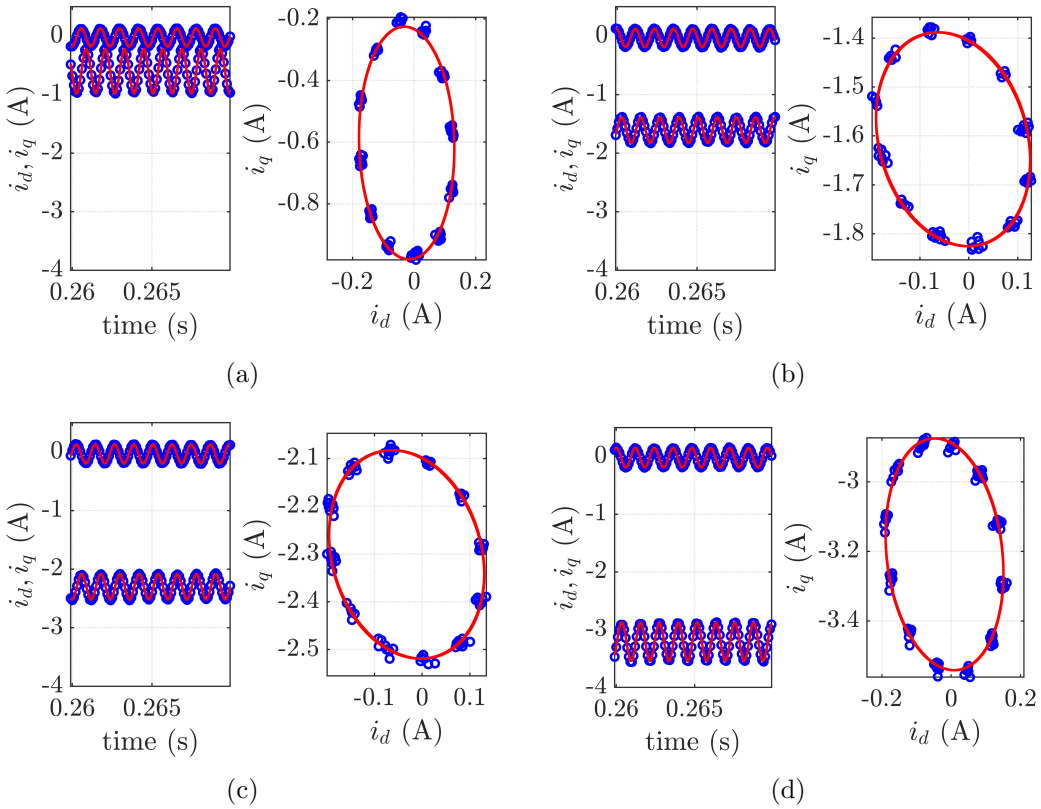

Figure 3.42: Saliency analysis along the q axis with a HF rotating voltage superimposed to a DC excitation of (a) $i_\mathrm{q} = 0.6$ A, (b) $i_\mathrm{q} = 1.6$ A (c) $i_\mathrm{q} = 2.3$ A (d) $i_\mathrm{q} = 3.2$ A. Blue: measurement points. Red: fitting function. Left: time waveforms. Right: dq plane.

The proposed i'_{qT0} identification test is described hereafter. The rotor position is sensorless evaluated once before starting the test and used for definition of dq reference frame during the identification stage. Then, the motor is controlled according to the scheme of Figure 4.11, which will also be adopted later for saliency analysis in Section 4.2.7. A DC current is forced in negative q axis through PI based current control loop ($i^*_\mathrm{d} = 0$), while a HF rotating voltage component is superimposed to the fundamental excitation.

The HF current response describes an elliptic trajectory, as will be demonstrated in Section 4.2.7. Figure 3.42 shows the time waveforms and trajectories in the dq plane of the measured currents in some key points of the q axis. The reference DC current is slowly moved along negative q axis, evaluating the local saliency and thus finding i'_{qT0}. Finally, λ_{pm} is evaluated from (3.68).

It must be noted that this test cannot provoke rotor movement, even

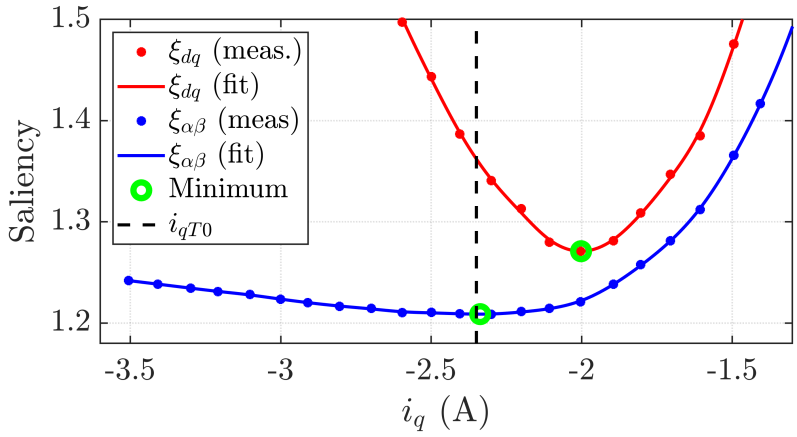

Figure 3.43: Evaluated saliency along the q axis. Red: ratio between $|i_{\mathrm{dh}}|$ and $|i_{\mathrm{qh}}|$. Blue: ratio between the amplitude of major and minor ellipses axes. Green: minimum of the two curves. Black: reference i_{qT0}.

at free shaft. Indeed, the motor is excited along the negative q axis, in the direction of the PM, therefore the test is self-aligning. Torque may be produced in case of inaccurate initial position estimation, but in this case it would align the rotor with $\hat{\theta}$, thus eliminating the position error.

To evaluate the saliency, the measured i_{d} and i_{q} are interpolated with a sinusoidal function having a frequency of the injected voltage. Equivalently, the Fourier transformation can be used to extract the desired current harmonic i_{dh} and i_{qh}. Thus, as a first attempt the saliency was obtained as the ratio between the amplitude of the two fitting sine curves, obtaining the red curve in Figure 3.43.

As can be seen in Figure 3.42, an unexpected phenomenon is observed. Moving along the negative q axis, the current ellipse is slightly rotated. This phenomenon is under investigation at the moment of this work. In any case, the saliency estimation calculated as $|i_{\mathrm{dh}}|/|i_{\mathrm{qh}}|$ demonstrated to be unreliable for determining i'_{qT0}. Conversely, i'_{qT0} can be conveniently obtained as the ratio between the major and the minor axes of the ellipse, thus taking into account the rotation effect. The saliency evaluated with this technique is represented in blue in Figure 3.43. In this way, the saliency is not anymore directly linked to the dq axes, so if desired the two sine waves can be evaluated also in $\alpha\beta$ coordinates. This is why the local anisotropy evaluated taking into account the ellipse rotation is called $\xi_{\alpha\beta}$ in the figure.

As can be seen from Figure 3.43, the estimated i'_{qT0} (-2.337 A) is very close to the value of i_{qT0} obtained from the reference flux maps (-2.35 A), thus producing an error in the estimation of λ_{pm} of -0.42 %.

In the test of Figure 3.42 and 3.43, the amplitude of the HF injected voltage was 20 V. For sake of evaluating the dependency of the λ_{pm} estimation respect to the HF voltage, the test was repeated injecting 5 to 25 V with steps of 5 V. In every set of tests, summarized in Table 3.8, the estimation of λ_{pm} resulted very accurate, with absolute relative error lower than 2 %.

Table 3.8: Sensitivity of λ_{pm} evaluation respect to the amplitude of injected voltage.

Injected voltage (V)	**estimated i'_{qT0} (A)**	**λ_{pm} error (%)**
5	-2.395	1.33
10	-2.335	-0.50
15	-2.389	1.24
20	-2.337	-0.42
25	-2.119	1.82

Chapter 4

Sensorless Control of SyR Machines

Part of the work described in this Chapter has been previously published in [9–11, 13].

Sensorless control (also called encoderless or self-sensing control), i.e. controlling the motor without using position transducers, is often required is many applications, including industry, traction and home appliances. In some cases, such as electrical fans, pumps, washing machines and other low cost applications, the absence of encoder is beneficial since it permits to limit the costs of the hardware. In other applications, like electrical propulsion systems, the cost of a position transducer is not relevant in percentage, but the required reliability level is very high, so a sensorless control strategy is often advisable at least as an emergency option in case of encoder failure.

The sensorless control for IM has been deeply analyzed in the literature [109, 110] but in the last decade, the interest in synchronous motors considerably grew, requiring proper encoderless techniques.

Traditionally, sensorless control techniques identify at least two regions of operation. At medium and high speed, the position information can be conveniently retrieved from a model based manipulation of the back-EMF. Since the motor is inverter supplied, the stator voltage is modulated so it is often not feasible to measure it. Therefore the back-EMF are calculated from the inverter commands and measured v_{dc}. At low speed, such back-EMF become too small to be reliable for position estimation, since the errors due to inaccurate compensation of inverter non-linear effects and imprecise knowledge of stator resistance become more relevant in percentage. The back-EMF totally vanishes at standstill. A common alternative for zero and low speed control is to adopt saliency based position tracking methods, consisting of

injecting a proper HF signal and retrieving the position information from the HF motor response. Several solutions were presented combining the two operating speed ranges in a unified control structure.

Since standstill position estimation techniques rely on rotor anisotropy, highly salient machines like SyR and PM-SyR are inherently suitable. Low speed sensorless control is still feasible for SPM motors exploiting the small anisotropy due to local saturation of the stator core induced by the PMs.

This chapter provides a detailed analysis of the literature (Section 4.1), followed by personal contribution in the field of saliency based (Section 4.2) and model based (Section 4.3) sensorless control, fusion of the two models (Section 4.4), automatic tuning procedure (Section 4.6) and experimental results (Section 4.7).

4.1 State of the Art of Sensorless Control

Sensorless control has been widely studied since the years 90's. In [111] the Authors proposed a state observer for PMSM, which has been the basis for many later papers, able to sensorless evaluate rotor speed and position at sufficiently high speed, supported by simulations and stability analysis. In [112], despite the rotor position is measured through low accuracy encoder, the measurement is enhanced by mechanical observer for torque estimation, improving the speed and position estimation and so increasing the dynamic of the speed loop. Similar structure was adopted for self-sensing control at low speed in [113, 114], where HF voltage was injected, and [115], which proposes HF current injection for machines presenting multiple saliencies.

The scientific literature presents several methods to sensorless evaluate the initial position of the rotor [98–101]. Despite most of these techniques cannot be adopted for online position monitoring during operation, they can be useful for effective start-up strategy of the drive.

4.1.1 Open Loop Start-up

At low speed, several Authors proposed to avoid saliency based algorithms by starting the motor in open loop control. In [34] and [116] the motor (SyR and PMSM respectively) is started with I-Hz control and when the speed is sufficiently high a smooth transition leads to model based sensorless control.

Similar structure was presented in [117] for BLDC machines and in [118] for SPM machines. More recently, [119] extended this technique to include SyRM and PM-SyRM and to exploit MTPA trajectory even at open loop.

Despite the implementation simplicity is a relevant advantage, those techniques can be hardly used if dynamic performances are required at low speed.

4.1.2 Saliency Based Techniques

A deep literature review of low speed sensorless techniques is given in [103], while [120] presents a survey specifically focused on wind turbines applications. In particular, [103] divides the sensorless algorithms depending on the type of HF injected signal, where the excitation can be continuous or discontinuous, periodic or based on PWM modification, rotating [121], pulsating [122] or other shapes. Moreover, the injected signal can be a voltage or a current. A comparison between pulsating and rotating voltage injection and between PI, PID and ESO observers is found in [123]. The same paper proposes a mechanical observer for robust position detection at low speed. Also, the injection can be done in rotor or stator reference frame [124]. In [104] the injection frequency was increased up to the Shannon limit of half the switching frequency, as done for extending the measurement domain in Section 3.3.2, while in [125] the injection frequency was pushed to the physical limit f_{sw}, but detecting a relevant sixth harmonic in the demodulated signal. A low speed sensorless control for SPM machines, exploiting the small anisotropy given by local saturation due to the PM, is given in [101]. This technique, based on rotating voltage injection, also identifies the polarity of the PM.

Arbitrary signal injection was adopted by [126,127], where [126] exploited the difference between predicted and measured current derivative online estimating the machine inductances and [127] presented a stability analysis based on Lyapunov criteria. In [122], suitable low speed control of IPM was retrieved based on flux injection and unconventional demodulation process, involving custom defined coordinates rotated by $\pi/4$ respect to dq frame.

The problem of non-sinusoidal inductance distribution along the rotor position was treated in [128], where a saliency based and a model based methods are merged with linear transition between them. A different approach was adopted in [129], where the stability of the transition between high and low speed range is studied. Also, the work [130] analyzes the stability of model based sensorless control, analytically identifying the minimum speed that can be reached. The analysis is based on the concept of dynamic stiffness, i.e. the ratio between torque disturbance and mechanical speed.

HF voltage injection with current demodulation was adopted for SyR machines in [131–133]. Despite this technique is not immune from position error related to cross-saturation, the demodulation BPF is avoided, thus slightly increasing the position estimation bandwidth. In these papers, the

transition between low and high speed is based on hysteresis control.

4.1.3 Model Based and Combined Techniques

A full speed sensorless control was proposed in [38] for SyR machines, exploiting at low speed HF voltage injection and demodulation of signal coming from the flux observer and a model based approach at high speed. A relatively smooth transition between the two speed ranges is achieved through a weighted average, while the speed was extracted through a system similar to resolver-to-digital converters. The method was then improved in [31] by injecting an HF flux and a better transition between low and high speed ranges. In both [38] and [31], the control variables for motor control are $(\lambda_\mathrm{d}, i_\mathrm{q})$ instead of the canonical $(i_\mathrm{d}, i_\mathrm{q})$ for better torque regulation. A further improvement was achieved in [32] to get rid of the position error introduced by cross-saturation effect.

The work in [134] bases the position estimation on the so called Extended Electromotive Force (EEMF). A proper vector based on measured current and observed speed is subtracted to the reference voltages and manipulated in a flux observer to obtain the EEMF, which is a vector aligned with the q axis. The rotor position is extracted from the phase of EEMF vector. An analytical method is also proposed for observer pole placement. The paper was followed by several others in the literature, e.g. combined with HF injection algorithms at low speed [135, 136]. In [137] the method is enhanced by online estimation of machine inductance by recursive algorithm, while in [138] the stability region of EEMF was defined considering magnetic saturation. In [139] the HF component of EEMF was exploited at low speed.

The Active Flux concept (AF), already analyzed in Section 2.4.3 was presented for the first time in [33] and then manipulated in [9,34,105,140,141]. This method turns a salient synchronous machine into an equivalent isotropic one, retrieving the rotor position from the observed AF vector. In particular, [140] adopted a flux observer similar to the one in [32], but the low and high speed models are merged by filtering the difference between the two position estimations in the transition speed range. A comparison between low speed performances of sensorless AF based algorithm for current vector control and DTC is presented in [141]. In [105], a hybrid active-flux and arbitrary signal injection for SyRMs was proposed, where the transition between the active-flux and signal injection modes was handled via a speed commanded hysteresis switch. Despite this method is not immune to cross-saturation, the related position error is compensated using predicted angle deviation.

An adaptive speed observer was proposed in [36] combining HF current injection and canonical state observer, with an analytical method for tuning

the observer gains. Later, similar state observer was adopted in [37,142–144]. In [37] a full order state observer is proposed, and the HF demodulation signal is modified for taking into account cross-saturation effect. The same paper defines the stability region for optimal gains selection in observer design. Online parameter adaptation is added in [143]. In [144] the state observer was directly designed in discrete time domain, avoiding the approximations related to Euler or Tustin transformations. In this way, the stability is improved for very high speed or low switching frequency.

Model based sensorless control is inherently more problematic when the machine is breaking, especially at low speed. This issue was analyzed in [110] for IMs and then extended to synchronous machines in [35].

4.1.4 Sensorless Combined with DTC, MPC and DFVC

DTC algorithms are often considered inherently sensorless control schemes [145]. The same paper defines the operational limits for reference flux amplitude and angle to maximize torque dynamic, although reducing the motor efficiency. However when the rotor speed is low and so the back-emf are not reliable, a current based flux observer is required, thus implying the knowledge of rotor position. Therefore, sensorless algorithms such as [30,146–150] have been developed for IPM machines and in [151] for PM-SyRM. Also, [152] proposes a DTC algorithm exploiting Kalman filter.

Encoderless controls are often combined with sliding mode observers, e.g. [148,153,154] for IPM machines, PLL schemes [155] or deadbeat control [156].

Dealing with MPC schemes, the work in [19] proposed a sensorless predictive DTC method for a SyR motor, extracting the rotor position through PWM modification. However, the performance of the drive at high speed and the transition between high-speed and low-speed regions is not clearly shown. Despite only steady state results are shown, in [157] a sensorless MPC-FOC for IPM machines is proposed. The position information is extracted from the difference between the flux estimates coming from current and voltage model. Considerably more convincing results were obtained in [21], where the electrical equations in d and q axes are separately used to retrieve the position error and speed respectively. Other examples of MPC are [158] and [20], based on explicit model inversion for flux leakage estimation either in dq or $\alpha\beta$ reference frame. In particular, the latter one presents an explicit solution of the optimization problem written in discrete time domain and based on 3 steps predictive horizon, but it is computationally very heavy.

Only a few papers propose sensorless DFVC. In [109], a sensorless DFVC method was proposed for IMs, but not at low speeds and standstill. In [9,10,159], sensorless DFVC is proposed for SyRM drives.

4.1.5 Sensorless for SyR Machines

The literature presents several papers dealing with sensorless control specifically for SyR machines [37,38,105,121,140,160]. However, all such methods use a constant level of excitation (constant i_d, i.e., almost constant λ_d) instead of taking advantage of the MTPA control law, to limit the machine's parameters variation with the load torque and guaranteeing an appropriate level of back-EMF signal also at zero torque. At the best of the Author knowledge, MTPA trajectory was adopted in sensorless control of SyRM for the first time in [9,10], together with other contributions like robustness in wide speed range, insensitivity to cross-saturation effect, saliency analysis defining the stable operating area at low speed and automatic tuning procedure.

4.2 Saliency Tracking

When the rotor speed is low or null, the back-EMF are too low for a reliable model based position estimation. Therefore, the rotor position has to be observed adopting saliency based techniques, which typically exploit the injection of an HF signal and retrieve the position information from the HF machine response. Being at low speed, the maximum inverter voltage is usually not limiting the available amplitude of the injected voltage, unless the machine inductance and the injection frequency are both very high.

A high rotor anisotropy is clearly welcome for such HF injection position estimation techniques. In this sense, SyR and PM-SyR motors are particularly suitable. A common problem for saliency based position tracking algorithm is that cross-saturation effect may produce relevant position error, if not properly taken into account. This Chapter is organized as follow. Section 4.2.1 gives a general formulation valid for any type of pulsating HF voltage injection technique. Two of them are described in Section 4.2.2 and 4.2.3, later compared in Section 4.2.4. Half switching frequency voltage injection is considered in Section 4.2.5. Then, the demodulation algorithm used for extracting the HF signal is described in Section 4.2.6. Finally, a deep analysis of machine local saliency is given in Section 4.2.7.

4.2.1 General Formulation for Pulsating Voltage Injection

In this section, a general formulation for position tracking based HF pulsating voltage injection is retrieved.

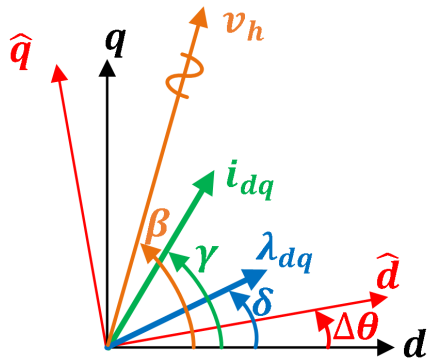

Figure 4.1: Definition of axes coordinates for pulsating voltage injection.

A sinusoidal pulsating voltage is injected in a generic axis with a phase shift β respect to the real rotor d axis, as shown in Figure 4.1.

$$v_{\mathrm{h}}(t) = u_{\mathrm{c}} cos\left(\omega_{\mathrm{c}} t\right) \tag{4.1}$$

$$\boldsymbol{v}_{\mathrm{dqh}} = u_{\mathrm{c}} cos\left(\omega_{\mathrm{c}} t\right) e^{\mathbf{J}\beta} \tag{4.2}$$

Where u_{c} and ω_{c} are the amplitude and angular frequency on the injected signal, respectively. From there on, the time dependency will be omitted for simplicity of notation. By projecting the HF voltage on the dq axes, the following HF quantities are obtained:

$$\begin{cases} v_{\mathrm{dh}} &= u_{\mathrm{c}} \cos\left(\omega_{\mathrm{c}} t\right) \cos\left(\beta\right) \\ v_{\mathrm{qh}} &= u_{\mathrm{c}} \cos\left(\omega_{\mathrm{c}} t\right) \sin\left(\beta\right) \end{cases} \tag{4.3}$$

The correspondent HF fluxes are given by the integral of (4.3):

$$\begin{cases} \lambda_{\mathrm{dh}} &= \frac{u_{\mathrm{c}} \sin(\omega_{\mathrm{c}} t)}{\omega_{\mathrm{c}}} \cos\left(\beta\right) &= k \cos\left(\beta\right) \\ \lambda_{\mathrm{qh}} &= \frac{u_{\mathrm{c}} \sin(\omega_{\mathrm{c}} t)}{\omega_{\mathrm{c}}} \sin\left(\beta\right) &= k \sin\left(\beta\right) \end{cases} \tag{4.4}$$

where $k = \frac{u_{\mathrm{c}} \sin(\omega_{\mathrm{c}} t)}{\omega_{\mathrm{c}}}$. The current in real dq coordinates can be retrieved from the differential inductance matrix, considering the cross-saturation:

$$\boldsymbol{i}_{\mathrm{dqh}} = \boldsymbol{l}_{\mathrm{dq}}^{-1} \boldsymbol{\lambda}_{\mathrm{dqh}} \tag{4.5}$$

$$\begin{bmatrix} i_{\mathrm{dh}} \\ i_{\mathrm{qh}} \end{bmatrix} = \frac{k}{l_{\mathrm{d}} l_{\mathrm{q}} - l_{\mathrm{dq}}^2} \begin{bmatrix} l_{\mathrm{q}} \cos\left(\beta\right) - l_{\mathrm{dq}} \sin\left(\beta\right) \\ -l_{\mathrm{dq}} \cos\left(\beta\right) + l_{\mathrm{d}} \sin\left(\beta\right) \end{bmatrix} \tag{4.6}$$

The HF current in estimated $\hat{d}\hat{q}$ reference frame are obtained rotating (4.6) by the angle $\Delta\theta$:

$$\boldsymbol{i}_{\hat{\mathrm{d}}\hat{\mathrm{q}}\mathrm{h}} = e^{-\mathbf{J}\Delta\theta}\boldsymbol{i}_{\mathrm{dqh}} = e^{-\mathbf{J}\Delta\theta}\boldsymbol{l}_{\mathrm{dq}}^{-1}\boldsymbol{\lambda}_{\mathrm{dqh}} \tag{4.7}$$

$$\begin{bmatrix} i_{\hat{\mathrm{d}}\mathrm{h}} \\ i_{\hat{\mathrm{q}}\mathrm{h}} \end{bmatrix} = \frac{k}{l_{\mathrm{d}}l_{\mathrm{q}} - l_{\mathrm{dq}}^2} \begin{bmatrix} l_{\mathrm{q}}\cos(\beta)\cos(\Delta\theta) - l_{\mathrm{dq}}\sin(\beta)\cos(\Delta\theta) + \\ \quad + l_{\mathrm{d}}\sin(\beta)\sin(\Delta\theta) - l_{\mathrm{dq}}\cos(\beta)\sin(\Delta\theta) \\ -l_{\mathrm{q}}\cos(\beta)\sin(\Delta\theta) + l_{\mathrm{dq}}\sin(\beta)\sin(\Delta\theta) + \\ \quad + l_{\mathrm{d}}\sin(\beta)\cos(\Delta\theta) - l_{\mathrm{dq}}\cos(\beta)\cos(\Delta\theta) \end{bmatrix} \tag{4.8}$$

According to the scheme in Figure 2.10 the flux and position observer is working on the observed rotor coordinates. Therefore, the HF flux estimation coming from the current model $\boldsymbol{\lambda}^{i}_{\hat{\mathrm{d}}\hat{\mathrm{q}}\mathrm{h}}$ is derived from (4.8) multiplied by the differential inductance matrix. Considering accurate parameters estimation, after straightforward manipulation $\boldsymbol{\lambda}^{i}_{\hat{\mathrm{d}}\hat{\mathrm{q}}\mathrm{h}}$ is given by:

$$\boldsymbol{\lambda}^{i}_{\hat{\mathrm{d}}\hat{\mathrm{q}}\mathrm{h}} = \boldsymbol{l}_{\mathrm{dq}}\boldsymbol{i}_{\hat{\mathrm{d}}\hat{\mathrm{q}}\mathrm{h}} = \boldsymbol{l}_{\mathrm{dq}}e^{-\mathbf{J}\Delta\theta}\boldsymbol{l}_{\mathrm{dq}}^{-1}\boldsymbol{\lambda}_{\mathrm{dqh}} \tag{4.9}$$

$$\begin{bmatrix} \lambda^{i}_{\hat{\mathrm{d}}\mathrm{h}} \\ \lambda^{i}_{\hat{\mathrm{q}}\mathrm{h}} \end{bmatrix} = k \begin{bmatrix} \cos(\beta)\cos(\Delta\theta) + \frac{l_{\mathrm{d}}^2 + l_{\mathrm{dq}}^2}{l_{\mathrm{d}}l_{\mathrm{q}} - l_{\mathrm{dq}}^2}\sin(\beta)\sin(\Delta\theta) - \frac{(l_{\mathrm{d}}+l_{\mathrm{q}})l_{\mathrm{dq}}}{l_{\mathrm{d}}l_{\mathrm{q}} - l_{\mathrm{dq}}^2}\cos(\beta)\sin(\Delta\theta) \\ \sin(\beta)\cos(\Delta\theta) - \frac{l_{\mathrm{q}}^2 + l_{\mathrm{dq}}^2}{l_{\mathrm{d}}l_{\mathrm{q}} - l_{\mathrm{dq}}^2}\cos(\beta)\sin(\Delta\theta) + \frac{(l_{\mathrm{d}}+l_{\mathrm{q}})l_{\mathrm{dq}}}{l_{\mathrm{d}}l_{\mathrm{q}} - l_{\mathrm{dq}}^2}\sin(\beta)\sin(\Delta\theta) \end{bmatrix} \tag{4.10}$$

Finally, the flux estimation in estimated $\hat{d}\hat{q}$ reference frame coming from the voltage model, i.e. EMF integration, is given by:

$$\boldsymbol{\lambda}^{v}_{\hat{\mathrm{d}}\hat{\mathrm{q}}\mathrm{h}} = e^{-\mathbf{J}\Delta\theta}\boldsymbol{\lambda}_{\mathrm{dqh}} \tag{4.11}$$

$$\begin{bmatrix} \lambda^{v}_{\hat{\mathrm{d}}\mathrm{h}} \\ \lambda^{v}_{\hat{\mathrm{d}}\mathrm{h}} \end{bmatrix} = k \begin{bmatrix} \cos(\beta)\cos(\Delta\theta) + \sin(\beta)\sin(\Delta\theta) \\ -\cos(\beta)\sin(\Delta\theta) + \sin(\beta)\cos(\Delta\theta) \end{bmatrix} \tag{4.12}$$

These equations can be adopted to analyze any sensorless control based on pulsating voltage injection, as will be shown in the following Sections.

4.2.2 Canonical Current Demodulation

The most common technique found in the literature [160] consists of injecting the HF voltage along the $\hat{d}$ axis and demodulating the HF current component in $\hat{q}$ direction. In this case, $\beta = \Delta\theta$, so equation (4.8) simplifies as:

$$\begin{bmatrix} i_{\hat{\mathrm{dh}}} \\ i_{\hat{\mathrm{qh}}} \end{bmatrix} = \frac{k}{l_{\mathrm{d}} l_{\mathrm{q}} - l_{\mathrm{dq}}^2} \begin{bmatrix} l_{\mathrm{q}} + (l_{\mathrm{d}} - l_{\mathrm{q}}) \sin^2(\Delta\theta) - l_{\mathrm{dq}} \sin(2\Delta\theta) \\ \frac{l_{\mathrm{d}} - l_{\mathrm{q}}}{2} \sin(2\Delta\theta) - l_{\mathrm{dq}} \cos(2\Delta\theta) \end{bmatrix} \tag{4.13}$$

If cross-saturation is neglected ($l_{\mathrm{dq}} \approx 0$), the amplitude of $i_{\hat{\mathrm{qh}}}$, once extracted through demodulation process, is proportional to the position error:

$$|i_{\hat{\mathrm{qh}}}| \approx \frac{u_{\mathrm{c}} (l_{\mathrm{d}} - l_{\mathrm{q}})}{4\omega_{\mathrm{c}} l_{\mathrm{d}} l_{\mathrm{q}}} \sin(2\Delta\theta) \approx k_{\epsilon} \Delta\theta \tag{4.14}$$

$$k_{\epsilon} = \frac{u_{\mathrm{c}} (l_{\mathrm{d}} - l_{\mathrm{q}})}{2\omega_{\mathrm{c}} l_{\mathrm{d}} l_{\mathrm{q}}} \tag{4.15}$$

The second term of (4.14) is obtained considering small position error ($\sin(2\Delta\theta) \approx 2\Delta\theta$). So, forcing to zero the amplitude of $i_{\hat{\mathrm{qh}}}$, e.g. through a PLL-based position tracking loop, is equivalent to forcing the position error to become null, thus the observed position converges to the real θ. Anyway, if cross-saturation is not neglected, the real amplitude of $i_{\hat{\mathrm{qh}}}$ becomes

$$|i_{\hat{\mathrm{qh}}}| = \frac{u_{\mathrm{c}}}{2\omega_{\mathrm{c}} \left(l_{\mathrm{d}} l_{\mathrm{q}} - l_{\mathrm{dq}}^2\right)} \left[\frac{l_{\mathrm{d}} - l_{\mathrm{q}}}{2} \sin(2\Delta\theta) - l_{\mathrm{dq}} \cos(2\Delta\theta)\right] \tag{4.16}$$

If (4.16) is forced to zero through a PLL, the tracking loop converges to:

$$(l_{\mathrm{d}} - l_{\mathrm{q}}) \sin(2\Delta\theta) - 2 l_{\mathrm{dq}} \cos(2\Delta\theta) = 0 \rightarrow \hat{\theta} = \theta + \Delta\theta_{\mathrm{dq}} \tag{4.17}$$

$$\Delta\theta_{\mathrm{dq}} = \frac{1}{2} \arctan\left(\frac{2 l_{\mathrm{dq}}}{l_{\mathrm{d}} - l_{\mathrm{q}}}\right) \tag{4.18}$$

It is worth noticing that in case $l_{\mathrm{dq}} = 0$, i.e. in absence of cross-saturation, $\Delta\theta_{\mathrm{dq}}$ would be zero. Anyway, if $l_{\mathrm{dq}} \neq 0$ the position observer would converge to a deviated position, with a fixed steady state error $\Delta\theta_{\mathrm{dq}}$. This position error is usually negligible for SPM and IPM machines, but it can be critical for SyR and PM-SyR motors, characterized by relevant cross-saturation effect [32]. In this case, $\Delta\theta_{\mathrm{dq}}$ can reach up to 20° if not properly compensated.

For sake of completeness, it should be remembered that some works presented in the literature adopt similar structure, but injecting the HF voltage in $\hat{q}$ direction and tracking the rotor position by demodulating $i_{\hat{\mathrm{dh}}}$. In this case, (4.8) is simplified considering $\beta = \Delta\theta + \pi/2$:

$$i_{\hat{\mathrm{dh}}} = \frac{k}{l_\mathrm{d} l_\mathrm{q} - l_\mathrm{dq}^2} \left[\frac{l_\mathrm{d} - l_\mathrm{q}}{2} \sin\left(2\Delta\theta\right) - l_\mathrm{dq} \cos\left(2\Delta\theta\right) \right] \tag{4.19}$$

As can be noticed, this is dual to (4.13), so by injecting in d or q axed produces equivalent dynamic performances and the tracking loop would converge to the same (wrong) position with a fixed error calculated as in (4.18). Despite injecting in q axis can be convenient for some specific applications, the injection is d direction is usually preferred since it produces a smaller current and torque ripple for equal amplitude of the demodulated signal.

4.2.3 Flux Demodulation

The literature presents several methods to compensate the position error $\Delta\theta_\mathrm{dq}$ [31, 37, 38, 105]. A feasible alternative is to use the HF flux estimate coming from the current model $\boldsymbol{\lambda}^i_{\hat{\mathrm{dqh}}}$ as a feedback error signal in place of $i_{\hat{\mathrm{dh}}}$. For injection in $\hat{d}$ axis, i.e. $\beta = \Delta\theta$, the second equation of (4.10) becomes:

$$\lambda^i_{\hat{\mathrm{qh}}} = \frac{k}{l_\mathrm{d} l_\mathrm{q} - l_\mathrm{dq}^2} \left[\left(l_\mathrm{q} \left(l_\mathrm{d} - l_\mathrm{q} \right) - 2 l_\mathrm{dq}^2 \right) \cos\left(\Delta\theta\right) + \left(l_\mathrm{d} + l_\mathrm{q} \right) l_\mathrm{dq} \sin\left(\Delta\theta\right) \right] \sin\left(\Delta\theta\right) \tag{4.20}$$

As can be seen, $\lambda^i_{\hat{\mathrm{qh}}}$ is proportional to the sine of the position error without any approximation. Without loss of generality, only for sake of simplicity the second term into the square brackets can be neglected, being at least one order of magnitude lower than the first one. With this assumption, retrieving the amplitude of $\lambda^i_{\hat{\mathrm{qh}}}$ by demodulation process as will be explained in Section 4.2.6, its relationship with the position error is given by:

$$|\lambda^i_{\hat{\mathrm{qh}}}| = \frac{u_\mathrm{c} \left[l_\mathrm{q} \left(l_\mathrm{d} - l_\mathrm{q} \right) - 2 l_\mathrm{dq}^2 \right]}{4 \omega_\mathrm{c} \left(l_\mathrm{d} l_\mathrm{q} - l_\mathrm{dq}^2 \right)} \sin\left(2\Delta\theta\right) \approx k'_\epsilon \Delta\theta \tag{4.21}$$

$$k'_\epsilon = \frac{u_\mathrm{c} \left[l_\mathrm{q} \left(l_\mathrm{d} - l_\mathrm{q} \right) - 2 l_\mathrm{dq}^2 \right]}{2 \omega_\mathrm{c} \left(l_\mathrm{d} l_\mathrm{q} - l_\mathrm{dq}^2 \right)} \tag{4.22}$$

Therefore, the cross-saturation effect is inherently taken into account and no compensations are required. In other words, a PLL based position tracking loop using $|\lambda^i_{\hat{\mathrm{qh}}}|$ as an error signal will converge to the correct rotor position. The dynamic of such convergence is given by (4.21). It should be noted that even without neglecting the second term of (4.20) the demodulated signal is proportional to $\sin\left(\Delta\theta\right)$, so there is not steady state error.

4.2.4 Comparison Between Current and Flux Demodulation

In order to compare the low speed sensorless control based on HF voltage injection with current and with flux demodulation, as in Sections 4.2.2 and 4.2.3, the two algorithms were simulated in Matlab-Simulink environment. The simulated motor is SR2kW2, whose specifications are report in Table 3.3. The motor under test is torque controlled using DFVC, while fixed low speed (20 rpm) is imposed. The reference torque is a slow ramp going from zero to 14 Nm. The simulation was repeated two times on varying the demodulation signal, and the results are shown in Figure 4.2.

In both the tests the observed torque follows the triangular reference, as imposed by the torque control, so it is not report in the plots for clarity reasons. As can be seen, in Figure 4.2(a) the position error at high load is

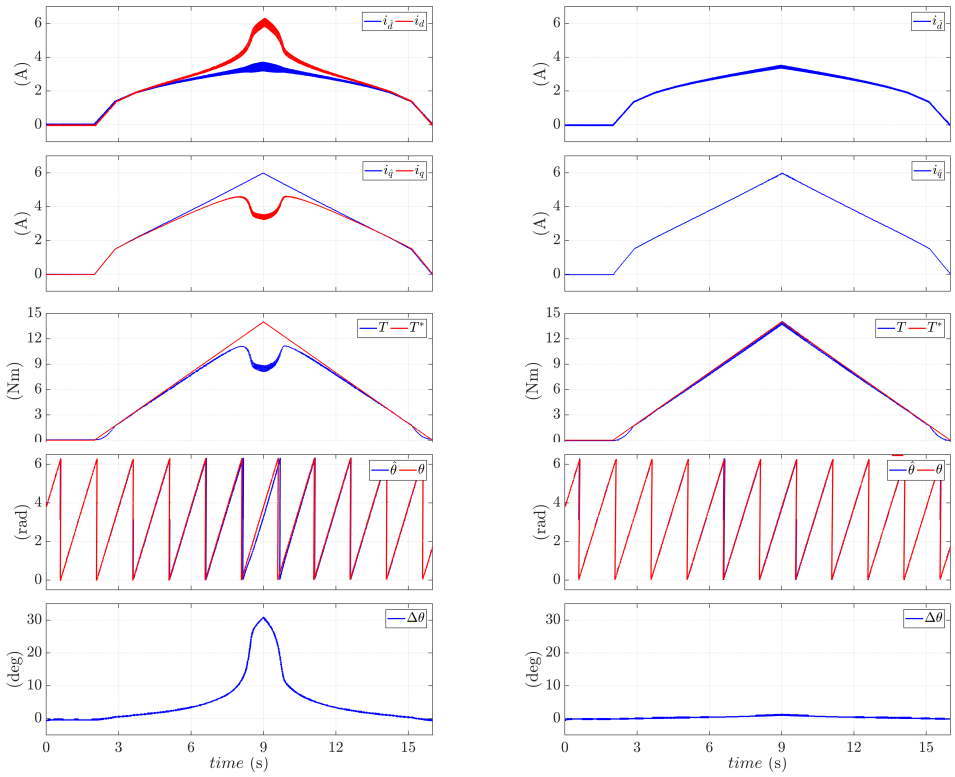

Figure 4.2: Simulation results: sensorless torque control at 20 rpm when 14 Nm ramp torque is applied. The demodulated signal is (a) i_{qh}, (b) $\lambda^{i}_{\hat{\mathrm{q}}\mathrm{h}}$.

relevant and the actual torque is very far from the estimated one. This large discrepancy is due to the cross-saturation error, compatible with (4.18).

Conversely, in Figure 4.2(b) the position error is negligible even at high overload, so the real torque strictly follows the reference, confirming that the flux demodulation is immune from cross-saturation error. These simulations will be experimentally proved in Section 4.7.1.2.

4.2.5 Injection at Half of the Switching Frequency

This Sections justifies the assumptions made in Section 3.3.2 for dynamic analysis and tuning of the magnetic model self-identification test augmented with online position tracking.

The injection at half of the switching frequency, as proposed in [104] and adopted also in Section 3.3.2, can be considered a particular case of pulsating injection where the HF signal is composed by two samples only, so it is necessarily of the square wave type.

As a first approximation, the first harmonic only of the HF square wave can be considered, therefore the analysis carried in Section 4.2.1 is still valid. So, considering an injection in $\hat{d}$ axis ($\beta = \Delta\theta$), the amplitude of the HF current and flux in $\hat{q}$ direction become as (4.16) and (4.21). Therefore, also in this case the current demodulation will suffer of position error due to cross-saturation while the flux demodulation is inherently immune. Obviously, the computation of $\lambda^i_{\hat{\mathrm{q}}\mathrm{h}}$ requires the knowledge of the flux maps, which is unavailable in the self-commissioning stage. Therefore, in the commissioning test #2 augmented with HF injection the demodulated signal was i_{qh}.

It should be pointed out that approximating the injected square wave with its first harmonic is more than acceptable. The higher harmonics would be at the switching frequency or more, therefore not significant from the point of view of the discrete time controller.

4.2.6 Demodulation Process and PLL-Based Position Tracking Loop

The HF pulsating injection produces an HF signal whose amplitude is proportional to the sine of the position error or, if $\Delta\theta$ is considered small, to the position error itself. Depending on the adopted injection technique, the error signal can be either (4.13) or (4.20). In a general form, such error signals $\epsilon_{\mathrm{c,HF}}$ can be expressed as:

$$\epsilon_{\mathrm{c,HF}} = k_{\epsilon 0} \sin(\omega_{\mathrm{c}} t) \sin(2\Delta\theta) \approx k_{\epsilon 0} \sin(\omega_{\mathrm{c}} t)\, 2\Delta\theta \tag{4.23}$$

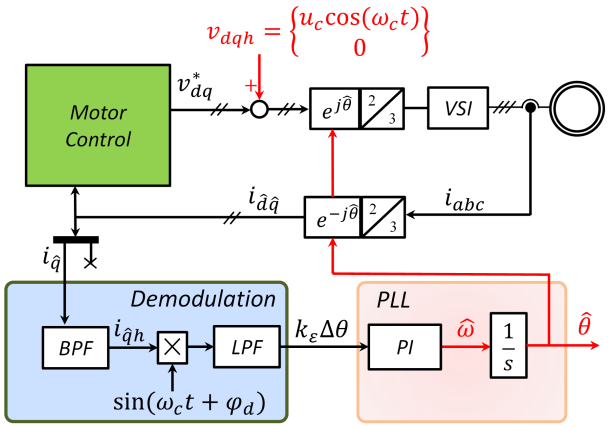

Figure 4.3: Block scheme for pulsating voltage injection in d axis and position retrieved from demodulation of i_{qh}.

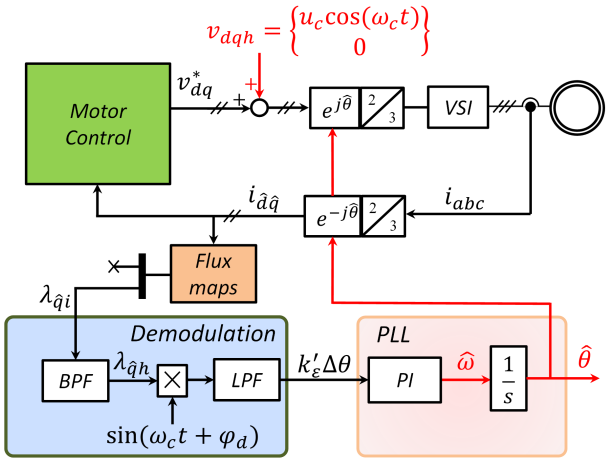

Figure 4.4: Block scheme for pulsating voltage injection in d axis and position retrieved from demodulation of $\lambda^i_{\hat{\mathrm{q}}\mathrm{h}}$.

where the term $k_{\epsilon 0}$ depends by the injection method. As an example, $k_{\epsilon 0} = k_\epsilon$ for injection in $\hat{d}$ axis and $i_{\hat{\mathrm{q}}\mathrm{h}}$ demodulation if l_{dq} is neglected as in Section 4.2.2 and $k_{\epsilon 0} = k'_\epsilon$ for injection in $\hat{d}$ axis and $\lambda^i_{\hat{\mathrm{q}}\mathrm{h}}$ demodulation as in Section 4.2.3. The signal $\epsilon_{\mathrm{c,HF}}$ is modulated at the injection frequency ω_{c}, therefore a demodulation process is necessary to extract the position information $\Delta\theta$. A possible method is to multiply the error signal by the sine of $\omega_{\mathrm{c}}t$, thus obtaining:

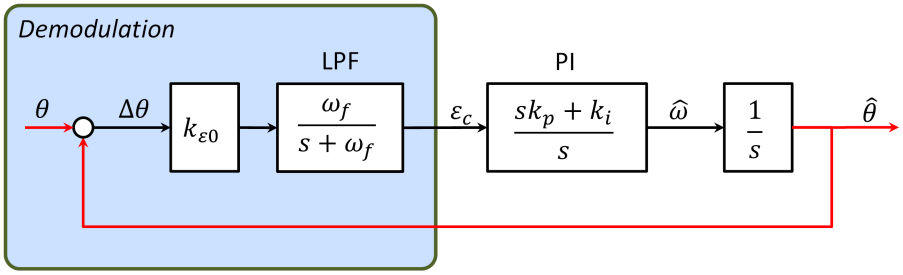

Figure 4.5: Equivalent block scheme for pulsating voltage injection in d axis and position retrieved from demodulation of i_{qh} or $\lambda^{i}_{\hat{\mathrm{q}}\mathrm{h}}$. In the first case, $k_{\epsilon 0} = k_{\epsilon}$; in the second case $k_{\epsilon 0} = k'_{\epsilon}$.

$$\begin{aligned} \epsilon'_{\mathrm{c,HF}} &= \epsilon_{\mathrm{c,HF}} \sin(\omega_{\mathrm{c}} t) = k_{\epsilon 0} \sin^2(\omega_{\mathrm{c}} t)\, 2\Delta\theta \\ \epsilon'_{\mathrm{c,HF}} &= \frac{1}{2}\left(1 - \cos(2\omega_{\mathrm{c}} t)\right) k_{\epsilon 0} 2\Delta\theta \end{aligned} \tag{4.24}$$

This signal presents a DC component plus an harmonic at two times the injection frequency, both proportional to the position error. It is convenient to Low Pass Filtering (LPF) $\epsilon'_{\mathrm{c,HF}}$, thus retrieving the position information from the DC component:

$$\epsilon_{\mathrm{c}} = LPF\left(\epsilon'_{\mathrm{c,HF}}\right) = \frac{1}{2} k_{\epsilon 0} 2\Delta\theta = k_{\epsilon 0}\Delta\theta \tag{4.25}$$

This signal, proportional to the position error, is closed loop forced to zero using a PLL tracking loop, as in Figure 4.3. As a consequence, $\Delta\theta$ becomes zero and the rotor position estimation $\hat{\theta}$ is obtained. Figure 4.3 and 4.4 show the implementation of the HF injection position tracking based on current and flux demodulation respectively. It should be noted that for digital implementation the HF signal is not multiplied by the sine of $\omega_{\mathrm{c}} t$ but to $\sin(\omega_{\mathrm{c}} t + \phi_{\mathrm{d}})$, where ϕ_{d} is introduced to take into account the actuation delay and corresponds to the angle described by the HF signal in two sampling periods:

$$\phi_{\mathrm{d}} = 2 \cdot \omega_{\mathrm{c}} T_{\mathrm{sw}} \tag{4.26}$$

The dynamic of such tracking loop can be evaluated and tuned according to the equivalent scheme report in Figure 4.5, where ω_{f} stands for the cut-off frequency of the LPF introduced in the demodulation process. The retrieved transfer function between observed and actual rotor position is:

$$H = k_{\epsilon 0} \frac{\omega_{\mathrm{f}}}{s + \omega_{\mathrm{f}}} \frac{s k_{\mathrm{p,PLL}} + k_{\mathrm{i,PLL}}}{s} \frac{1}{s} \tag{4.27}$$

$$\frac{\hat{\theta}}{\theta} = \frac{H}{1 + H} \tag{4.28}$$

where H is the open loop transfer function. Proper tuning of this tracking loop will be given in Section 4.6.3.

4.2.7 Saliency Analysis of SyRM and PM-SyRM

The feasibility of low speed sensorless control is strictly linked to the machine saliency, whatever injection and demodulation techniques are used. As an example, the amplitude of the feedback error signal is proportional to the difference $(l_{\mathrm{d}} - l_{\mathrm{q}})$ both in case of current or flux demodulation, as shown in (4.16) and (4.21). Similar expressions can be found for most of the other injection based sensorless controls presented in the literature. So, the higher is the saliency, the higher is the signal-to-noise ratio for position tracking.

Despite SyR and PM-SyR motors are considered high anisotropy motors, rotor saliency varies with the operating point in the dq current plane due to magnetic saturation, leading to sensitivity to the operating point and possible loss of information in certain conditions. Such phenomenon was studied in [161] for IPM motors. In addition, the SyR motor presents specific issues treated in [10]. In the low-current region the incremental inductance of the q axis tends to be very similar to the one of the d axis, leading to lack of saliency and so lack of position information. This phenomenon can be noticed from the curves $\lambda_{\mathrm{d}}(i_{\mathrm{d}}, i_{\mathrm{q}} = 0)$ and $\lambda_{\mathrm{q}}(i_{\mathrm{d}} = 0, i_{\mathrm{q}})$ in Figure 3.3, presenting similar slope around zero current. This problem, inherently solved in PM-SyR machines, has to do with the saturation of the structural ribs in the rotor, as will be later described. Another characteristic of SyRM is that cross-saturation is usually more relevant than in PM machines, also affecting the saliency. This Section investigates all these issues through a comprehensive saliency analysis on varying the operating point.

4.2.7.1 Saliency Evaluation through Rotating Excitation

The saliency of the SyRM over the i_{d}, i_{q} operational plane is explored using the current response to a rotating HF voltage signal. Such rotating voltage is superimposed to a fundamental current vector, defining the operating point $(i_{\mathrm{d0}}, i_{\mathrm{q0}})$. Imposing an HF voltage corresponds to imposing an HF flux component:

$$\boldsymbol{v}_{\mathrm{dqh}} = V e^{j\omega_{\mathrm{c}} t + \frac{\pi}{2}} \quad \rightarrow \quad \boldsymbol{\lambda}_{\mathrm{dqh}} = \frac{V}{\omega_{\mathrm{c}}} e^{j\omega_{\mathrm{c}} t} = \Lambda e^{j\omega_{\mathrm{c}} t} \tag{4.29}$$

where V is the amplitude of the injected rotating voltage and Λ the amplitude of the correspondent flux component. By using first order Taylor series expansion, the flux in dq axes in a neighborhood of the considered operating point is given by:

$$\begin{cases} \lambda_{\mathrm{d}}\left(i_{\mathrm{d}}, i_{\mathrm{q}}\right) & \approx \lambda_{\mathrm{d}}\left(i_{\mathrm{d0}}, i_{\mathrm{q0}}\right) + \frac{\partial \lambda_{\mathrm{d}}}{\partial i_{\mathrm{d}}} \Delta i_{\mathrm{d}} + \frac{\partial \lambda_{\mathrm{d}}}{\partial i_{\mathrm{q}}} \Delta i_{\mathrm{q}} \\ \lambda_{\mathrm{q}}\left(i_{\mathrm{d}}, i_{\mathrm{q}}\right) & \approx \lambda_{\mathrm{q}}\left(i_{\mathrm{d0}}, i_{\mathrm{q0}}\right) + \frac{\partial \lambda_{\mathrm{q}}}{\partial i_{\mathrm{d}}} \Delta i_{\mathrm{d}} + \frac{\partial \lambda_{\mathrm{q}}}{\partial i_{\mathrm{q}}} \Delta i_{\mathrm{q}} \end{cases} \tag{4.30}$$

Considering small signal analysis, i.e. the HF signal does not considerably changes the working point so the differential inductances are constant in such operating condition, (4.30) gives:

$$\begin{cases} \lambda_{\mathrm{d}}\left(i_{\mathrm{d}}, i_{\mathrm{q}}\right) & \approx \lambda_{\mathrm{d}}\left(i_{\mathrm{d0}}, i_{\mathrm{q0}}\right) + l_{\mathrm{d}} i_{\mathrm{dh}} + l_{\mathrm{dq}} i_{\mathrm{qh}} \\ \lambda_{\mathrm{q}}\left(i_{\mathrm{d}}, i_{\mathrm{q}}\right) & \approx \lambda_{\mathrm{q}}\left(i_{\mathrm{d0}}, i_{\mathrm{q0}}\right) + l_{\mathrm{dq}} i_{\mathrm{dh}} + l_{\mathrm{q}} i_{\mathrm{qh}} \end{cases} \tag{4.31}$$

where $\boldsymbol{\lambda}_{\mathrm{dq}}\left(i_{\mathrm{d0}}, i_{\mathrm{q0}}\right)$ is the fundamental component and the terms containing differential inductances are related to the HF injection. So, these latter terms are equal to the HF flux component identified in (4.29):

$$\begin{cases} \Lambda \cos\left(\omega_{\mathrm{c}} t\right) & = l_{\mathrm{d}} i_{\mathrm{d}} + l_{\mathrm{dq}} i_{\mathrm{q}} \\ \Lambda \sin\left(\omega_{\mathrm{c}} t\right) & = l_{\mathrm{dq}} i_{\mathrm{d}} + l_{\mathrm{q}} i_{\mathrm{q}} \end{cases} \tag{4.32}$$

By manipulating these equations, the time dependency can be eliminated, obtaining the expression of the trajectory described by the HF current component around the operating point $\left(i_{\mathrm{d0}}, i_{\mathrm{q0}}\right)$:

$$\left(l_{\mathrm{d}}^2 + l_{\mathrm{dq}}^2\right) i_{\mathrm{dh}}^2 + \left(l_{\mathrm{q}}^2 + l_{\mathrm{dq}}^2\right) i_{\mathrm{qh}}^2 + 2 l_{\mathrm{dq}} \left(l_{\mathrm{d}} + l_{\mathrm{q}}\right) i_{\mathrm{dh}} i_{\mathrm{qh}} = \Lambda^2 \tag{4.33}$$

This expression describes an ellipse in the dq plane tilted respect to the reference Cartesian axes. The rotation angle, which can be analytically found by standard geometrical methods, is exactly $\Delta\theta_{\mathrm{dq}}$ identified in (4.18) in case of current demodulation. The amplitude major and minor axes of the tilted ellipse are approximately equal to $\sqrt{l_{\mathrm{d}}^2 + l_{\mathrm{dq}}^2}/\Lambda$ and $\sqrt{l_{\mathrm{q}}^2 + l_{\mathrm{dq}}^2}/\Lambda$ respectively.

Therefore, the superposition of a rotating voltage excitation produces an elliptic current response, superimposed to the average operating point. The main direction of the ellipse indicates the direction with the lowest local incremental inductance, its sharpness indicates the local machine saliency while the deviation of such ellipse from dq orientation indicates the possible cross-saturation error $\Delta\theta_{\mathrm{dq}}$. In other words, if pulsating voltage injection

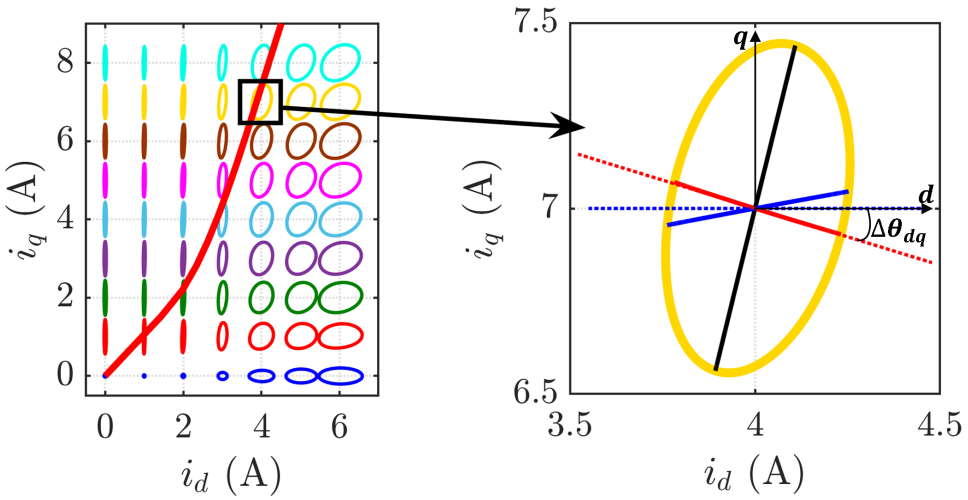

Figure 4.6: Saliency analysis based on FEM flux maps and rotating voltage injection. Left: selected points in the dq plane and MTPA trajectory (red). Right: zoom in an MTPA point. Blue lines refer to pulsating injection in real d axis, red lines refer to the convergence point in case of current demodulation. Motor: SR2kW2.

with current demodulation is adopted as in Section 4.2.2, the estimated rotor position will converge to the ellipse minor axis.

Figure 4.6 presents the current ellipses obtained in several points of the qd plane predicted using a manipulation of a fine mesh flux map evaluated with FEA. The motor under test is SR2kW2, and the rotating voltage has an amplitude of 50 V. In safe operating points, i.e. approximately for $i_\mathrm{d} \leq 3\ A$, the ellipse is sharp and oriented along q axis, so a saliency based position tracking loop can easily converge to the correct rotor position. For higher i_d, the cross-saturation effect becomes more relevant, so the ellipse is clockwise rotated, leading to a position estimation error and even loss of position tracking. An example is given in the right-end side of the Figure, highlighting a point close to the MTPA. Such subplot compares the current responses of rotating and pulsating injections, where the pulsating voltage is injected in three different directions, indicated by the dashed lines. The continuous lines represent the computed path of the pulsating current in the three cases, accounting for the cross saturation effect. The results can be summarized as:

Blue lines: the HF voltage is injected along the correct d axis, and the obtained current deviates from the injection direction.

Red lines: the blue lines tell what happens with open loop voltage injection

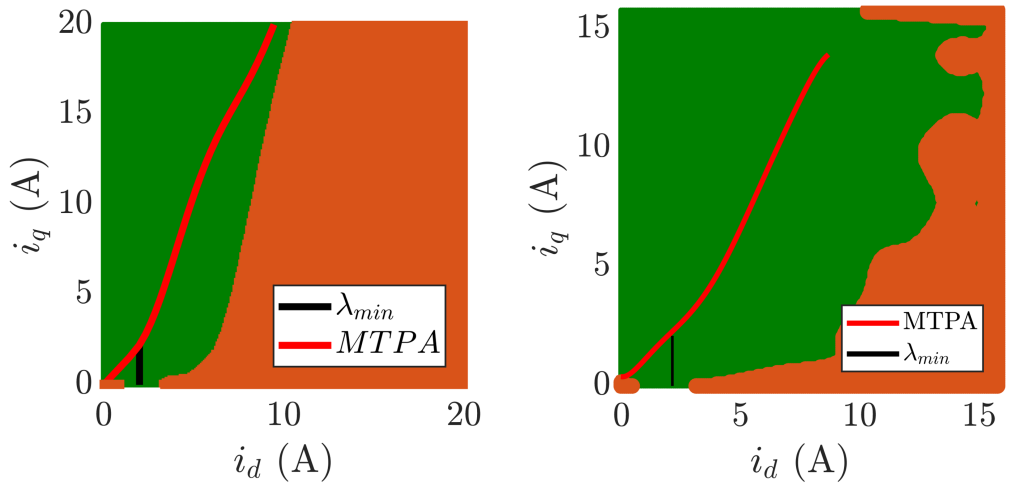

Figure 4.7: Feasible operating region for low speed sensorless control. Green: $\Delta\theta_{\text{dq}} < 45°$. Brown: $\Delta\theta_{\text{dq}} > 45°$. Red: MTPA trajectory. (a) Motor SR2kW2. (b) Motor LGV.

along the d axis. If the current component on the estimated q axis is used as input of a position tracking loop, the blue situation would produce a fictitious position error that the tracking loop would correct, converging in the steady state situation $\hat{\theta} = \Delta\theta_{\text{dq}}$, where the HF current and voltage are aligned (red).

Black lines: a position observer might also converge at $\hat{\theta} = \Delta\theta_{\text{dq}} + \pi/2$ (black), for symmetry reasons. Anyway, this is an unstable converging point and can be neglected.

Altogether, Figure 4.6 shows that the current ellipses summarize the information coming from all possible injection directions, when using a pulsating signal. Also, the expected position error is easily visualized as the deviation between the ellipse minor axis and the horizontal directions. Figure 4.12 compares FEA and experimental results for selected operating points.

4.2.7.2 Stability Region

As said, the position error is negligible where the ellipse is sharp and vertical, i.e., left wise respect to the MTPA curve. Conversely, in the right end side of the dq plane (Figure 4.6), the position error becomes significant, and in the lower right corner (around the d axis) the saliency even reverses (sharp

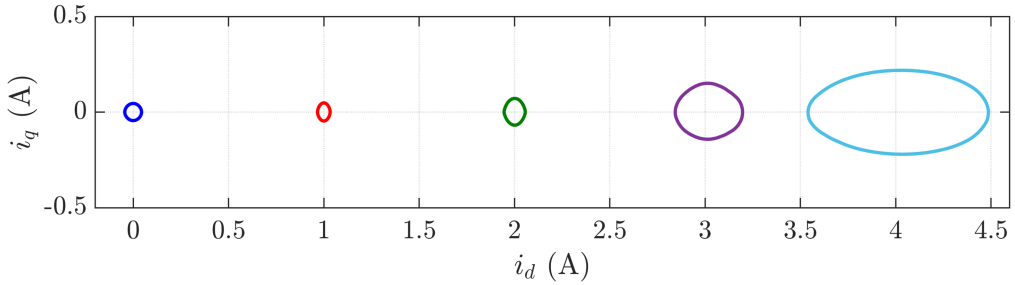

Figure 4.8: Zoom of the saliency analysis report in Figure 4.6 for low i_q.

horizontal ellipses), indicating that the position tracking error could be equal to 90°. This is because in this area the saliency is reversed ($l_\mathrm{d} < l_\mathrm{q}$).

The stable region of saliency-based sensorless methods is summarized in Figure 4.7, in green, for two SyR motors. The unstable region is indicated in brown, covering those points where the cross saturation error $\Delta\theta_\mathrm{dq}$ is larger than 45°, so the saliency tracking would converge 90° away from the d axis. As can be seen, the MTPA trajectory is well into the stable region, therefore the sensorless position estimation is generally stable in normal operating conditions. The same result was found by analyzing the flux maps of several different SyR motor prototypes.

4.2.7.3 Low i_q Region: Comparison between SyR and PM-SyR

In case of pure SyR motors only, a special case of lack of position information is in the origin, where the saliency is very low. Besides the origin, the d-axis region altogether ($i_\mathrm{q} \to 0$) tends to be critical for saliency, for the combination of the non-saturated ribs and the direct saturation due to the d-axis component. Figure 4.8 presents a zoom of the saliency analysis around the d axis for the SyR motor SR2kW2. As can be seen, close to the origin of the plane the current trajectory resembles a circle rather than an ellipse, indicating very limited saliency and therefore low position information. By increasing the i_d over a certain value, the d axis slowly starts so saturate, so l_d decreases, but l_q is still small since $i_\mathrm{q} = 0$. Therefore, the already limited saliency tends to become erroneously oriented along the d axis, thus leading to possible instability. All these effects are visible for pure SyR motors, but they are inherently not present for PM-SyR machines.

This difference is explained considering the rotor structure of the two machines. Without PMs, if i_q is low the structural ribs are not saturated and so the flux crosses the rotor as if there were no flux barriers. In other words, under those circumstances, the reluctance in the q axis is unexpectedly low,

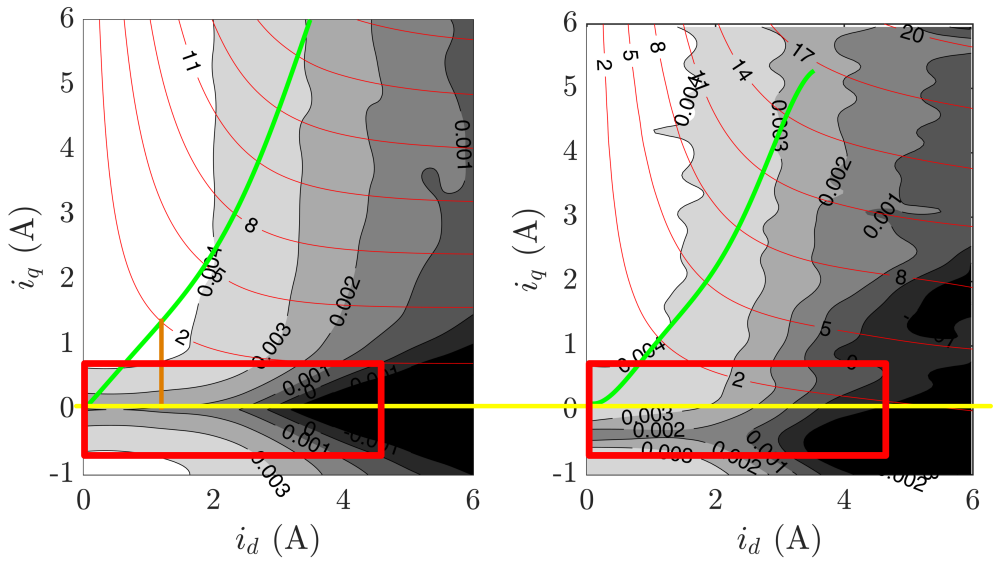

Figure 4.9: Maps of k'_ϵ in the dq plane based on the experimental flux characteristics and equation (4.22) for the motors SR1kW1 (left) and NdSR1kW1 (right). Green: MTPA. Red: torque contour.

as well as the machine saliency. This phenomenon harms the stability of sensorless control of SyR at low speed in no-load conditions. The problem can be overcome by imposing a minimum excitation current or flux to the machine. If sufficient current is given in the d axis, the ribs tend to partially saturate for cross-saturation effect, leading the machine saliency to acceptable levels. In the PM-SyRMs, the magnets have the precious function of saturating the ribs, also at zero current, thus preventing saliency drops.

Beside the SR2kW2 motor, the saliency analysis was performed in [11] on two prototypes called SR1kW1 and NdSR1kW1, properly designed for comparison purposes. These two motors present exactly the same stator while the rotors were accurately designed with the same geometry of the flux barriers, but if the first is a pure SyR machine, NdFeB magnets were added to the second obtaining a PM-SyR motor. Therefore, the two prototypes differ only for the presence or absence of the PM. Details can be found in [11].

To compare the two motors, at first the parameter k'_ϵ was computed from the experimental flux maps of the two motors and plotted in Figure 4.9. High k'_ϵ indicates high local anisotropy. Sensorless control is theoretically possible if the machine presents saliency, even if it is minimal, and in the correct direction (i.e. $k'_\epsilon > 0$). However, the smaller the saliency, the more difficult it is to track it, so the PLL may not converge or may converge

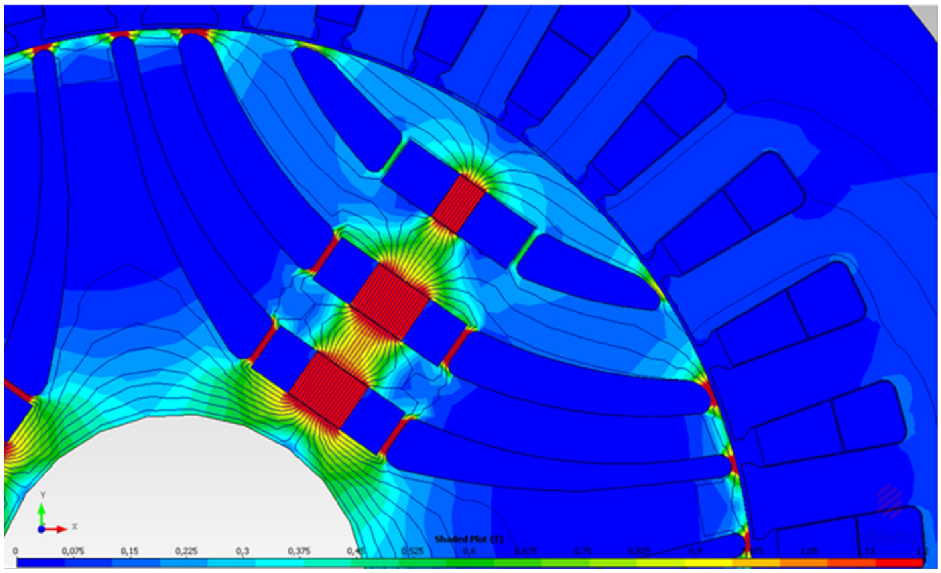

Figure 4.10: FEM model of NdSR1kW1 motor at zero current

to an incorrect position. In other words, the control is more sensitive to parameter uncertainty, such as stator resistance variation, inaccurate flux maps, imperfect compensation of inverter non-linearities, and noise in current measurement. Therefore, a high value of k'_ϵ corresponds to high signal-to-noise ration while negative k'_ϵ leads to instability. As expected, the SyR motor presents a critical area along the d axis (red rectangle in Figure 4.9) since k'_ϵ drops, while such marginally stable region is shifted downwards in case of PM-SyR motor, out of the operating quadrant ($i_\mathrm{q} < 0$). Therefore, with PM-assistance, low-speed sensorless position estimation can be performed even at no-load without any need for a minimum flux excitation.

Finally, Figure 4.10 shows the field distribution in the PM-SyR motor under test obtained by FEM analysis at zero current. As can be seen, even in absence of stator current the ribs are saturated, so the saliency is guaranteed.

4.2.7.4 Experimental Validation

A dedicated experimental test was performed to investigate the machine saliency in the whole dq plane. Each tested motor was kept at standstill by an external speed controlled drive, while fundamental i_d and i_q were imposed to define the operating point under investigation. A HF rotating voltage was superimposed to the fundamental voltage signals at the output of the PI regulators, as in Figure 4.11. The HF current is removed from the current loop using a Band Stop Filter (BSF) to avoid interference with

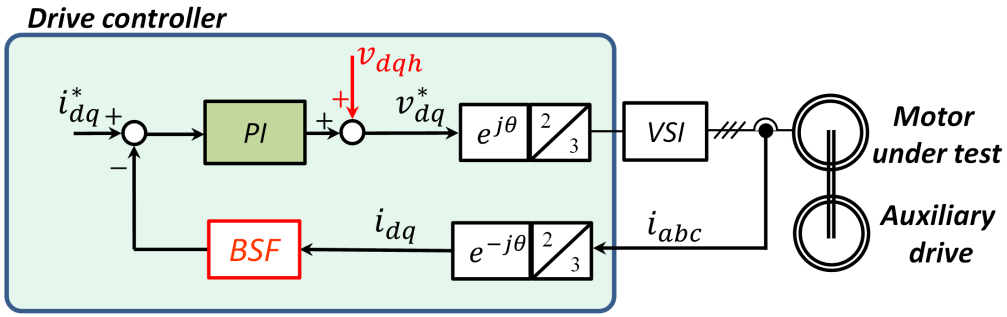

Figure 4.11: Equivalent block scheme for experimental saliency analysis.

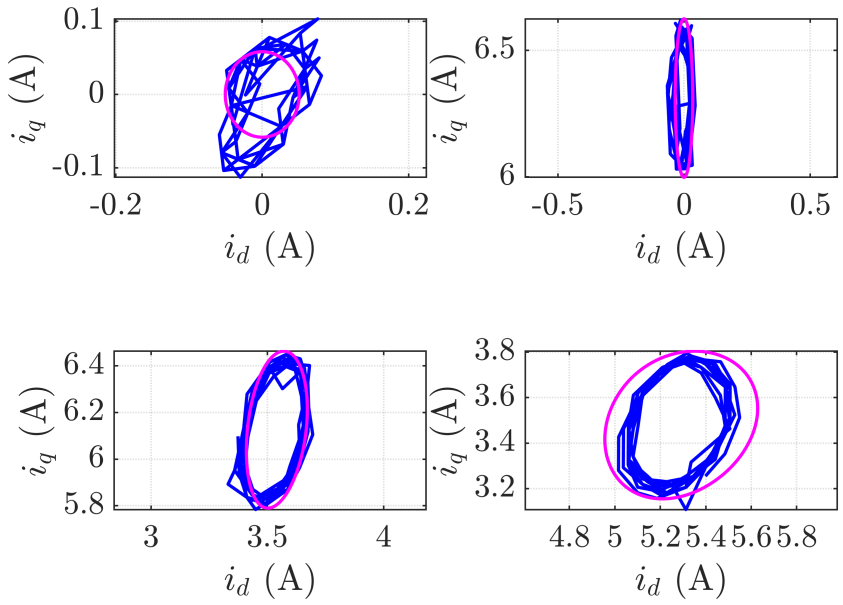

Figure 4.12: Comparison between predicted (magenta) and measured (blue) current ellipses for the SyR motor SR2kW2.

the PI regulators. Neglecting manufacturing asymmetries, the results are independent of rotor position since the dq frame is employed.

The current response was compared with the predicted ellipse in Figure 4.12 for the SyR motor SR2kW2, showing a good agreement. Unfortunately, relevant measurement noise was introduced by the experimental setup and it could not be totally filtered. Figure 4.13 compares the results obtained for SR1kW1 and NdSR1kW1 machines. As expected from the theo-

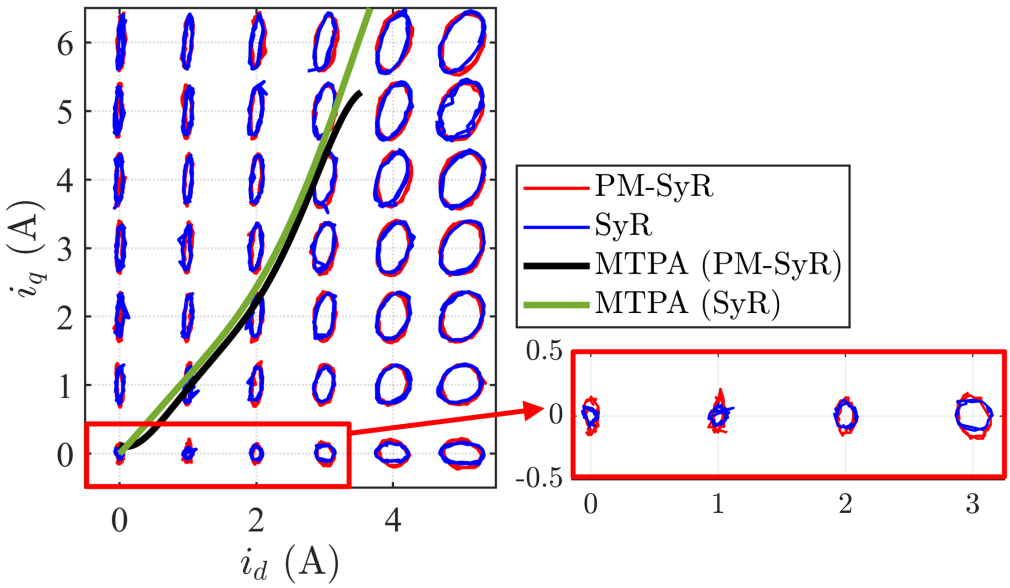

Figure 4.13: Experimental results for saliency analysis through rotating voltage injection for SR1kW1 and NdSR1kW1 motors.

retical analysis, the two machines present very similar saliency characteristic and optimal sensorless control capability in most of the dq current plane. The only relevant difference is at low i_{q} region, where the saliency of pure SyRM drastically drops while such phenomenon is shifted to $i_{\mathrm{q}} < 0$ for the PM-SyR motor. Also, the two machines present similar deviation due to cross-saturation effect at high i_{d} and high i_{q}.

4.2.8 FCS-MPC Injectionless Control

An alternative to the HF injection methods was presented in [13]. The motor control is based on deadbeat FCS-MPC algorithm, so at every sampling time one of the seven reference vectors of the voltage hexagon is applied without using PWM modulation, as discussed in Section 2.2.2. The control variables are the stator flux components in dq reference frame $\boldsymbol{\lambda}_{\mathrm{dq}}$. The reference quantities $\boldsymbol{\lambda}^{*}_{\mathrm{dq}}$ are established from the reference torque, where the correspondence between torque and flux is obtained from the flux maps. In such relationship, MTPA trajectory is adopted, but a minimum λ_{q} is always imposed to ensure the saturation of structural ribs, and therefore a sufficient machine saliency for sensorless position estimation. The reference torque can be either given by the user (torque control) or extracted from a speed loop (speed control). The control block scheme is given in Figure 4.14.

A flux observer similar to Figure 2.10 is adopted, but dealing with MPC

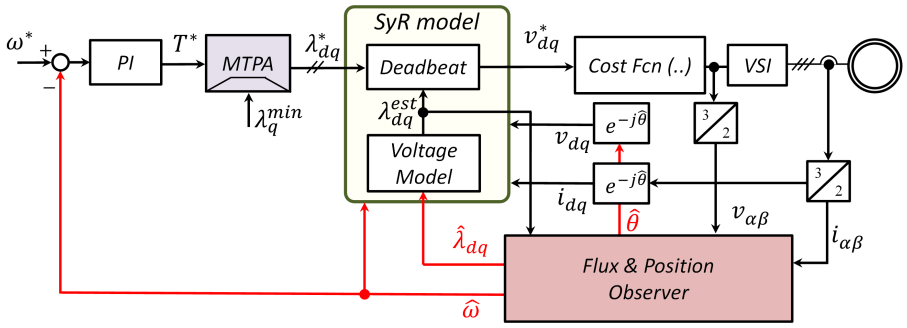

Figure 4.14: Block scheme for sensorless FCS-MPC.

algorithms a discrete time expression of the observed flux has to be used. The notation $\Delta x(k) = x(k) - x(k-1)$ will indicate the difference between quantities at two consecutive sampling times. The flux vector $\boldsymbol{\lambda}_{\mathrm{dq}}$ is estimated for the next sampling time $k+1^{th}$ for taking into account digital delay:

$$\boldsymbol{\lambda}_{\mathrm{dq}}^{est}(k+1) = \hat{\boldsymbol{\lambda}}_{\mathrm{dq}}(k) + T_{\mathrm{sw}}\left[\boldsymbol{v}_{\mathrm{dq}}(k) - R_{\mathrm{s}}\boldsymbol{i}_{\mathrm{dq}}(k) - \hat{\omega}\mathbf{J}\,\hat{\boldsymbol{\lambda}}_{\mathrm{dq}}(k)\right] \tag{4.34}$$

where $\boldsymbol{v}_{\mathrm{dq}}$ is estimated from the inverter commands properly compensating inverter non-linear voltage drops. The deadbeat voltage $\boldsymbol{v}_{\mathrm{dq}}^{*}(k+1)$ necessary to reach the desired $\boldsymbol{\lambda}_{\mathrm{dq}}^{*}$ within one sampling time is given by:

$$\boldsymbol{v}_{\mathrm{dq}}^{*}(k+1) = R_{\mathrm{s}}\boldsymbol{i}_{\mathrm{dq}}(k) + \frac{\boldsymbol{\lambda}_{\mathrm{dq}}^{*} - \boldsymbol{\lambda}_{\mathrm{dq}}^{est}(k+1)}{T_{\mathrm{sw}}} + \hat{\omega}\mathbf{J}\,\boldsymbol{\lambda}_{\mathrm{dq}}^{est}(k) \tag{4.35}$$

In this expression, the resistive voltage drop is compensated based on the current at the present sampling time $\boldsymbol{i}_{\mathrm{dq}}(k)$. Limited improvement would be obtained estimating the current vector at the next sampling time $\boldsymbol{i}_{\mathrm{dq}}(k+1)$ at the cost of additional computational burden. The cost function adopted to decide the voltage vector for the next sampling instant is given by:

$$g\left(\boldsymbol{v}_{\mathrm{j}}\right) = \left|\boldsymbol{v}_{\mathrm{dq}}^{*}(k+1) - \boldsymbol{v}_{\mathrm{dq,j}}\right| \tag{4.36}$$

$$\boldsymbol{v}_{\hat{\mathrm{d}}\hat{\mathrm{q}}}(k+1) = \underset{j=0,1..7}{\operatorname{argmin}}\, g(\boldsymbol{v}_{\mathrm{dq,j}}) \tag{4.37}$$

Therefore, the voltage vector having the smaller Euclidean distance from $\boldsymbol{v}_{\mathrm{dq}}^{*}(k+1)$ computed in (4.35) is chosen among the six active vectors of the inverter ($\mathrm{n} = 1 \div 6$) and the zero vectors ($\mathrm{n} = 0{,}7$). The position estimation is based on the instantaneous machine response upon an active voltage vector.

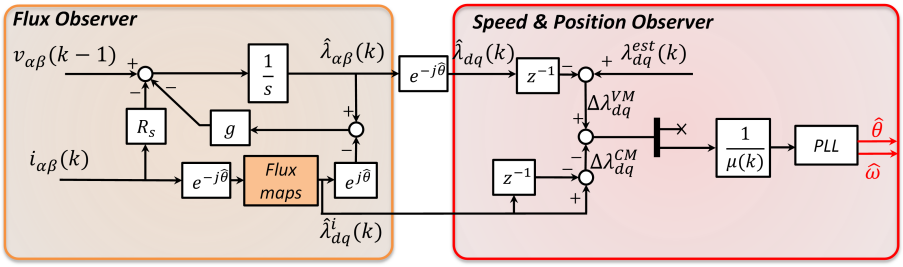

Figure 4.15: Block scheme for flux and position observer for FCS-MPC.

Figure 4.15 describes the block diagram of the flux and position observer. $\hat{\theta}$ is retrieved from the discrepancy in stator flux ripple estimated from voltage model $\Delta\boldsymbol{\lambda}^{v}_{\hat{\mathrm{dq}}}$ and from the current models $\Delta\boldsymbol{\lambda}^{i}_{\hat{\mathrm{dq}}}$, given by:

$$\boldsymbol{\epsilon}_{\mathrm{dq}} = \Delta\boldsymbol{\lambda}^{v}_{\hat{\mathrm{dq}}} - \Delta\boldsymbol{\lambda}^{i}_{\hat{\mathrm{dq}}} \tag{4.38}$$

where

$$\Delta\boldsymbol{\lambda}^{v}_{\hat{\mathrm{dq}}}(k) = T_{\mathrm{sw}}\left[\boldsymbol{v}_{\mathrm{dq}}(k-1) - R_{\mathrm{s}}\boldsymbol{i}_{\hat{\mathrm{dq}}}(k) - \hat{\omega}\mathbf{J}\,\hat{\boldsymbol{\lambda}}_{\mathrm{dq}}(k)\right] \tag{4.39}$$

$$= \boldsymbol{\lambda}^{est}_{\mathrm{dq}}(k) - \hat{\boldsymbol{\lambda}}_{\mathrm{dq}}(k-1) \tag{4.40}$$

$$\Delta\boldsymbol{\lambda}^{i}_{\hat{\mathrm{dq}}}(k) = \boldsymbol{L}_{\mathrm{dq}}\boldsymbol{i}_{\hat{\mathrm{dq}}}(k) - \boldsymbol{L}_{\mathrm{dq}}\boldsymbol{i}_{\hat{\mathrm{dq}}}(k-1) \tag{4.41}$$

In the computation of $\Delta\boldsymbol{\lambda}^{v}_{\hat{\mathrm{dq}}}$, the flux estimate $\boldsymbol{\lambda}^{est}_{\mathrm{dq}}(k)$ is adopted since it is completely voltage based, with no influence from the current model. By proper equations manipulation, (4.38) can be retrieved as

$$\boldsymbol{\epsilon}_{\mathrm{dq}} = \left(\mathrm{e}^{\mathrm{j}\Delta\theta}\boldsymbol{l}_{\mathrm{dq}}\mathrm{e}^{-\mathrm{j}\Delta\theta}\Delta\boldsymbol{i}_{\mathrm{dq}}\right) - \left(\boldsymbol{l}_{\mathrm{dq}}\Delta\boldsymbol{i}_{\mathrm{dq}}\right) \tag{4.42}$$

where $\boldsymbol{l}_{\mathrm{dq}}$ is updated every control cycle based on $\boldsymbol{i}_{\mathrm{dq}}$. Considering small $\Delta\theta$, (4.42) can be written as:

$$\boldsymbol{\epsilon}_{\mathrm{dq}} = \begin{bmatrix} -2l_{\mathrm{dq}} & l_{\mathrm{d}} - l_{\mathrm{q}} \\ l_{\mathrm{d}} - l_{\mathrm{q}} & 2l_{\mathrm{dq}} \end{bmatrix} \Delta\boldsymbol{i}_{\mathrm{dq}} \cdot \Delta\theta \tag{4.43}$$

From this expression it can be seen that the position information could be retrieved from either one or the other axis. Anyway, the q component is preferred since a larger current ripple (and therefore more reliable position information) is obtained for equal applied voltage. Therefore, the position error is obtained as:

$$\Delta\theta = \frac{\epsilon_{\mathrm{q}}}{\mu} \tag{4.44}$$

where μ is a gain containing the differential inductances, so it depends on the working point. Neglecting cross-saturation ($l_{\mathrm{dq}} = 0$), such gain becomes:

$$\mu(k) \approx (l_{\mathrm{d}} - l_{\mathrm{q}})\, \Delta i_{\mathrm{d}}(k) \tag{4.45}$$

The term Δi_{d} is small, so it may be difficult to be properly measure it. If necessary, Δi_{d} can eventually be retrieved as

$$\mu(k) \approx (l_{\mathrm{d}} - l_{\mathrm{q}})\, \frac{T_{\mathrm{sw}}}{l_{\mathrm{d}}} v_{\hat{\mathrm{d}}}(k-1) \tag{4.46}$$

Since $\mu(k)$ appears in the denominator of (4.44), it is not evaluated in case $v_{\hat{\mathrm{d}}}(k-1)$ is lower than a defined threshold. In this case, the gain μ is not updated and so $\mu(k-1)$ is used also at the sampling time k. In this way, if the cost function (4.37) defines a sequence of consecutive vectors so that $v_{\hat{\mathrm{d}}}(k-1)$ is lower the threshold for a given number of sampling periods N_{thres}, the control would be lost. Therefore, a hard constrain is applied to (4.37) in this case, ensuring sufficient $v_{\hat{\mathrm{d}}}(k-1)$ and so control stability:

$$g(\boldsymbol{v}_{\mathrm{j}}) = |\boldsymbol{v}^{*}_{\mathrm{dq}}(k+1) - \boldsymbol{v}_{\mathrm{dq,j}}| + (n > N_{thres})\, \boldsymbol{C}_j \tag{4.47}$$

$$\boldsymbol{C}_j = (|v_{d,j}| \leq V_{thres})\, 0 + (|v_{d,j}| > V_{thres})\, \infty \tag{4.48}$$

where n is the number of consecutive voltage vectors to have failed to meet the threshold. Thus, when n exceeds N_{thres}, the hard constraint $\boldsymbol{C}_j$ is activated which enables only those voltage vectors that meet the threshold. A proper value for N_{thres} was experimentally found as $N_{thres} = 5$. More implementation details were given in [13].

4.3 Model Based Position Estimation

At medium and high rotor speed, HF injection techniques may not be applicable for several reasons. The available voltage may be limited, especially getting closer to the flux weakening range. Moreover, the demodulation signal is based on the measured current, which is available with one time step delay, and eventual demodulation filters further increase such time delay, which becomes more relevant when the speed increases.

But, as soon as the back-EMF are sufficiently high, model based position observers can be conveniently used instead, where the position information is retrieved from manipulation of the machine equations. Several techniques were proposed in the literature, as described in Section 4.1. The two techniques described in Section 2.4.2 and 2.4.3, called "observer based" and "active flux", were adopted specifically for SyRM in [10] and [9] respectively.

Considering the active flux observer, traditionally a fixed value is adopted for L_{q}. In [9], the $\boldsymbol{\lambda}^{\mathrm{AF}}$ vector is calculated from (2.32) using an L_{q} look-up-table, which is calculated offline by dividing the q axis flux linkage to q axis current considering the cross axis current i_{d} for the sake of including cross-saturation effect, as expressed in (4.49). In this way, the position estimation accuracy was considerably improved.

$$L_{\mathrm{q}}\left(i_{\mathrm{d}}, i_{\mathrm{q}}\right) = \frac{\lambda_{\hat{\mathrm{q}}}^{i}\left(i_{\mathrm{d}}, i_{\mathrm{q}}\right)}{i_{\mathrm{q}}} \tag{4.49}$$

In both cases, the speed was retrieved from discrete derivation of $\hat{\theta}^{\mathrm{HS}}$ based on (2.31) or (2.34) calculated in two consecutive sampling times:

$$\begin{aligned}\hat{\omega} &= f_{\mathrm{sw}} \cdot \sin\left(\hat{\theta}^{\mathrm{HS}}(k) - \hat{\theta}^{\mathrm{HS}}(k-1)\right) \\ &= f_{\mathrm{sw}}\left(\sin\hat{\theta}^{\mathrm{HS}}(k)\cos\hat{\theta}^{\mathrm{HS}}(k-1) - \cos\hat{\theta}^{\mathrm{HS}}(k)\sin\hat{\theta}^{\mathrm{HS}}(k-1)\right)\end{aligned} \tag{4.50}$$

In this formulation, it is assumed that the variation in rotor position within one sampling period is small, i.e. $\sin(\hat{\theta}^{\mathrm{HS}}(k) - \hat{\theta}^{\mathrm{HS}}(k-1)) \approx \hat{\theta}^{\mathrm{HS}}(k) - \hat{\theta}^{\mathrm{HS}}(k-1)$.

4.4 Models Fusion

For a sensorless control able to operate in a wide speed range, e.g. from stand-still to flux weakening, hybrid solutions based on combinations of saliency based and model based techniques are commonly used. In these solutions, HF signal injection is adopted at low speed, where the EMF are low, and the injection is dropped when the speed is sufficiently high to allow reliable model based position estimation, to avoid additional iron losses and acoustic noise and to not affect the available voltage.

The transition between the two position estimation techniques is a relevant problem that must be addressed. At the boundary between high and low speed range, the position estimations coming from the two approaches are usually not perfectly coincident. A smooth transition is often desired to avoid discontinuity in the observed position and speed.

The saliency based and model based techniques were merged in a unique structure in [9, 10], where flux demodulation was adopted at low speed as in Section 4.2.3. The block scheme is report in Figure 4.16, where $\hat{\theta}^{\mathrm{HS}}$ can be obtained either from (2.31) as in [10] or exploiting active flux concept [9]. At high speed, the PLL structure in Figure 2.12 and 2.14 is removed.

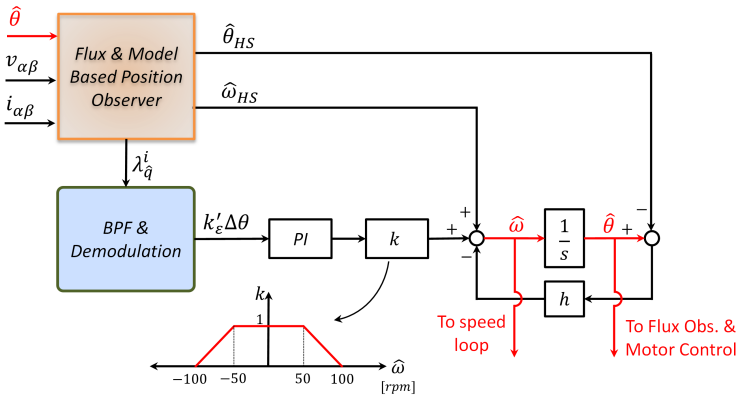

Figure 4.16: Block scheme of the fusion structure combining model based and saliency based position estimation.

The gain $k(\hat{\omega})$ is responsible of progressively switching on and off the contribution of the saliency based algorithm to the rotor position estimate. Such gain is equal to 1 when the mechanical speed is lower than 100 rpm and it is linearly decreased to 0 between 50 and 100 rpm. Above such speed range, the PI output is dropped out completely. In this situation, the fusion structure acts as a PLL for the model based position observer.

These speed boundaries were efficaciously adopted in [9, 10], where a full speed range was achieved. Anyway, different tuning may be necessary depending on the application. All tuning aspects will be addressed in Section 4.6, including the PI bandwidth and the gains k and h. As will be better explained in Section 4.5, the amplitude if the injected HF voltage is also proportional to the gain $k(\hat{\omega})$, therefore it is switched off at high speed.

The feedback gain h in Figure 4.16 helps the smooth transition between the two position estimations, with and without the low speed branch. After manipulation, of the block diagram, $\hat{\theta}$ is obtained as

$$\hat{\theta} = G_{\mathrm{HF}} \cdot \theta + G_{\mathrm{HS}} \cdot \hat{\theta}^{\mathrm{HS}} \tag{4.51}$$

where G_{HF} and G_{HS} are the transfer function related to HF injection and model based position estimation respectively:

$$G_{\mathrm{HF}} = \frac{H}{H+1} \tag{4.52}$$

$$G_{\mathrm{HS}} = \frac{1}{H+1} \tag{4.53}$$

In this formulation, H is the open loop transfer function of the saliency based tracking loop:

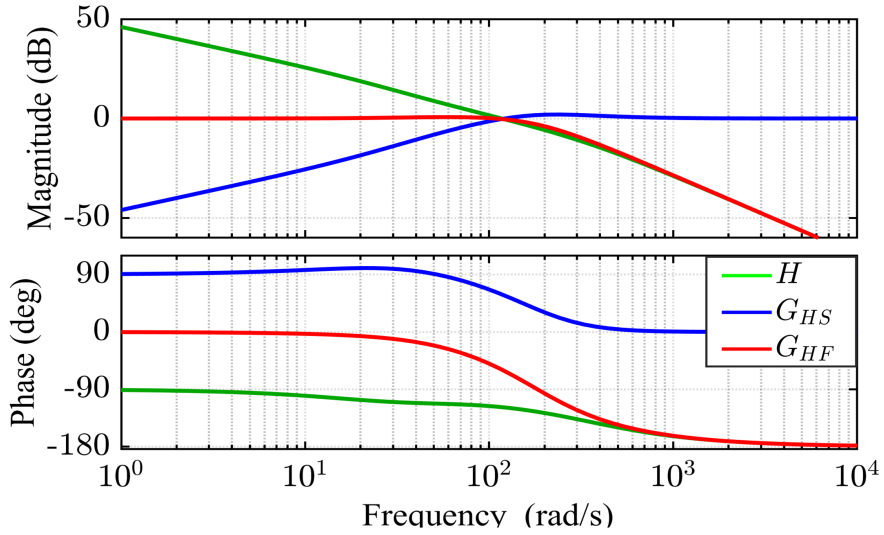

(a)

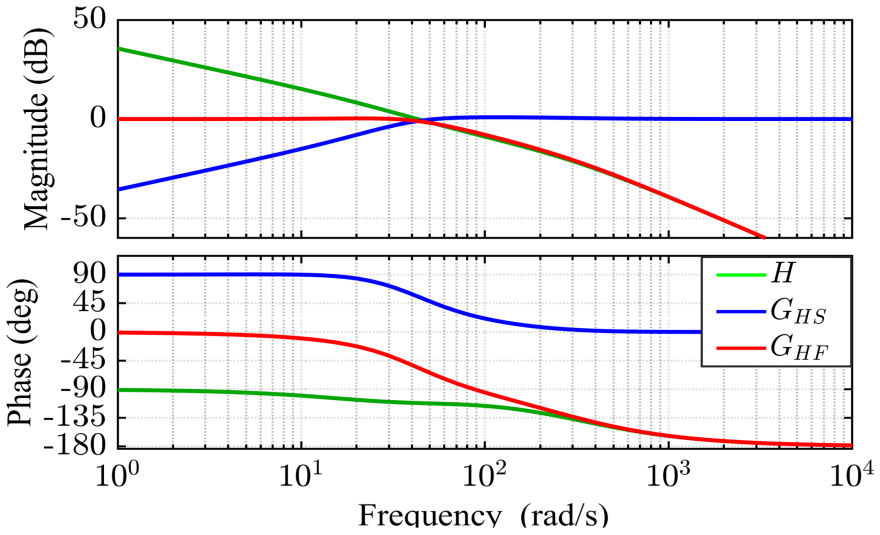

(b)

Figure 4.17: Bode diagram of the fusion structure for (a) $k = 1$ and (b) $k = 0.3$.

$$H = \frac{\omega_{\mathrm{f}}}{s + \omega_{\mathrm{f}}} \cdot k'_{\epsilon} \frac{k_{\mathrm{i,PLL}} + s k_{\mathrm{p,PLL}}}{s} \cdot k \cdot \frac{1}{s + h} \tag{4.54}$$

The Bode diagram of the two transfer functions G_{HF} and G_{HS} is reported in Figure 4.17(a), referring to the case $k = 1$ (rotor speed lower than 50 rpm, HF-injection activated) and setting $h = 25\ rad/s$. As can be seen, G_{HF} is lowpass filtered while G_{HS} is high-pass filtered, with a common cutoff

frequency (17 Hz with this tuning), corresponding to the crossover of H.

Although the HF injection is ON, the information coming from back-EMF position estimation (G_{HS} component) is yet covering the HF range of the Bode diagram, i.e., in case of mechanical transients. In the speed area between 50 and 100 rpm the gain k progressively decreases to zero, shifting down the open-loop $|H|$ diagram, and so shifting backwards the crossover between the high and low speed models.

As an example, Figure 4.17(b) shows the Bode diagrams at 85 rpm, when $k = 0.3$. At this speed, the cross-over frequency is decreased to 7 Hz. When the speed goes beyond 100 rpm ($k = 0$), the HF injection is dropped out completely. The crossover frequency vanishes, G_{HF} disappears from the diagram and G_{HS} diagram is equal to 0 dB in the whole frequency range. The position estimation is now purely model based.

4.5 Direct Flux Vector Control of SyRM

This Section describes the DFVC implemented on the SyR machine SR2kW2 in a wide speed range in [9, 10], to test the validity and robustness of both saliency based and model based approaches. The key equations of DFVC are report in Section 2.2.3 and not repeated here for brevity reasons. The block diagram of sensorless DFVC is illustrated in Figure 4.18. The fusion structure presented in Section 4.4 merges the saliency tracking based on HF voltage injection and flux demodulation (Section 4.2.3) with two alternative model based techniques, described in Sections 2.4.2 and 2.4.3.

The stator flux observer is the one shown in Figure 2.10. As can be seen, the low speed position is extracted by injecting HF voltage ($u_{\text{c}} \cos(\omega_{\text{c}} t)$) to the estimated rotor $\hat{d}$ axis and the HF flux component coming from current model $\lambda^{i}_{\hat{\text{q}}\text{h}}$ is demodulated. The gain k, the same parameter introduced in the fusion structure presented in Section 4.4, is intercalated in HF injection branch to switch ON and OFF the HF injection depending on the observed speed. As discussed in Section 2.3, the transfer function of flux observer is expressed in Laplace domain is:

$$\hat{\boldsymbol{\lambda}}_{\alpha\beta} = \frac{s}{s+g}\left(\frac{\boldsymbol{v}_{\alpha\beta} - R_{\text{s}}\boldsymbol{i}_{\alpha\beta}}{s}\right) + \frac{g}{s+g}\boldsymbol{\lambda}^{i}_{\alpha\beta} \tag{4.55}$$

Based on this equation, the current is predominant at low speed, while voltage model overcomes for angular frequency higher than the observer gain g, set here to 35 rad/s. Therefore, the low speed region where flux estimation is based on the current model is approximately [0-50] rpm, in the range [50-500] rpm both current and voltage models contribute to flux observation

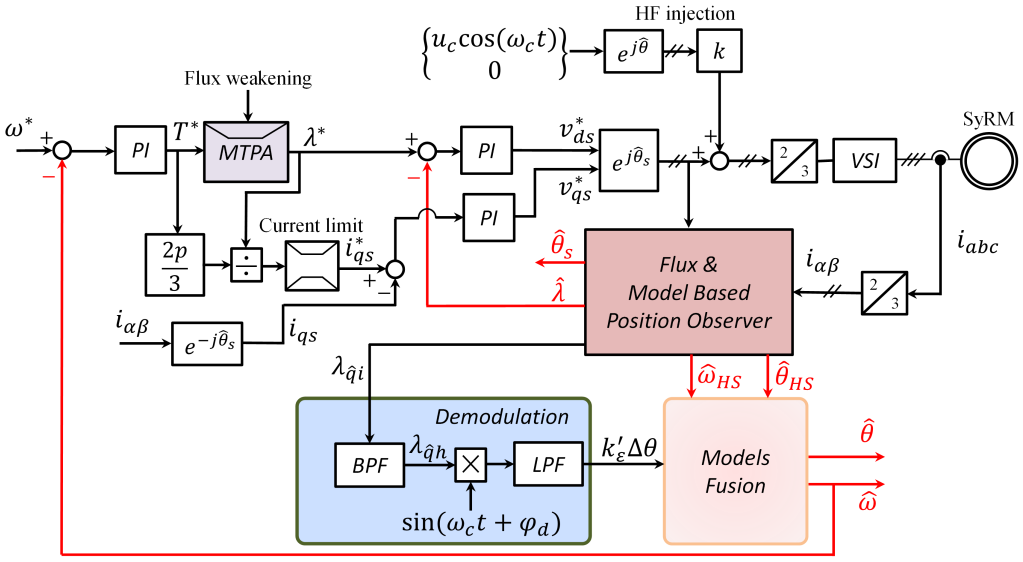

Figure 4.18: Block scheme of sensorless DFVC.

and above 500 rpm the back-EMF integration model takes over. The high frequency signal injection is progressively dropped out between 50 rpm and 100 rpm, as in Figure 4.16.

4.5.1 MTPA and Lower Flux Limit

Depending on T^*, the reference flux amplitude is set according to the MTPA law for the sake of copper loss minimization, thus maximizing the machine efficiency. The correlation between T^* and λ^* is shown in Figure 4.19.

The key obstacle in using MTPA for encoderless control of pure SyR motors is the zero torque, zero current condition. At zero torque reference, the MTPA law for a SyR machine would correspond to zero current ($i_\mathrm{d} = 0, i_\mathrm{q} = 0$). In DFVC, this would mean using zero flux amplitude for zero torque ($\lambda^* = 0$). However, in this condition the machine back-EMF would be canceled, thus harming flux and position estimations at high speed. Therefore, a minimum excitation flux must be guaranteed for the sake of back-EMF tracking also around zero torque. The minimum excitation level λ_min is highlighted in red in Figure 4.19. So, the flux reference follows the MTPA and it is lower saturated to λ_min. In addition, such minimum flux level is also necessary to guarantee a minimum level of saliency in zero torque conditions as explained in Section 4.2.7, so that the HF injection method can operate correctly. The flux lower limit guarantees rotor position tracking over the whole speed operating range. The tuning of the lower flux limit, which is set

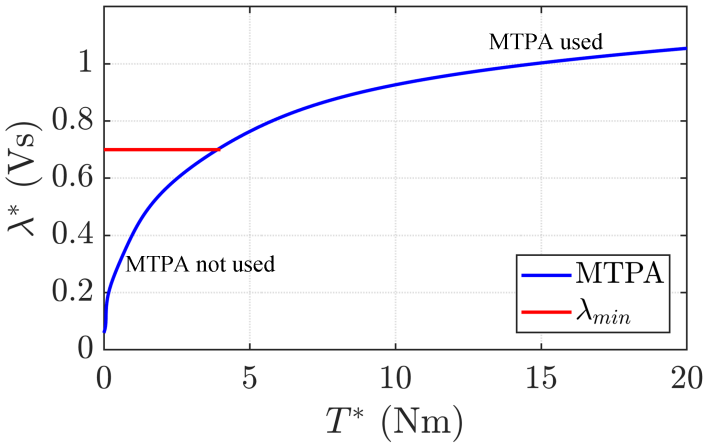

Figure 4.19: MTPA trajectory and lower flux limit. Motor: SR2kW2

here to $\lambda_{\min} = 0.7\ Vs$, will be better detailed in Section 4.6.

It is worth mentioning that PM synchronous motors do not suffer from the aforementioned problems, because the PM produce back EMF also at zero current, and because they do not present such saliency issue.

4.5.2 Current Limitation and Flux Weakening

The maximum stator current and voltage ($i_{\max}$ and $v_{\max}$), defined by inverter limitations[1], are taken into account in the block diagram of Figure 4.18. The current is kept below $i_{\max}$ by saturating the reference value in q_s axis:

$$|i_{qs}^*| \leq \sqrt{i_{\max}^2 - i_{ds}^2} \tag{4.56}$$

One of the main advantages of DFVC is the simplicity and accuracy in implementing flux weakening algorithm. The stator voltage can be kept lower than $v_{\max}$ by limiting the flux reference, depending on rotor speed:

$$\lambda^* \leq \frac{v_{\max} - R_s i_{qs} \cdot sign(\omega)}{|\omega|} \tag{4.57}$$

[1]For sake of precision, $v_{\max}$ is always defined based on inverter v_{dc} but in some applications $i_{\max}$ may be defined by the maximum overload current allowed by the motor to fulfill its thermal constrains. Anyway, this case is not common, since SyR machines are usually designed for high overload capability while the inverter is rarely oversized.

4.5.3 Effect of HF Injection on the Observed Flux

At low speed, the measured current $\boldsymbol{i}_{\alpha\beta}$ contains the HF component due to voltage injection. However, the current is not LPF when used for control or flux estimation purposes. Looking at the flux observer scheme in Figure 2.12 and 2.14 and its corresponding equation in Laplace domain (4.55), the flux observer is a high-pass filter for the back-EMF signals, and a low-pass filter with cutoff frequency g for the current-model-based flux estimate. Therefore, the impact of HF noise of the observer's input $\boldsymbol{i}_{\alpha\beta}$ on the back-EMF term is minor, because limited to the compensation of resistive voltage drop, and it is inherently LPF in the current model branch of the observer.

The other observer's input is the reference voltage $\boldsymbol{v}^*_{\alpha\beta}$, that is sampled before HF injection, as evidenced in Figure 4.18 and therefore immune from HF component. As a consequence, $\hat{\boldsymbol{\lambda}}_{\alpha\beta}$ is not affected by HF distortion.

4.6 Tuning Criteria and Auto-Tuning

This Section describes a feasible tuning procedure for the full speed sensorless control report in Section 4.5. Stability constrains are highlighted, together with suggested and typical parameters values. The following subsections, pursued step by step, permit to automatically tune the sensorless control based only on the machine flux maps and hardware limitations, e.g. switching frequency and accuracy of current measurement. Therefore, combining this auto-tuning with the self commissioning procedure described in Chapter 3, a plug-in control strategy is effectively reached.

4.6.1 Amplitude and Frequency of Injected Signal

The necessary condition related to the HF voltage injection is that the HF current component must be sufficiently high to be accurately detected by the available current sensors, thus allowing reliable demodulated signal for the position tracking loop. Anyway, the HF current produces torque oscillations, which amplitude grows together with the magnitude of the injected current. Figure 4.20 gives a visual representation of the current movement on the dq plane due to HF component and the torque variation for three given working point ($T = 0.5$ pu, $T = 1$ pu and $T = 1.5$ pu).

In this respect, amplitude and frequency of the injected HF voltage u_c and ω_c should be set in order to obtain the desired HF current, with a trade-off solution considering several constrains. Higher ω_c leads to better decoupling between HF and fundamental current components, therefore the demodulation process can be easier and more accurate. Moreover, the introduced

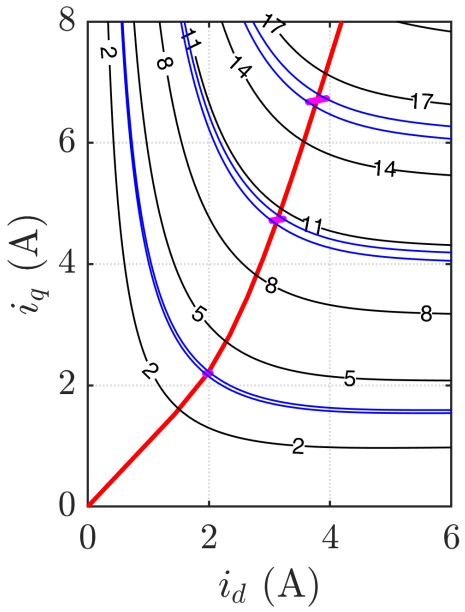

Figure 4.20: Torque ripple introduced by HF injection for the DFVC presented in Section 4.7. Black: torque contour. Red: MTPA. Blue: maximum and minimum torque due to HF component for three given working points. Violet: current movement.

torque ripple is better filtered by the mechanical inertia, thus not producing significant speed oscillations. Unfortunately, for a given amplitude of HF current the amplitude of u_c grows proportionally to ω_c, according to (4.58). Therefore, depending on the motor inductance, a high ω_c may require a too high u_c, thus strongly limiting the fundamental voltage component available for motor control.

$$|i_{dh}| \approx \frac{u_c}{l_d \omega_c} \tag{4.58}$$

For digital implementation of the sensorless control, it is appropriate that the number of samples per period of the HF component is an integer number, which means the switching frequency f_{sw} must be a multiple of the HF injection frequency:

$$f_{sw} = n_c f_c \tag{4.59}$$

where n_c is an integer number. Usually, n_c is imposed to be an even number for the sake of reducing some of the introduced harmonic components. Other limitations may apply depending on the application. For example,

in low cost applications such as washing machines or pumps, the available controller may have limited computational and memory storage capability. In this case, the sine of the HF angle is usually obtained from a look-up-table instead of online computed. Considering (4.59), the HF angle always drops in the same position at every HF cycle, therefore also $\sin(\omega_c t)$ has a limited number of values which can be stored in a vector, further reducing the computational effort. In this case, it is convenient that n_c should be a multiple of 4, so that one quarter only of the sine function can be stored, exploiting the sine symmetry and reducing the size of such vector. Another issue that may apply in specific applications, especially home appliances, is that the introduced vibration should be out of the audible frequency, in order to avoid audible noise. Typical values for n_c are 12, 16 and 24.

Considering all these issues, ω_c is usually chosen first, and then u_c is set in order to achieve the desired HF current depending on the machine differential inductance. In the DFVC presented in [9, 10], the values of $u_c = 50\ V$ and $\omega_c = 833\ Hz$ (corresponding to $n_c = 12$ with $f_{sw} = 10\ kHz$) were chosen.

4.6.2 Selection of the Minimum Excitation Flux

Dealing with SyR motors, the flux is null in absence of current. Therefore, at high speed a minimum flux excitation is required to guarantee sufficient back-EMF for position tracking even at no-load. In this case, the amplitude of the minimum flux is not relevantly affecting the position estimation robustness, as long as the back-EMF can be accurately detected.

In low speed range the calibration of λ_{min} is much more critical, since it has to guarantee feasible position estimation at no load. As demonstrated in Section 4.2.7, the local machine saliency drops at low i_q due to unsaturated structural ribs. In particular, the machine is almost isotropic in the origin, and the saliency is reversed along the d axis for sufficiently high i_d. In this latter case, the saturation of d axis leads to a low l_d while l_q is still high due to unsaturated ribs, therefore $l_d < l_q$. In between these two unstable regions, an optimal solution has to be found.

Starting from the origin of the dq plane, increasing i_d leads to higher λ_d and possible saturation of the d axes, but also partial saturation of the ribs due to cross-saturation effect. The ribs saturation becomes more relevant when increasing i_d. The optimal solution for minimum flux limit, corresponding to highest possible saliency at no load, is when i_d is high enough to sufficiently saturate the ribs but without saturating the d axis, in order to maintain a high l_d. This point corresponds to the current slightly lower than the saturation knee on the $\lambda_d(i_d)$ curve. In particular, for the motor SR2kW2 the optimum minimum flux resulted $\lambda_{min} = 0.7\ Vs$, roughly corresponding

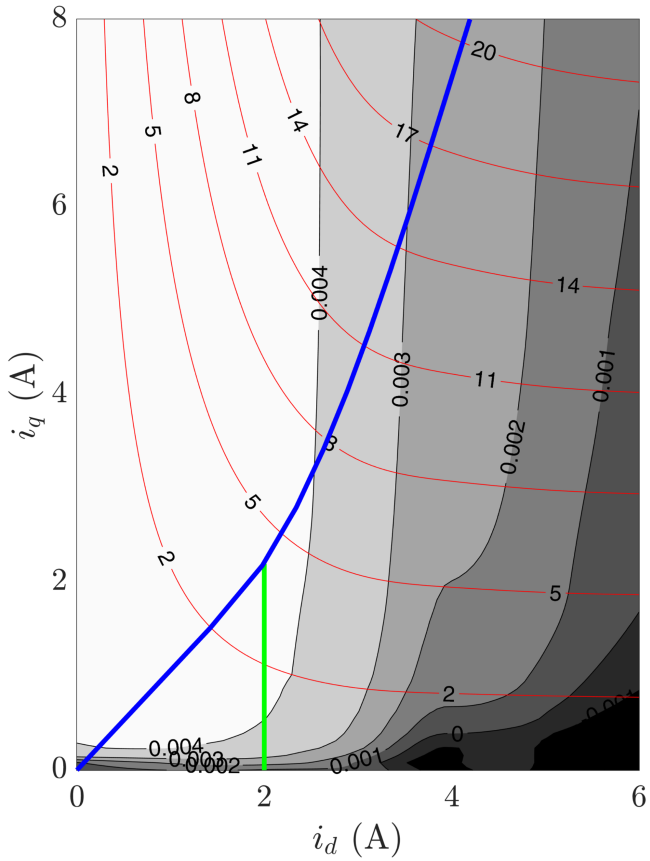

Figure 4.21: Black: Contour of k'_ϵ in the $i_\mathrm{d}, i_\mathrm{q}$ plane. Blue: MTPA trajectory. Green: minimum flux limit (0.7 Vs). Red: torque contours (Nm).

to $i_\mathrm{d} = 2\ A$. This minimum flux limit is represented as a vertical black line in Figure 4.7. As can be seen, the black line falls inside the green area of stability. The choice of a lower flux (i.e. $i_\mathrm{d} < 2\ A$) would shift the vertical black line closer to the instability area in the origin of the plane. Similarly, if a higher λ_min was chosen, the black line might have fallen into the instability region to the right end side of the plane.

An alternative way to evaluate the calibration of λ_min is to compute the amplitude of k'_ϵ as a function of $i_\mathrm{d}, i_\mathrm{q}$ according to (4.22), using the machine flux maps. As said, the magnitude of k'_ϵ is strictly related to the signal-to-noise ratio of the HF demodulated signal: high k'_ϵ leads to robust position estimation while negative k'_ϵ corresponds to instability. The map of k'_ϵ is reported in Figure 4.21 for the motor under test (SR2kW2) considering $\omega_\mathrm{c} = 833\ Hz$ and $u_\mathrm{c} = 50\ V$. As expected, the critical area is around $i_\mathrm{q} = 0$ (i.e. zero torque), where k'_ϵ tends to vanish and even to become negative. Anyway,

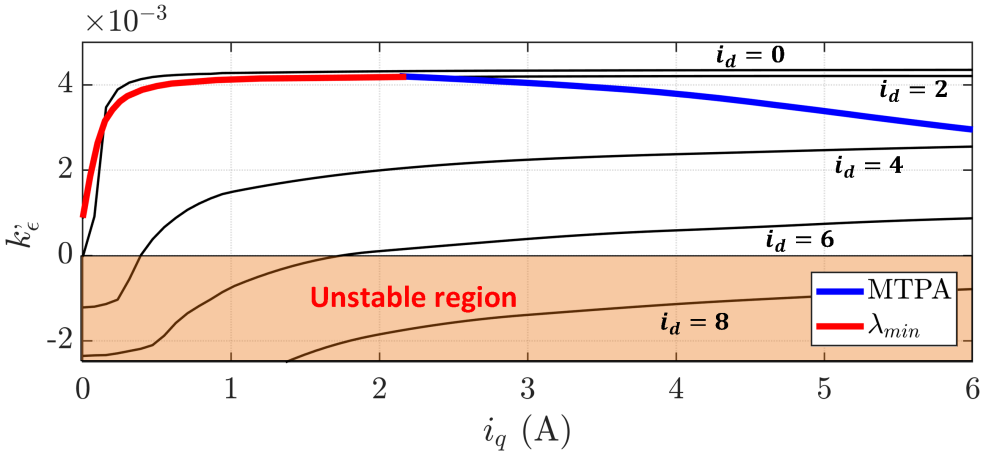

Figure 4.22: Value of k'_ϵ as a function of i_q calculated for different values of i_d. The highlighted line corresponds to MTPA (blue) and minimum flux limit (red).

the choice of $\lambda_\mathrm{min} = 0.7\ Vs$ always guarantees $k'_\epsilon > 0$ and therefore stable position observation even at no load.

Finally, Figure 4.22 reports the amplitude of $k'_\epsilon(i_\mathrm{q})$ for different values of i_d. As can be seen, with the adopted tuning k'_ϵ spans between 1 and 4 mVs. So, the PLL is always stable and the position estimation bandwidth varies in a limited range, with constant PI parameters, according to (4.62). If the λ_min limitation was not imposed, thus following MTPA trajectory until zero torque, the value of k'_ϵ would significantly drop, thus arming the accuracy of position tracking. Conversely, the red line representing k'_ϵ for $i_\mathrm{d} = 2$ is always above zero, meaning that the rotor position can be always estimated using saliency tracking. This is why below a certain reference torque, the condition $i_\mathrm{d} = 2\ A$ (i.e. $\lambda^* = 0.7\ Vs$) is used instead of the MPTA. As an example, choosing $i_\mathrm{d} = 4\ A$ or more would lead k'_ϵ gain to negative values.

This minimum excitation condition corresponds to circa 70% of rated flux linkage, so it is a significant level of excitation for guaranteeing that also the back-EMF-based part of the flux and position observer can properly work.

4.6.3 Calibration of PLL and Tracking Loop

Saliency based and model based position estimation techniques are merged together using the fusion structure described in Section 4.4. Anyway, for tuning purposes it is convenient to study the two systems separately. At first, the saliency based tracking loop is calibrated as if it was working alone, neglecting the influence of model based position estimation in the fusion

structure ($k = 1$, $h = 0$), to define the LPF cut-off frequency and $k_{\mathrm{p,PLL}}$ and $k_{\mathrm{i,PLL}}$ gains. The dynamic of demodulation process and PLL are tuned based on the equivalent scheme report in Figure 4.5. Then, the whole structure of Figure 4.16 is considered to tune the gain h and the speed thresholds for k.

At first, the cut-off frequency of the demodulation LPF ω_{f} is determined. This LPF is necessary to remove the HF component from the demodulation feedback signal, as explained in Section 4.2.6. From (4.24), the HF component that have to be filtered out is at twice the frequency of the injected signal. In order to properly filter it, the cut-off frequency of the LPF has to be at least 10 times lower than such component, so:

$$\omega_{\mathrm{f}} < \frac{1}{5} \cdot \omega_{\mathrm{c}} \tag{4.60}$$

Eventual noise introduced in the system, e.g. from inaccurate current transducers, may further limit ω_{f}. Once determined ω_{f}, it is possible to choose an appropriate bandwidth $\omega_{\mathrm{b},\theta}$ for the position tracking loop. This bandwidth is given by the cross-over of the open loop transfer function between real and estimated rotor position:

$$H = k'_{\epsilon} \frac{\omega_{\mathrm{f}}}{s + \omega_{\mathrm{f}}} \cdot \frac{s k_{\mathrm{p,PLL}} + k_{\mathrm{i,PLL}}}{s} \cdot \frac{1}{s} \tag{4.61}$$

By neglecting the integrative gain, the bandwidth $\omega_{\mathrm{b},\theta}$ is given by:

$$\omega_{\mathrm{b},\theta} = k'_{\epsilon} k_{\mathrm{p,PLL}} \ll \omega_{\mathrm{f}} \tag{4.62}$$

where $k_{\mathrm{p,PLL}}$ is the proportional gain of the PLL. Therefore, once estimated k'_{ϵ} from (4.22) and the flux maps[2], the magnitude of $k_{\mathrm{p,PLL}}$ is chosen in order to obtain the desired $\omega_{\mathrm{b},\theta}$. For a fixed $k_{\mathrm{p,PLL}}$, the variation of k'_{ϵ} with the working point in the dq plane, described in Figure 4.21, produces a non-constant bandwidth of the tracking loop. It means the convergence time of saliency based position estimation varies with the applied torque. For precautionary tuning, it is appropriate that the condition $\omega_{\mathrm{b},\theta} \ll \omega_{\mathrm{f}}$ applies in the most demanding conditions, characterized by the maximum k'_{ϵ}, i.e. at medium load (see Figure 4.22). This approach gives stable control, but it may decrease the performance at high load. A feasible alternative is to adapt the $k_{\mathrm{p,PLL}}$ gain depending on the reference torque, in order to obtain a constant bandwidth. Anyway in this case the dynamic of $k_{\mathrm{p,PLL}}$ variation may interfere with the position tracking, introducing additional noise.

[2]Equation (4.22) also requires the amplitude and frequency of the injected voltage, that were determined according to Section 4.6.1.

The integrative part of the PI regulator introduces a zero in the transfer function. For obtaining a phase margin larger than 45°, such zero must be placed at a frequency lower than the bandwidth, therefore:

$$\begin{aligned} \frac{k_{\mathrm{i,PLL}}}{k_{\mathrm{p,PLL}}} &< \omega_{\mathrm{b},\theta} \\ k_{\mathrm{i,PLL}} &< k'_{\epsilon}\omega^2_{\mathrm{b},\theta} \end{aligned} \tag{4.63}$$

A reasonable tuning criteria is to set $\frac{k_{\mathrm{i,PLL}}}{k_{\mathrm{p,PLL}}} = (0.1 \div 0.5) \cdot \omega_{\mathrm{b}}$. If the LPF is neglected (as said, its cut-off frequency must be sufficiently out of bandwidth), the closed loop transfer function between θ and $\hat{\theta}$ is:

$$\frac{\hat{\theta}}{\theta} = \frac{sk'_{\epsilon}k_{\mathrm{p,PLL}} + k'_{\epsilon}k_{\mathrm{i,PLL}}}{s^2 + sk'_{\epsilon}k_{\mathrm{p,PLL}} + k'_{\epsilon}k_{\mathrm{i,PLL}}} \tag{4.64}$$

So, a further limitation of $k_{\mathrm{i,PLL}}$ applies if non-imaginary poles are desired:

$$\frac{k_{\mathrm{i,PLL}}}{k_{\mathrm{p,PLL}}} \leq \frac{k'_{\epsilon}k_{\mathrm{p,PLL}}}{4} \tag{4.65}$$

At this point, it is possible to tune the remaining parameters considering the fusion structure of Figure 4.16. Thanks to this scheme, the bandwidth of the position tracking is considerably increased. From (4.52),(4.53),(4.54) it can be seen that the feedback branch $h(\hat{\theta} - \hat{\theta}^{\mathrm{HS}})$ replaces the pure integrator with a pole in the open loop transfer function H. Therefore, the tuning of the parameter h influences the bode diagram of G_{HF} and G_{HS} for frequencies lower than h, while higher frequencies are not considerably affected. In order to avoid any influence of this pole to the phase margin of G_{HF}, h should be lower than the bandwidth of the saliency based tracking loop:

$$h \leq k'_{\epsilon}k_{\mathrm{p,PLL}} \tag{4.66}$$

The last parameter that has to be tuned is the threshold speed for the smooth transition between low and high speed, defined by the parameter k. The adopted criteria is that the contribution of the saliency based tracking loop must be dropped for an electrical speed sufficiently lower (e.g. one third) than $\omega_{\mathrm{b},\theta}$. As an example, in [9,10] the gain k (and so the HF injection branch in the fusion structure) is completely dropped to zero when the mechanical speed is 100 rpm, corresponding to an electrical pulsation of 20.9 rad/s, while, taking into account the variability of k'_{ϵ}, the bandwidth of the saliency based tracking loop is bounded between 60 and 100 rad/s.

Finally, in the PLL structure adopted in Figure 4.4 the observed speed $\hat{\omega}$ is directly obtained from the integral of $\hat{\theta}$, therefore the dynamic of speed estimation is the same as for position tracking. In [13] the PLL for injectionless low speed control was slightly modified, extracting $\hat{\omega}$ from the integrative branch of the PI regulator instead of the total PI output (integrator plus proportional contributions). Unlike the HF injection scheme, the bandwidth of the position observer is not anymore limited by the demodulation LPF. In this scheme, the transfer function between θ and $\hat{\theta}$ is the same as (4.64), but the dynamic of speed estimation is given in Laplace domain by:

$$\frac{\hat{\omega}}{\omega} = \frac{k'_\epsilon k_{\mathrm{i,PLL}}}{s^2 + s k'_\epsilon k_{\mathrm{p,PLL}} + k'_\epsilon k_{\mathrm{i,PLL}}} \tag{4.67}$$

The poles of such transfer function are the same as in (4.64), so the same condition (4.65) applies to avoid imaginary poles in the speed observation. From trivial manipulation of (4.67) the bandwidth of speed estimation is mostly determined by the $k_{\mathrm{i,PLL}}$ gain.

4.6.4 Tuning of Control PI Regulators

Last, the PI regulators of the DFVC scheme report in Figure 4.18 must be tuned. The bandwidth of the speed loop $\omega_{b,\omega}$ should be lower than the one of the speed observer defined in the previous Section. In this way, the PLL is able to correctly track the speed variations. Representing the mechanical load as a pure inertial system, $\omega_{b,\omega}$ is approximately given by:

$$\omega_{b,\omega} = \frac{k_{p,\omega}}{J} \tag{4.68}$$

where J is the total mechanical inertia. This relation can be used to tune $k_{p,\omega}$. The zero introduced by the PI speed regulator must be sufficiently lower than the bandwidth, so:

$$k_{i,\omega} < k_{p,\omega}\omega_{b,\omega} \tag{4.69}$$

Thanks to the DFVC scheme, the tuning of PI regulator controlling the flux amplitude is completely independent from the motor parameters [26] and only depends on the adopted inverter characteristics. Also in this case, the proportional gain is calibrated to define the loop bandwidth, which must be higher than $\omega_{b,\omega}$, while the integral gain must place so that the introduced zero is lower than this bandwidth. Finally, the PI regulator controlling i_{qs} is calibrated to obtain approximately the same bandwidth of the flux control.

4.7 Experimental Results

Several of the control strategies described in the previous Sections of this Chapter were experimentally implemented on SyR motors, to prove their validity and robustness and to compare the different solutions. Figure 4.23 shows the experimental set-up, which is the same that has been used in Chapter 3. The tests have been performed using dSpace 1103 PPC controller board and IGBT-based 2 level inverter. If not differently specified in dedicated sub-sections, the main hardware parameters are collected in Table 4.1.

Table 4.1: Characteristics of experimental test bench.

f_{sw}	10	kHz
v_{dc}	560	V
Rated dead-time	3	μs
Maximum current	40	A

Figure 4.23: Experimental test bench for sensorless control of SyRM. Highlighted in red rectangles: motor under test and power electronic converter.

4.7.1 Combined Observer Based and HF Voltage Injection with Flux Demodulation

Sensorless DFVC was experimentally implemented combining the HF voltage injection with flux demodulation (Section 4.2.3) with observer based high speed model as in Section 2.4.2. The control scheme is described in Figure 4.18, while the picture in Figure 4.23 shows the experimental set-up. The adopted motor is the SyR machine SR2kW2, the same used as reference in Chapter 3.

According to the auto-tuning procedure proposed in Section 4.6 and considering the hardware limitations, the control was tuned as in Table 4.2[3].

4.7.1.1 Torque Step Response

At first, the torque dynamic at low speed was tested. In this test, the motor is torque controlled and positive and negative step of reference torque are applied at standstill (Figure 4.24) and 50 rpm (Figure 4.25). The speed is imposed by an external speed controlled drive. For both the Figures, the subplot (a) reports the test result for positive torque step of 12 Nm while in (b) the applied torque is negative (-12 Nm). It can be seen that for both torque polarities and speeds under test, the position estimation error is close

[3]The variability of $\omega_{\mathrm{b},\theta}$ is due to the variability of k'_ϵ with the applied torque.

Table 4.2: Tuning parameters for sensorless DFVC.

f_{sw}	10	kHz
ω_{c}	833	Hz
n_{c}	12	–
u_{c}	50	V
λ_{min}	0.7	Vs
ω_{f}	50	Hz
$k_{\mathrm{p,PLL}}$	30000	$rad/(Vs^2)$
$k_{\mathrm{i,PLL}}$	125000	$rad^2/(Vs^3)$
$\omega_{\mathrm{b},\theta}$	60÷100	rad/s
h	25	rad/s

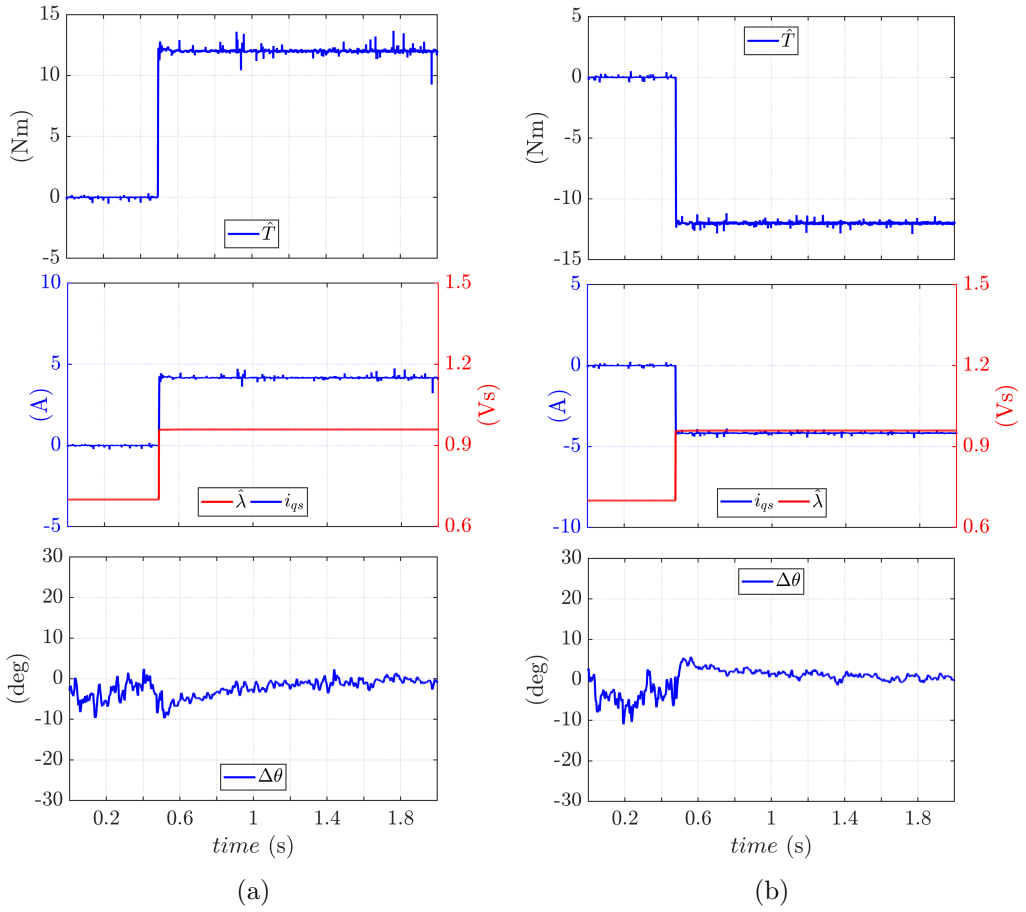

Figure 4.24: Torque control at standstill with ±12 Nm step torque. (a) positive torque; (b) negative torque. From top to bottom: observed torque, i_{qs} and observed flux amplitude, position error.

to zero. It can also be noted that the performance of the position tracking is symmetrical respect to the polarity of the torque.

4.7.1.2 Zero Cross-Saturation Error

As proved mathematically in Section 4.2.3, the demodulation process of the $\lambda^i_{\hat{q}h}$ signal instead of i_{qh} overcomes the cross-saturation effect in HF-based position estimation. This is experimentally proven in Figure 4.26(a), where the motor under test was torque controlled with a slow triangular reference T^* bounded between 0 and 14 Nm. Also in this case, the speed was forced to zero by the load drive. During this test, it has not been possible to measure the real applied torque due to experimental limitations, therefore

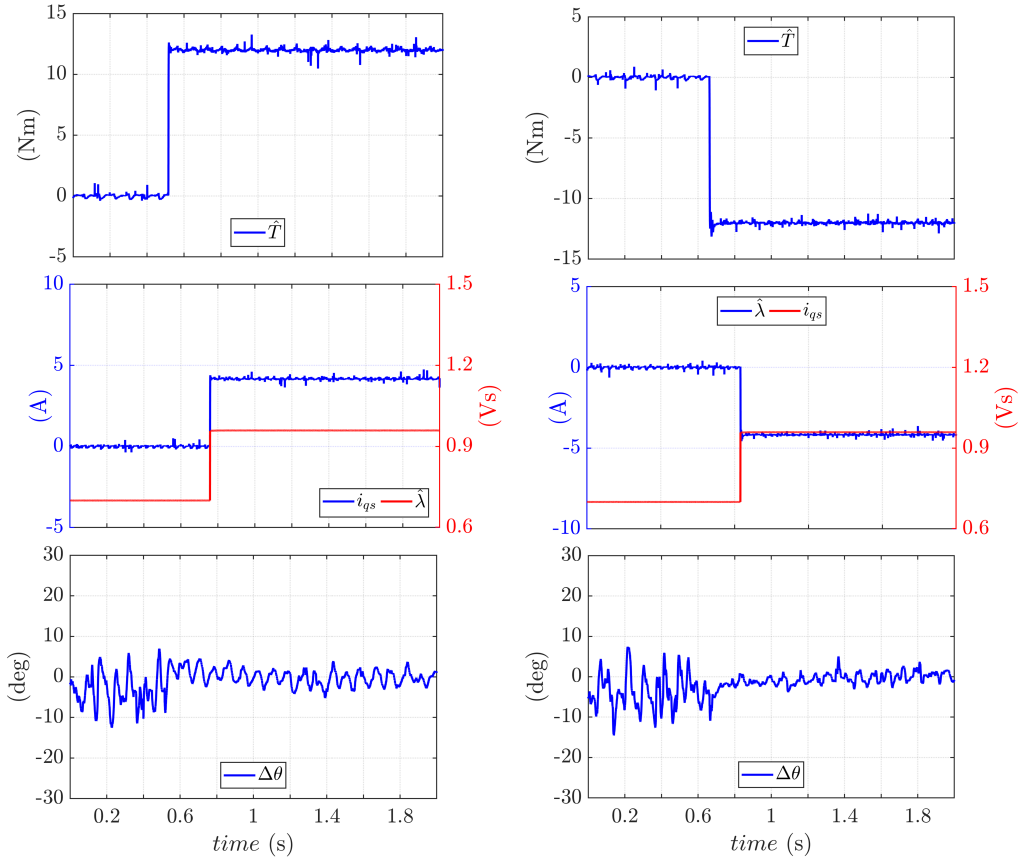

Figure 4.25: Torque control at 50 rpm with ±12 Nm step torque. (a) positive torque; (b) negative torque. From top to bottom: observed torque, i_{qs} and observed flux amplitude, position error.

the estimated torque only is plotted. As seen, the position estimation error is close to zero at every torque values.

For comparison purposes, the test has been repeated using a demodulation process based on i_{qh} (Figure 4.26(b)). The position estimation error moves almost proportionally with the torque, unless model-based compensation is added to the position tracking process, as done e.g. in [37, 105].

It should be noted that the torque and flux waveforms shown in Figure 4.26 are the observed quantities. Since these tests were performed in torque control mode, in both tests the same profiles of the references $\left(\lambda^*, i^*_{\mathrm{qs}}\right)$ were imposed and consequently the PI regulators force the feedbacks $\left(\hat{\lambda}, i_{\mathrm{qs}}\right)$ to follow the respective references. Therefore, the two tests seem to deliver

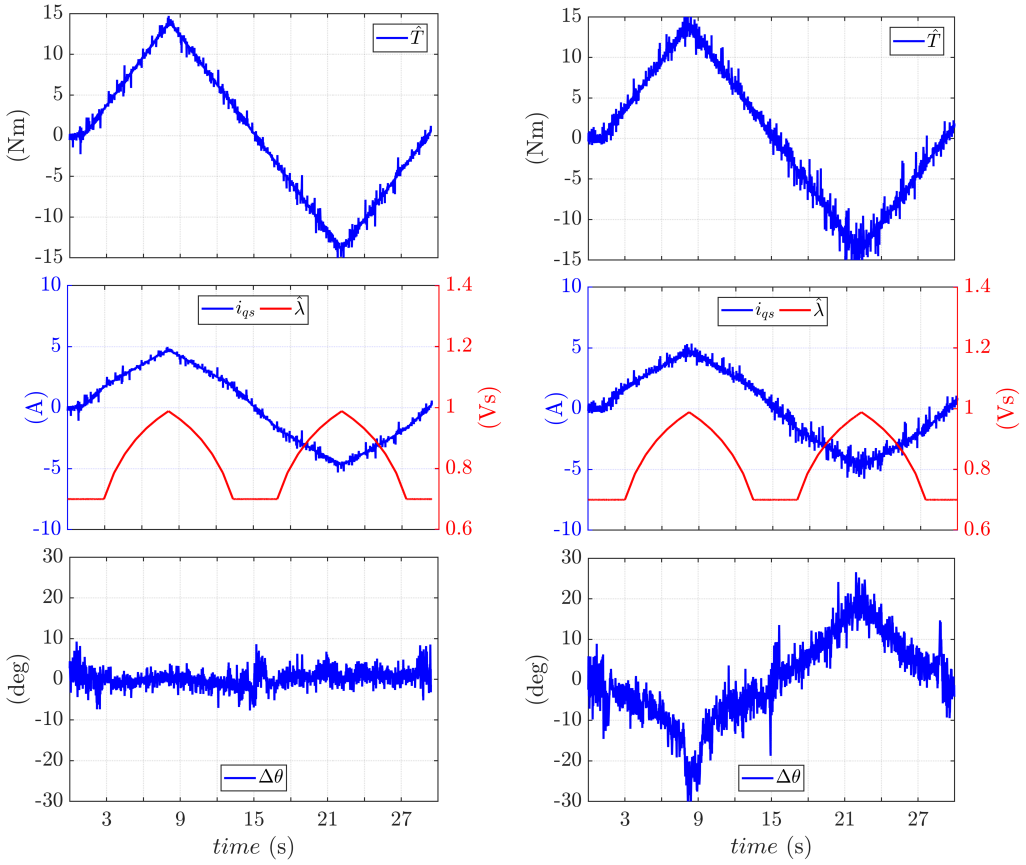

Figure 4.26: Torque control at standstill with T^* ramp-wise increased up to 14 Nm. The HF demodulated signal is (a) $\lambda^i_{\hat{\mathrm{qh}}}$, (b) i_{qh}.

the same torque, despite the non-negligible position error in Figure 4.26(b).

Anyway, the torque estimate in Figure 4.26(a) is reasonably correct, since the position error is negligible and so the flux observer works properly, while actual torque values are different from estimated ones in the test of Figure 4.26(b), characterized by strong position error. These results are well in accordance with the predictions highlighted by the simulations in Section 4.2.4.

4.7.1.3 Speed Response to Load Steps at Standstill

The motor is speed controlled at standstill under 17 Nm load steps (121% of full load). Results are reported in Figure 4.27. As can be seen, load is

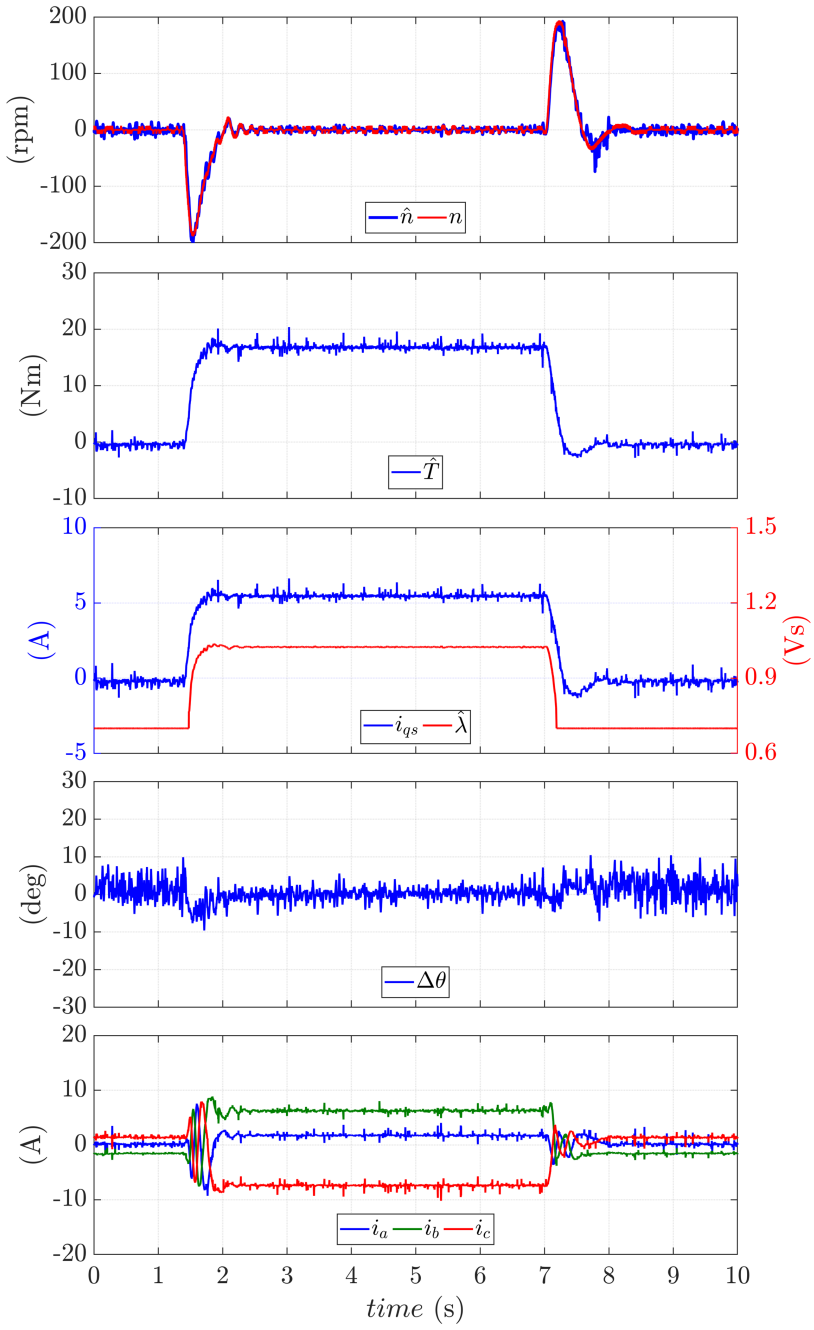

Figure 4.27: Drive performance in speed control at standstill under 17 Nm step load. From the top: estimated and measured mechanical speed, observed torque, i_{qs} and observed flux amplitude, position error, 3-phase currents.

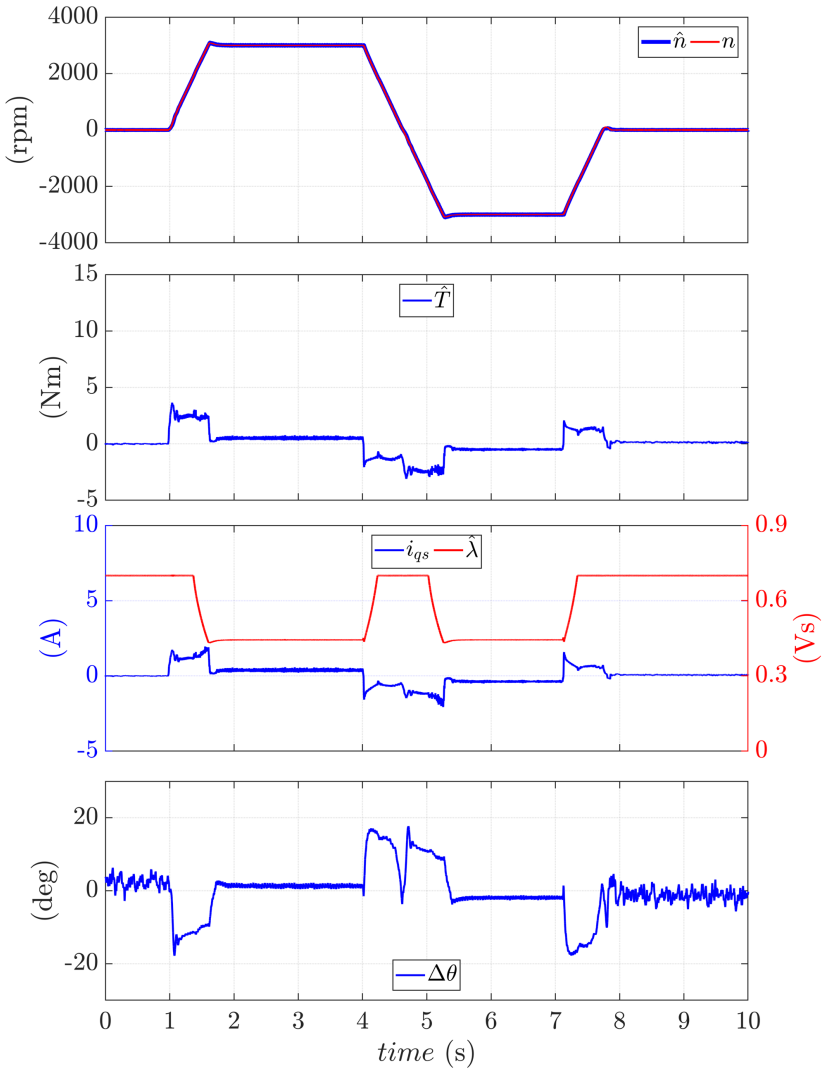

Figure 4.28: Drive performance in speed control from zero to 3000 rpm to -3000 rpm (flux weakening). From the top: estimated and measured mechanical speed, observed torque, i_{qs} and observed flux amplitude, position error.

applied to the motor at $t = 1.5\ s$ and released at $t = 7\ s$. The response of the system during transients and in steady state is acceptable and position estimation error is close to zero. Small position error is detected during the transient, but still bounded between $\pm 8°$.

4.7.1.4 Flux Weakening Operation

Figure 4.28 reports fast ramp responses from 0 to 3000 rpm and then speed reversal to -3000 rpm while the motor under test was speed controlled. As can be seen, flux kicks in around 2000 rpm. The position estimation error is close to zero in steady state and under control in transients, with a maximum overshoot of 16°. The transition between low and high speed range is proved to be smooth, with no discernible effects.

4.7.1.5 Speed Response to Sinusoidal Torque Disturbances

As a last test, the proposed sensorless speed control is tested by applying a sinusoidal torque disturbance having a frequency that progressively increases from 0 to 5 Hz, while the motor under test was in speed control mode. The reference speed was zero and the sinusoidal load has an amplitude of 50% rated load, superimposed to a constant load torque equal to another 50% of nominal one. Altogether, the load torque during the test oscillates from zero to full load.

The same test was repeated with and without the encoder (Figures 4.29 and 4.30, respectively), with the same tuning of the PI speed regulator, for the sake of performance comparison and validation of the sensorless technique. The speed and torque response of the drive to the torque disturbances is very similar in the two tests. In both cases, the observed torque follows the applied disturbance up to roughly 2.5 Hz with negligible position estimation error in the sensorless case thanks to the bandwidth of the sensorless control and the inherent compensation of the cross-saturation effect. After 2.5 Hz, the amplitude of the torque response tends to vanish, due to bandwidth limitations.

Negligible discrepancies are observed in the tests with and without encoder, proving the validity of the sensorless scheme. Anyway, it should be noted that in case of sensored control the tuning of the speed PI could be improved, thus obtaining slightly higher bandwidth.

4.7.2 Combined Active Flux and HF Voltage Injection with Flux Demodulation

This Section reports the experimental results related to the combination of active flux model based position estimation, as in Section 2.4.3, with the HF voltage injection and flux demodulation described in Section 4.2.3 for sensorless DFVC of SyR motor. Also in this case, the machine under test

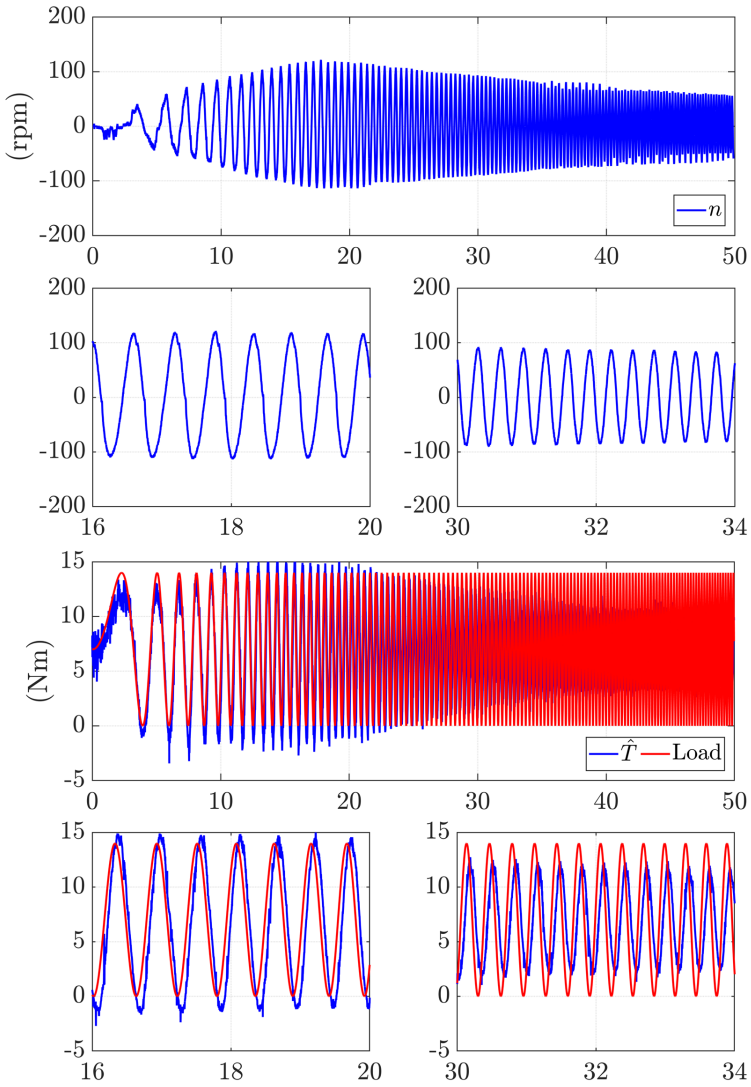

Figure 4.29: Motor response to torque disturbances in DFVC with encoder.

is SR2kW2. The low and high speed techniques are merged thanks to the fusion structure of Figure 4.16.

The same test bench and tuning parameters of the previous Section were adopted, as report in Table 4.2. Differently from most of the papers present in scientific literature [33], L_q is online calculated based on the flux maps and updated on varying the working point, as in Figure 2.14. Thanks to this expedient, the position estimation accuracy at high speed is considerably improved.

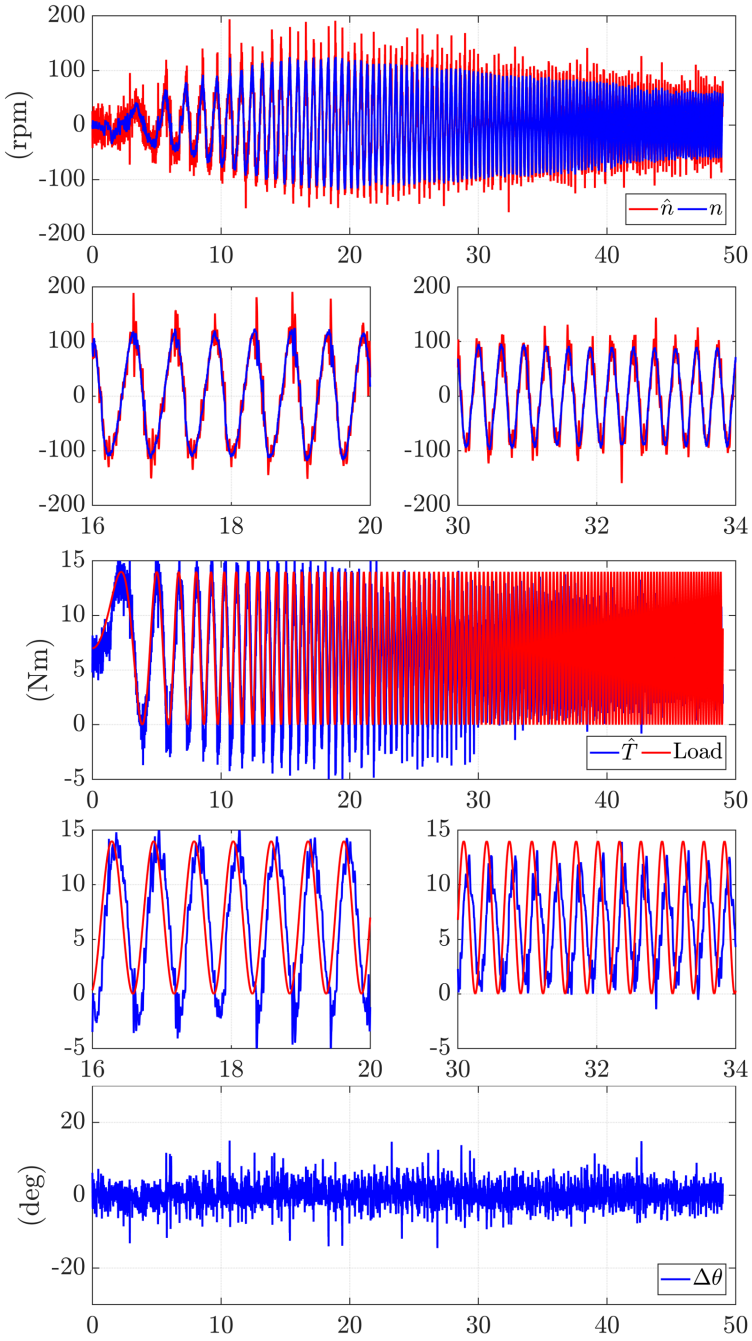

Figure 4.30: Motor response to torque disturbances in sensorless DFVC.

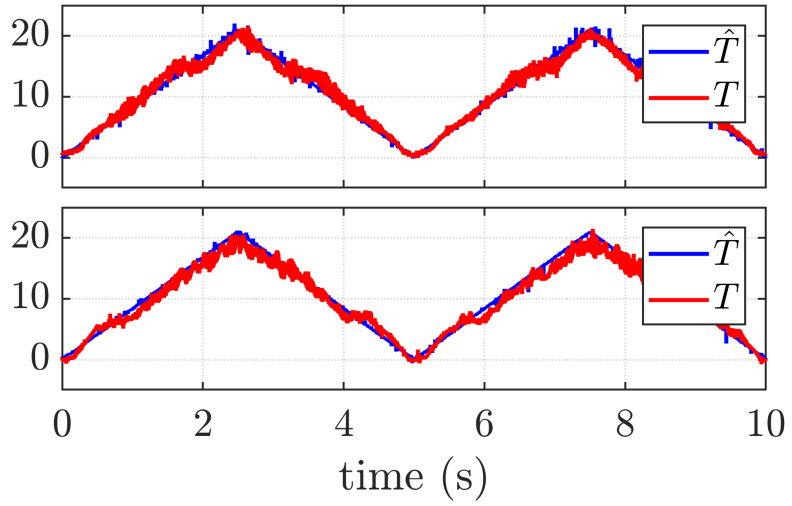

Figure 4.31: Sensorless torque control at standstill of the SyRM under test using the reference flux maps (upper) and the flux curves obtained from self commissioning (lower). Triangular torque reference up to 150 % of the rated torque. Blue: observed torque. Red: measured with torque meter.

4.7.2.1 Validation of Self-commissioning Test: Sensorless Torque Control of SyR

In this control scheme the flux maps are one of the key building blocks of the flux and position observer: at high speed for L_q adaptation depending on the working point, and even more important at zero and low speed operation for manipulating the HF signal.

To experimentally prove the validity of the magnetic characteristic obtained from standstill self-commissioning proposed in Section 3.3, the motor was torque controlled with a slow triangular torque reference up to 21 Nm (150 % of the rated value) while a driving machine imposed zero speed, which is the most demanding condition for sensorless position observers. The torque was accurately measured by HBM T40 torque meter mounted on the shaft between the motor under test and the speed controlled load. The test was repeated two times: at first using the reference flux maps and then using the saturation characteristics obtained from the self-commissioning augmented by HF injection.

The results are presented in Figure 4.31. As can be seen, in both cases the observed torque $\hat{T}$ strictly follows the reference T^*, as a consequence of the closed loop torque control. The correspondence between measured and

observed torque proves the accuracy of flux and position estimation. It can be noticed that the torque tests obtained with the two methods are strictly compatible, proving the validity of the self-identification technique.

As a last remark: the measured torque presets small irregularities at specific torque levels due to the slot-teeth interaction occurring at zero speed. Since the flux maps do not take into account slot harmonics, as common for sensorless control, the $\hat{T}$ cannot track this phenomenon, explaining the small deviation.

4.7.2.2 Response of Closed-Loop Speed Control

The performance of the drive at standstill is depicted in Figure 4.32. The motor under test is speed controlled with $\omega^* = 0$, while a 17 Nm load (121% of rated torque) is step-wise applied at $t = 1.2\ s$ and removed at $t = 8.2\ s$ using a torque controlled external auxiliary drive. Estimated and actual speed, estimated torque, current on q_s axis, observed flux, position estimation error, and three-phase currents are shown in this Figure.

As can be seen, the steady state position estimation error is negligible and dynamic response of the system is fairly good. Being at standstill, the steady state position estimation is extracted from the saliency based algorithm, while model based approach helps in improving the dynamic performances during transients.

Results of a similar test run at 300 rpm, again with 17 Nm step load, are presented in Figure 4.33. The position estimation at this speed is purely based on active flux concept.

Figure 4.34 shows the response to speed reference reversal in no-load condition, from +10 to -10 rpm. Again, the position estimation error is approximately zero and dynamic response of the system is acceptable. In addition, the speed estimation results accurate.

It should be commented that the residual noise on measured speed is due to the discretized position signal from encoder. The measured speed is calculated from the derivative of the position coming from a 512 cycles per revolution encoder and then LPF to reduce the quantization noise.

Nevertheless, the quantization of the position produces relevant noise, more evident at low speed. Moreover, the measured speed contains fourth harmonic probably due to rotor mechanical defects.

Estimated speed has the same noise components of measured speed, plus a sixth harmonic residual oscillation due to non perfectly compensation of inverter nonlinear errors.

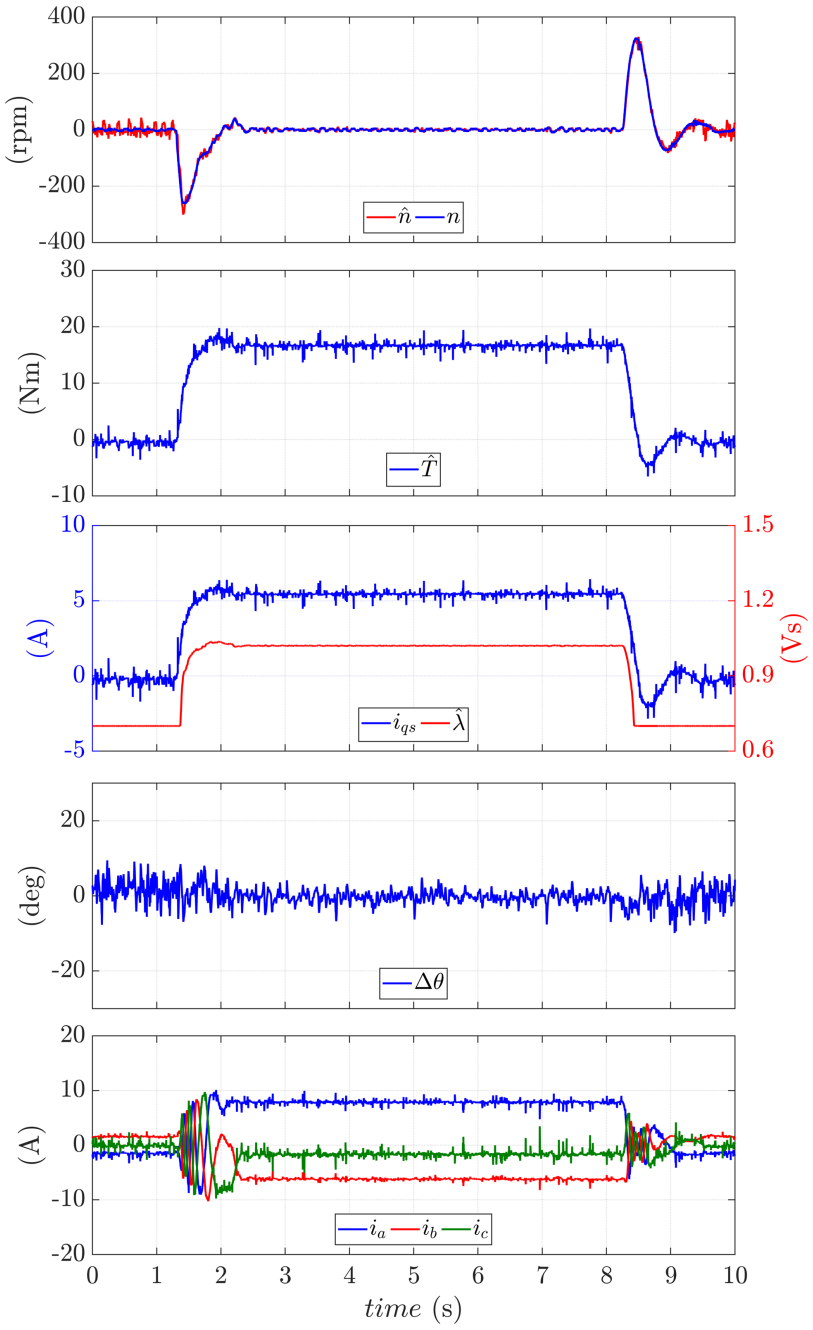

Figure 4.32: Load steps applied while the motor under test is speed controlled at standstill. The load goes from 0 to 17 Nm (121% of rated torque) and vice-versa. From top to bottom: measured and observed speed, observed torque, i_{qs} and observed flux, position error, three-phase currents.

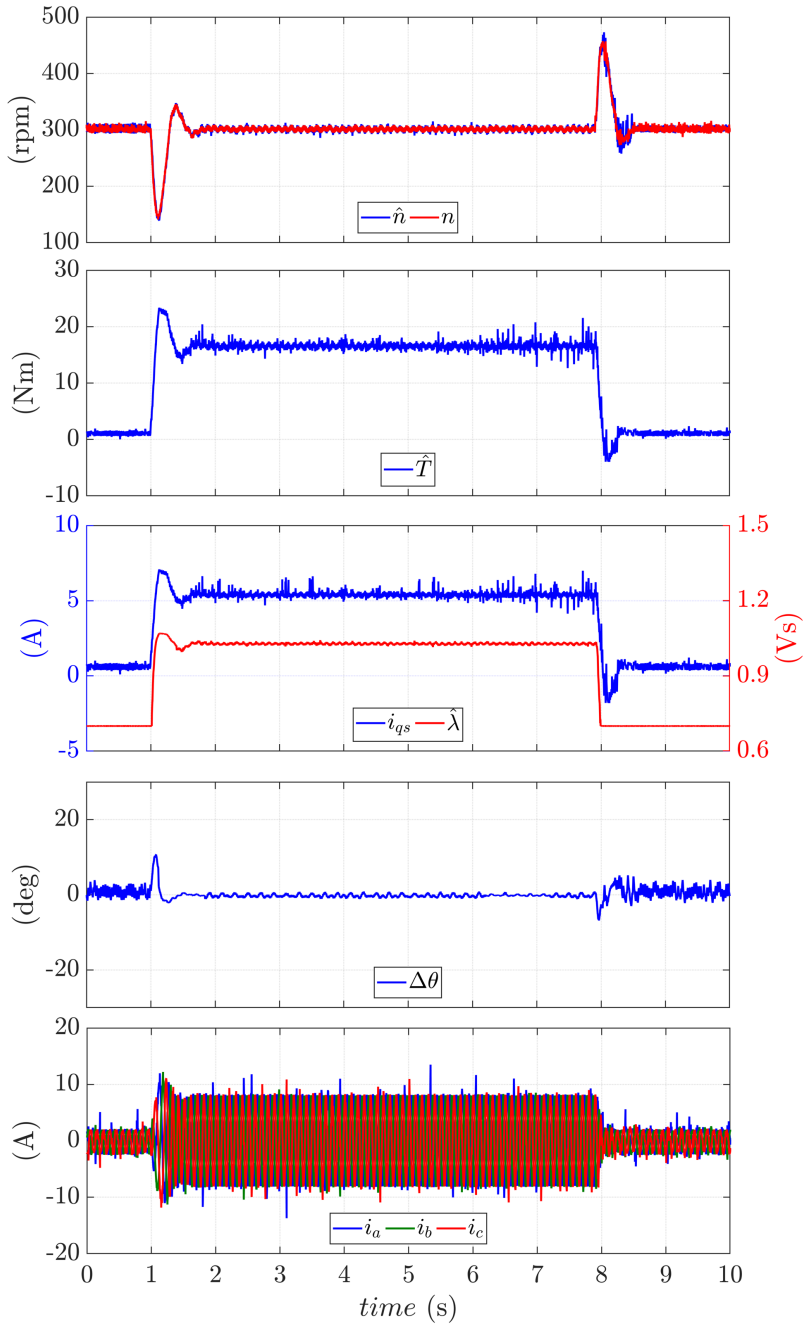

Figure 4.33: Load steps applied while the motor under test is speed controlled at 300 rpm. The load goes from 0 to 17 Nm (121% of rated torque) and vice-versa. From top to bottom: measured and observed speed, observed torque, i_{qs} and observed flux, position error, three-phase currents.

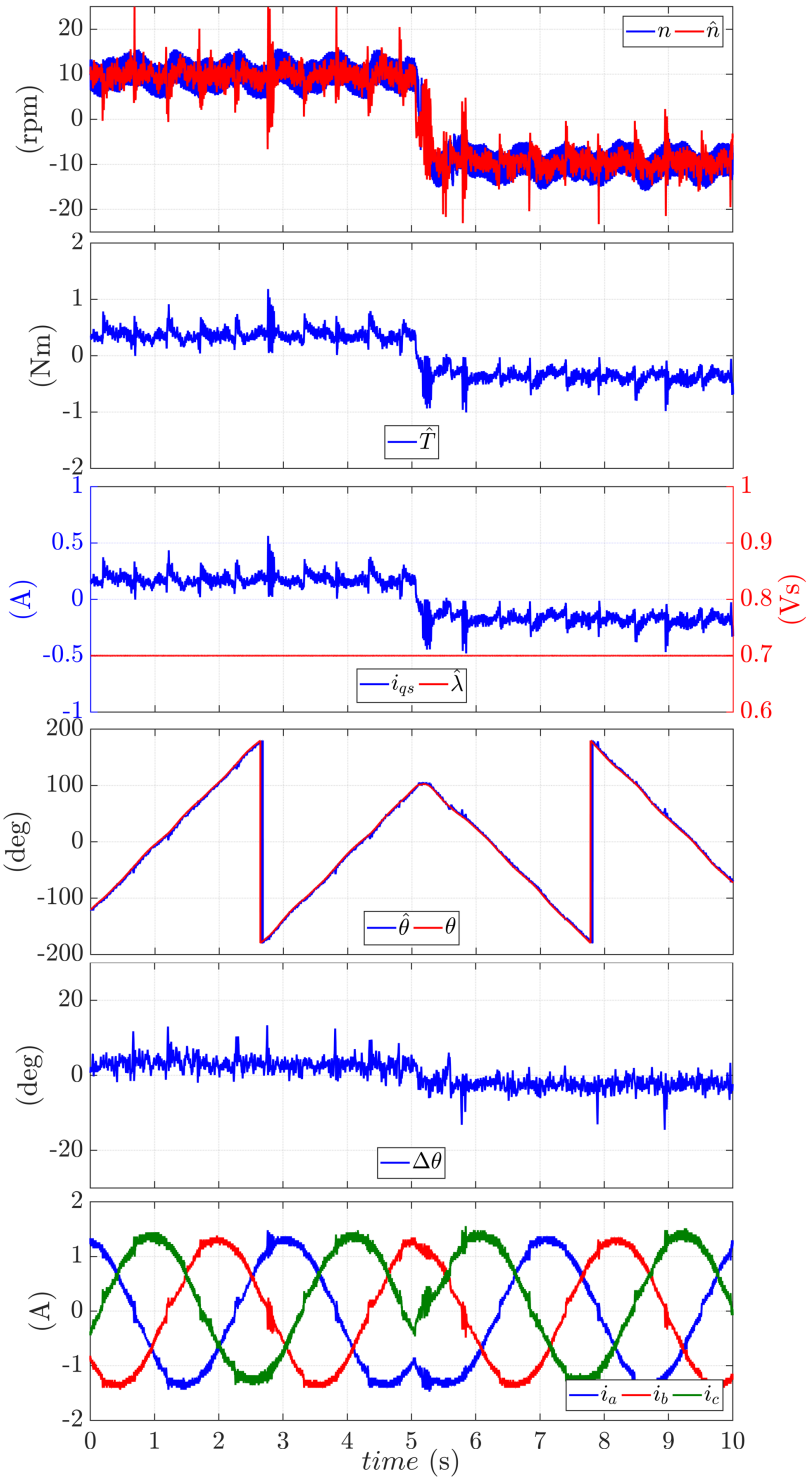

Figure 4.34: No-load speed reversal from 10 to -10 rpm. From top to bottom: measured and observed speed, observed torque, i_{qs} and observed flux, measured and observed position, position error, three-phase currents.

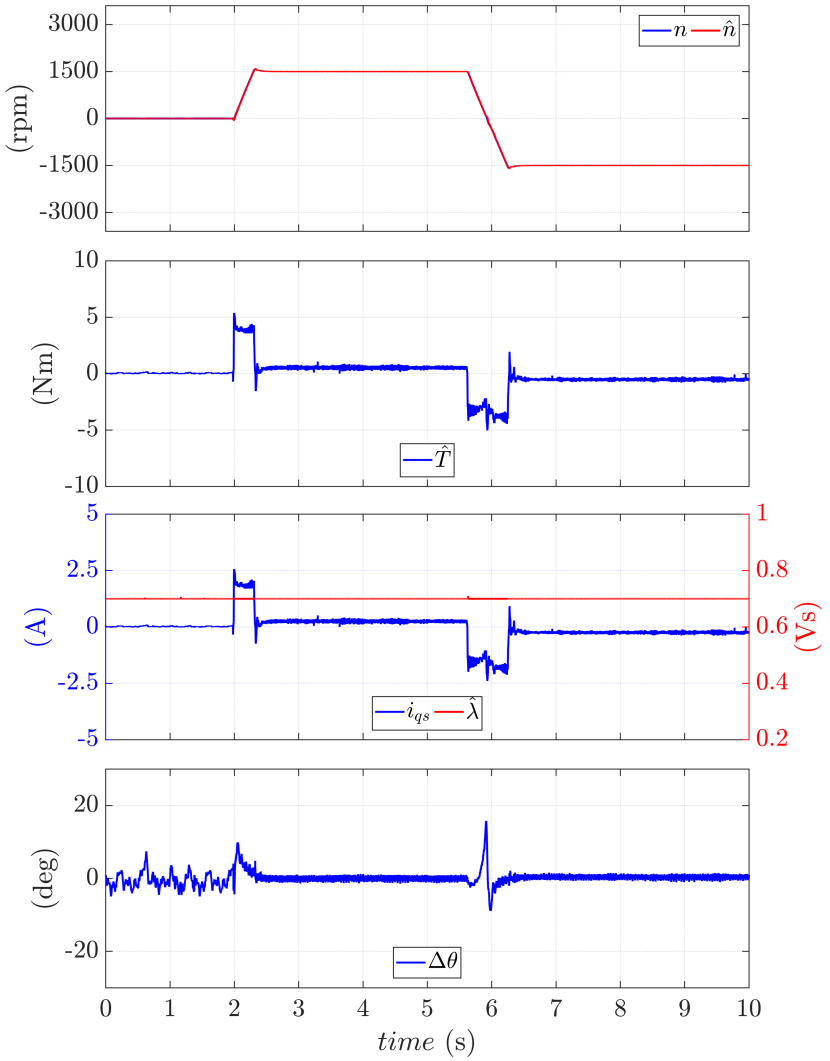

Figure 4.35: No-load high-speed reversal from 0 to 1500 rpm and back to -1500 rpm. From top to bottom: measured and observed speed, observed torque, i_{qs} and observed flux, position error.

4.7.2.3 Transition Between the Two Sensorless Models

To investigate the performance of the proposed method during transition between low-speed and high-speed regions, motor is speed commanded to 1500 rpm at $t = 2\ s$ and again to -1500 rpm at $t = 5.9\ s$ as illustrated in Figure 4.35. It is seen that the position estimation error is around zero in steady states and acceptable during transients. Also, the transition between the two speed ranges is very smooth and it does not produces any discontinu-

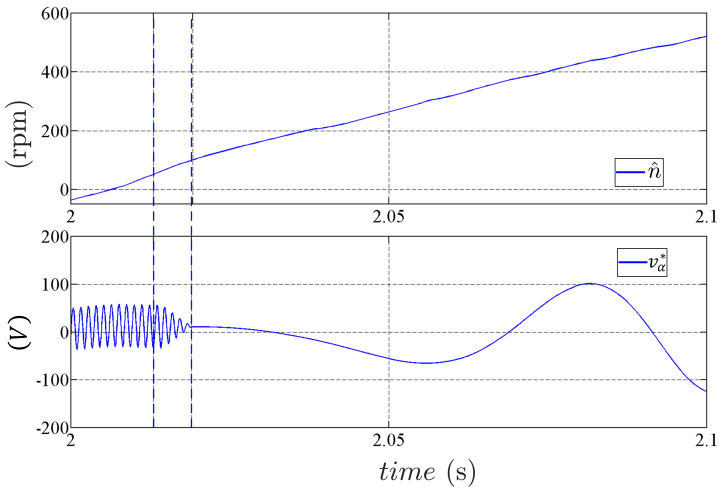

Figure 4.36: HF injection and dropping out methodology: Zoom of estimated speed and v_α^* in the transition region.

ity in position or speed observation. Considering the bandwidth of the speed loop, an acceleration rate of 5000 rpm/s was adopted. Faster accelerations, although possible, resulted in higher distortion in the torque response.

As said, the HF injection starts to decrease gradually above 50 rpm and is completely dropped out above 100 rpm. To validate this, estimated speed and v_α^* have been magnified in Figure 4.36.

4.7.2.4 Flux Weakening Operation

Finally, in Figure 4.37, the motor under test was pushed to flux weakening operation by means of fast speed reversals from 0 to 3000 rpm at $t = 0.8\ s$ and down to -3000 rpm at $t = 5\ s$. As can be seen, above 2000 rpm the machine goes to flux weakening region, so the reference flux amplitude is imposed by (4.57). From torque, i_{qs}, and flux waveforms, it can be seen that in the range of 2000-3000 rpm, flux is decreasing while i_{qs} increases to produce a constant torque. Also, the position estimation error is close to zero at steady state and bounded between -10°and +18°during transients, which is considered acceptable and not compromising the control stability.

It should be noted that in flux weakening speed range the λ^* is reduced below the selected minimum excitation value ($\lambda_{\text{min}} = 0.7\ Vs$), to comply with the voltage constraint. Anyway, the position estimation is not compromised, since in such high speed HF algorithm is not adopted (and therefore there are no saliency-related problems) and the back-emf are sufficiently high for reliable model based position detection even with reduced flux amplitude.

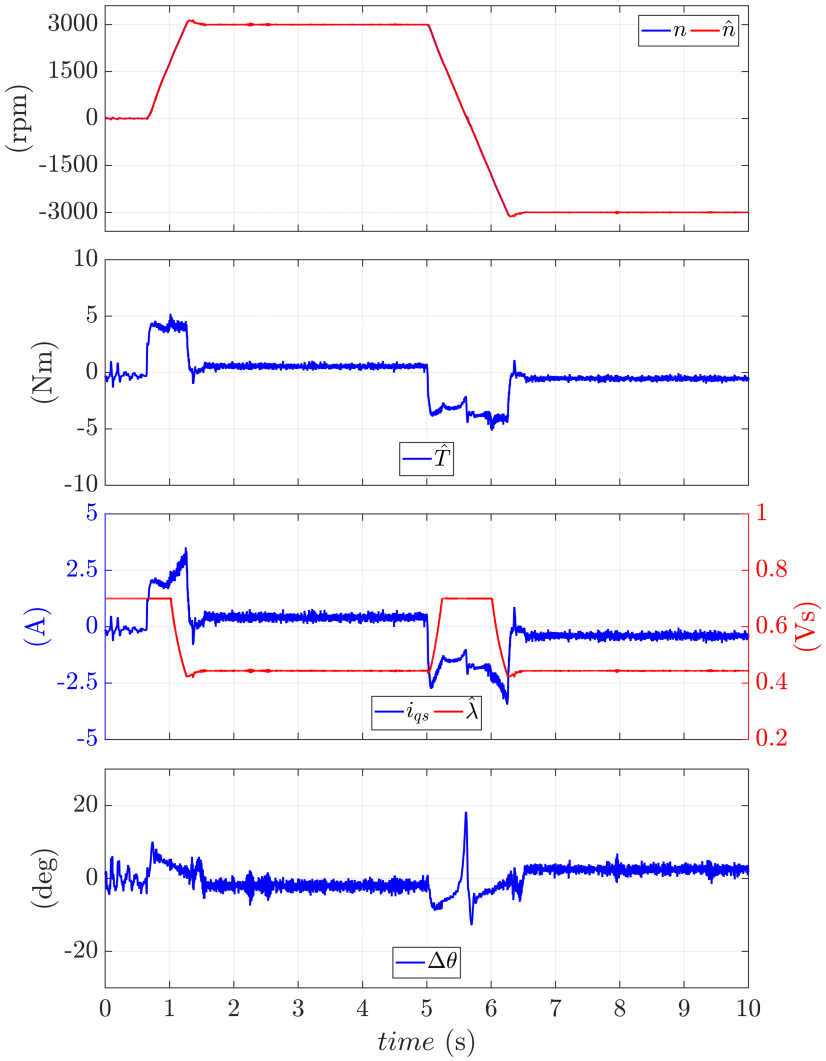

Figure 4.37: No-load high-speed reversal from 0 to 3000 rpm and back to -3000 rpm (flux weakening region). From top to bottom: measured and observed speed, observed torque, i_{qs} and observed flux, position error.

4.7.3 Low Speed: Injectionless FCS-MPC

The low speed sensorless control based on finite control set model predictive control described in Section 4.2.8 was tested on the 1.1 kW motor named SR1kW1, whose specification are reported in Table 3.3. Despite the different motor, the same test bench of the previous tests was adopted.

In all the tests reported in this Section, the SyR machine was closed loop speed controlled while the load torque was imposed by the external auxiliary

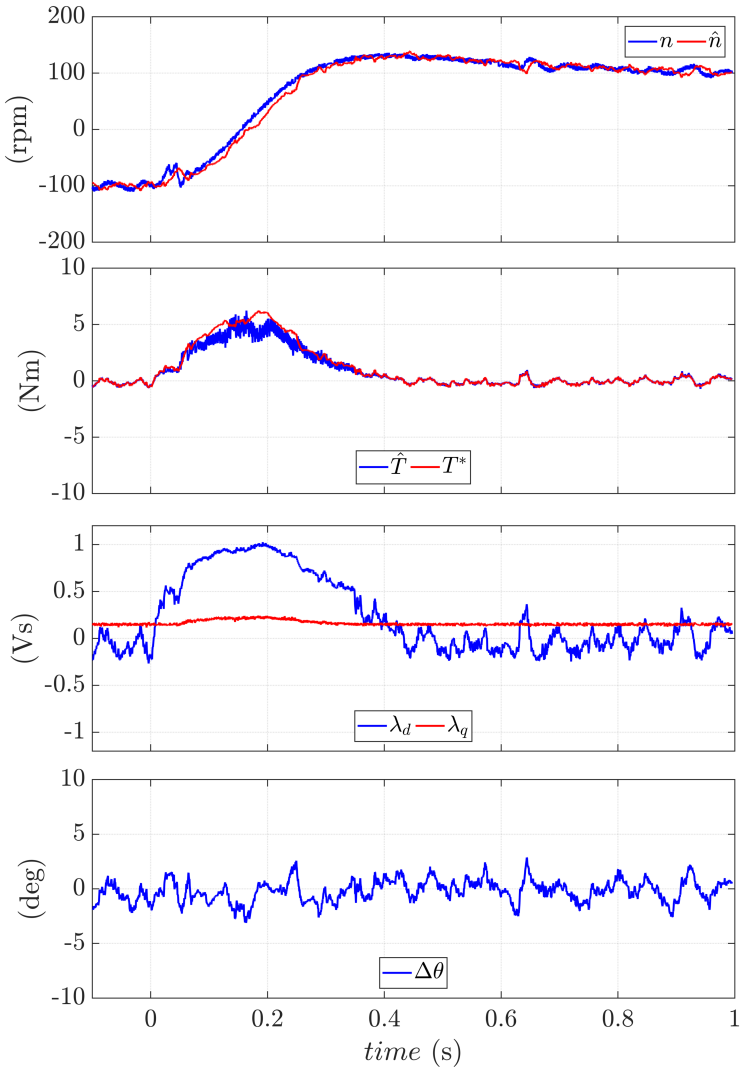

Figure 4.38: Transient response to speed reversal (±100 rpm) under sensorless FCS-MPC. Motor: SR1kW1.

drive, whose size is considerably predominant respect to the motor under test. The feasibility and accuracy of the proposed control algorithm is investigated in both steady state and transient conditions.

4.7.3.1 Response to Speed Reversal

In this test, the reference speed was step-wise reversed from -100 to +100 rpm at $t = 0$ s. The auxiliary drive was disabled, so the load torque was zero. Figure 4.38 reports the machine transient response. As can be seen, the

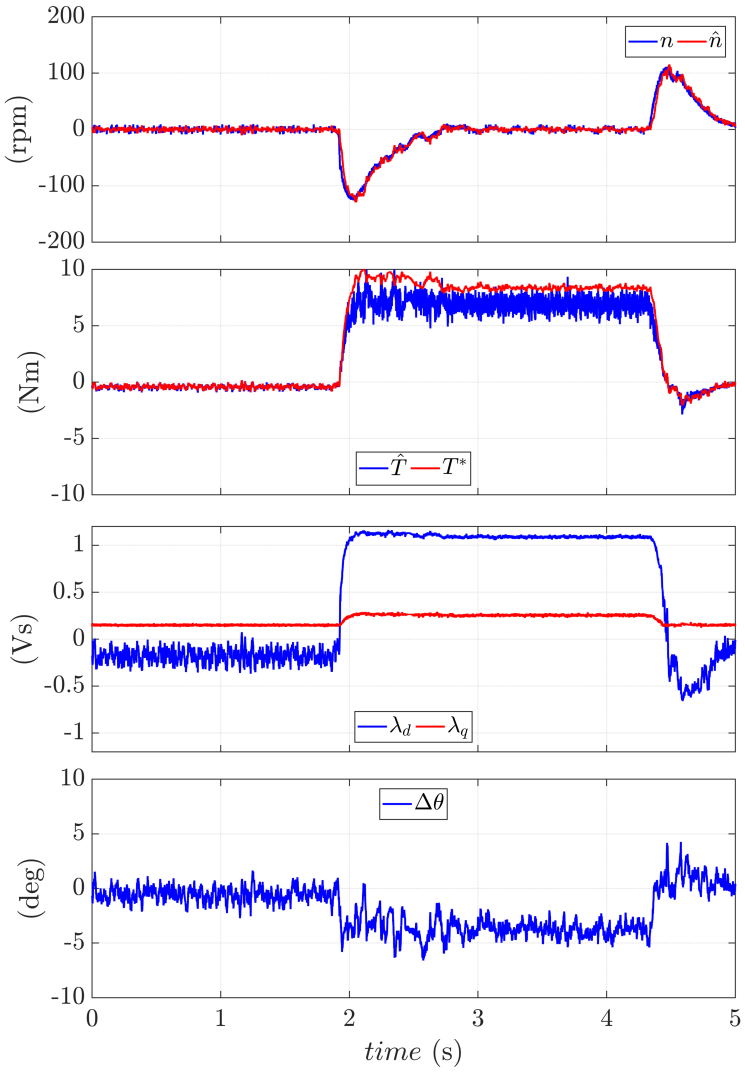

Figure 4.39: Transient response to rated torque step under sensorless FCS-MPC. Motor: SR1kW1.

sensorless algorithm converges to the rotor position with negligible discrepancy even in transient conditions, with $\Delta\theta$ limited between $\pm 4°$. A small overshoot is observed in the speed response, mostly due to the tuning of the PI regulator of the speed loop. In particular, for a given k_p, the k_i gain is a tradeoff between stiffness to load disturbances and overshoot in speed transient.

4.7.3.2 Response to Torque Step

The robustness of the sensorless control is tested by applying the nominal load at standstill, which is the most demanding condition. A step torque is imposed by the auxiliary drive from 0 to 7 Nm at the instant $t = 0.9\ s$ and then released at $t = 3.3\ s$. The results are plotted in Figure 4.39. As can be seen, also in this case the position estimation is accurate with small position error at full load (around 4°). The persistence of this error at steady state is mostly due to non perfect compensation of inverter non-linear effects. The high bandwidth of the position tracking is evident from the fast convergence of the position observer during transient. The speed overshoot is in accordance with the predicted value based on the tuning of speed PI regulator.

4.7.3.3 Steady-State Response at Low Speeds

Finally, the steady state stability at low speed is tested by means of a slow speed ramp at no load, to find out the presence of eventual critical speeds. The speed ramp goes from -50 to +50 rpm in 2 s. The test results, presented in Figure 4.40, demonstrate that the sensorless control is stable and robust at any tested speed with negligible position error, at least in the low speed range.

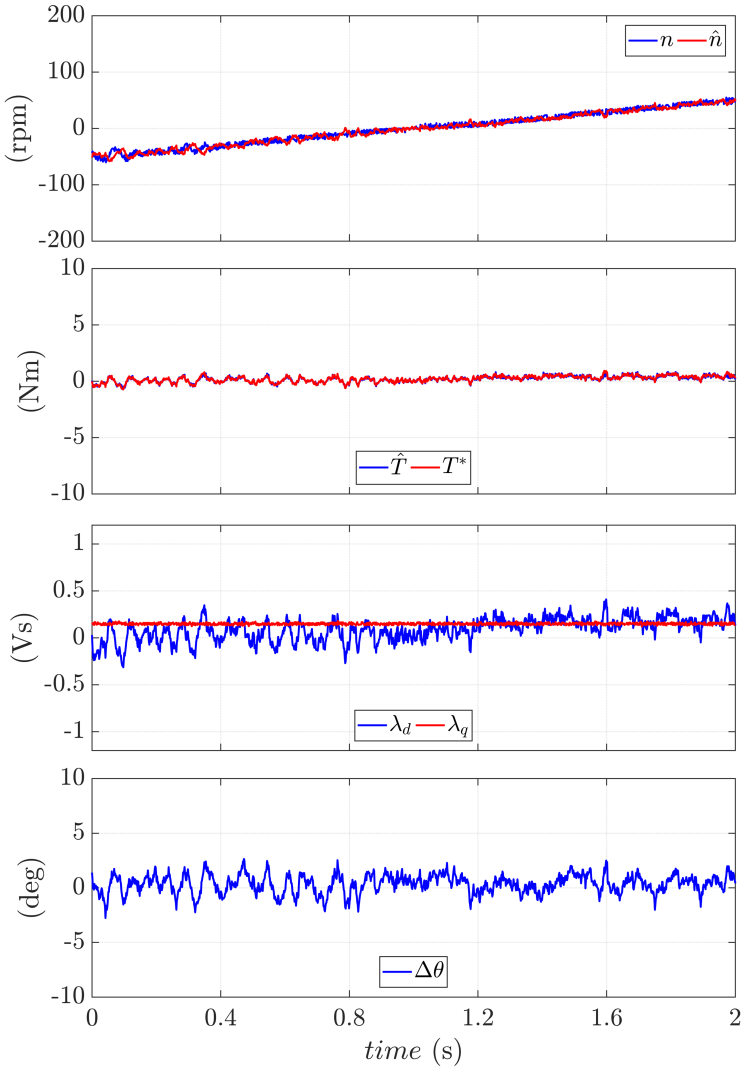

Figure 4.40: Steady-state response at low speed (between ±50 rpm) under sensorless FCS-MPC. Motor: SR1kW1.

Chapter 5

SyRM and PM-SyRM for More Electric Aircraft

Recent trends in avionic applications push for replacing many hydraulic, pneumatic and mechanical systems and other auxiliary services with electrical drives, with the benefits of volume and weight reduction and therefore lower fuel consumption. This evolution is normally referred to as More Electric Aircraft (MEA) and further developments are expected in the near future [162–165]. As an example, flight surface actuators and fuel pumps are now often replaced with electrical counterparts. Research effort has been recently put in hybrid propulsion systems for aircrafts, even if it is not feasible at the moment. With the nowadays available technology, considering as an example an Airbus A380, an All Electric Airplane (AEA) presents a weight reduction of 10% and a 9% lower fuel consumption respect to its counterparts not adopting MEA concept [165]. This is reflected both in commercial and environmental benefits, with relevant reduction of CO2 emission [164].

Most of the electrical power is supplied by generators mechanically connected with the turbine. In some aircrafts, such machines are also used as motors for starting the turbine; in this case the machine is commonly referred to as Starter Generator.

The progressive increase of electrical actuators requires increasing the electrical power capability installed onboard. In particular, the size of both the on-board generators and power electronic converters is growing more and more in the last decade, reaching in some case up to 1.5 MW of installed power. Obviously, the management of very high power machines also leads to considerable technological challenges. The use of motors with multiple three-phase winding systems, originally adopted in naval and wind applications, has been recently extended to recently in aviation environment [166–168].

In any avionic application, the reliability issue is of top importance, and

very strict safety margins are imposed. From the point of view of the motor control, this means that a sensorless algorithm must be ready to operate in case of resolver failure. Both the size of the machine and the environmental constrains considerably increase the complexity of the sensorless control, as will be detailed in Section 5.1.3.

This Chapter describes, in Section 5.1, the control, testing procedure and experimental results on a high current - high power prototype of SyR motor originally designed to serve as an avionic starter generator. The results include both self-commissioning and sensorless control. Despite these machine are custom designed and individually tested, and so there is not practical reason for a self-commissioning routine, the magnetic model self-injection technique described in Chapter 3 was adopted to prove its robustness and validity. The flux maps obtained from the self-commissioning were adopted for implementing sensorless control. Then, in Section 5.2, an innovative technology called "Dual Winding", which is expected to considerably reduce the size of the on-board power electronic converter, is described and experimentally tested.

5.1 High Current SyR Prototype

In this Section, the experiments conducted on a very high current motor, namely SR250kW, are described. This machine has been custom designed by other researchers within a research project including DENERG department of Politecnico di Torino and other institutions. The project was aiming to increase the efficiency of the avionic starter generators and possibly reducing their size in terms of volume and weight by using high anisotropy machines. The choice of passive rotor design, i.e. without permanent magnets, was required for avoiding possible uncontrolled generator operation in case of machine fault[1].

At first, the machine, converter and test bench are described. Then, the experimental results are reported and commented. The results include, but are not limited to, the evaluation of the inverter voltage drop and stator resistance, the identification of the flux maps based on the self-commissioning square-wave voltage injection method, the evaluation of rotor inertia and sensorless control, both at high and low speed. It should be mentioned that the tests on this machine are currently ongoing, therefore some of the results have to be considered as preliminary.

[1] With the development of the project, this choice has been modified, as will be described in Section 5.2.

Table 5.1: Ratings of the SR250kW motor prototype.

	rated ÷ max
$v_{\mathrm{dc}}(V)$	560
Current (A_{RMS})	800 ÷ 1600
Torque (Nm)	190 ÷ 380
Speed (rpm)	12500 ÷ 15000
Power (kW)	250 ÷ 500
Pole pairs	2
Efficiency	0.97
R_{s} ($m\Omega$)	5
L_{d} (μH)	372
l_{q} (μH)	30

Table 5.2: Ratings of the power electronic converter.

Power modules technology	IGBT
Power modules model	CM1400DUC-24S
$f_{\mathrm{sw}}(kHz)$	5
$v_{\mathrm{dc}}(V)$	420÷600
Dead-time (μs)	3.5
Max. current (A)	2800

5.1.1 Motor Characteristics and Experimental Setup

The main ratings of the SR250kW prototype are report in Table 5.1[2], while Table 5.2 highlights the main features of its power electronic converter. The test bench is shown in Figure 5.1, while Figure 5.2 gives an equivalent scheme.

The test rig is composed by two SR250kW motors, nominally identical and mechanically coupled, and a custom designed power electronic converter controlled using dSpace 1202 PPC controller board (also called MicroLab-

[2]The value of L_{d} refers to the linear region in d axis, while l_{q} is referred to differential inductance for saturated structural ribs.

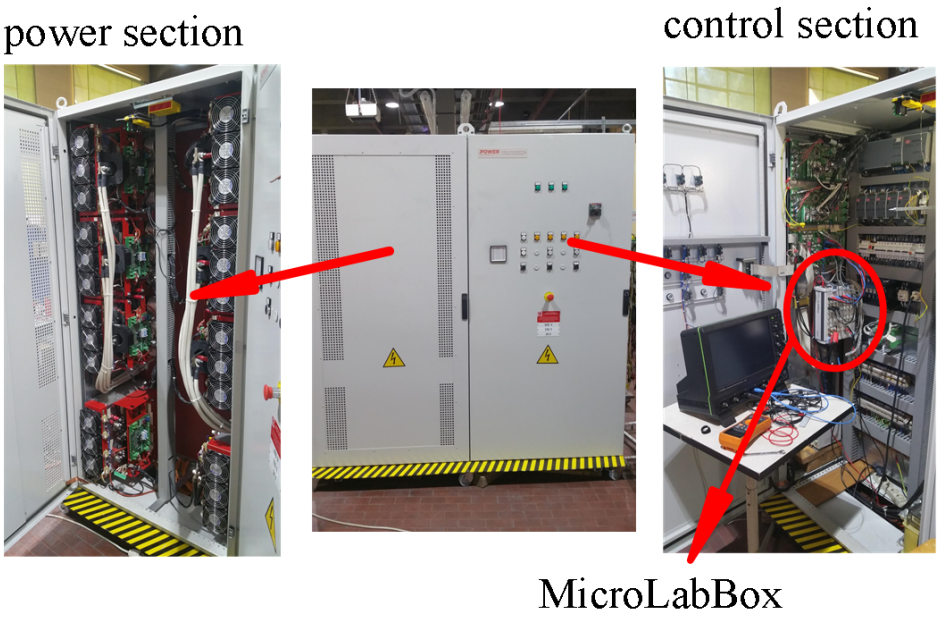

(a)

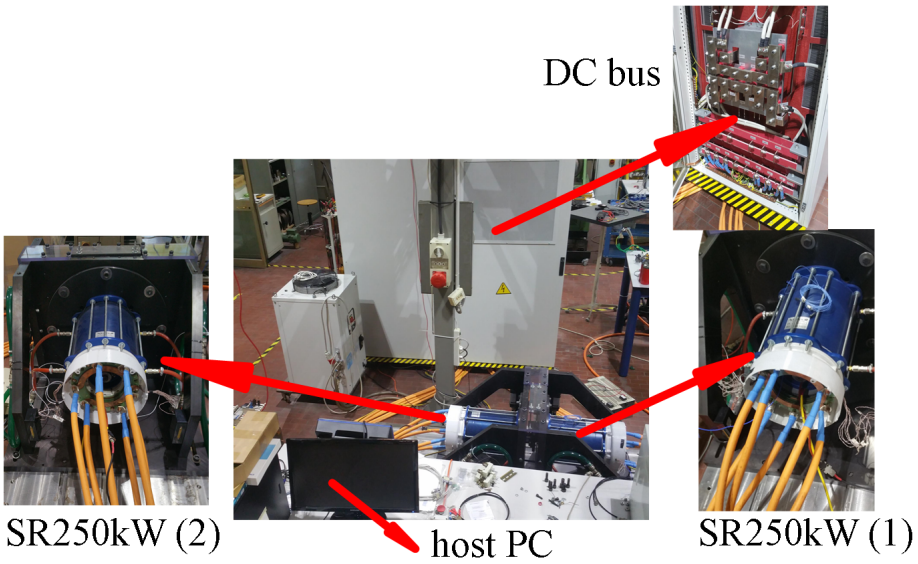

(b)

Figure 5.1: Experimental test bench for testing high current prototype (SR250kW). (a) Converter cabinet; (b) motors and DC bus.

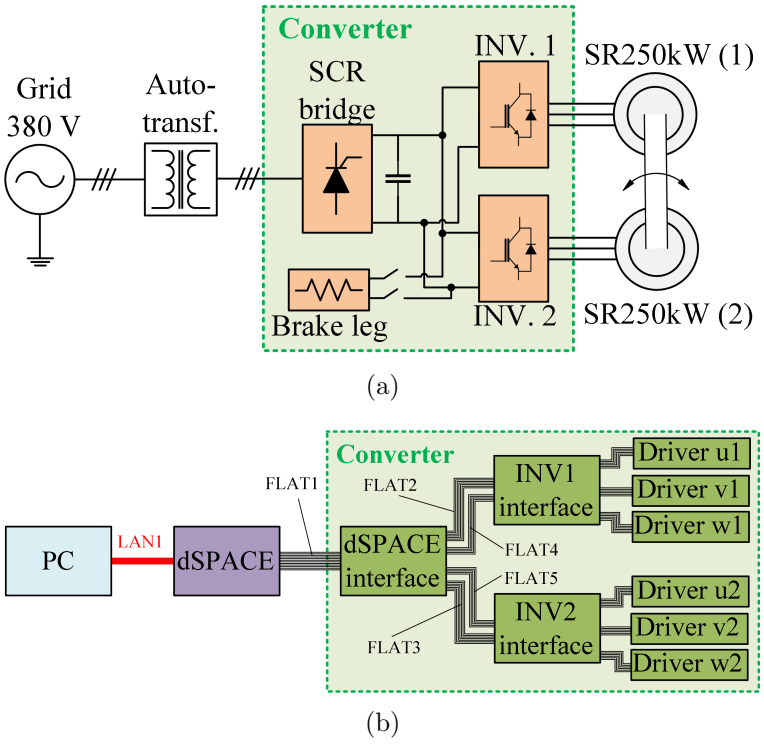

Figure 5.2: Block diagram representing the experimental setup. (a) Test bench. (b) Control boards.

Box) connected to a host PC. The converter contains two standard 3-phase two level voltage source inverter (INV1 and INV2) connected to the same DC-link. A brake leg is automatically connected in parallel to the DC bus in case of overvoltage protection, e.g. if the two machines are braking, thus dissipating eventual excessive power in a series of resistors. The DC-bus is obtained by SCR diode bridge supplied by dedicated auto-transformer, which allows to regulate the v_{dc} (rated: 560 V) and provides galvanic insulation from the grid. Because of the high current rating (2800 A), the switching frequency is limited to 5 kHz. For each inverter leg both the top and bottom switches are made with the parallel of two IGBT modules rated 1400 A.

The control of the converter, over the dSpace platform, is composed by the aggregate of several boards, as represented in Figure 5.2. A first board provides the interface with MicroLabBox. Then, each inverter presents an FPGA board communicating the gate signals to the drivers. The dSpace MicroLabBox allows to easily switching between different motor control techniques● the PWM modulation of the two inverters can be separately activated and deactivated, permitting to run the test with and without load. Moreover, the

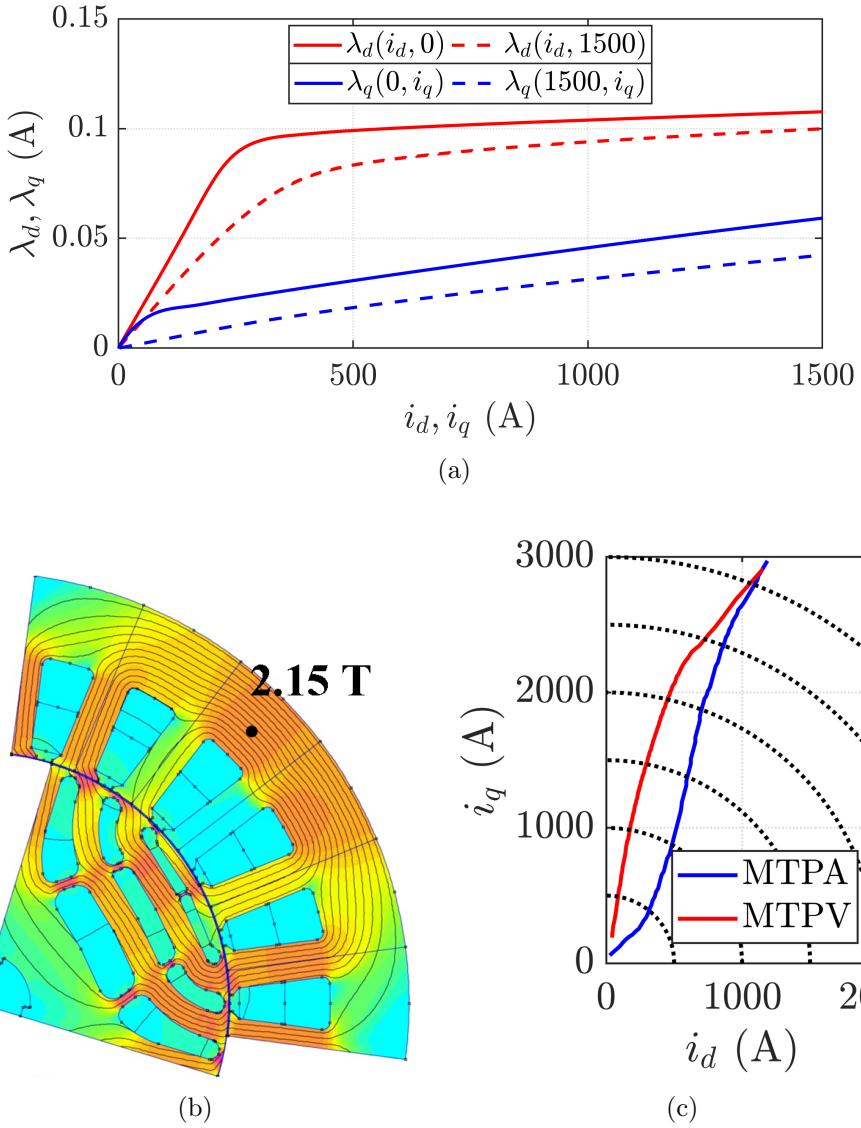

Figure 5.3: Characteristics of SR250kW motor according to FEM simulations. (a) Flux maps; (b) field distribution in the machine at rated load; (c) MTPA and MTPV trajectories.

Double Sampling-Double Refresh (DSDR) technique can be adopted, leading the control frequency to an equivalent of 10 kHz. The main drawback of DSDR method is that the sampled current is not exactly the average in the PWM period, thus introducing additional measurement noise.

During testing, one of the SR250kW machine works as a motor, while the other one simulates a load, thus regenerating electrical power on the DC-

link. This configuration permits to test the machines with minimum power absorption from the electrical grid. At the same time, the risk of breaking overvoltage is reduced, since when one of the motors is regenerating power on the DC-link the other one is commonly absorbing similar power.

For each motor, the three phase currents and the rotor position, measured from an embedded resolver, are acquired. Moreover, an HBM Gen3i Data Recorder, not shown in Figure 5.1, is placed in parallel to the inverter measurements to acquire with high resolution and high sampling frequency (2 MHz, 18 bit, 0.01% class voltage channels and 0.1% class current probes) the currents and voltages of one of the motor, plus the torque measured by a dedicated torque meter placed at the shaft. These data are not used for motor control, but are useful for offline analysis.

The SR250kW prototype is a two pole pairs water cooled SyR machine with three flux barriers per pole designed for high torque density (3.6 Nm/kg at rated load, 7.2 Nm/kg at maximum overload, corresponding to 4.3 kW/kg and 8.6 kW/kg respectively or 18 and 36 Nm/l). According to the specifications, the machine has 100% overload capability, so twice the rated torque can be applied for up to 10 seconds. Conversely, being a pure SyR machine, the constant power range is limited (12.5 to 15 krpm). Also, the power factor is relatively low, causing a high rated and maximum current (800 to 1600 A_{RMS}). Figure 5.3 reports the machine flux maps based on FEM analysis and the correspondent MTPA trajectory.

5.1.2 Inverter Commissioning

As known, from the control point of view the motor voltage is not measured but estimated based on the inverter commands and measured v_{dc}. For accurate voltage reconstruction, it is necessary to compensate the voltage drop on the inverter, which is a current dependent non-linear function. It must be remarked that, considering the current ratings of this converter and the very low motor inductances, the voltage drops are particularly significant and accurate inverter compensation is necessary.

According to [44], the rotor was aligned along the α axis. Then, the current in $\alpha\beta$ axes was closed loop controlled adopting simple PI regulators, with a steps sequence of reference i^*_α, while $i^*_\beta = 0$. The preliminary alignment permits to avoid further shaft rotations during the inverter commissioning.

The value of i^*_α was increased up to 330 A with steps of 5 A. For current higher than 330 A, the characteristic is almost linear and can be easily extrapolated. For each step, the current was maintained enough time for firmly reach the steady state condition, and the reference v^*_α given by the PI regulators was monitored. The obtained results are plotted in Figure 5.4(a), which

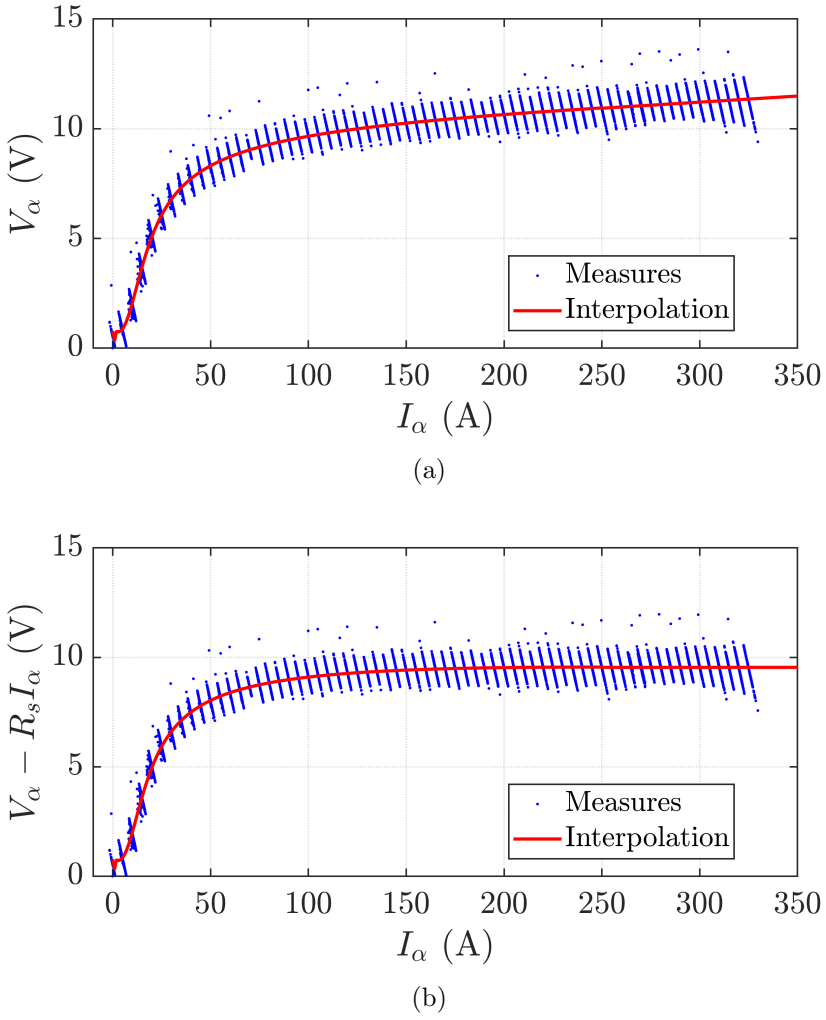

Figure 5.4: Commissioning of the inverter voltage drop. (a) Total voltage in α axis; (b) inverter voltage drop considering $R_\mathrm{s} = 5.5\ m\Omega$.

also shows the interpolated function. This voltage is the aggregate of voltage drop on the stator resistance, dead time non-linear effect and conductive voltage drops on the IGBT modules of the inverter.

An equivalent resistance of 5.5 $m\Omega$ aggregating the voltage drop on R_s and conductive inverter losses is estimated from the slope of the obtained curve after the non-linear region, i.e. for $i_\alpha > 150\ A$. This contribution has been removed in Figure 5.4(b), which represents the current dependent non-linear term of inverter voltage drop and will be used in all the following experimental tests for inverter compensation.

5.1.3 Magnetic Model Identification: Self-Commissioning

The test sequence described in Section 3.3.1, namely test #1, #2 and #3, was applied to evaluate the flux maps of the machine. Despite the test could be run in sensorless mode, considering the elevated machine currents the rotor position acquired from the resolver was conveniently used for safety reasons. The results are report in Figure 5.5 and 5.6.

When this test was executed, a magnetic identification at constant speed (based e.g. on [40]) was not jet conducted. To maintain the chronological test sequence, the saturation characteristics measured in self-commissioning will be compared with the FEM model adopted in the machine design stage. This comparison is report in Figure 5.5(c) for test #1 and #2 and in Figure 5.6(b) and 5.6(c) for test #3. Precise flux maps identification will be conducted in Section 5.1.6, also presenting a comparison with the self-commissioning results.

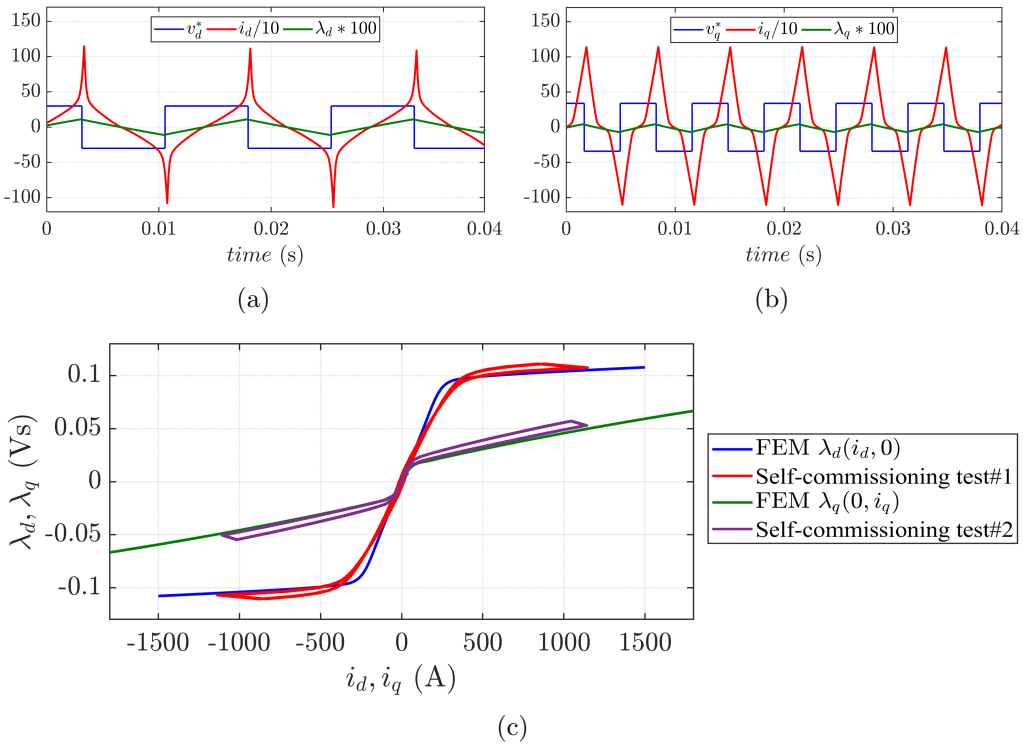

Figure 5.5: Reference voltage, measured current and online computed flux for (a) test #1 and (b) test #2. (c) Comparison between the obtained self-axis saturation characteristics and the FEM model.

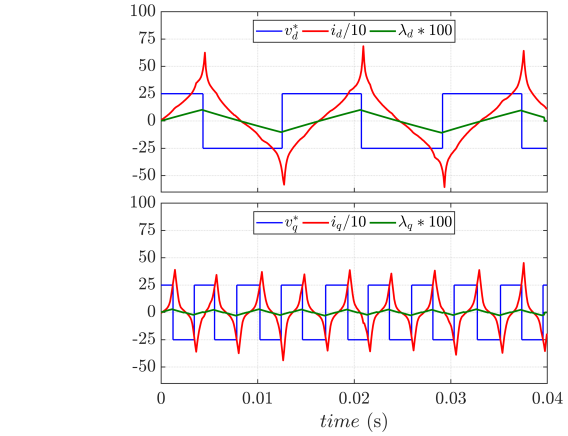

(a)

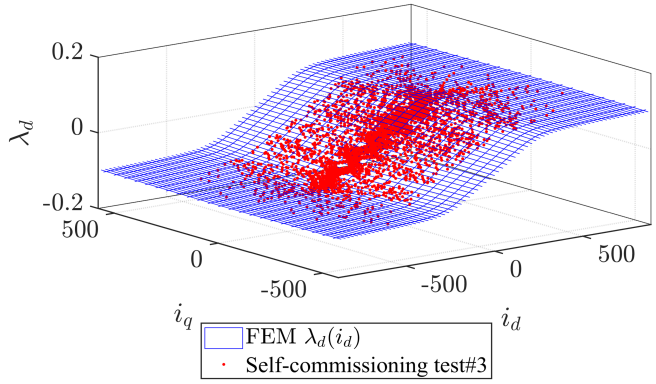

(b)

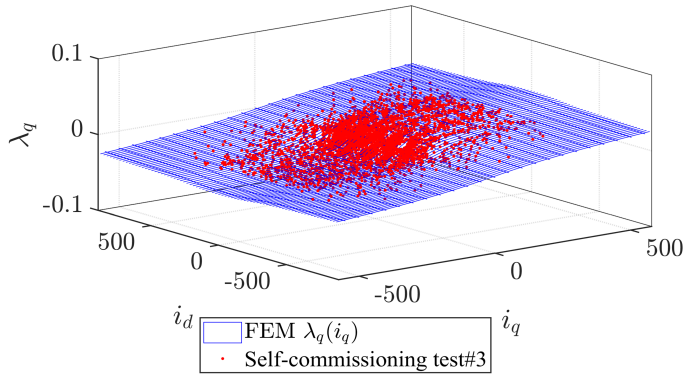

(c)

Figure 5.6: (a) Reference voltage, measured current and online computed flux for test #3. (b) and (c) Comparison between the obtained characteristics and the FEM model for d and q axes respectively.

Table 5.3: Fitted Parameters Given in SI Units

S	T	U	V	a_{d0}	a_{dd}	a_{q0}	a_{qq}	a_{dq}
7	1	1	0	2842	$23.97 \cdot 10^9$	659.9	$356.4 \cdot 10^3$	$17.30 \cdot 10^6$

The identification measurement was pushed up to 1100 A both in d and q axes in tests #1 and #2 (Figure 5.5), where the not-excited axis was current controlled forcing zero current reference. In addition, the cross-saturation was extracted from test #3 in Figure 5.6(b) and 5.6(c), where the maximum current overshoots in the two axes were $i_{\mathrm{d}} = 750\ A$ and $i_{\mathrm{q}} = 400\ A$.

It must be remarked that the inductance of this motor is very low, therefore a relatively low test voltage has to be applied in self-commissioning stage (e.g. 30 V). So, the flux estimation is not completely immune to inaccurate parameters estimation as for the motors in Chapter 3. The curve obtained in Figure 5.1.2 was adopted for properly taking into account the inverter and resistive voltage drops, thus accurately evaluating the applied electromotive force. Another consequence of having so low inductances is that even in case of small misalignment relevant current spikes were detected in the not-excited axis during tests #1 and #2, in the order of magnitude of tens of ampere. The DSDR technique was conveniently adopted to virtually increase the equivalent switching frequency.

As can be seen from Figure 5.5, the estimated λ_{d} characteristic presents a lower inductance in linear region respect to the value predicted with the FEM analysis. After deep investigation, it was found that the machine airgap was increased from 0.5 to 0.7 mm due to mechanical tolerance stack-up, thus explaining the lower L_{d}. From the control point of view, this basically means that the machine requires a higher magnetizing current in d axis. Conversely, the increased airgap does not affect the $\lambda_q(i_{\mathrm{q}})$ characteristic, since in this case the inductance is mostly due to leakage fluxes.

The inverse machine model (3.35) was retrieved through LLS procedure, as described in Section 3.4.4. Table 5.3 reports the obtained model parameters. As previously said, the value of L_{d} in linear region can be computed as $1/a_{\mathrm{d0}} = 352\ \mu H$, resulting compatible with the inductance directly obtained from the measurement data. Despite the very different size of the machine the optimal exponents are in accordance with the ones established in Section 3.4.4, confirming that a reduced number of possible sets of integer exponents can be usefully adopted for this analytical model. The fitted curves (blue lines) are compared with the measured data and FEM-based characteristic in Figure 5.7. As can be seen, the analytical curves well represent the measured data at least within the measurement domain. The

cross-saturation effect retrieved from test #3 results reasonably compatible with the prediction, considering the lower L_d in linear region. A deviation between the fitted curve and the measured λ_d is observed for $i_\mathrm{d} > 1000$ A, where the analytical model estimates a higher l_d. A better estimation of the saturated region would require a higher measurement domain during test #1. Anyway, the MTPA trajectory never falls in that current domain.

Based on the obtained flux maps, the MTPA curve was retrieved and adopted in the following tests.

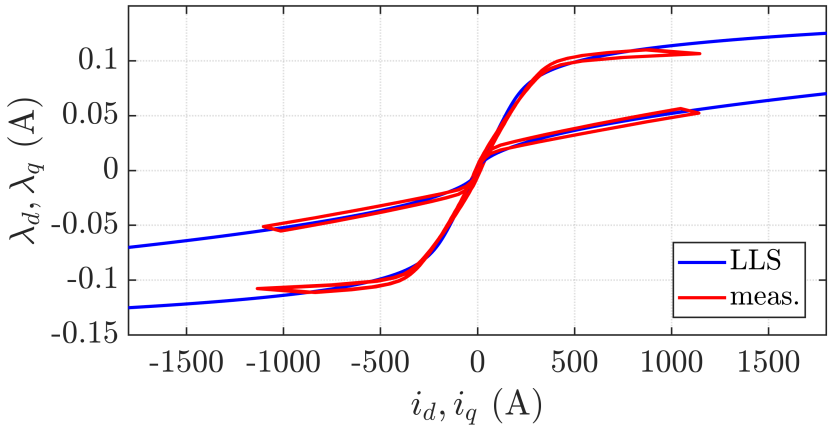

(a)

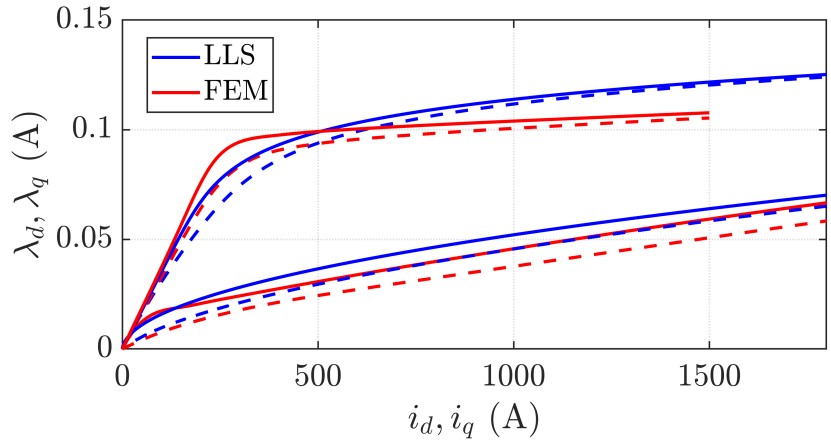

(b)

Figure 5.7: Comparison between fitted model (blue lines) based on (3.35) with (a) measurement data from test #1 and #2 and (b) with the FEM model. In this second Figure, the solid lines represent the self-axis characteristic, while for the dashed lines the other axis was excited at 600 A.

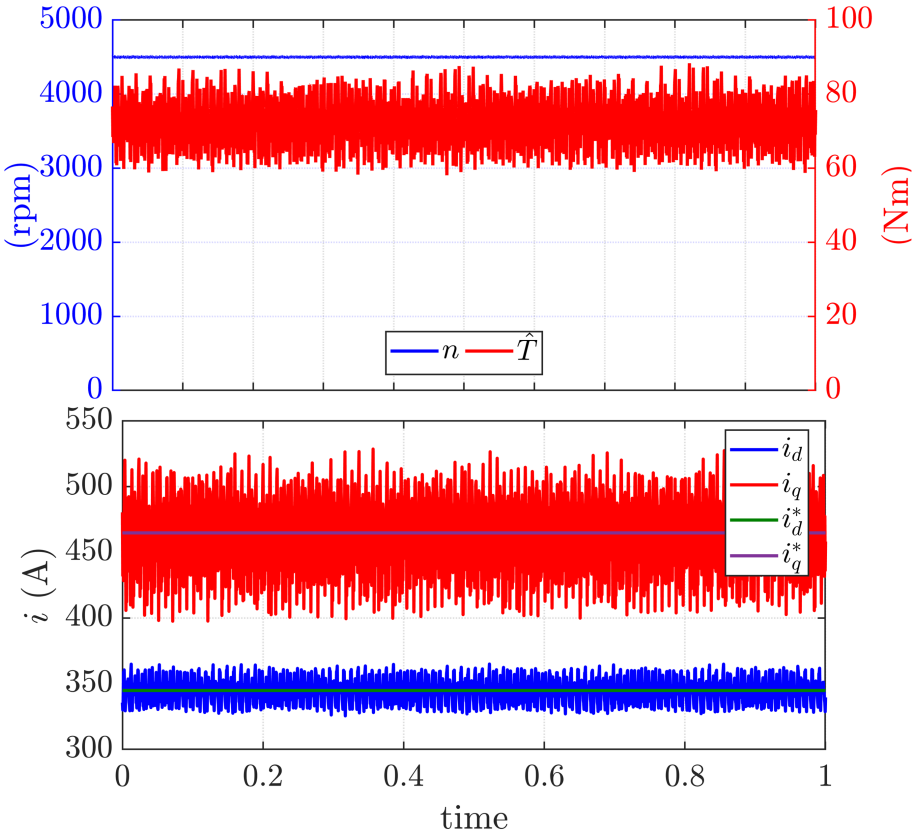

Figure 5.8: Steady state speed control test at 4500 rpm and 75 Nm.

5.1.4 Steady State Operation And Harmonic Fields

In this test, the two motors were simply run at constant speed in order to evaluate the harmonic content of the back-EMF. One of the motors was speed controlled, imposing $n = 4500\ rpm$, while the other was torque controlled with $T^* = 75\ Nm$. For both motors, a minimum i_d of 60 A was imposed to guarantee sufficient level of excitation. For simplicity, the motor control was dq current control as described in Section 2.2.1, often called Field Oriented Control (FOC). The results are shown in Figure 5.8.

As can be seen, the motor presents a relevant harmonic noise, resulting in high current overshoots that cannot be controlled from the current loops. In particular, the 6^{th} and 12^{th} harmonics are predominant, as can be observed in Figure 5.9. This phenomenon strongly limits the operating region of the machine, especially in the speed range. Several techniques for getting rid of this problem are under investigation.

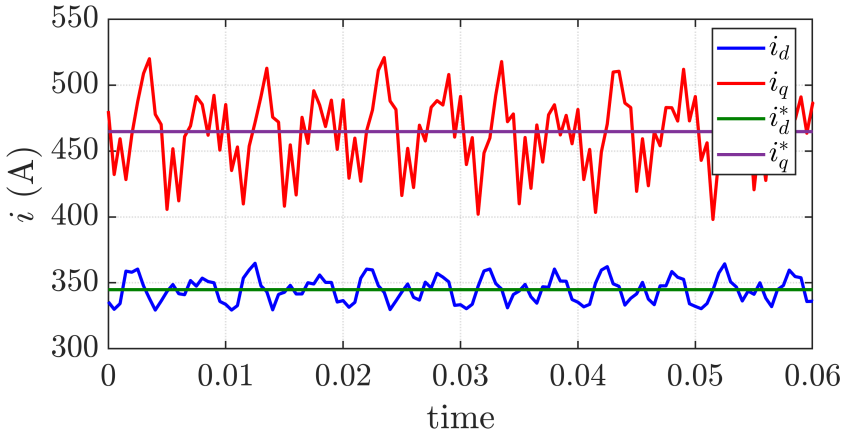

Figure 5.9: Zoom of the steady state speed control test.

5.1.5 Speed Control and Inertia Evaluation

In this Section, the motor inertia was estimated, with the goal of properly tuning a speed control loop.

One of the two machines was turned off, while the other one was speed controlled. The reference torque T^* was converted into $(i_{\mathrm{d}}^*, i_{\mathrm{q}}^*)$ coordinates relying on MTPA trajectory. Several speed transients were applied; as an example, Figure 5.10 reports a steps from zero to 4000 rpm with an acceleration of 4000 rpm/s and the following natural deceleration until 3000 rpm, simply obtained by deactivating the PWM modulation.

Thanks to the flux maps identification, the current loops in d and q axis were properly tuned and a reliable flux observer was implemented according to Figure 2.10. Based on the measured current and observed flux, also the motor torque could be conveniently estimated during the acceleration transient, while during the natural deceleration the only torque present at the shaft was due to mechanical friction.

From the analysis of the two transients, the inertia and an equivalent mechanical friction torque of the system, composed by the two SR250kW machines and the shaft torque meter, was retrieved as 0.1021 kg/m and 0.171 Nm respectively. Despite the mechanical friction is speed dependent, its value is very small compared to the rated torque thanks to the adopted high performance bearings, so a constant value can be adopted being the error not relevant in percentage.

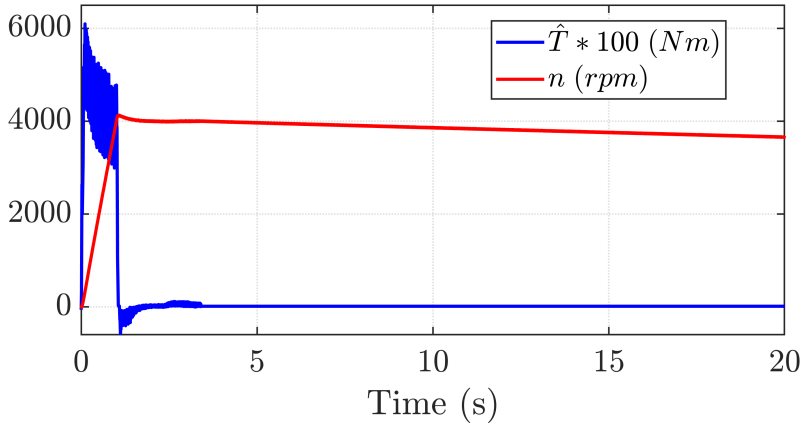

Figure 5.10: Speed control test from zero to 4000 rpm followed by natural deceleration.

5.1.6 Constant Speed Flux Mapping

A more precise test to evaluate the machine flux maps was carried out according to [40]. One of the two machines was speed controlled at constant reference speed, acting as a driving machine, while the motor under test was current controlled with a proper sequence of current reference. The speed control loop was tuned considering the mechanical inertia estimated in Section 5.1.5, while both the torque control of the driving machine and the current control of the motor under test were calibrated based on the self-commissioning flux maps and MTPA trajectory obtained in Section 5.1.3.

The imposed speed was 1200 rpm, a trade-off between sufficiently high back-emf and low iron losses. A grid of equally spaced points was defined in the first quadrant of the dq plane. The current was kept in each of those points for a sufficient number of mechanical revolutions, then i_{q} was reversed moving the current vector in the fourth quadrant (again for sufficient time) and then back to positive i_{q}. In this way, a motor-braking-motor average was exploited to minimize the sensitivity of the computed flux maps respect to non-perfect compensation of the inverter voltage drop, inaccurate stator resistance estimation and temperature drifting. Details can be found in [40].

Being at steady state, for each measurement point in the current plane, the correspondent dq flux was computed as:

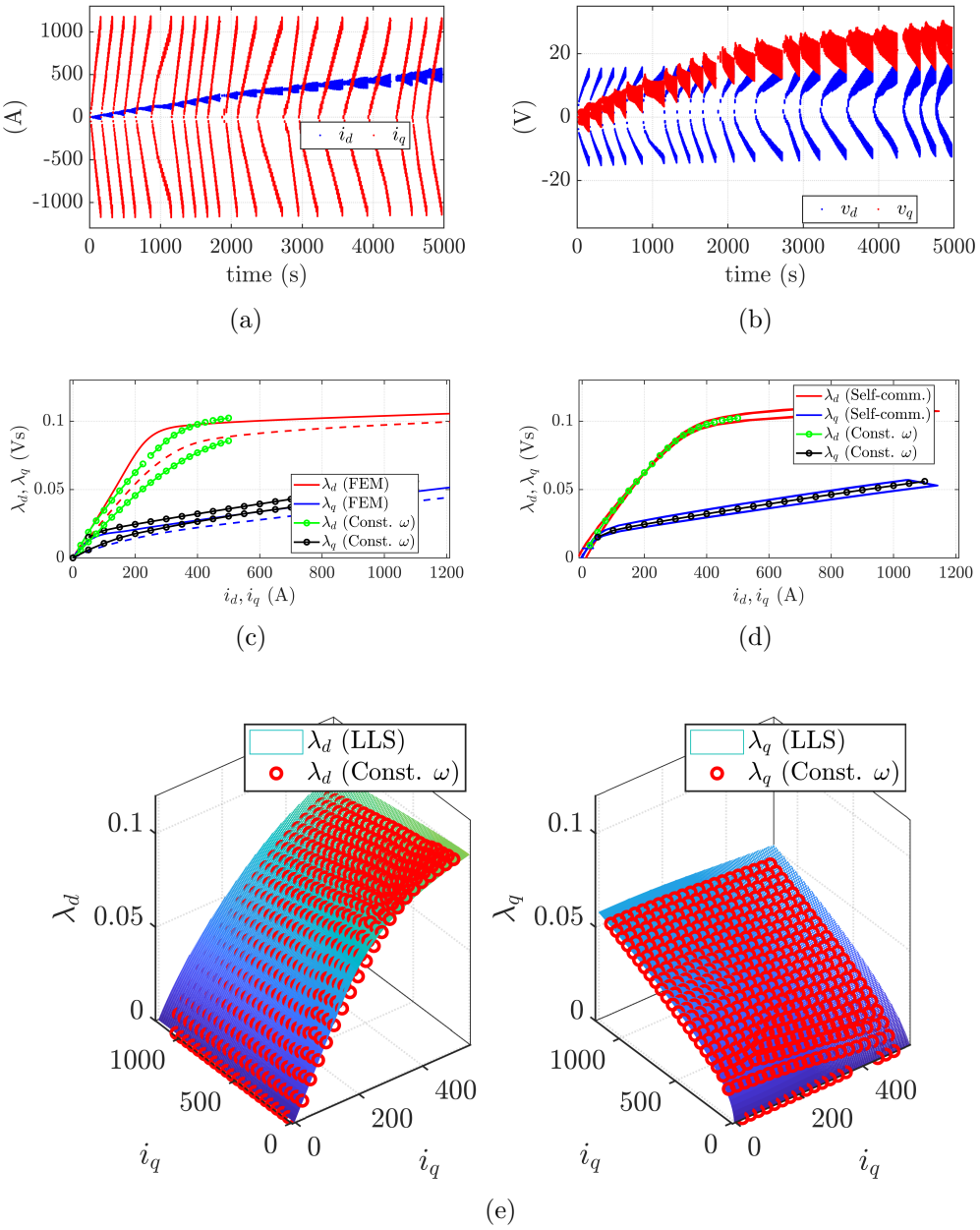

Figure 5.11: Magnetic model identification at constant speed. Time waveform of (a) currents and (b) voltages; comparison with (c) the FEM model and (d) self-commissioning; (e) computed flux maps.

$$\lambda_{\mathrm{d}} = \frac{v_{\mathrm{q}} - R_{\mathrm{s}} i_{\mathrm{q}}}{\omega} \tag{5.1a}$$

$$\lambda_{\mathrm{q}} = -\frac{v_{\mathrm{d}} - R_{\mathrm{s}} i_{\mathrm{d}}}{\omega} \tag{5.1b}$$

where the $\boldsymbol{v}_{\mathrm{dq}}$ and $\boldsymbol{i}_{\mathrm{dq}}$ were obtained as the average over two integer mechanical revolutions. In this way, the average flux characteristic is extracted, immune from harmonic content due to winding distribution and slots effect.

The results of this test are highlighted in Figure 5.11. In particular, Figures 5.11(a) and 5.11(b) show the trajectories of the *dq* current and voltage during the test for each measurement point. Figure 5.11(c) compares the flux maps extracted from the FEM (red and blue) with the points computed from the constant speed test (green and black dots). In this plot, the solid lines represent self-axis saturation curves while the dashed line is in presence of strong cross-coupling. Figure 5.11(d) compares the same points computed at constant speed with the trajectories obtained from the self-commissioning test #1 and #2, so in absence of cross-saturation. As can be seen, a good agreement is achieved between the two flux estimates, proving once more the accuracy of the adopted self-commissioning technique. Both the self-commissioning and the constant speed data highlight a lower L_{d} in the linear region respect to the one predicted based on the FEM, explained with the above mentioned stack-up of mechanical tolerances. Finally, the 3D model retrieved LLS optimization in Section 5.1.3 and measured with constant speed test are compared in Figure 5.11(e).

5.1.7 Test in Sensorless Control

This Section details the implemented sensorless control technique, imposed by the very high safety standards in case of resolver fault. For simplicity, as a first attempt the main motor control was based on *dq* current control as in Figure 5.12, where the $(i_{\mathrm{d}}^*, i_{\mathrm{q}}^*)$ are calculated relying on MTPA trajectory. A minimum excitation current of $i_{\mathrm{d}} = 60\ A$ was imposed at low torque. The speed loop can be active or not, moving from speed to torque control. The transition to DFVC is under investigation at the moment of this manuscript. The flux maps retrieved from self-commissioning test were adopted in the flux observer.

The relevant size of the machine impose several issues to the sensorless control that must be taken into account. First of all, the current size imposes a low switching frequency and large inverter dead-time. The DSDR technique virtually increases the switching frequency, but at the cost of not measuring

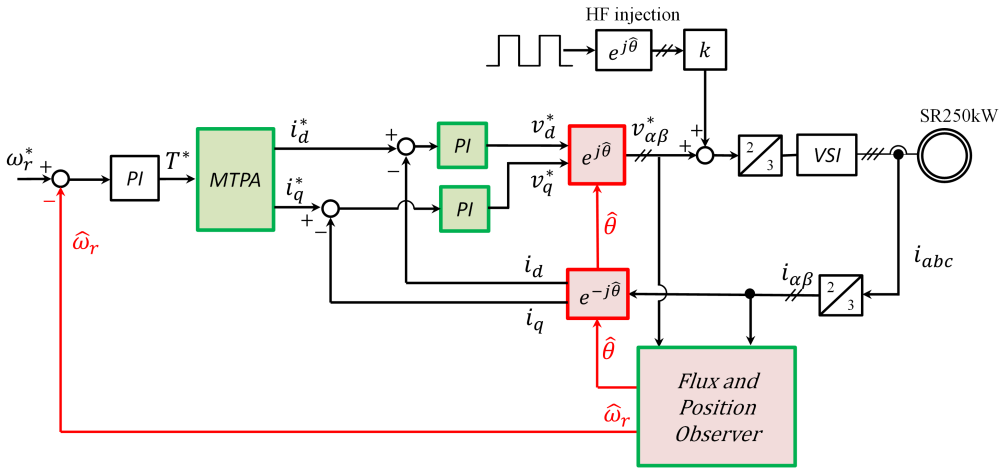

Figure 5.12: Block diagram for sensorless control of the SR250kW motor prototype.

the average current in the PWM period, thus introducing additional uncertainty in the position estimation. Also, the inverter compensation is rather critical and proper characterization as in Section 5.1.2 is necessary. Also, the low machine inductances introduce the risk of losing the current control in case inappropriate voltage is applied. Finally, it must be considered that, being the maximum speed 15000 rpm, the structural ribs are designed thick enough to guarantee mechanical robustness, which means a relatively high current is necessary to saturate them. As a consequence, the lack of saliency at no-load discussed in Section 4.2.7 is rather critical and the machine is almost isotropic up to $i_q = 60\ A$.

At the moment of this work, separate techniques were implemented for low and high speed region, as detailed in the following Sections. The same flux observer (see Figure 2.10) is adopted at every speed, while different position observers are used. The parameter k is used to switch on and off the HF voltage injection. In both cases, the automatic tuning procedure guidelines detailed in Section 4.6 were adopted. For each test, the motor under test was either torque or speed sensorless controlled, while the twin machine imposed the shaft speed or torque respectively.

5.1.7.1 Position Error at Low Speed

The no-load lack of saliency is a relevant problem at low speed, where a HF injection algorithm must be adopted. In this Section, pulsating HF voltage injection in estimated $\hat{d}$ axis is adopted (k=1 in Figure 5.12). The

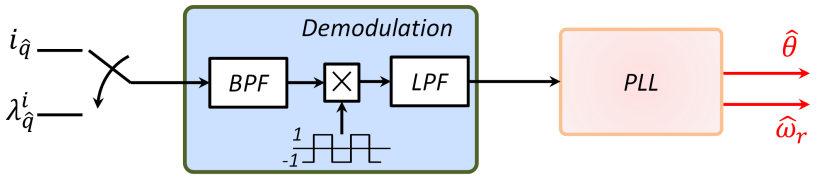

Figure 5.13: Demodulation scheme for low speed sensorless control of the SR250kW motor prototype.

low machine inductances suggest to increase as far as possible the injection frequency. Thanks to the DSDR, it would be possible to inject the HF signal at the switching frequency (5 kHz), but in this case the demodulated signal presented a very high 6^{th} harmonic, according to [125]. Therefore, it was preferred to inject at half of the switching frequency, i.e. 2.5 kHz. In this way, DSDR is adopted for motor control only, but not for position tracking.

The demodulation scheme is report in Figure 5.13. Either the q axis current or flux estimate coming from current model can be used as error signal, which is demodulated. Since the HF voltage is injected at half of the switching frequency, the amplitude of the error signal is demodulated by simply reversing one sample every two time steps. Then, a standard PLL is adopted for extracting the rotor position and speed.

Similarly to Section 4.7.1.2, the speed was imposed by the second machine at 100 rpm, (i.e. 0.008 pu) while the motor under test was torque controlled with slow torque ramps up to 120 Nm, i.e. 70 % of the rated value. The test was repeated extracting the position estimation from current and flux demodulation for comparison purposes. The results are reported in Figure 5.14.

The lower sub-Figures show the position error directly calculated from the measured and the observed position in blue. This error is very noisy, mostly due to the relevant harmonic content of the machine. Only for comparing the two demodulation techniques, it was offline low-pass filtered (red line). The filtered position error was not adopted for motor control. As can be seen, the test performed with current demodulation (Figure 5.14(a)) present relevant cross-saturation error, which is considerably reduced adopting flux demodulation (Figure 5.14(b)). A small cross-saturation error is still present, again mostly because of the spatial harmonic content. It should be reminded that the adopted flux maps are retrieved from standstill self-commissioning, therefore they correspond to the flux characteristic in only one of the possible rotor positions.

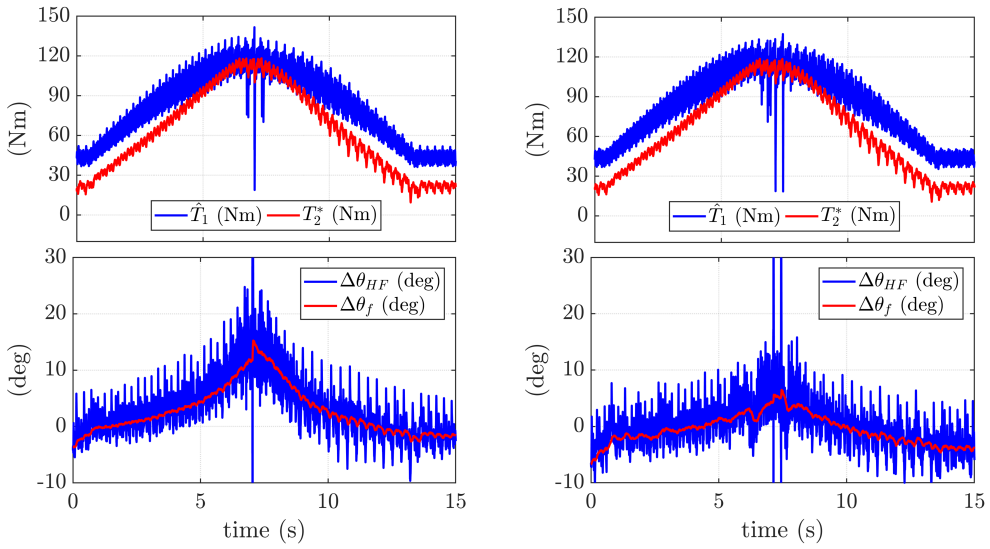

Figure 5.14: Slow torque ramps at 100 rpm when the rotor position is sensorless evaluated based on HF voltage injection and demodulation of (a) i_{q} current; (b) $\lambda^{i}_{\hat{\mathrm{q}}\mathrm{h}}$ flux estimate.

5.1.7.2 Step Response of Torque Control

At high speed, the flux observer was conveniently adopted for estimating the stator flux vector in $\alpha\beta$ reference frame. The HF injection is dropped off (k=0 in Figure 5.12) and the rotor position and speed are purely model based estimated exploiting the active flux concept, according the scheme in Figure 2.14. Because of the relatively high i_{q} current needed for ribs saturation (approximately 60÷80 A), the variation of apparent L_{q} with the working point is relevant and must be taken into account, especially at low speed. In any case, because of the drastic lack of ribs saturation at no load and for the very high harmonic content it was not possible to accurately retrieve the rotor position for torque lower than 20 Nm. The flux maps obtained in self-commissioning were adopted both for flux observer and L_{q} adaptation. A PLL position tracking loop was adopted to filter the estimated position and at the same time estimate the rotor speed.

At first, the motor under test was torque controlled while the speed was imposed by the twin machine. In Figure 5.15,[3] the mechanical speed was

[3]In the Figures 5.15-5.19, the subplots present, from top to bottom: 1. reference, measured and estimated speed; 2. reference and observed torque; 3. dq currents in the motor under test; 4. dq current in the twin machine; 5. position error.

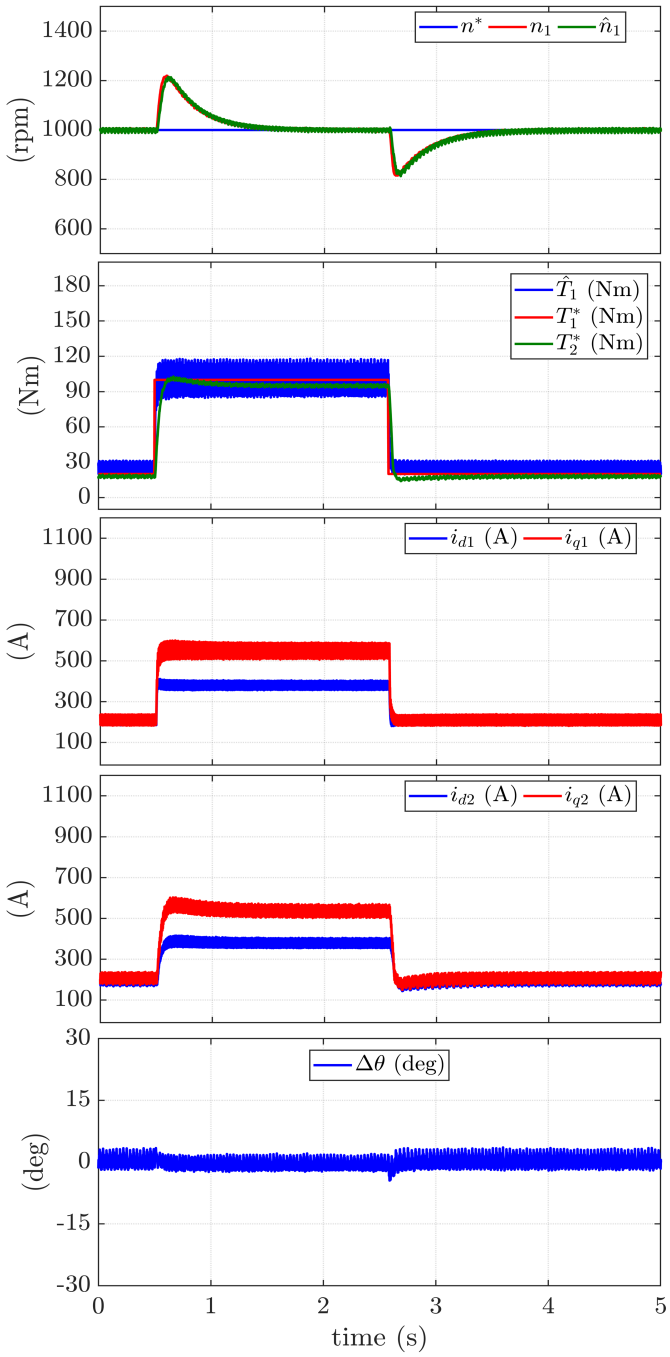

Figure 5.15: Sensorless torque control at 1000 rpm with a reference step $T^* = 100\ Nm$. Respect to the rated parameters: $n = 0.077\ pu$, $T = 0.52\ pu$.

1000 rpm while a step reference torque of 100 Nm was applied. As can be

seen, the torque response is very fast and the position error is negligible even during transient. The speed overshoot is related to the speed loop dynamic of the second motor, and not dependent on the sensorless algorithm.

Then, the test was repeated at lower speed (250 rpm, i.e. 2% of the rated speed), as can be seen in Figure 5.16. According to the theory, the reliability of the model based position estimation is reduced under such low pu speed. Anyway, despite larger, the position error was still under control and the torque dynamic is similar to the previous test. A small discrepancy between reference and observed torque is visible. This is explained considering that the motor control is based on *dq* current vector control, so the reference $i_{\mathrm{d}}^{*}, i_{\mathrm{q}}^{*}$ are set based on MTPA trajectory, computed from the flux maps. Conversely, at sufficiently high speed the motor flux (and so the torque) are estimated from back-EMF integration. A possible mismatch between the two flux estimates explains the discrepancy between T^{*} and the observed torque.

A last test in torque control mode was performed at 1000 rpm but with a step of T^{*} up to 160 Nm, i.e. 92% of the rated load. As can be seen in Figure 5.17, despite the higher required torque the position error is still negligible both in steady state and transient conditions.

5.1.7.3 Sensorless Speed Control

Then, the motor under test was speed controlled, while the load was imposed by the twin machine. The observed speed was retrieved from the integral gain of the PLL without need of further filters. As a first test, the reference speed was stepwise increased from 1000 to 4000 rpm with a maximum acceleration rate of 2000 rpm/s in Figure 5.18. The auxiliary machine imposed a minimum load of 20 Nm. As can be seen, the speed estimation is reliable and the position error bounded between ±5 °.

Finally, a load step of 90 Nm was applied while the motor under test was speed controlled at 1000 rpm. The results are report in Figure 5.19. Despite the low pu speed, the position tracking successfully worked, again with a position error bounded between ±5 °. The speed dynamic is fairly good and capable of recovering the speed overshoot due to the applied load.

5.1.7.4 Conclusions

In conclusion, the preliminary results on sensorless control of this machine are satisfactory and promising. The future development of this research topic will include the migration to DFVC for motor control, the fusion between low and high speed regions in a unique sensorless algorithm and possible improvement of the position and speed estimation bandwidth. Particular

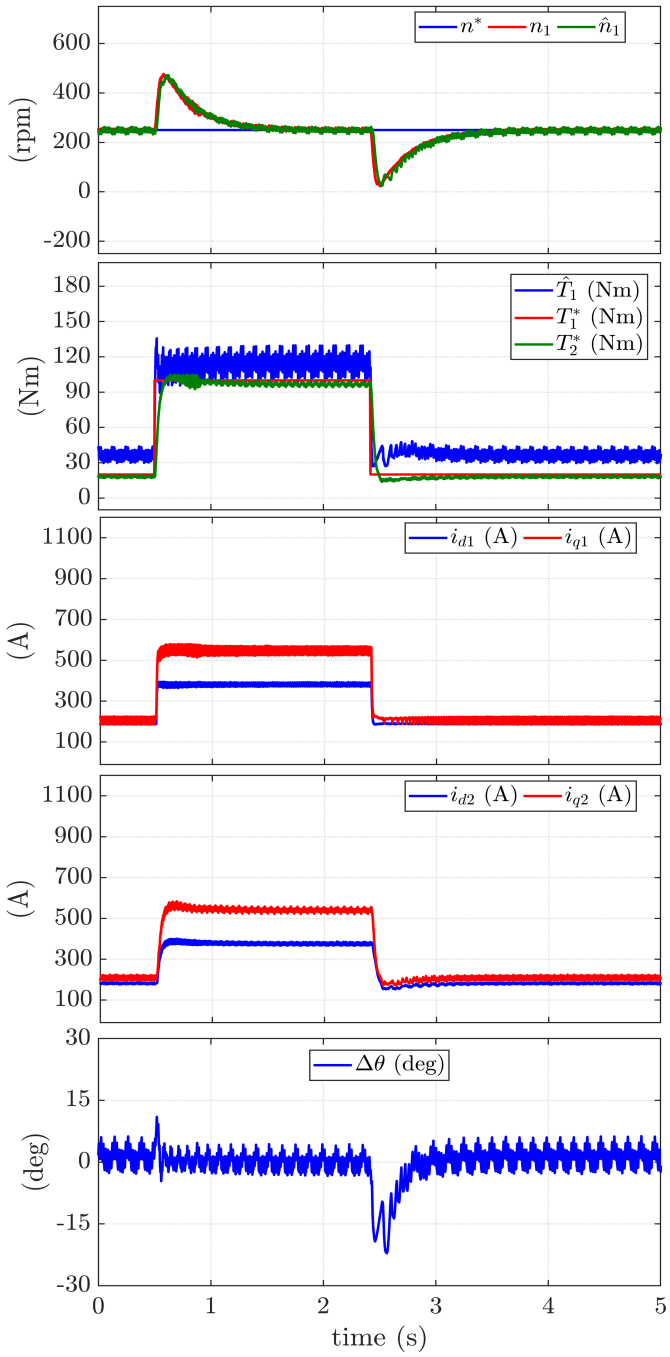

Figure 5.16: Sensorless torque control at 250 rpm with a reference step $T^* = 100\ Nm$. Respect to the rated parameters: $n = 0.019\ pu$, $T = 0.52\ pu$.

attention will be given to the harmonic content of the machine, which resulted

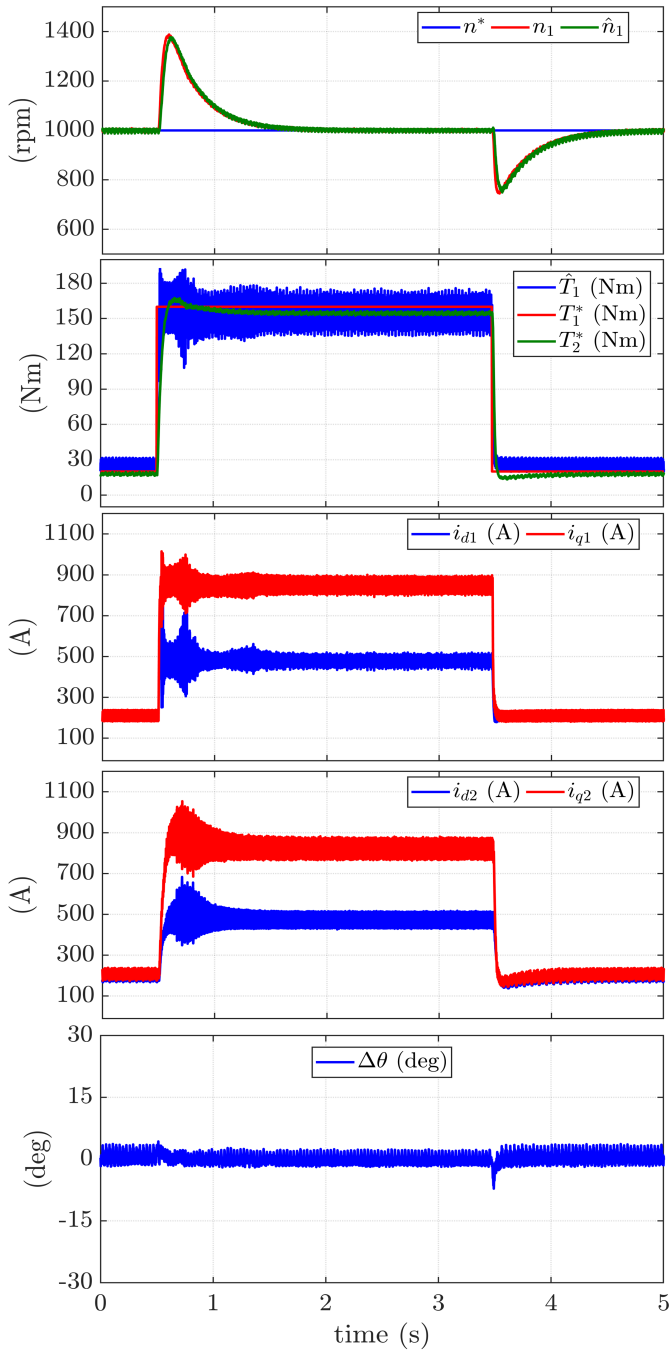

Figure 5.17: Sensorless torque control at 1000 rpm with a reference step $T^* = 160\ Nm$. Respect to the rated parameters: $n = 0.077\ pu$, $T = 0.92\ pu$.

the most limiting factor for the control development.

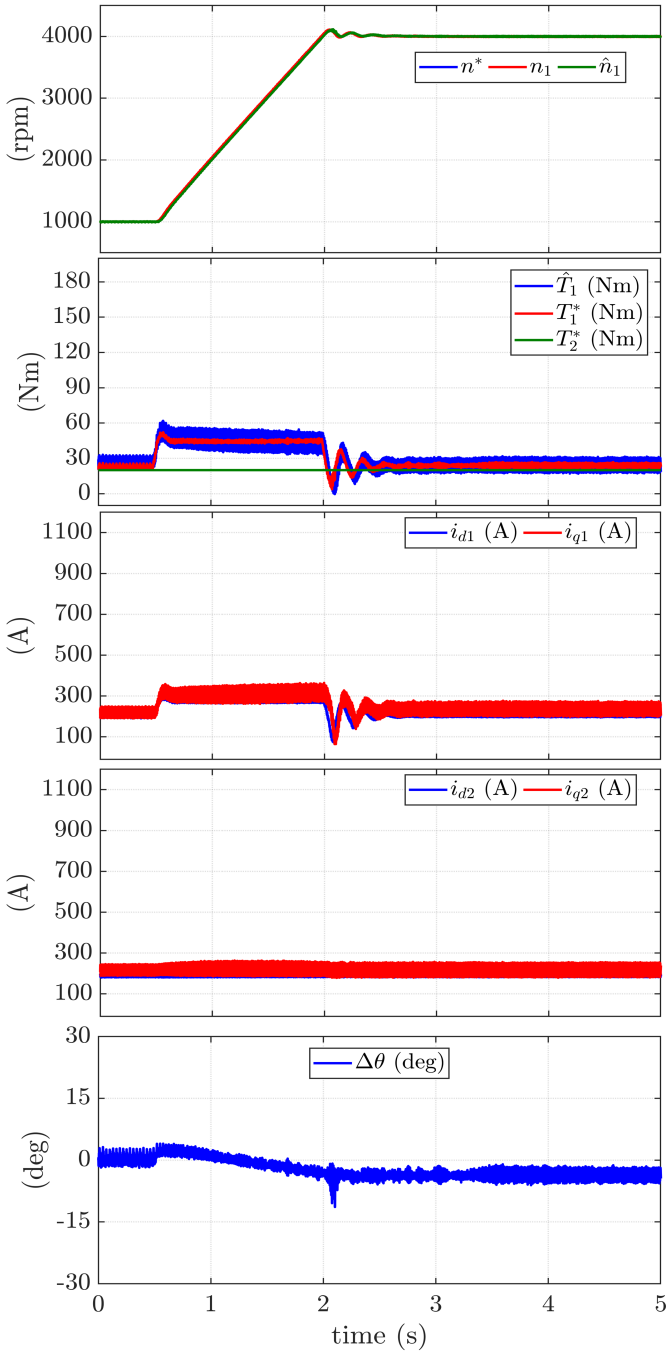

Figure 5.18: Sensorless speed control with a reference step $\omega^* = 4000\ rpm$.

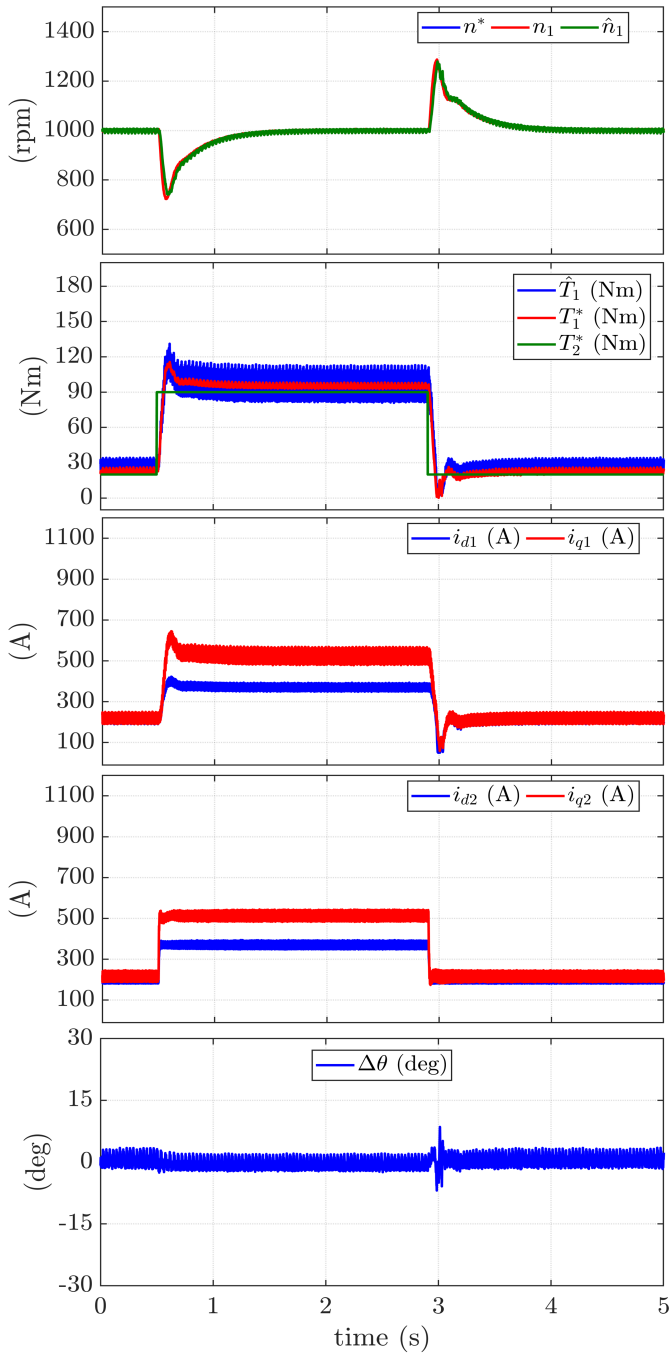

Figure 5.19: Sensorless speed control with a step load of 90 Nm.

5.2 Dual Winding Technology

Part of the work described in this Section has been previously published in [15].

One of the main problems related to the application of SyR machines for high power starter alternators in aviation applications is the relevant current size due to low power factor, which leads to a big power electronic converter.

This Section investigates an innovative technology, called Dual Winding (DW), which is expected to considerably reduce the size of the converter, with relevant volume and weight reduction. First of all, the power factor of the machine is considerably increased, and so the current rating is decreased, by adding PM to the rotor, thus adopting a PM-SyR generator. Then, the DW concept is based on an innovative architecture and custom dual-three-phase winding, which further limits the current rating of the converter.

This research analyzed the feasibility of DW technology for avionic applications. Within the project, an existing PM-SyR machine, called PM7kW5, was custom re-winded after preliminary simulation analysis to build a DW-SyR prototype. The prototype was then experimentally tested emulating real operating conditions. Finally, guidelines for future DW machine design were retrieved.

The Section is developed as follow. At first, the DW concept is explained, together with the definition of the main machine parameters (Section 5.2.1). The characteristic of the original PM-SyR machine and the target DW-SyR prototype are detailed in Section 5.2.2. The state equations of a proper machine model were retrieved in Section 5.2.3, which also presents two simulation models: the first using Finite Element Analysis and the second using Matlab-Simulink environment (lumped parameters model). Both these models have been necessary to properly design the DW machine prototype, as will be discussed in Section 5.2.4. Proper control strategies and efficiency optimization are discussed in Section 5.2.5 and 5.2.6 respectively. The machine prototype was experimentally tested in Section 5.2.7. The results highlighted a relevant problem of unbalanced temperature distribution inside the motor. Therefore, a proper thermal model was investigated in Section 5.2.8. Finally, Section 5.2.9 summarizes the guidelines for future DW machine design.

5.2.1 DW Concept and Definitions

A DW machine is a particular case of PM-SyR multiple 3-phase machine with two 3-phase sets, which will be called primary and secondary and indicated with the subscript 1 and 2 respectively. In the following, the two sets will

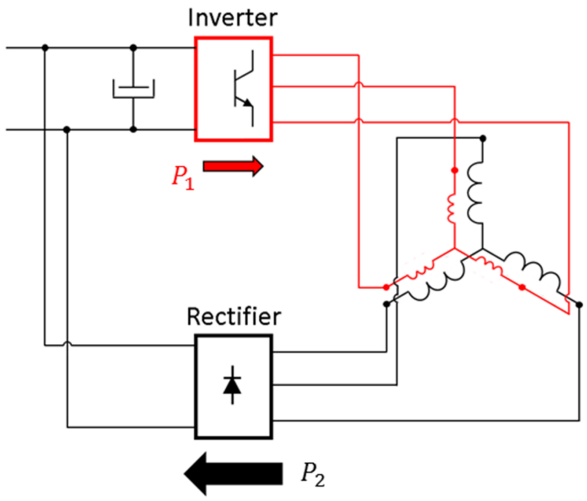

Figure 5.20: Scheme of DW-SyR machine operated as a generator, with common dc-link.

be also called excitation and armature circuits respectively. Despite it can be used in motoring mode, this machine is mainly designed for working as generator, to supply the DC bus for all the on-board auxiliary services and charging an eventual battery.

The main goal of DW technology is to reduce the size of the power electronic converter. For doing this, a dedicated architecture is adopted, as depicted in Figure 5.20. Both the winding sets are connected to the same DC bus, but the primary winding is supplied by a standard 3-phase inverter, while the secondary winding is connected through a simple diode bridge. So, the primary winding only is voltage controlled, while the voltage and current in the secondary winding depend on the conditions of the system.

The primary winding is designed to supply the excitation current, while the secondary winding is expected to generate the output active power. Considering, as an example, the SR250kW prototype, at the maximum load the excitation current is only 30% of the maximum current. It means that, potentially, the 3-phase inverter supplying the primary winding should be sized for 30% only of the rated current, while the main part of the current would flow into a simple and compact diode bridge.

Some of the key parameters and notations are defined here. Similarly to PM-SyR machines, the d axis is aligned with the maximum inductance direction, so the λ_{pm} flux is pointing negative q axis. The voltages, currents, flux linkages and stator resistances in the primary and secondary windings are called, respectively, $\boldsymbol{v}_{1,\text{dq}}$, $\boldsymbol{v}_{2,\text{dq}}$, $\boldsymbol{i}_{1,\text{dq}}$, $\boldsymbol{i}_{2,\text{dq}}$, $\boldsymbol{\lambda}_{1,\text{dq}}$, $\boldsymbol{\lambda}_{2,\text{dq}}$, R_{s1} and R_{s2}.

The definition of machine efficiency η is not univocal. The DW machine

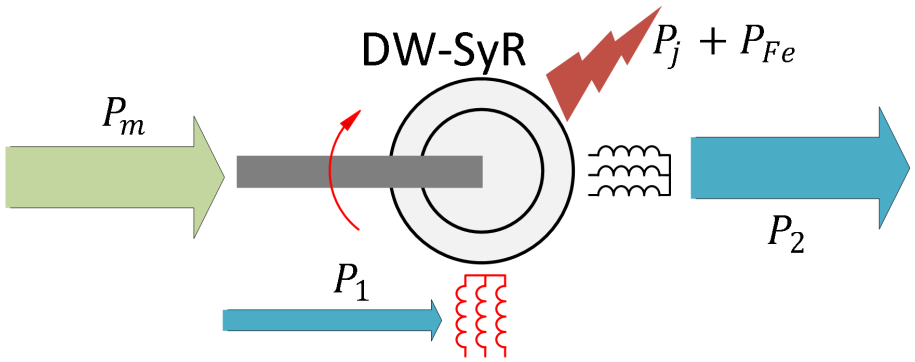

Figure 5.21: Adopted conventions for input and output power.

has two electrical ports (primary and secondary windings) and one mechanical port. Energy conversion involves all such three ports. The input/output power convention of the DW machine are defined as in Figure 5.21, where P_1 and P_2 are the power in the excitation and armature circuits, P_m is the mechanical power and P_j and P_Fe are the total joule and iron losses, respectively. The figure was built assuming the DW machine is a generator, where the mechanical power is the input power and the armature power P_2 is the main output power. In normal circumstances, the excitation circuit is absorbing power as in the figure, and accounts for loss involved in the excitation process. Nevertheless, the inverter driven excitation windings can be controlled to generate active power, so that a negative P_1 is produced, in addition to the output power P_2. Therefore, the machine efficiency is calculated in as:

$$\eta = \frac{P_2}{P_1 + P_\mathrm{m}} \qquad P_1 > 0 \tag{5.2a}$$

$$\eta = \frac{P_2 - P_1}{P_\mathrm{m}} \qquad P_1 < 0 \tag{5.2b}$$

In addition to the machine efficiency η, two more quantities are defined to consider the losses into the converter, considered as the aggregate of excitation inverter and diode rectifier. The converter efficiency is given by the ratio between its input and output electrical power:

$$\eta_\mathrm{conv} = \frac{P_\mathrm{dc}}{P_2 - P_1} \tag{5.3}$$

Where P_dc is the electrical power supplied to the load and the term $(P_2 - P_1)$ is the net electrical output power produced by the machine, independently by the sign of P_1. Finally, the total efficiency (machine + converters) is given by:

Table 5.4: Specifications of the original PM-SyR machine.

v_{dc}	350 V
Rated current (peak)	24 A
Max current (peak)	48 A
Rated torque	22 Nm
Max torque	44 Nm
Rated power	7.5 kW
Max power at 3000 rpm	13.5 kW
Rated speed	3000 rpm
Max speed	9000 rpm
Pole pairs	2
Number of slots	36
Number of turns per phase	72
Windings	Single layer full pitch

$$\eta_{tot} = \frac{P_{dc}}{P_m} \tag{5.4}$$

Figure 5.33 helps describing the above defined powers.

5.2.2 Original PM-SyR Machine and Target DW-SyR Prototype

A 7.5 kW PM-SyR machine, originally called PM7kW5, was rewinded to obtain the DW-SyR prototype. The nameplate of the PM7kW5 is report in Table 5.4. The stator and rotor geometry were maintained, and only the original winding was replaced with the two 3-phase sets. Table 5.5 defines the target performances of the rewinded DW machine.

It must be noted that for this motor the current angle on the MTPA at the rated load is considerably lower than for the SR250kW machine, which means a higher excitation current is required in percentage. For this reason,

Table 5.5: Target performances of the DW-SyR prototype.

v_{dc}	270 V
Rated DC load	40 A
Peak DC load	80 A
Rated power	10.8 kW
Peak power	21.6 kW
Rated speed	3000 rpm
Const. P speed range	3000 ÷ 6000 rpm
Pole pairs	2

the current in the primary channel $\boldsymbol{i}_{1,\mathrm{dq}}$ cannot be reduced at 30% of the rated current, as previously declared, but to roughly 50%, with consequent lower advantages on the inverter size. Anyway, being the first DW prototype, the main goal was to prove the applicability of the DW concept and define proper design guidelines for future machines.

5.2.3 Machine Modeling

In this Section, proper model of the DW-SyR machine is obtained, with a double goal: defining the design parameters of the DW-SyR prototype and testing the machine controllability and stability.

Two models of the DW-SyR machine were adopted: one based on the Finite Elements Method (FEM) and one based on lumped parameters and state equations (Simulink). Both the models were calibrated using the available information coming from the original PM7kW5.

The FEM model is used to precisely determine the steady-state performance of the machine in single operating points. Conversely, the Matlab/Simulink dynamic model is more adaptable and it is used for testing the dynamic response of the machine, the closed-loop control strategy of the field channel and the performances under different control strategies with reduced computational time, at the cost of neglecting second order phenomena, e.g. iron loss and field harmonics caused by the stator and rotor slots effects. Moreover, it is possible to calibrate the control.

Finally, the information coming from both the models were merged to

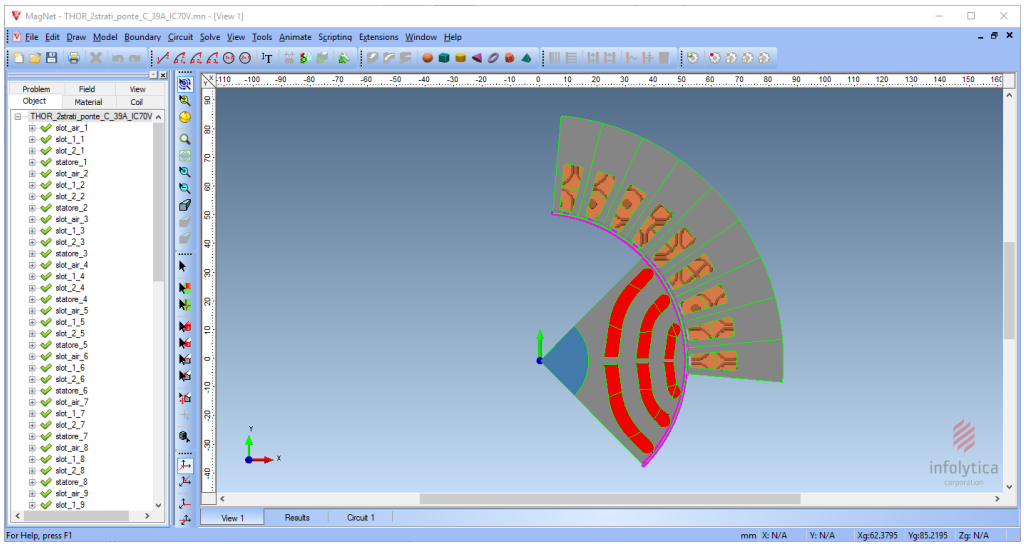

(a)

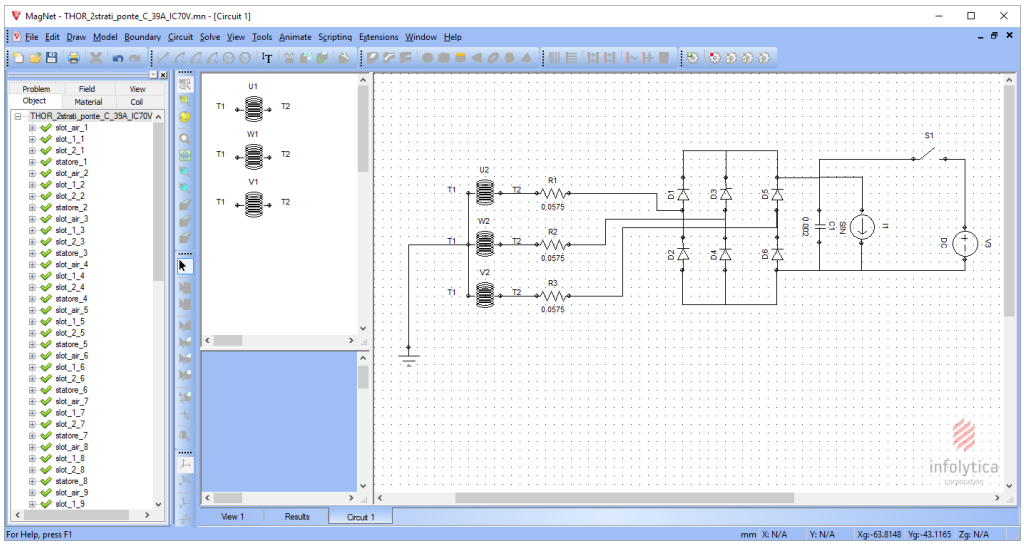

(b)

Figure 5.22: FEM model in Infolytica/MagNet and its circuit model.

design the DW-SyR prototype, combining the machine design stage with the controllability issues.

5.2.3.1 Finite Element Model

The FEM model of the DW-SyR machine, shown in Figure 5.22, is implemented using MagNet, by Infloytica. The FEM model covers the electro-

magnetic and electro-mechanical aspects of the machine, including shaft speed and torque and iron loss evaluation. One pole only is represented to reduce the computational burden, using anti-periodic boundary conditions.

The rotor speed is set to a constant value, the field windings are current supplied with sinusoidal waveforms and the power windings are connected to a rectifier bridge plus a load, using the circuital interface feature of Infolytica/Magnet. The rotor and stator mesh are connected through a sliding mesh placed in the airgap area that permits the rotor movement from one time step of the solver to the next one. The results are the key electrical (current, voltage, flux linkage, copper and iron loss) and mechanical quantities (position, speed, torque, force), in the form of instantaneous values in the time range of the simulation.

5.2.3.2 State Space Model of DW-SyR Machine

This Section summarizes the state space equations retrieved to model the DW-SyR machine. Extending the PM-SyRM model in rotor *dq* coordinates, the voltage vectors for the primary and secondary circuit are obtained:

$$\boldsymbol{v}_{1,\mathrm{dq}} = R_{\mathrm{s1}}\boldsymbol{i}_{1,\mathrm{dq}} + \frac{\mathrm{d}\boldsymbol{\lambda}_{1,\mathrm{dq}}}{\mathrm{d}t} + j\omega\boldsymbol{\lambda}_{1,\mathrm{dq}} \tag{5.5a}$$

$$\boldsymbol{v}_{2,\mathrm{dq}} = R_{\mathrm{s2}}\boldsymbol{i}_{2,\mathrm{dq}} + \frac{\mathrm{d}\boldsymbol{\lambda}_{2,\mathrm{dq}}}{\mathrm{d}t} + j\omega\boldsymbol{\lambda}_{2,\mathrm{dq}} \tag{5.5b}$$

Where j is the imaginary unit in the complex numbers vector notation. The flux linkage vector in each winding set is given as:

$$\boldsymbol{\lambda}_{1,\mathrm{dq}} = L_{\sigma 1}\boldsymbol{i}_{1,\mathrm{dq}} + \boldsymbol{\lambda}_{1,\mathrm{m}} \tag{5.6a}$$

$$\boldsymbol{\lambda}_{2,\mathrm{dq}} = L_{\sigma 2}\boldsymbol{i}_{2,\mathrm{dq}} + \boldsymbol{\lambda}_{2,\mathrm{m}} \tag{5.6b}$$

where $L_{\sigma 1}$ and $L_{\sigma 2}$ are the leakage inductances of the two circuits and $\boldsymbol{\lambda}_{1,\mathrm{m}}$ and $\boldsymbol{\lambda}_{2,\mathrm{m}}$ are the magnetizing fluxes. Similarly to a transformer, the relationship between $\boldsymbol{\lambda}_{1,\mathrm{m}}$ and $\boldsymbol{\lambda}_{2,\mathrm{m}}$ is given by the number of turn ratio:

$$\boldsymbol{\lambda}_{2,\mathrm{m}} = \frac{N_2}{N_1}\boldsymbol{\lambda}_{1,\mathrm{m}} \tag{5.7}$$

where N_1 and N_2 are the number of turns in the primary and secondary circuits respectively. For each winding set, the magnetizing flux is a function of the correspondent magnetizing current $i_{1,\mathrm{m}}$, $i_{2,\mathrm{m}}$. As an example, for the excitation circuit we have:

$$\boldsymbol{\lambda}_{1,\mathrm{m}} = \begin{cases} \lambda_{1\mathrm{m,d}}(i_{1\mathrm{m,d}}, i_{1\mathrm{m,q}}) \\ \lambda_{1\mathrm{m,q}}(i_{1\mathrm{m,d}}, i_{1\mathrm{m,q}}) \end{cases} \tag{5.8}$$

This non-linear relationship is given by an extended concept of flux maps, where the magnetizing current is the weighted sum of the two currents considering the number of turns:

$$\boldsymbol{i}_{1,\mathrm{m}} = \boldsymbol{i}_{1,\mathrm{dq}} + \frac{N_2}{N_1}\boldsymbol{i}_{2,\mathrm{dq}} \tag{5.9}$$

As can be seen, up to here the machine equations are similar to a transformer with variable coupling between the windings. Finally, the electromagnetic torque is given by the cross-product between magnetizing flux and current, either at the primary or secondary side:

$$T = \frac{3}{2}p\left(\lambda_{1\mathrm{m,d}} i_{1\mathrm{m,q}} - \lambda_{1\mathrm{m,q}} i_{1\mathrm{m,d}}\right) \tag{5.10}$$

5.2.3.3 Lumped Parameter Model

An overview of the model is given in Figure 5.23(a). It is a circuital model built using Simscape power components to simulate the three-phase primary and secondary windings of the machine. The former are in the form of three controlled current generators (in the upper part of the violet box) and the latter are three controlled voltage generators (lower part of the violet box). Parasitic series and parallel resistances were added to both the circuits to improve the stability of the simulation without affecting the machine model.

The secondary side is connected to a diode bridge, this is connected to the dc-link capacitor, and finally to a current generator, simulating a programmable DC load. The primary side is supplied by three controlled voltage generators representing the voltage source inverter controlling the excitation current, commanded by the CONTROL box.

The dc-link voltage is closed-loop controlled by regulating the excitation circuit. Several control strategies were implemented, as later explained.

The orange block in Figure 5.23(a) contains the state-space equations of the electrical machine, which command the controlled voltage and current generators introduced above. The subsystem within the orange box is report in Figure 5.23(b). This subsystem is based on the *dq* flux maps of the original PM-SyR machine (single three phase) experimentally obtained through [40]. The main approximation introduced with this modelling approach is that slot harmonics are not taken into account. Minor approximations refer to neglected iron loss and leakage inductances. According to FEM simulations,

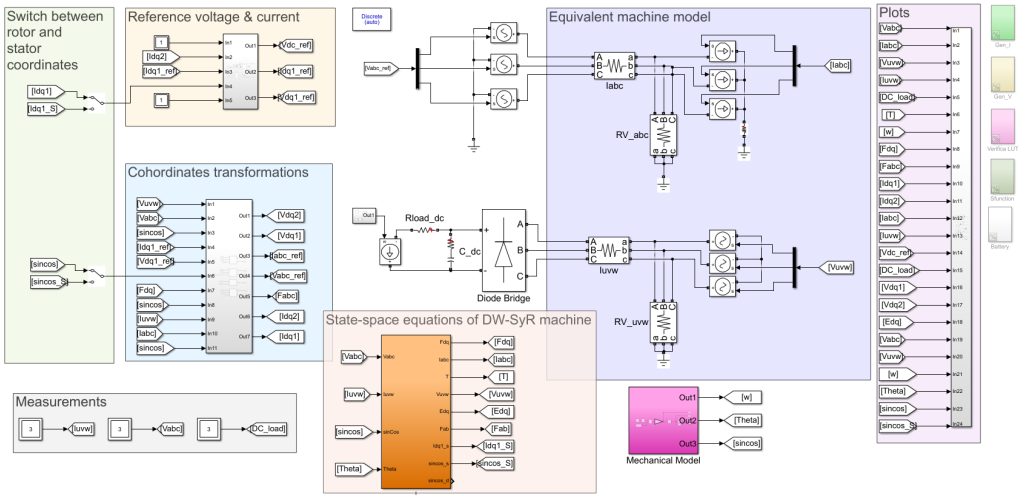

(a)

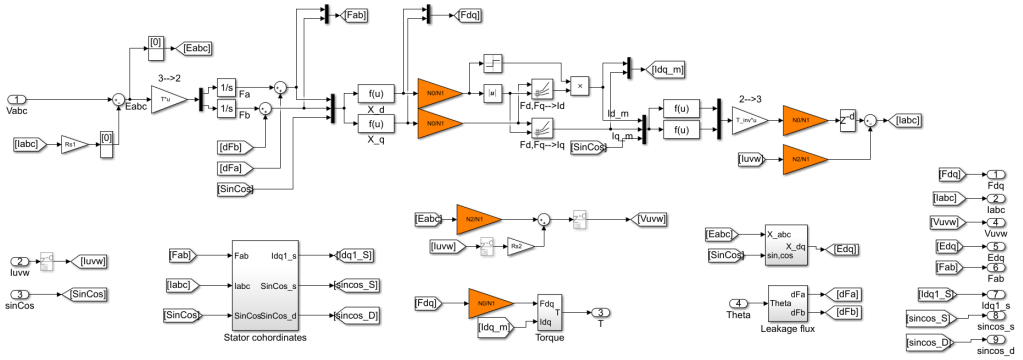

(b)

Figure 5.23: (a) Simulink model of the DW-SyR machine and implementation of state space equations.

those two effects have minor impact on the control dynamics. Iron loss can be off-line computed, when dealing with efficiency evaluation.

Since leakage inductances are neglected, the magnetizing and total flux linkages are equal:

$$L_{\sigma 1} = L_{\sigma 2} = 0 \tag{5.11}$$

$$\begin{cases} \boldsymbol{\lambda}_{1,\mathrm{dq}} = \boldsymbol{\lambda}_{1,\mathrm{m}} \\ \boldsymbol{\lambda}_{2,\mathrm{dq}} = \boldsymbol{\lambda}_{2,\mathrm{m}} \end{cases} \tag{5.12}$$

The vectors $\boldsymbol{v}_{1,\mathrm{dq}}$ and $\boldsymbol{i}_{2,\mathrm{dq}}$ are considered input quantities, while $\boldsymbol{v}_{2,\mathrm{dq}}$ and $\boldsymbol{i}_{1,\mathrm{dq}}$ are the outputs. The voltage $\boldsymbol{v}_{1,\mathrm{dq}}$ is imposed by the inverter, $\boldsymbol{i}_{2,\mathrm{dq}}$ is

measured at the armature circuit, $\boldsymbol{i}_{1,\mathrm{dq}}$ is the closed-loop controlled excitation current and $\boldsymbol{v}_{2,\mathrm{dq}}$ sets the output voltage of the armature circuit, connected to the diode bridge. The model is solved in stator coordinates $\alpha\beta$. The flux is obtained through back-EMF integration:

$$\boldsymbol{\lambda}_{1,\alpha\beta} = \int \boldsymbol{e}_{1,\alpha\beta}\mathrm{d}t = \int \boldsymbol{v}_{1,\alpha\beta} - R_{\mathrm{s}1}\boldsymbol{i}_{1,\alpha\beta}\mathrm{d}t \tag{5.13}$$

By computing the voltage integration in $\alpha\beta$ frame the motional term does not appear in the equation, avoiding an algebraic loop in the model. Then, the flux is rotated to the dq frame. The primary flux vector is reported to a different number of turns $N_0 = 72$, which is the number of turns of the original PM-SyR machine PM7kW5:

$$\boldsymbol{\lambda}_{0,\mathrm{dq}} = \frac{N_0}{N_1}\boldsymbol{\lambda}_{1,\mathrm{dq}} \tag{5.14}$$

From the flux vector in PM7kW5 coordinates, the equivalent magnetizing current $\boldsymbol{i}_{0,\mathrm{dq}}$ is obtained from two dimensional look-up-table in (5.15), still referring to a machine with N_0 turns. This permits to use the flux maps of the original PM-SyRM, experimentally identified. In other words, $\boldsymbol{i}_{0,\mathrm{dq}}$ is considered an equivalent magnetizing current producing the same excitation as the aggregate of primary and secondary currents (5.16).

$$\boldsymbol{i}_{0,\mathrm{dq}} = f(\boldsymbol{\lambda}_{0,\mathrm{dq}}) \tag{5.15}$$

$$N_0\boldsymbol{i}_{0,\mathrm{dq}} = N_1\boldsymbol{i}_{1,\mathrm{dq}} + N_2\boldsymbol{i}_{2,\mathrm{dq}} \tag{5.16}$$

The following set of equations complete the machine model in $\alpha\beta$ reference frame.

$$\boldsymbol{i}_{0,\alpha\beta} = e^{j\theta}\boldsymbol{i}_{0,\mathrm{dq}} \tag{5.17}$$

$$\boldsymbol{i}_{1,\alpha\beta} = \frac{N_0}{N_1}\boldsymbol{i}_{0,\alpha\beta} - \frac{N_2}{N_1}\boldsymbol{i}_{2,\alpha\beta} \tag{5.18}$$

$$\boldsymbol{v}_{2,\alpha\beta} = \frac{N_2}{N_1}\boldsymbol{e}_{1,\alpha\beta} + R_{\mathrm{s}2}\boldsymbol{i}_{2,\alpha\beta} \tag{5.19}$$

5.2.3.4 Validation of the lumped parameter model

In this section, the FEM model is considered as the reference model, and used for validating the Simulink lumped parameter model in a reference steady operating point at constant speed (3000 rpm). The excitation current is

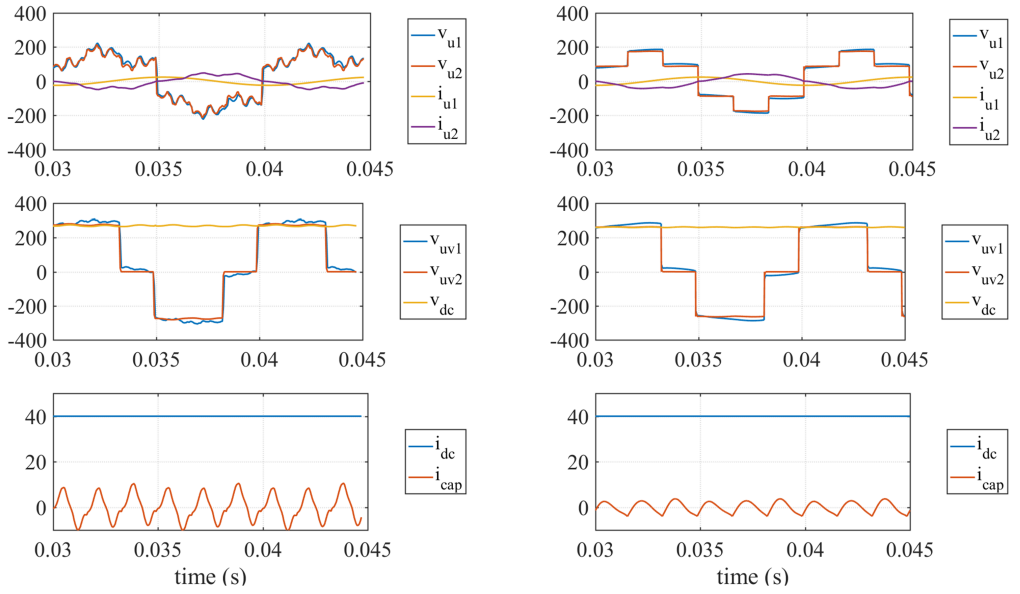

(a)

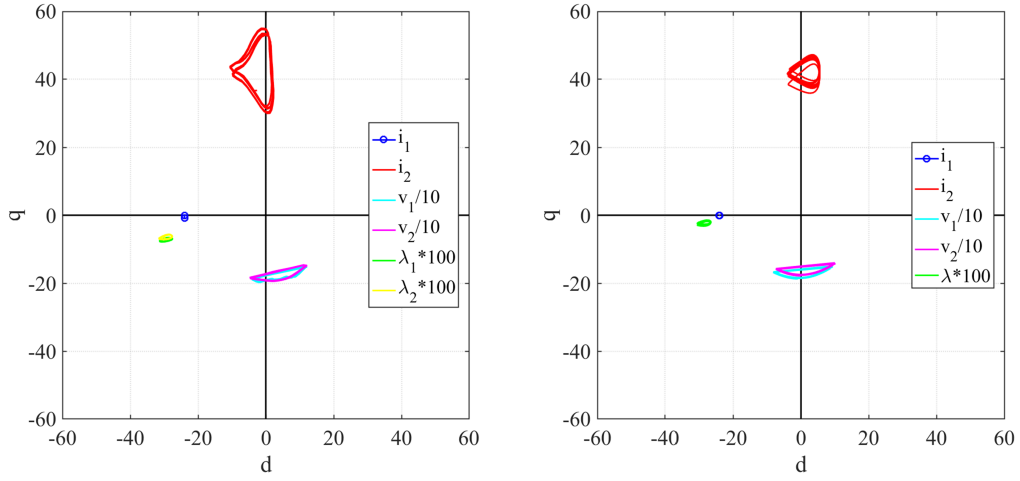

(b)

Figure 5.24: Comparison between FEM (left) and Simulink (right) models. (a) Time waveforms; (b) vectors in the *dq* plane.

closed-loop controlled at $i_{1,\mathrm{d}}$=-24 A,$i_{1,\mathrm{q}}$=0 A and the dc load is set to i_{dc}=40 A. The current and voltage waveforms from the two models are compared in Figure 5.24(a), while Figure 5.24(b) shows the instantaneous space vectors in the *dq* plane. As can be seen, the results of the two models are compatible. The higher oscillations in the phase voltage and capacitor current in the FEM simulation can be explained considering the slot harmonics are not

represented in the Simulink model.

5.2.4 Prototype Design

In the DW-SyR prototype, every slot is filled with windings belonging to both the 3-phase sets. The two windings share the total slot space available in the existing prototype, so optimal split ratio of the cross-sectional area between the two windings was determined based on the FEM simulations. Despite the machine efficiency resulted low sensitive to the choice of the split ratio, using 38 % of the slot area for the primary winding and 62 % for the secondary set resulted to minimize the total copper losses at maximum load.

Several solutions were considered for defining the number of layers (single, double or four layers) and windings configuration (full pitch or pitch shortening, by 1, 2 or 3 slots in case of four layers). After this analysis, the two layers solution was selected as the best compromise between performances, ease of manufacturing and axial length.

The choice of the appropriate number of turns in the two windings involved both FEM and Simulink simulations. The stator and rotor design define saturation characteristic of the core in terms of airgap induction. Then, neglecting the leakage fluxes, the induced voltage on the two windings is proportional to the respective number of turns. Therefore, considering that the armature winding is connected to the DC bus through a diode bridge, the number of turns of the secondary winding was chosen in such a way that at the rated operating point the induced voltage in the secondary winding

Table 5.6: Description of the DW-SyR prototype.

	Primary	Secondary
Stack length (mm)	120	
End-winding length (mm)	120	134
Number of turns per phase	30	60
Number of turns per coil	5	9
Number wires in parallel	5	5
Elementary wire diameter (mm)	0.8	0.8
Phase resistance (Ω)	0.194	0.372
Slot filling factor	>0.38	

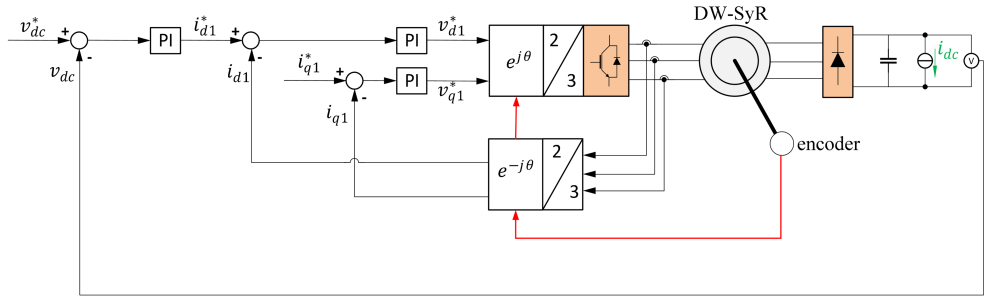

Figure 5.25: Block scheme of the current vector control strategy in rotor coordinates.

could supply the v_{dc}. From this analysis, N_2=60 was chosen considering the v_{dc} and base speed specifications of 270 V and 3000 rpm, respectively.

As the primary and secondary converters are connected to the same dc-link, the choice $N_1 = N_2$ might sound reasonable, since similar voltage ratings are expected. In fact, the back-emf voltages seen by the two winding sets are practically identical for equal number of turns, thanks to the good mutual coupling between the two 3-phase sets. However, when the effect of resistance voltage drop at the primary and the secondary sides plus the inverter voltage drop are taken into account, it turns out that the primary inverter cannot effectively closed loop regulate the excitation current with $N_1 = N_2$. In turn, the common dc-link configuration strictly dictates $N_1 < N_2$. As the feasible numbers of turn values for this machine are multiple of 6, the Simulink model was run to test closed-loop control of the excitation current for N_1=54, N_1=48 and N_1=42, resulting that sufficient voltage margin is not guaranteed using 54 or 48 turns, but it is sufficient at N_1=42.

It must be remarked that that the ratio N_2/N_1 >1 is also representative of inverter size upscaling, respect to the minimum size condition $N_1 = N_2$, since the excitation current grows proportionally with $1/N_1$. Since the designed DW prototype was a first proof of concept machine, and considering that the available converter has a redundant current rating, a large precautionary margin was kept, adopting N_1=30, despite in this configuration it will not be observed a relevant reduction of the inverter size.

Table 5.6 reports the obtained specifications of the DW-SyR prototype.

5.2.5 Current Vector Control of the DW-SyR Machine

A first control strategy for the excitation circuit is represented in Figure 5.25, where $\boldsymbol{i}_{1,\mathrm{dq}}$ vector is regulated through dq current loops. For simplicity, the

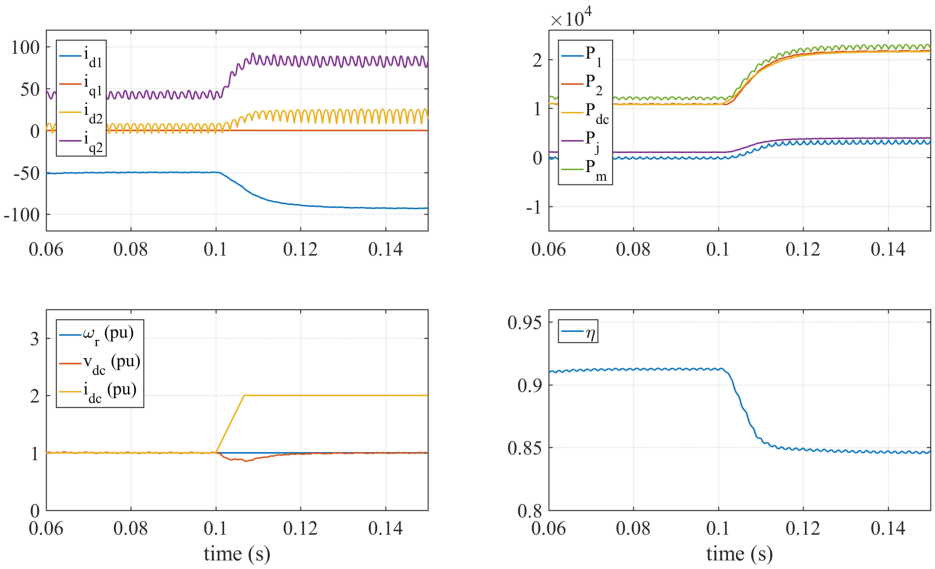

Figure 5.26: Simulated response to a fast load ramp: $i_{\mathrm{dc}} = 40$ A to 80 A in 0.05 s.

$i^*_{1,\mathrm{d}}$ component is used as the field current with the other component set to zero $i^*_{1,\mathrm{q}}$=0. A cascaded voltage loop regulates the dc-link voltage by setting the $i^*_{1,\mathrm{d}}$ reference value.

This control strategy is easy to implement and efficaciously controls the v_{dc}, but it has the disadvantage that a non-zero average excitation power P_1 is produced and regenerated to the dc-link and ultimately to the load. In principle, having power generated also on the P_1 channel is not a problem, as this power is also delivered to the load. However, having active power on this port dedicated to excitation goes against the minimization of the inverter size, and must be avoided or at least controlled.

The stability of this control was simulated applying a fast load ramp (Figure 5.26), a voltage reference step (Figure 5.27) and a speed variation (Figure 5.28). In each case it is visible that P_1 is not null and can be positive or negative at steady-state, i.e. a minor part of the generated power flows through the primary winding instead of the secondary one.

In Figure 5.26, the generator's speed was kept constant (3000 rpm) while the rectified current i_{dc} was rapidly increased from the rated value to two times overload. It can be noticed that the v_{dc} control works properly and is able to regulate the voltage to the rated value. Anyway it is also evident the relevant drop in the efficiency, due to the increased resistive losses. This is reasonable considering the higher excitation current required at high load.

In Figure 5.27, the control response to a step variation of the reference

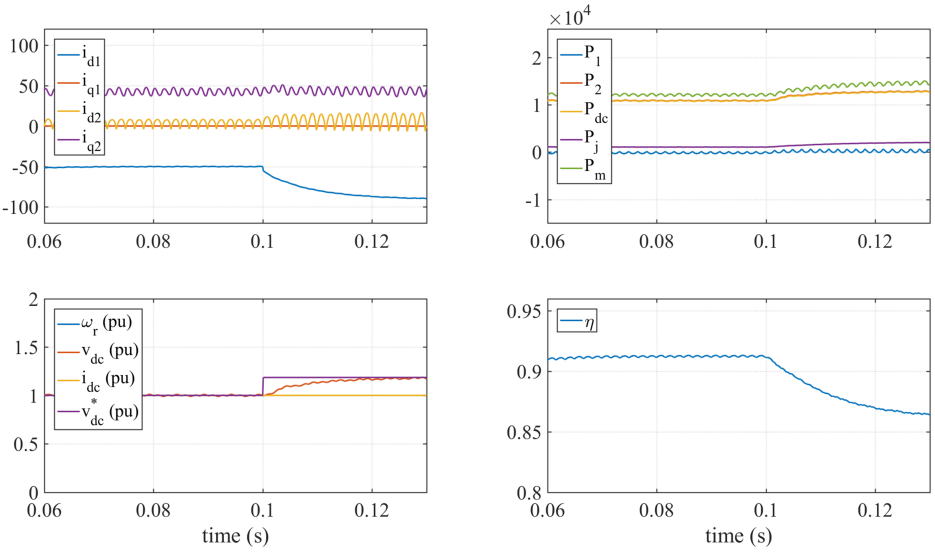

Figure 5.27: Simulated response to a voltage reference step variation: v_{dc} from 270 V to 320 V.

voltage v_{dc}^{*} from 270 V (nominal value) to 320 V (maximum value) is analyzed. The motor speed and load are kept constant at the rated values (i_{dc}=40 A at 3000 rpm). Also in this case, the obtained v_{dc} follows the reference with acceptable delay.

In Figure 5.28, the shaft was accelerated from the rated speed to two times this value under constant i_{dc}. The efficiency increase is evident: at higher speed a lower flux is necessary to achieve the desired v_{dc}, leading to a drastic reduction of the excitation current $\boldsymbol{i}_{1,\mathrm{dq}}$. This effect is even more important considering that in this operating point the relationship between current and flux is nonlinear because of magnetic saturation, so at double speed corresponds roughly half of the flux, but much less than half of the excitation current. Also in this case the control of v_{dc} works properly, since after a first overshoot the voltage loop converges to the reference value.

Finally, the *dq* vector diagram in four selected operating points is report in Figure 5.29. The simulated points[4] are at rated load and two times overload (i_{dc}= 40 A or 80 A) when the machine was rotating at the base speed or two times its value (3000 rpm or 6000 rpm). As can be noticed, thanks to the adopted number of turns ratio, the primary voltage is well below the secondary one, confirming the large voltage margin provided to the inverter

[4]It must be remarked that in this analysis the load current i_{dc} represents the DC current obtained from the armature circuit after the diode bridge rectifier and dc-link capacitor, and not the total DC current, which would also include the supply of the excitation circuit.

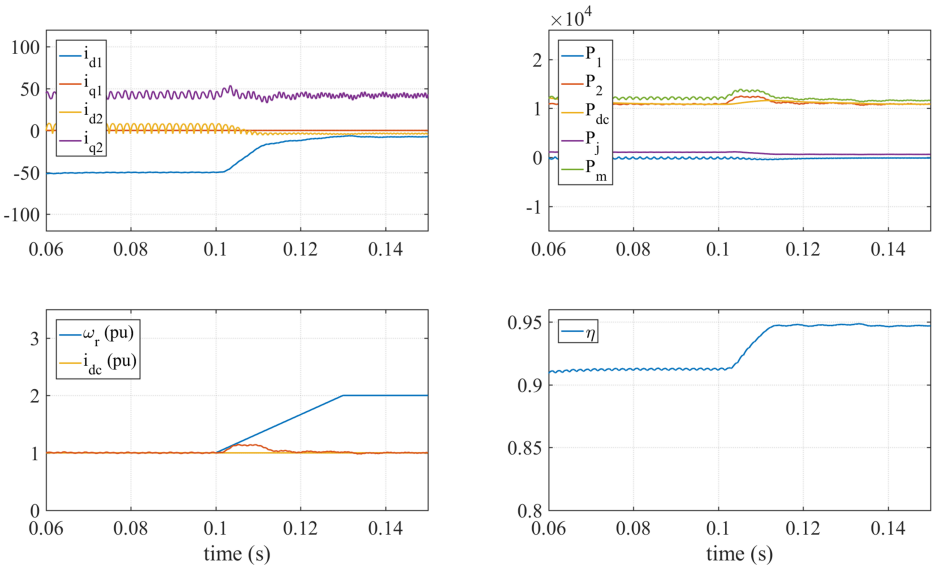

Figure 5.28: Speed transient from rated speed 3000 rpm to max speed 6000 rpm.

for current control. Even at overload conditions the dc-link voltage (270 V) is always considerably higher than the line-to-line excitation voltage. Moreover, being v_{dc} fixed, the amplitude of the primary and secondary voltages is almost constant in every operating point. Finally, it can be noticed that a high load causes a clockwise rotation of the $\boldsymbol{i}_{2,\mathrm{dq}}$ and voltage vectors. If the $\boldsymbol{i}_{2,\mathrm{dq}}$ falls in the first quadrant, as in Figure 5.29(b) and 5.29(d), the armature current tends to de-excite the machine ($i_{2,\mathrm{d}} > 0$), therefore a very high $\boldsymbol{i}_{1,\mathrm{dq}}$ is required.

5.2.6 Control Optimization

This Section describes three techniques for improving the control of the primary winding, to increase the machine efficiency and reliability. Each of them was simulated using the Simulink model.

5.2.6.1 Adopting Flux Weakening to Reduce the Inverter Size

From Figure 5.28 it can be noticed that, for fixed v_{dc}, at higher speed corresponds lower required flux linkage and so lower excitation current, leading to an increased efficiency. Figure 5.30 reports a flux weakening test, where the speed is ramped at constant output power from 3000 rpm to 9000 rpm under constant load current i_{dc}=40 A, and the bus voltage closed loop con-

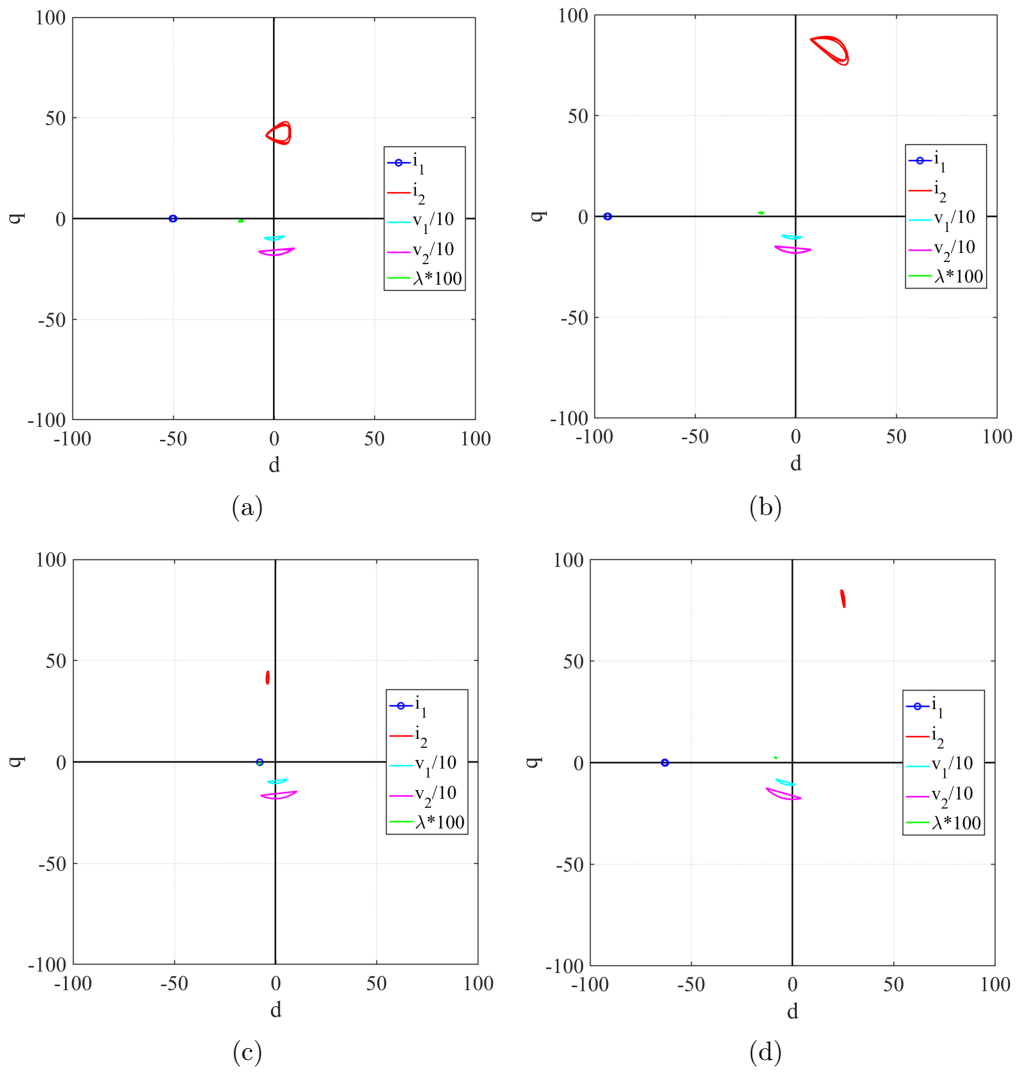

Figure 5.29: Simulated steady state vector diagram in the dq plane at (a) 40 A, 3000 rpm; (b) 80 A, 3000 rpm; (c) 40 A, 6000 rpm; (d) 80 A, 6000 rpm.

trolled at v_{dc}=300 V. As can be seen, the efficiency considerably improves when speed is increased. Such a large constant power speed range, typical for PM-SyR machines, allows relevant reduction of the required field current, and the related joule losses and inverter size. For these reasons, the number of turns of the two windings could be modified for a higher base speed and lower excitation current, to exploit more favorable working points.

It should be noted that the efficiency advantage in Figure 5.30 is probably overestimated, because iron loss is not considered in this simulation. Never-

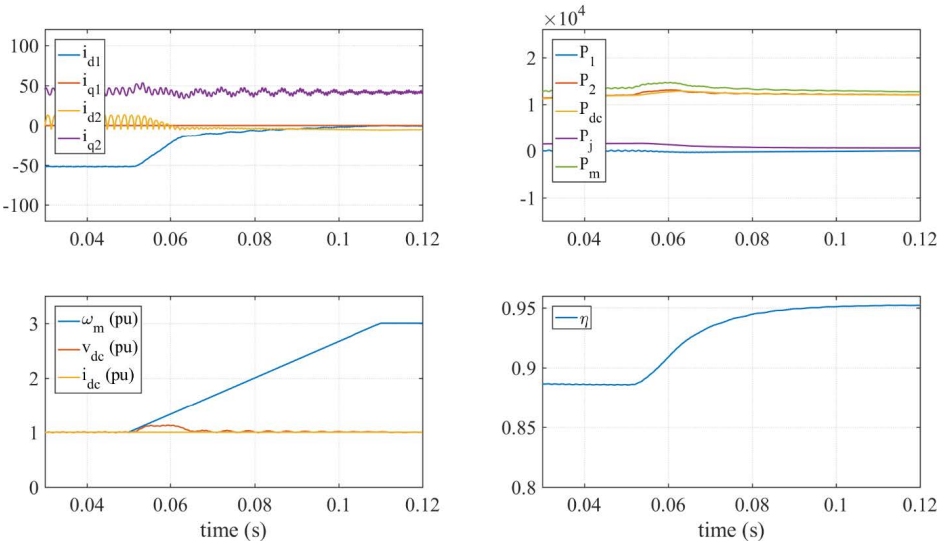

Figure 5.30: Speed ramp simulation up to deep flux weakening using the Simulink model.

theless, the aggregate inverter size and efficiency advantage is significant.

5.2.6.2 Phase Shift of the Inverter Current

In all the previous tests, the field current was imposed in the negative d axis, i.e. $i^*_{1,\mathrm{q}} = 0$, and the amplitude of v_{dc} was regulated simply by $i^*_{1,\mathrm{d}}$. This Section analyses the possible benefits of setting $i^*_{1,\mathrm{q}} \neq 0$. A ramp of $i^*_{1,\mathrm{q}}$ was imposed (from 0 to 50 A) while the generator is rotating at 3000 rpm under rated load (i_{dc}=40 A). In this condition, with $i_{1,\mathrm{q}}$=0, the field circuit is only giving reactive power ($P_1 \approx$0) but increasing $i_{1,\mathrm{q}}$ the primary channel active power P_1 becomes negative, that means the machine is generating power also from the field circuit. Therefore, for a fair analysis, in order to maintain a constant P_{m} the rectified armature current i_{dc} was progressively reduced while increasing $i^*_{1,\mathrm{q}}$.

The results are shown in Figure 5.31. As can be seen, the increase of $i_{1,\mathrm{q}}$ gives an improvement of the efficiency from 0.912 to 0.936 thanks to a better power distribution and lower resistive losses. $\boldsymbol{i}_{1,\mathrm{dq}}$ rotates in an almost elliptic trajectory, so its amplitude gradually increases. It is reasonable considering that the additional $i_{1,\mathrm{q}}$ is compensated by a lower $i_{1,\mathrm{d}}$. The dotted black trajectory represents the excitation current limit, dictated by the inverter and calculated in overload conditions. As can be seen, using $i^*_{1,\mathrm{q}} \neq 0$ should not increase the required inverter size.

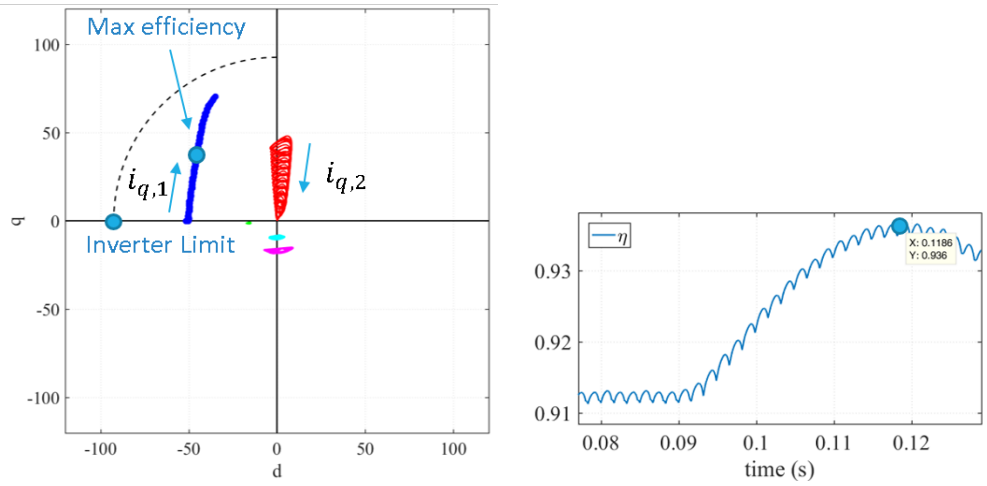

(a) (b)

Figure 5.31: Machine response on varying $i_{1,q} \neq 0$. (a) vectors movement in the dq plane, (b) machine efficiency.

5.2.6.3 DFVC for DW-SyR Machine

In alternative to the current vector control, a modified DFVC could be exploited, as shown in Figure 5.32. In this way it is possible to directly set the reference flux amplitude λ to guarantee the desired v_{dc}, while the orthogonal current i^*_{qs} is set to regulate the excitation active power P_1. As an example, $P_1 = 0$ can be obtained by simply forcing $i^*_{\mathrm{qs}} = 0$. This solution is also expected to be robust against the nonlinear effects introduced by the core saturation. The implementation is a little more complicated and requires a flux observer, but it is a good solution if active power on the excitation circuit must be avoided.

5.2.7 Experimental Validation

The schematic of the experimental setup is shown in Figure 5.33. The selected power converter is consists of two IGBT Voltage Source Inverters (VSI), back-to-back connected into a single prototypal structure named E3. The two VSIs are named Left and Right (INV.L and INV.R) respectively. The safe operating area of these modules permits a maximum dc-bus voltage of 450 V and a maximum peak current of 100 A.

For testing the DW-SyR machine, the inverter INV. L is not commanded and used as a diode rectifier, while INV. R regulates the excitation current in closed loop according to the scheme in Figure 5.25. A dSpace 1104 PPC

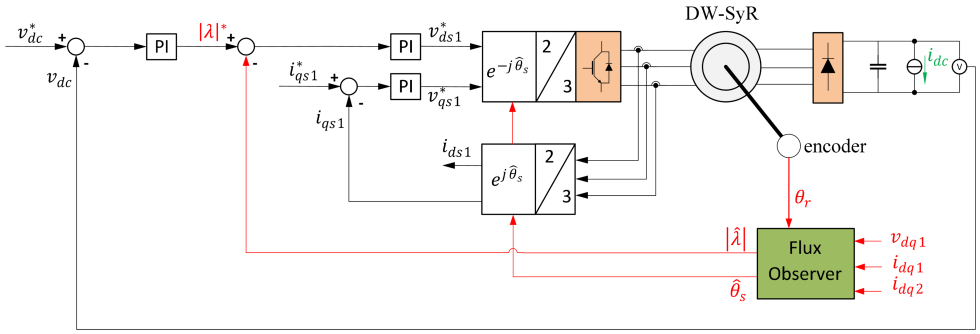

Figure 5.32: Block scheme of the DFVC strategy in stator flux coordinates applied to DW-SyR machine.

controller board is used for real-time control.

A 50 kW battery emulator is used to impose either the bus voltage or current, emulating the presence of a battery in parallel to the dc-link, which can either supply or absorbing DC power. Another synchronous machine is used as speed controlled driving machine (DM), having a nominal power of 16 kW, a base speed of 1500 rpm and a maximum speed of 6000 rpm. The HBM GEN3i data recorder already adopted in Section 5.1.1 is used for monitoring and post-processing analysis purposes, measuring all the currents and voltages in the two channels, the shaft torque and speed and the temperature of windings and case.

5.2.7.1 Steady State Operation

After straightforward preliminary tests, the gains of PI current regulators were tuned with a bandwidth of 330 and 150 rad/s for d and q axes respectively, while the bandwidth of the voltage loop regulating the v_{dc} was 15 rad/s. Then, according to Figure 5.25 the v_{dc} was closed loop controlled while the battery emulator acts as a current generator, imposing the load current. At first, the voltage loop sets the reference excitation current in the negative d axis $i^*_{1,\mathrm{d}}$, while $i^*_{1,\mathrm{q}}$=0. The rated working point (v_{dc}=270 V,i_{dc}=40 A, 3000 rpm) is shown in Figure 5.34.

As can be seen, the excitation voltages are modulated, and the modulation noise is partially reflected on the secondary channel. Because of the resistive voltage drops on the machine windings, v_{dc} is slightly higher than the envelope of the line voltages in the primary circuit and slightly lower than the correspondent envelop in the secondary channel. As expected, the dc-current presents a 6^{th} harmonic due to the presence of the three-phase diode bridge. It must be noted that the amplitude of this oscillation is also related

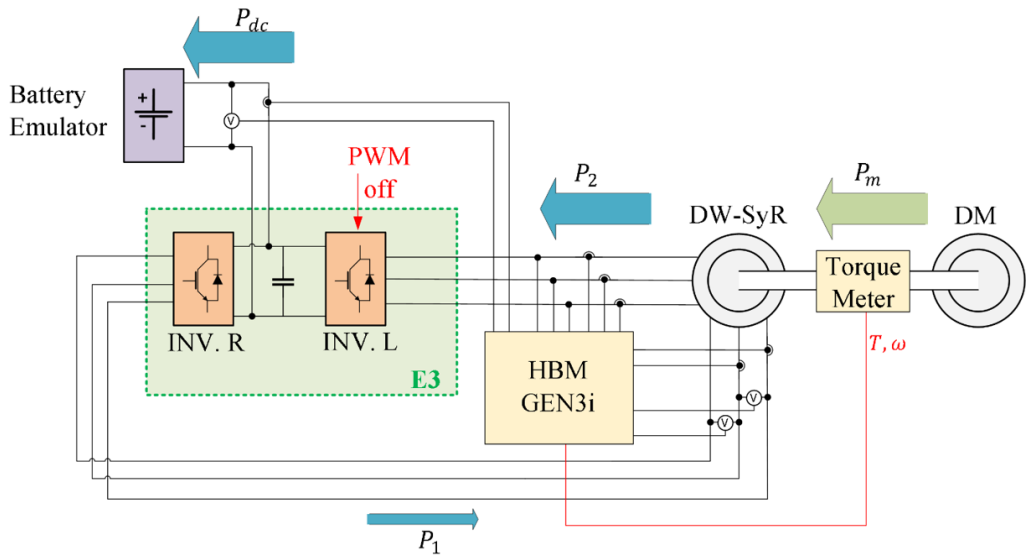

(a)

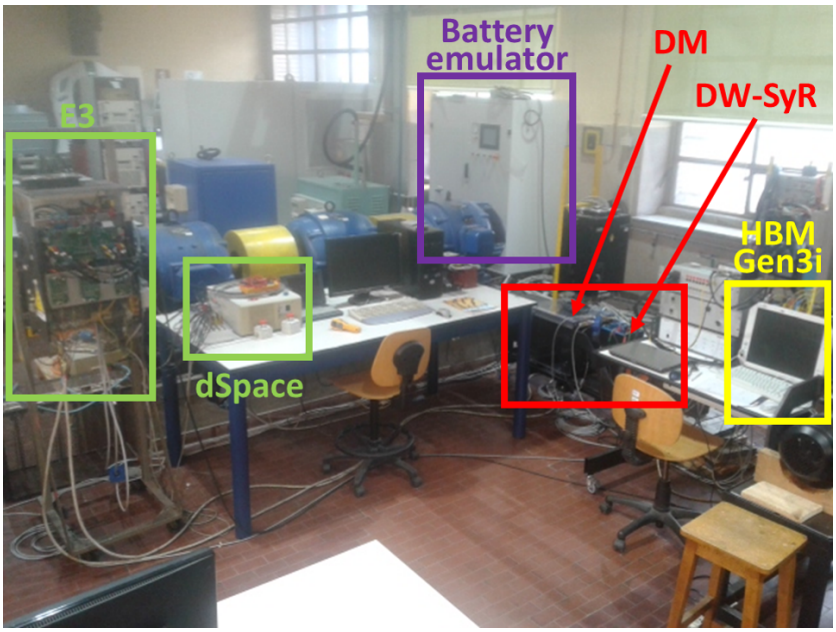

(b)

Figure 5.33: Experimental set-up for DW-SyR testing. (a) Block scheme; (b) test rig.

to the response of the battery emulator, which is not capable of maintaining a perfectly constant load current. Conversely, the v_{dc} voltage is maintained

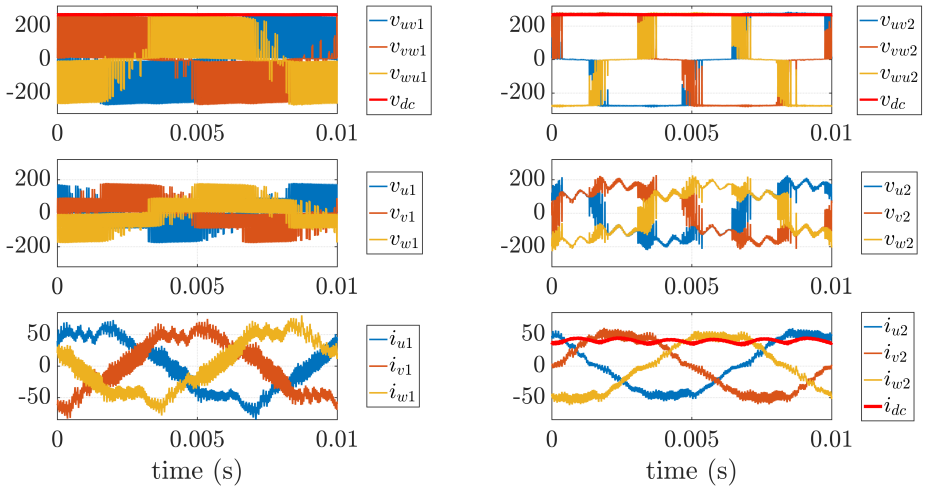

Figure 5.34: Experimental performances of DW-SyR prototype under rated conditions.

constant thanks to the closed loop control, with a ripple lower than 2 Vpp. As expected, since N_1 was chosen very low to guarantee a very large voltage margin, this machine does not bring a significant reduction of the inverter size, if compared to a full power PWM front-end. In a real application, N_1 would be higher, thus considerably reducing $\boldsymbol{i}_{1,\mathrm{dq}}$.

The measured voltages and currents are compared with the FEM model in Figure 5.35, both in terms of time waveforms and vectorial diagram. The voltage and current of only one phase at a time are reported for clarity reasons. The comparison shows a good agreement between experimental and simulated waveforms. The main difference is that the FEM simulation does not represent the modulation of the excitation voltage.

Analyzing the vectors in dq plane, it can be noted that, in the experiment, the flux linkage of the primary winding (light green vector) is well aligned with the negative d axis. Therefore, the primary and secondary voltages are close to the negative q axis (light blue and magenta). The armature current, is close to the positive q axis, with a phase shift slightly lower than 180° respect to the voltage vector. Therefore, a relatively high excitation current is necessary (around 50 A).

The vector diagram related to the FEM simulation is not dissimilar to the experimental one, but the flux is slightly rotated counterclockwise. Accordingly, the two voltage vectors are also rotated and the armature current lies on the second quadrant. This means that the armature current tends to excite the machine and a lower $\boldsymbol{i}_{1,\mathrm{dq}}$ is required (38 A). This different behavior can be explained considering that in experiment the machine was at a

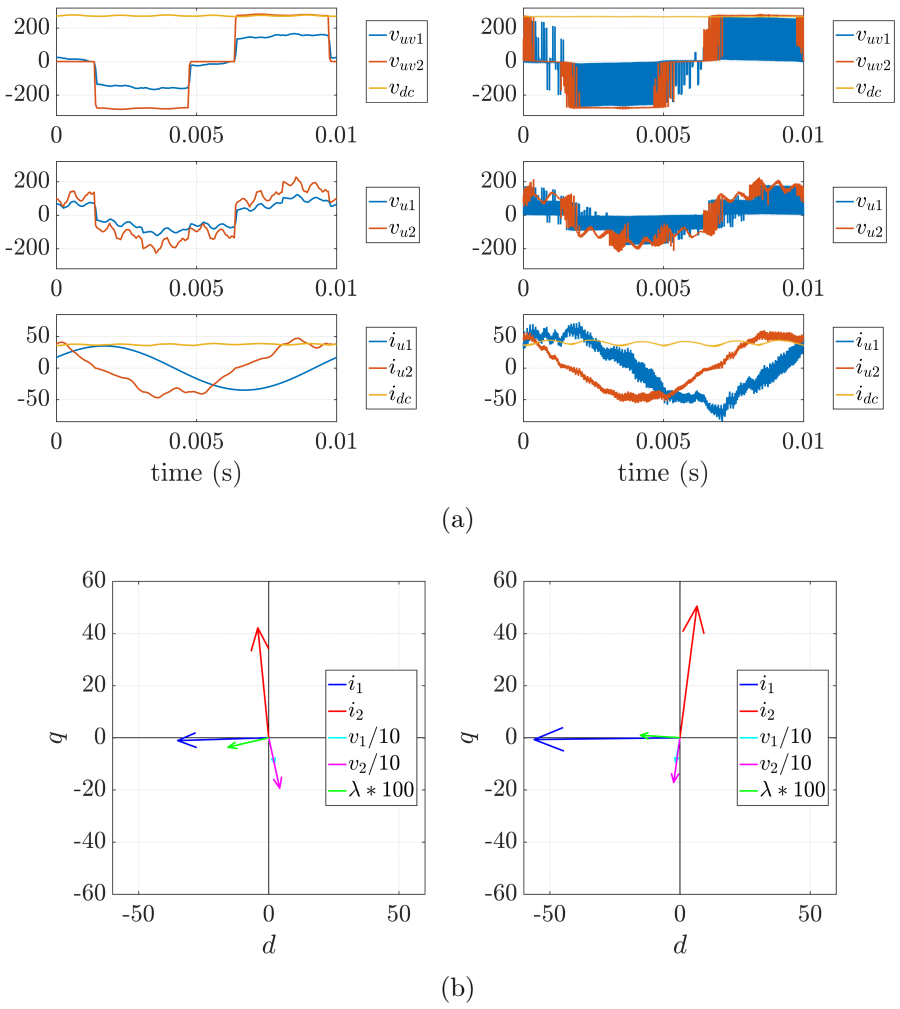

Figure 5.35: Comparison between FEM simulation (left) and experimental results (right) in rated conditions (v_{dc}=270 V, i_{dc}=40 A, 3000 rpm).

higher temperature, so the magnet flux contribution was slightly lower than expected, causing the above-mentioned rotation.

Finally, Table 5.7 compares the machine efficiency, current and voltage amplitude of the machine under test obtained in the experiments and with the Simulink model at reduced and full load (P_{m}=5.4 kW and P_{m}=10.8 kW). Also, the data are compared with the original PM-SyR machine (PM7kW5).

As can be seen, the experimental efficiency is slightly lower than what expected from the simulations, mostly due to iron loss, high order harmonics, friction and mechanical loss that were not included in the Simulink model. The experimental results show that a higher excitation and armature cur-

Table 5.7: Comparison between original PM-SyR, Simulink model and experimental results at 3000 rpm

	PM7kW5	DW-SyR (Sim.)		DW-SyR (Exp.)	
P_{m} (kW)	5.4	5.4	10.8	5.4	10.8
η (%)	93.3	93	88.8	89.1	89.4
$\lvert\boldsymbol{i}_{1,\mathrm{dq}}\rvert$ (RMS)	16.2	18.4	25.4	27.2	33.2
$\lvert\boldsymbol{i}_{2,\mathrm{dq}}\rvert$ (RMS)		14.8	31.1	22.7	34.1
$\lvert\boldsymbol{v}_{1,\mathrm{dq}}\rvert$ (RMS)	158	64.4	64.4	61.8	87.2
$\lvert\boldsymbol{v}_{2,\mathrm{dq}}\rvert$ (RMS)		122.3	122.3	120.4	127.3

rents are necessary for equal electrical load. Also this phenomenon can be explained with the above-mentioned rotation of the vector diagram. On the other hand, the experimental voltage amplitude is in good agreement with simulations. Respect to the original single winding machine, the working point is not exactly the same, since the PM7kW5 machine was working as a motor while the DW-SyR prototype works as generator. Moreover, the two machines have different number of turns, which explains the difference in the phase current and voltage. Finally, the PM7kW5 efficiency is higher than the efficiency of the DW-SyR prototype. This can be explained considering that in this case two stator windings have to be placed in the slot area that was dedicated to the original standard 3-phase winding, with consequent higher current density and copper losses. Anyway, it must be considered that the PM7kW5 machine was working on the maximum efficiency locus (MTPA), while the efficiency of the DW-SyR prototype was not optimized.

5.2.7.2 Dynamic Response

This Section analyzes the dynamic response of the current vector control.

The results obtained for a step load variation are report in Figure 5.37, where the speed and v_{dc}^{*} were kept constant at the rated values (3000 rpm and 270 V). The battery emulator forced a step variation of the load current from i_{dc}=20 A to i_{dc}=40 A, corresponding to an output power of P_{dc}=5.4 kW and P_{dc}=10.8 kW. Unfortunately, the battery emulator cannot produce a proper current step, so the load variation is actually a stair. As can be seen, the excitation and armature currents increase because of the higher load, with

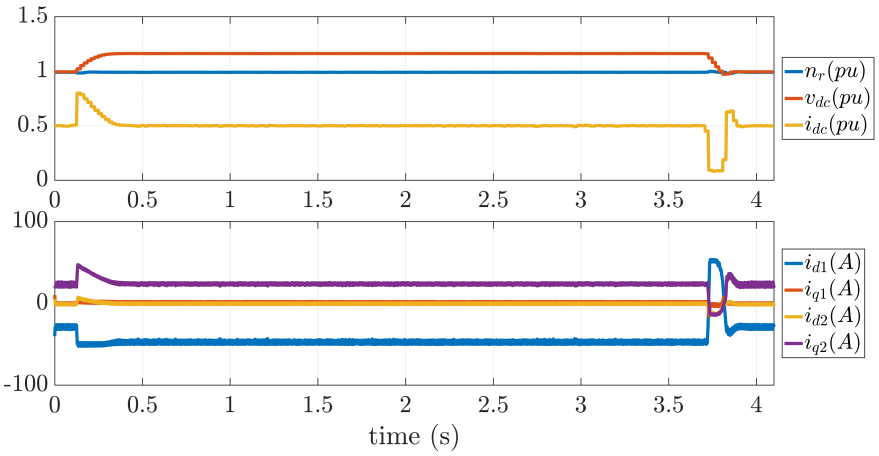

Figure 5.36: Dynamic response for step variation of the reference dc-link voltage v^*_{dc} from 270 V to 330 V at 3000 rpm, i_{dc}=20 A.

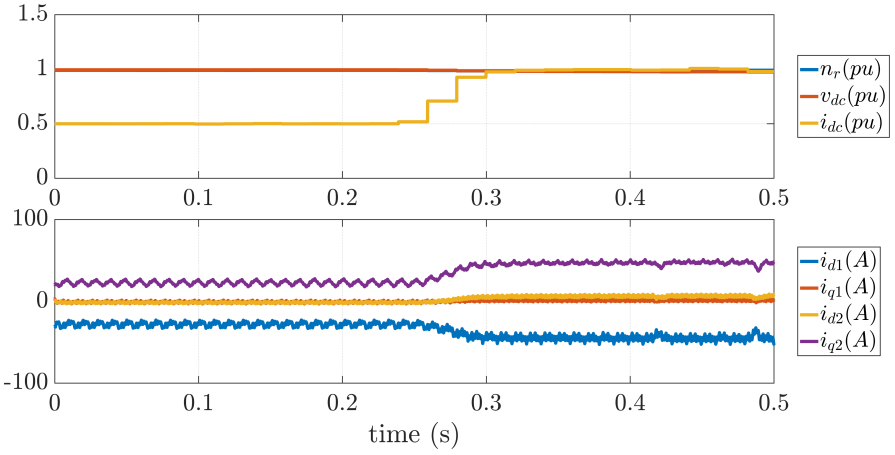

Figure 5.37: Dynamic response for step load variation i_{dc} from 20 A to 40 A at 3000 rpm, v_{dc}=270 V.

negligible influence on the bus voltage. The variation of v_{dc} was lower than 2%.

Then, the bandwidth and stability of the v_{dc} control loop was tested (Figure 5.36) at constant speed and load (i_{dc}=20 A at 3000 rpm), while the reference v^*_{dc} was stepwise increased from 270 V to 330 V and then back to 270 V. As can be seen, the dynamic response is quite fast. Also in this case, the battery emulator was not able to maintain a constant load current, which varied during the transients. The increased v^*_{dc} requires higher excitation

current, which suddenly rises. The overshoot in the excitation current is very small, lower than 4% of the final value. It should be remarked that the dynamic of v_{dc} regulation depends on the rotor speed, therefore in an optimized control the PI gains should vary with the operating conditions.

5.2.7.3 Efficiency as a Function of the Working Point

The variability of the DW-SyR machine with speed and load was investigated.

At first, the rotor speed was increased over the rated 3000 rpm. As previously explained, the higher is the speed the lower the flux linkage needs to be. Therefore, the excitation current and the related copper losses decrease at the higher speeds from 37 to 24 A. On the other hand, the iron loss increases with the rotor speed, according to the augmented electrical frequency. The aggregate of these phenomena explains the efficiency versus speed characteristic represented in Figure 5.38(a), referring to rated load conditions (i_{dc}=40 A, v_{dc}=270 V) at different speeds, with excitation current on the d-axis (non optimized).

It can be noted that the reduction of $\boldsymbol{i}_{1,\mathrm{dq}}$ also corresponds to a better η_{conv}, aggregating the losses in the inverter and in the diode bridge. Dealing with the efficiency of the electrical machine, this grows from 85% to 87% when the speed varies from 3000 rpm to 3700 rpm, while at higher speed it slowly falls because of iron loss. Altogether, the global efficiency η_{tot} reaches its maximum around 4000 rpm, roughly 82%. It must be remarked once

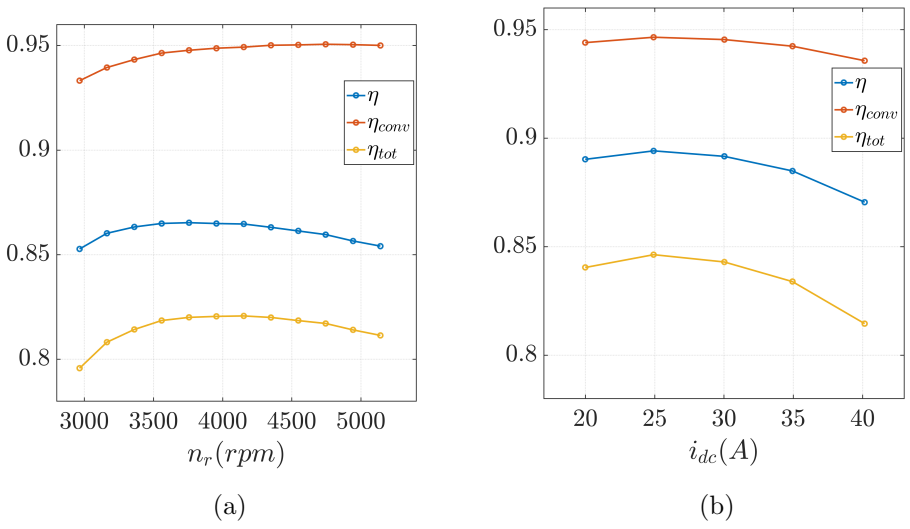

Figure 5.38: DW-SyR efficiency as a function of (a) rotor speed and (b) electrical load

more that neither the electrical machine nor the converter where designed for maximum efficiency. Moreover, the control strategy is non optimized in this respect.

Then, the machine behavior upon varying the electrical load was investigated at constant speed (3000 rpm) while the dc-link voltage was closed loop controlled at v_{dc}=270 V, still with $i_{1,\mathrm{q}}$=0. The electrical load was varied by slowly changing the i_{dc} from 20 A to 40 A, corresponding to P_{dc}=5.4 to 10.8 kW.

The results, summarized in Figure 5.38(b), show an efficiency drop when increasing the output power. The fact can be explained considering the above described rotation of the voltages and flux (see Section 5.2.5). In turn, the excitation circuit ends up absorbing positive active power, which must be additionally produced by the armature winding, with negative effect on the machine efficiency. This phenomenon is highly undesired, because part of the electrical power produced by the secondary channel is re-absorbed by the primary one, with consequent increase of the currents in the two windings, additional copper loss and eventually increased inverter size. Finally, also the switching losses rise, as demonstrated by the drop in the converter efficiency η_{conv}.

These downsides can be mitigated acting on the control strategy, as will be described in the next Section. Moreover, a different design of the electrical machine, with the PM contribution designed for higher current loading, can also shift the maximum efficiency operating point.

5.2.7.4 Efficiency Improvement

In this test, $i^*_{1,\mathrm{q}}$ was arbitrary set to be different from zero, looking for the maximum efficiency locus. Accordingly, the excitation current can lie either in the second or third quadrant of the dq plane, as shown in Figure 5.39. Also in this case, the test was performed at the rated conditions (i_{dc}=40 A, v_{dc}=270 V, 3000 rpm).

As can be seen, the efficiency grows with $i^*_{1,\mathrm{q}}$ and the higher efficiency region is where also the excitation circuit is generating active power ($P_1 < 0$), thus avoiding recirculating power as mentioned before. Therefore, for equal load conditions, the power in the secondary channel P_2 decreases, together with the armature current.

It must be noted that the q-axis component does not considerably increase the amplitude of the excitation current for two reasons. First, $i_{1,\mathrm{q}}$ is in quadrature with the main component of the excitation current $i_{1,\mathrm{d}}$, therefore it has limited effect on its amplitude. Second, the additional $i_{1,\mathrm{q}}$ contributes to the excitation flux, so the v_{dc} loop imposes lower $i_{1,\mathrm{d}}$.

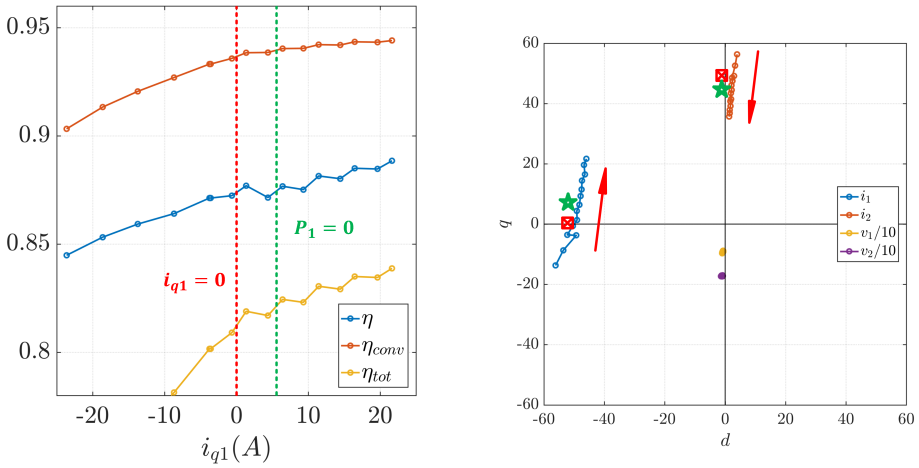

(a) (b)

Figure 5.39: (a) DW-SyR efficiency on varying the reference $i^*_{1,q}$. (b) movement of current vectors in the dq plane.

Therefore, the copper and switching losses at the primary side remain approximately constant, whereas the armature current at the secondary side is reduced, together with the power losses in the armature channel. In conclusion, the machine efficiency increases, according to the simulations. By increasing $i_{1,q}$ to 21 A, the efficiency of the electrical machine η was improved from 87% to 89% while the converter efficiency η_{conv} grows from 93% to 94%. This brings the total efficiency η_{tot} from 81% to 84%.

5.2.7.5 Load Test and Temperature Transient

Finally, the thermal response of the machine was investigated, aiming to:

- Evaluate the continuous output power of the machine, given a target temperature of 120°C;
- Evaluate the thermal time constant of the machine;
- Extrapolate the transient overload output power at maximum insulation temperature (200°C).

The machine temperature is measured via PT100 thermistors embedded into the windings end connections. Each phase of the primary and the secondary circuits has two thermistors, one in the front and one in the back of the machine stack, for a total of twelve thermal sensors. In this test, only one

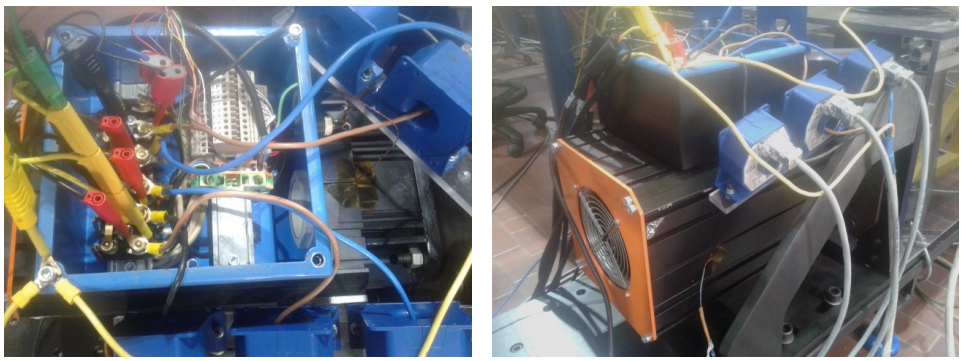

(a) (b)

Figure 5.40: Picture of the DW-SyR machine during load test.

phase of each three-phase set is monitored, assuming symmetrical conditions in the others. Moreover, the machine presents an internal and an external case, and their temperature is monitored by two additional thermocouples, one in the back of the external case and the other one in the front of the internal case (see Figure 5.40). All the measured temperatures are acquired by the HBM GEN3i data logger with a sampling rate of 30 s.

For this test, the DW machine was run at rated speed but half rated load (i_{dc}=20 A, v_{dc}=270 V, 3000 rpm) and $i^*_{1,\mathrm{q}}$=0 was initially set for simplicity. The room temperature was equal to 19°C, and the machine was initially cold. The test results are report in Figure 5.41, where $\theta_{1,a}$, $\theta_{1,p}$, $\theta_{2,a}$, $\theta_{2,p}$, $\theta_{ext,a}$ and $\theta_{ext,p}$ stand for anterior and posterior temperature of the primary and secondary windings and external case respectively. As can be seen, after the thermal transient the temperatures of the primary winding are stabilized at $\theta_{1,a}$=115°C, $\theta_{1,p}$=118°C, while in the secondary winding where $\theta_{2,a} = \theta_{2,p}$=112°C. The steady state temperature of the case resulted $\theta_{ext,a}$=50°C, $\theta_{ext,p}$=33°C, standing for a relatively high thermal impedance between the windings and the case.

Once reached the stationary temperature, the working point was moved to i_{dc}=24 A. Contemporary, an additional excitation component on the q axis ($i^*_{1,\mathrm{q}}$=20 A). In this second condition, the total loss in the machine is about the same as before the load change (P_{j}=780 W), but the power loss of the primary side increased from 388 W to 575 W, whereas the loss of the secondary side was accordingly reduced from 392 W to 205 W. As can be noticed, the temperature of the primary circuit increased to $\theta_{1,a}$=127°C, $\theta_{1,p}$=123°C, while the temperature of the secondary channel dropped to $\theta_{2,a} = \theta_{2,p}$=106°C.

The thermal class of the insulation withstands a maximum temperature

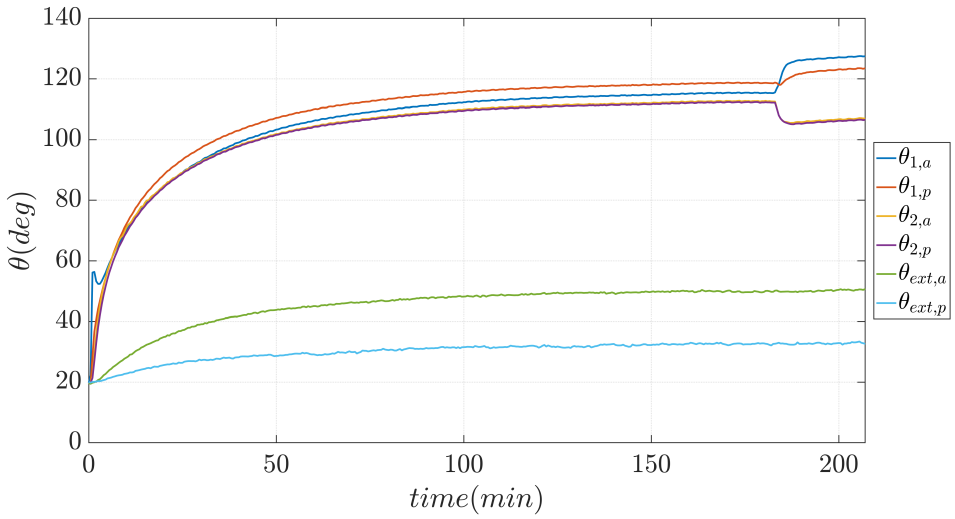

Figure 5.41: Machine temperature during the thermal test. v_{dc}=270 V, i_{dc}=20 A, 3000 rpm.

of 200°C. Based on the temperature transient shown in Figure 5.41, it is estimated that the expected continuous output power at 200°C is equal to P_{dc}=10.8 kW (V_{dc}=270 V,i_{dc}=40 A), assuming that the maximum efficiency control technique is adopted. Moreover, an output power of 16.2 kW (150% of continuous power), can be generated for 10 minutes and a 200% overload of 21.6 kW is tolerated for 5 minutes. Overall, it can be assert that the target specifications detailed in Table 5.5 were respected.

5.2.8 Thermal Model

Dealing with machine design, the emphasis on the thermal aspects has progressively grown, for the strong influence of the thermal behavior on both motor efficiency and reliability. In the case of DW-SyR prototype, the temperature mismatch between primary and secondary windings shown in Figure 5.41 suggest that the thermal model of the machine must be further investigated if higher efficiency control strategies want to be pursued. Indeed, the non-zero quadrature current $i_{1,\mathrm{q}}$ in the excitation circuit produces an unbalance in the temperature distribution, with possible overcome of the thermal limit of the excitation winding. This problem can be eventually mitigated with appropriate slot and winding design. Proper thermal model of the machine was retrieved in [15] and summarized here.

The two sets are placed in the same slots, as shown in Figure 5.42. Every stator slot is occupied by both the sets of windings, one placed in the inner-

most part of each slot and the other one in the outermost. Therefore, they present different thermal behavior and strong thermal coupling.

The fact that the secondary winding tends to be colder than the primary one comes from its better positioning, in the outside part of the slots, with easier access to ventilation and in better contact with the iron core. Moreover, the slot area was split unevenly between the two windings, with additional advantage for the secondary side.

In the last years many thermal simulation models where developed to assist the design of electrical machines [169, 170], mainly based on Lumped Parameters Thermal-Network (LPTN) [171] or numerical methods [172]. LPTN methods provide faster response with respect to the numerical ones and can be better handled for geometry optimization during the motor design stage [173, 174]. Dealing with multiple winding machine, an accurate thermal model must be capable of covering the thermal coupling among the different winding sets, either in steady state and transient conditions, for proper monitoring and preventing fault occurrence [175, 176].

5.2.8.1 LPTN for Standard Three-Phase Machines

The short-time thermal transient method was demonstrated in [175, 176] to be effective in identifying the parameters of a LPTN of various three-phase induction motors of different size for industrial applications. The adopted model is shown in Figure 5.43(a), where the current generator stands for Joule loss P_j in the winding, the capacitor C_{eq} represents the thermal capacitance of winding plus insulation and R_{eq} is the thermal resistance from the winding to the stator core iron.

Starting with the motor at room temperature T_0, the three phases are connected in series and excited with direct current while the resistance is

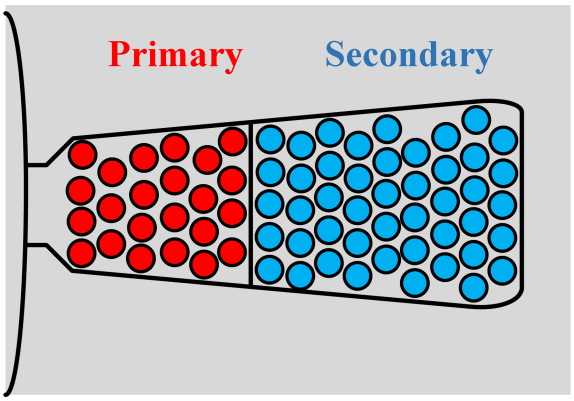

Figure 5.42: Schematic of winding allocation in the slot of the DW machine.

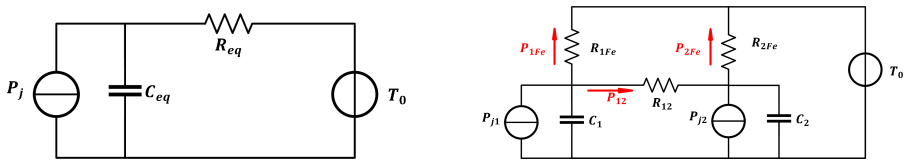

(a) (b)

Figure 5.43: LPTN for (a) single three-phase machines and (b) dual three-phase machines.

online monitored. The amplitude of the injected current is around the rated value. Since the initial temperature T_0 and winding resistance R_0 are known, the average winding temperature can be estimated from the well-known relationship:

$$T = \frac{R_T}{R_0} \cdot (234.5 + T_0) - 234.5 \tag{5.20}$$

where R_T is the winding resistance at the temperature T and 234.5 is the inverse of copper temperature coefficient. According to the scheme in Figure 5.43(a), the thermal transient is approximated by an exponential curve:

$$T(t) = T_0 + T_\infty \left(1 - e^{-\frac{t}{\tau}}\right) \tag{5.21}$$

where $T_\infty = P_j R_{eq}$ and $\tau = R_{eq} C_{eq}$ is the time constant. The initial stage of the temperature transient is adiabatic, i.e. iron core temperature is fixed to T_0. So, the accumulated energy W versus winding temperature is almost a straight line, whose slope equals the equivalent thermal capacitance:

$$C_{eq} = \frac{dW}{dT} \tag{5.22}$$

After evaluating C_{eq} from (5.22), the equivalent resistance R_{eq} is extracted from the time constant τ evaluated in (5.21). Details are found in [175, 176].

5.2.8.2 Extension to Multiple Three-phase Windings

The LPTN is extended to the case of dual three-phase machine, including DW-SyRM (see Figure 5.43(b)). Each three-phase set has its proper thermal capacitance, called C_1 and C_2, aggregating the respective winding copper and insulation. Two thermal power generators P_{j1} and P_{j2} represent the respective stator Joule losses. Each winding exchanges heat with the stator iron through the thermal resistances R_{1Fe} and R_{2Fe}. A quota of thermal power P_{12} is exchanged between the two windings, flowing through the resistance R_{12}. In this specific machine the two windings share the same slots,

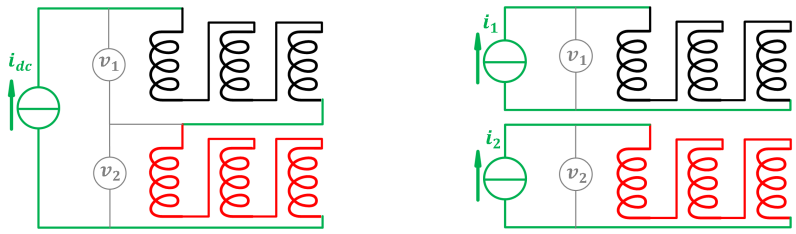

(a) (b)

Figure 5.44: Winding configuration for (a) test 1 and (b) test 2 and 3.

therefore the contact surface between them is relatively high compared with other types of multiple three-phase machines adopting different slots for the different windings. So, the value of R_{12} is comparable with R_{1Fe} and R_{2Fe}.

In principle, the stator iron has its thermal capacitance, too. However, thanks to the adiabatic hypothesis, the iron temperature is considered constant during the first part of the transient (approximately one minute) and represented by the voltage generator T_0.

5.2.8.3 Test Sequence

The test procedure described in Section 5.2.8.1 is slightly complicated here to find the five parameters of the LPTN of Figure 5.43(b). The three phases of each winding set are always series connected, as shown in Figure 5.44. The identification procedure consists of three tests:

1. all windings: primary three-phase set connected in series to secondary, and excited with constant current $i_{dc} = 20\ A$;

2. primary only: the two windings are separated and only the primary channel is excited at 20 A;

3. secondary only: the two windings are separated and only the secondary channel is excited at 20 A;

The 20 A excitation current is chosen similar to the rated current. During each test, the dc resistances of the two windings R_1 and R_2 are online measured using the voltage measurement indicated in Figure 5.44, divided by the imposed current. In the "primary only" and "secondary only" tests, a small current (1 A) is injected into the non excited winding for online monitoring the winding resistance, with negligible thermal effect. From the measured thermal transients, it is estimated that the hypothesis of short time thermal transient, i.e. adiabatic conditions, holds for the first 60 s of the test. Based

on the measured resistances, the average temperatures of the two windings are estimated:

$$T_1 = \frac{R_{1,T1}}{R_{1,0}} \cdot (234.5 + T_0) - 234.5 \tag{5.23a}$$

$$T_2 = \frac{R_{2,T2}}{R_{2,0}} \cdot (234.5 + T_0) - 234.5 \tag{5.23b}$$

where $R_{1,T1}$ and $R_{2,T2}$ are the two resistances at the temperatures T_1 and T_2 and $R_{1,0}$ and $R_{2,0}$ are the resistances at the initial temperature T_0. The thermal energy dissipated in the two windings is calculated from the electric power:

$$W_1 = \int v_1 \cdot i_1 dt \qquad W_2 = \int v_2 \cdot i_2 dt \tag{5.24}$$

After measuring the thermal transient, the parameters of the equivalent LPTN are obtained via data manipulation. Two approaches are proposed, called "rapid data manipulation" and "formal approach".

5.2.8.4 Rapid Data Manipulation

In the test all windings, the two sets present similar power loss density and temperature rise. For this reason, it is assumed that the thermal energy exchange P_{12} between the two windings can be neglected, so the thermal network is simplified as in Figure 5.46(a).

$$P_{12} = 0 \tag{5.25}$$

By using this simplified model, the windings are decoupled and separately studied as two independent single winding machines. Therefore, the same procedure described in Section 5.2.8.1 is adopted to evaluate R_{1Fe}, R_{2Fe}, C_1 and C_2. The thermal capacitances are obtained from the slope of the dissipated energy as a function of the overtemperature approximated with a straight line, while the resistances are calculated from the time constants of the fitting exponential functions:

$$C_1 = \frac{dW_1}{dT_1} \qquad C_2 = \frac{dW_2}{dT_2} \tag{5.26}$$

$$T_1(t) = T_0 + \Delta T_{1,\infty} \left(1 - e^{-\frac{t}{\tau_1}}\right) \tag{5.27a}$$

$$T_2(t) = T_0 + \Delta T_{2,\infty} \left(1 - e^{-\frac{t}{\tau_2}}\right) \tag{5.27b}$$

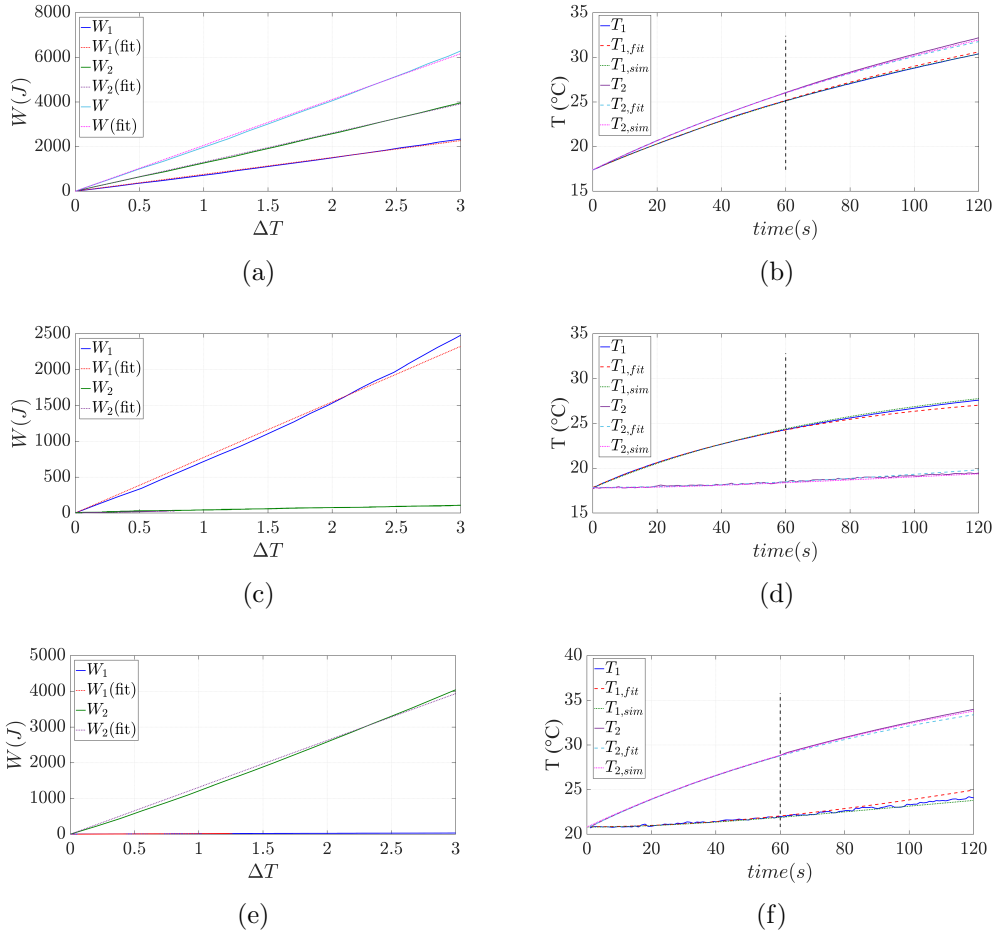

Figure 5.45: (a,c,e) Energy Vs overtemperature and (b,d,f) temperature transient in the test (a,b) all windings, (c,d) primary only and (e,f) secondary only. Solid lines: measured data. Dashed: interpolation based on the first 60 s. Dotted: simulation with LPTN in Figure 5.43(b).

where $\Delta T_{1,\infty} = P_{j1}R_{1Fe}$, $\Delta T_{2,\infty} = P_{j2}R_{2Fe}$, $\tau_1 = R_{1Fe}C_1$, $\tau_2 = R_{2Fe}C_2$.

In the test primary only, the temperature of the secondary winding varies by less than 1°C respect to the initial room temperature. Therefore, the heat exchange between the secondary coil and the iron is negligible. Moreover, it is considered that the power loss in the secondary winding is null. The LPTN is then simplified as in Figure 5.46(b). It must be remarked once more that this analysis is valid only in the initial part of the thermal transient, when adiabatic condition holds (60 seconds). Using the simplified circuit, the power flow between the two windings is:

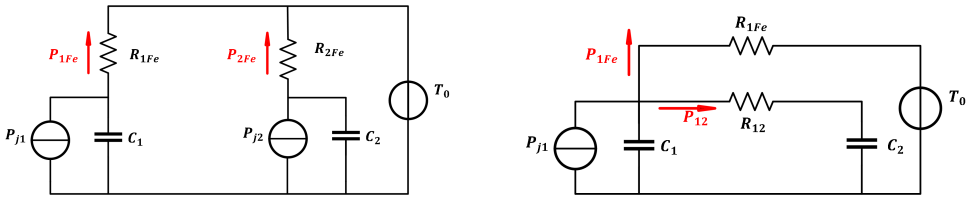

(a) (b)

Figure 5.46: LPTN in the test where (a) the winding are series connected and (b) primary winding only is excited.

$$P_{j2} = 0 \qquad P_{12} = C_2 \frac{dT_2}{dt} \tag{5.28}$$

where C_2 is known from the first test. The mutual exchange thermal resistance R_{12} is calculated after the exchanged power P_{12}, as:

$$R_{12} = \frac{T_1 - T_2}{P_{12}} \tag{5.29}$$

It must be noted that T_1, T_2 and P_{12} are a function of time, therefore a variable R_{12} is found through (5.29). Anyway, the thermal system is linear, so the value of R_{12} changes very little, as can be noticed from Figure 5.47 and it can be reasonably considered as constant. The average of R_{12} in the first 60 s is reported in Table 5.8.

Different hypothesis are separately adopted to find an analytical expression of T_1 and T_2. According to the LPTN of Figure 5.46(b) if the temperature variation of the secondary winding is neglected, T_1 follows a first order exponential transient:

$$T_1 = T_0 + \Delta T'_{1,\infty} \left(1 - e^{-\frac{t}{\tau'_1}}\right) \tag{5.30}$$

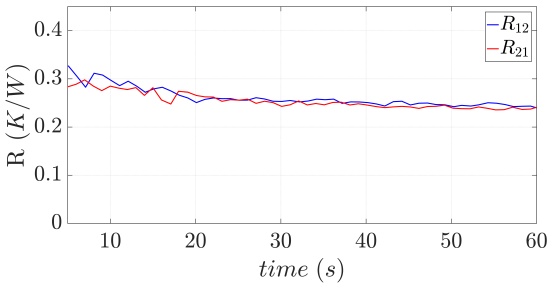

Figure 5.47: Variation of R_{12} with time when calculated by (5.29).

where $\Delta T'_{1,\infty} = P_{j1} R_{1,eq}$, $\tau'_1 = C_1 R_{1,eq}$ and $R_{1,eq} = R_{12} \parallel R_{1,Fe}$. This formulation has the advantage of being suitable for numeric optimization, since P_{j1} is measured and $R_{1,Fe}$ and C_1 are known form the test "all windings".

After calculating T_1 through (5.30), different hypothesis are adopted to find an analytical expression of T_2. In this case, the primary winding is seen as a current generator providing the thermal power P_{12}. Therefore, the temperature in the secondary winding is approximated as:

$$T_2 = T_0 + \frac{1}{C_2} \int_0^t P_{12}\, dt \tag{5.31}$$

From (5.29) and (5.30):

$$\begin{aligned} T_2 &= T_0 + \frac{1}{C_2} \int_0^t \frac{T_1 - T_2}{R_{12}}\, dt \\ &\approx T_0 + \frac{1}{C_2 R_{12}} \int_0^t \Delta T'_{1,\infty} \left(1 - e^{-\frac{t}{\tau_e}}\right)\, dt \\ &= T_0 + \frac{P_{j1} R_{1,eq}}{C_2 R_{12}} \left(t + \tau'_1 e^{-\frac{t}{\tau'_1}} - \tau'_1\right) \end{aligned} \tag{5.32}$$

As said, T_2 is measured via R_2, using a small current value (1 A). As a consequence, T_2 is noisy, significantly affecting the derivative in (5.28). Therefore, it may be necessary to preliminary filter the measured temperatures. Alternatively, an analytical expression of T_2 derivative can be conveniently obtained from (5.32), assuming constant Joule losses P_{j1}:

$$\frac{dT_2}{dt} = \frac{P_{j1} R_{1,eq}}{C_2 R_{12}} \left(1 + e^{-\frac{t}{\tau'_1}}\right) \tag{5.33}$$

Finally, the "secondary only" test follows the same steps of the latter one. Under the same hypothesis, R_{12} is calculated again. The good match of R_{12} estimates from the two tests, report in Table 5.8, proofs the consistency of the test sequence. The two estimates differ for less than 5 %, which is considered acceptable for most of the LPTN applications.

5.2.8.5 Formal Approach to Data Manipulation

A feasible alternative to the procedure described in Section 5.2.8.4 is to analytically solve the LPTN of Figure 5.43(b). With constant winding currents, the variation of thermal power due to the dependence of the electrical resistance on the temperature can be modeled with a Norton equivalent circuit, with constant thermal power in parallel to a negative thermal resistance [176].

The negative resistances are required to take into account the increase of dissipated power on varying the winding resistance. In this way, the input of the system becomes a step function, and the admittance matrix can be written in Laplace domain to analytically solve the LPTN.

Based on the analytical solution it is possible to predict the winding temperature for a given parameters set. The three tests present the same analytical solution, and differ one from the other only for the amplitude of input thermal power. The aggregate Root Mean Square Error (RMSE) between measured and predicted temperatures is calculated as:

$$RMSE = \sqrt{\frac{\sum_{p=1}^{3}\left(\widehat{T}_1 - T_1\right)^2 + \sum_{p=1}^{3}\left(\widehat{T}_2 - T_2\right)^2}{2\sum_{p=1}^{3}\left(N_p - 1\right)}} \tag{5.34}$$

where $\widehat{T}_1$ and $\widehat{T}_2$ are the predicted winding temperatures, p is the index of the test and N_p the number of measurement point for a given test. Several optimization algorithms, e.g. [177], can be used to minimize the RMSE calculated in (5.34), obtaining the parameters set report in Table 5.8.

As can be noticed, the two proposed methods gave compatible results, and the discrepancy between them is acceptable for the practical application of LPTN. The advantage of the formal approach is that it permits to easily extended the model to an n^{th} order system, e.g. to take into account finite iron thermal capacitance. The drawback is that, differently to the rapid data manipulation, the parameters of the LPTN are not directly retrieved from physical hypothesis.

5.2.8.6 Experimental Validation

The thermal model identification procedure was experimentally tested on the DW machine. The experimental set-up is simple and it only requires two dc current sources, two current and two voltage probes. The above described HBM Gen7i was adopted for all the measurements.

It is considered that the hypothesis of short transient operation (e.g. adiabatic conditions) hold up to 60 s. A sufficiently high time range is desirable in order to have a high number of measurement points to be used in the curve fitting and parameters estimation. Conversely, if a too long time limit is chosen the adiabatic condition falls and the thermal transient cannot be well approximated with a first order exponential. The time window limit was chosen based on the energy Vs overtemperature plot: when adiabatic conditions fall the curve is not anymore represented by a straight line.

Table 5.8: Estimated parameters of the LPTN.

	C_1 $(J/°C)$	C_2 $(J/°C)$	R_{1Fe} $(°C/W)$	R_{2Fe} $(°C/W)$	R_{12} $(°C/W)$	
Rapid data manipulation	765	1313	0.191	0.131	0.260	0.248
Formal approach	793	1325	0.208	0.146	0.218	

Using the obtained parameters, the LPTN of Figure 5.43(b) was implemented in Matlab-Simulink. The three tests were simulated imposing the correspondent power loss. The obtained temperatures were plotted in Figure 5.2.8.3 (dotted lines). The agreement with the measured temperatures is excellent in every tests, with a maximum discrepancy of 1% between measured and predicted temperatures up to 120 s. For the test "all windings", the differences between the measured and predicted overtemperatures in the two windings are bounded between -0.15 and 0.23 °C in the first 180 s of test. In the same time range, the temperature discrepancies for the test "primary only" were limited between -0.28 and 0.32 °C, and for the test "secondary only" between -0.09 and 0.57 °C. In conclusion, the LPTN with the calculated parameters matches very well with the measurements.

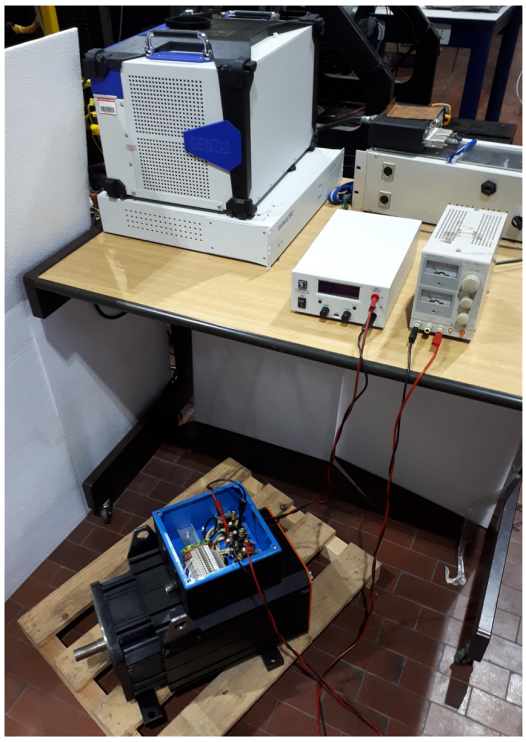

Figure 5.48: Experimental setup for short-time thermal transient: dual winding machine prototype, two DC power supplies and HBM Gen7i data logger.

The same figures also show the temperature transient interpolated with analytical functions based on the first 60 s. The interpolating functions are (5.27) for the test series and (5.30), (5.32) for the test primary. The complete model of figure 5.43(b) results more accurate, at least after the 60 s frame.

5.2.9 Guidelines for Future DW Machine Design

In conclusion, based on the experimental results on the DW machine prototype, synthetic guidelines for a future design of a new DW machine are given.

1. Neglecting the current dependency of the voltage drop on the diode bridge, **the rated v_{dc} imposes the amplitude of $\boldsymbol{v}_{2,\mathrm{dq}}$**.

2. $\boldsymbol{v}_{2,\mathrm{dq}}$ and **minimum speed define the maximum flux**; higher speed results in lower flux amplitude, lower excitation current $\boldsymbol{i}_{1,\mathrm{dq}}$ and so lower copper losses with reasonably higher efficiency, taking into account the increased iron losses.

3. For a given stator and airgap design, **the number of turns in the armature winding is defined** so that **the maximum flux** retrieved at the point 2. **is slightly below the saturation knee**: higher N_2 means less saturated machine, lower $\boldsymbol{i}_{1,\mathrm{dq}}$ and higher efficiency; in any case **magnetic saturation must be avoided**, since it would lead to very high $\boldsymbol{i}_{1,\mathrm{dq}}$.

4. To minimize the inverter size, **the number of turns of the excitation winding is set as high as possible** considering constrains imposed by the control stability, i.e. having sufficient voltage margin for the PI regulators even at maximum current despite the voltage drop on stator resistance and converters

5. The **magnet flux λ_{pm} is chosen so that at the maximum load the total flux is along negative d axis**. In this way, $\boldsymbol{i}_{2,\mathrm{dq}}$ is always in the second quadrant and helps exciting the machine (or in the worst case it is in q axis) but it is never in the first quadrant. Therefore, it is avoided that $\boldsymbol{i}_{2,\mathrm{dq}}$ de-excites the machine, resulting in low efficiency, high current in both the 3-phase sets and relevant active power recycling between them.

6. The two windings must be designed in order to **maximize the thermal coupling** between them, to exploit high efficiency control strategies.

Conclusions and Future Development

The main conclusions of this PhD experience are summarized here.

- An effective test sequence for automatic magnetic model self-identification of SyR and PM-SyR machines was developed. A precise flux maps measurement was obtained in an extended current domain compared to previous works thanks to saliency based online position tracking.
- The test fulfills all the requirements of self-commissioning constrains, and it is performed at free shaft without rotor locking or movement, considered the most demanding condition. Automatic tuning procedure was defined in order to minimize the human intervention.
- The test sequence was combined with a five parameters analytical model, which accurately represented every tested motor. Two mathematical procedures to obtain these five parameters were defined. Other valuable solutions for extracting the flux maps are discussed as well.
- In case of PM-SyR machines, two novel methods for identifying the PM flux linkage at standstill or quasi-standstill were proposed and resulted very precise on the motor under test.

- The sensorless control of SyRMs at low speed was extensively analyzed, highlighting benefits and drawbacks of different sensorless techniques in low and high speed ranges.
- An appropriate low speed method based on HF voltage injection and flux demodulation was adopted, immune from position error due to cross-saturation effect. This technique was combined with two different back-EMF based algorithms, achieving a robust sensorless control able

to work in full speed range, from standstill to flux weakening with smooth transition between different operating regions, and using the MTPA trajectory for the first time in sensorless control of SyRM.

- Fine analysis of local saliency characteristic of SyRM in the dq plane was conducted, identifying the critical operating areas were saliency tracking via HF injection is armed. This problem was solved with proper modification of MTPA trajectory, increasing the control stability.

- Automatic tuning criteria were proposed for control self-calibration. Altogether, the proposed self-commissioning test and sensorless control give a fully plug and play strategy for SyRM.

- A novel low speed injectionless position estimation algorithm was defined based on FCS-MPC.

- The magnetic model self-commissioning was successfully tested on a high current SyR prototype (250 kW) designed for aviation applications, and the results were used for tuning a sensorless control. The magnetic model identification was also verified versus the reference curves obtained with constant speed methods, proving the accuracy of the adopted self-commissioning test sequence also for high power ratings.

- This experience highlighted that the main drawback of this avionic SyR generators is the size of the power electronic converter. Therefore, a novel technique, called Dual Winding, for reducing the on-board inverter size was discussed. A reduced size motor prototype was designed and successfully tested, proposing several solutions for its motor control and efficiency optimization.

- These tests also highlighted a relevant unbalance in temperature distribution between windings, therefore proper thermal model of the machine was developed, as well as a dedicated test sequence able to accurately retrieve its parameters.

Some of the main remaining open topics, which will be the subject of future research projects, include:

- Extend the standstill and free-shaft commissioning to PMSMs with more relevant PM flux contribution. In particular, the standstill method to evaluate the λ_{pm} term was tested on one motor only and it should be tested on different machines to further prove its validity. It should be noted that during the test the motor works in a deeply non-linear region, which makes any simulation inaccurate. Therefore, a direct experimental approach would be preferred.

- The analytical inverse magnetic model adopted for SyR should be modified to take into account the PM flux term for PMSMs.

- The method for iron losses evaluation during magnetic model identification resulted accurate in simulation, but it has yet to be experimentally proved.

- The sensorless control algorithm may be improved further. Possible directions include adding a mechanical observer to improve the speed loop and position estimation bandwidths, at the cost of a higher parameters sensitivity and tuning effort. Different solutions are under investigation.

- Considering the high current SyR prototype, transition to DFVC control is under investigation at the moment of this work. Moreover, several methods for limiting the harmonic content in the current will be analyzed and tested. Once reduced the harmonic noise, a more performing sensorless algorithm may be pursued.

Published Papers

Journal papers:

- S. A. Odhano, P. Pescetto, H. A. A. Awan, M. Hinkkanen, G. Pellegrino and R. Bojoi, "Parameter Identification and Self-Commissioning in AC Motor Drives: a Technology Status Review," in *IEEE Transactions on Power Electronics*.

- P. Pescetto and G. Pellegrino, "Automatic Tuning for Sensorless Commissioning of Synchronous Reluctance Machines Augmented With High-Frequency Voltage Injection," in *IEEE Transactions on Industry Applications*, vol. 54, no. 5, pp. 4485-4493, Sept.-Oct. 2018.

- A. Yousefi-Talouki, P. Pescetto, G. Pellegrino and I. Boldea, "Combined Active Flux and High-Frequency Injection Methods for Sensorless Direct-Flux Vector Control of Synchronous Reluctance Machines," in *IEEE Transactions on Power Electronics*, vol. 33, no. 3, pp. 2447-2457, March 2018.

- A. Yousefi-Talouki, P. Pescetto and G. Pellegrino, "Sensorless Direct Flux Vector Control of Synchronous Reluctance Motors Including Standstill, MTPA, and Flux Weakening," in *IEEE Transactions on Industry Applications*, vol. 53, no. 4, pp. 3598-3608, July-Aug. 2017.

- M. Hinkkanen, P. Pescetto, E. Mölsä, S. E. Saarakkala, G. Pellegrino and R. Bojoi, "Sensorless Self-Commissioning of Synchronous Reluctance Motors at Standstill Without Rotor Locking," in *IEEE Transactions on Industry Applications*, vol. 53, no. 3, pp. 2120-2129, May-June 2017.

- G. Crotti, D. Giordano, M. Luiso and P. Pescetto, "Improvement of Agilent 3458A Performances in Wideband Complex Transfer Function Measurement," in *IEEE Transactions on Instrumentation and Measurement*, vol. 66, no. 6, pp. 1108-1116, June 2017.

Conference papers:

- P. Pescetto, S. Ferrari, G. Pellegrino, E. Carpaneto, and A. Boglietti, "Short-Time Transient Thermal Model Identification of Multiple Three-Phase Machines," *2018 IEEE Energy Conversion Congress and Exposition (ECCE)*, Portland, OR, 2018.

- A. Varatharajan, P. Pescetto and G. Pellegrino, "Injectionless Sensorless Control of Synchronous Reluctance Machine for Zero to Low Speeds Region," *2017 IEEE International Symposium on Sensorless Control for Electrical Drives (SLED)*, Catania, 2018

- P. Pescetto and G. Pellegrino, "Sensorless magnetic model and pm flux identification of synchronous drives at standstill," *2017 IEEE International Symposium on Sensorless Control for Electrical Drives (SLED)*, Catania, 2017, pp. 79-84.

- P. Pescetto and G. Pellegrino, "Sensorless commissioning of synchronous reluctance machines augmented with high frequency voltage injection," *2017 IEEE Energy Conversion Congress and Exposition (ECCE)*, Cincinnati, OH, 2017, pp. 1909-1916.
  → **Industrial Drives Committee Paper Award, third prize**

- P. Pescetto and G. Pellegrino, "Sensorless standstill commissioning of synchronous reluctance machines with automatic tuning," *2017 IEEE International Electric Machines and Drives Conference (IEMDC)*, Miami, FL, 2017, pp. 1-8.

- R. Leuzzi, P. Cagnetta, S. Ferrari, P. Pescetto, G. Pellegrino and F. Cupertino, "Analysis of overload and sensorless control capability of PM-assisted synchronous reluctance machines," *2017 IEEE Workshop on Electrical Machines Design, Control and Diagnosis (WEMDCD)*, Nottingham, 2017, pp. 172-178.

- M. Hinkkanen, P. Pescetto, E. Mölsä, S. E. Saarakkala, G. Pellegrino and R. Bojoi, "Sensorless self-commissioning of synchronous reluctance motors at standstill," *2016 XXII International Conference on Electrical Machines (ICEM)*, Lausanne, 2016, pp. 1174-1180.
  → **Brian J. Chalmers Best Paper Award**

- D. Giordano, P. Pescetto, G. Crotti and M. Luiso, "Improvement of Agilent 3458A performances in wideband complex transfer function measurement," *2016 Conference on Precision Electromagnetic Measurements (CPEM 2016)*, Ottawa, ON, 2016, pp. 1-2.

- P. Pescetto, G. Bergna-Diaz, I. Zubimendi and E. Tedeschi, "Comparison of parallel connected medium voltage grid side VSCs for offshore wind turbines," *2015 Tenth International Conference on Ecological Vehicles and Renewable Energies (EVER)*, Monte Carlo, 2015, pp. 1-8.
  → **Best Paper Award on Renewable Energies**

Bibliography

[1] P. Pescetto, G. Bergna-Diaz, I. Zubimendi, and E. Tedeschi. Comparison of parallel connected medium voltage grid side vscs for offshore wind turbines. In *2015 Tenth International Conference on Ecological Vehicles and Renewable Energies (EVER)*, pages 1–8, March 2015.

[2] D. Giordano, P. Pescetto, G. Crotti, and M. Luiso. Improvement of agilent 3458a performances in wideband complex transfer function measurement. In *2016 Conference on Precision Electromagnetic Measurements (CPEM 2016)*, pages 1–2, July 2016.

[3] G. Crotti, D. Giordano, M. Luiso, and P. Pescetto. Improvement of agilent 3458a performances in wideband complex transfer function measurement. *IEEE Transactions on Instrumentation and Measurement*, 66(6):1108–1116, June 2017.

[4] M. Hinkkanen, P. Pescetto, E. Mölsä, S. E. Saarakkala, G. Pellegrino, and R. Bojoi. Sensorless self-commissioning of synchronous reluctance motors at standstill. In *2016 XXII International Conference on Electrical Machines (ICEM)*, pages 1174–1180, Sept 2016.

[5] M. Hinkkanen, P. Pescetto, E. Mölsä, S. E. Saarakkala, G. Pellegrino, and R. Bojoi. Sensorless self-commissioning of synchronous reluctance motors at standstill without rotor locking. *IEEE Transactions on Industry Applications*, 53(3):2120–2129, May 2017.

[6] P. Pescetto and G. Pellegrino. Sensorless standstill commissioning of synchronous reluctance machines with automatic tuning. In *2017 IEEE International Electric Machines and Drives Conference (IEMDC)*, pages 1–8, May 2017.

[7] P. Pescetto and G. Pellegrino. Sensorless commissioning of synchronous reluctance machines augmented with high frequency voltage injection. In *2017 IEEE Energy Conversion Congress and Exposition (ECCE)*, pages 1909–1916, Oct 2017.

[8] P. Pescetto and G. Pellegrino. Sensorless magnetic model and pm flux identification of synchronous drives at standstill. In *2017 IEEE International Symposium on Sensorless Control for Electrical Drives (SLED)*, pages 79–84, Sept 2017.

[9] A. Yousefi-Talouki, P. Pescetto, G. Pellegrino, and I. Boldea. Combined active flux and high-frequency injection methods for sensorless direct-flux vector control of synchronous reluctance machines. *IEEE Transactions on Power Electronics*, 33(3):2447–2457, March 2018.

[10] A. Yousefi-Talouki, P. Pescetto, and G. Pellegrino. Sensorless direct flux vector control of synchronous reluctance motors including standstill, mtpa, and flux weakening. *IEEE Transactions on Industry Applications*, 53(4):3598–3608, July 2017.

[11] R. Leuzzi, P. Cagnetta, S. Ferrari, P. Pescetto, G. Pellegrino, and F. Cupertino. Analysis of overload and sensorless control capability of pm-assisted synchronous reluctance machines. In *2017 IEEE Workshop on Electrical Machines Design, Control and Diagnosis (WEMDCD)*, pages 172–178, April 2017.

[12] S. A. Odhano, P. Pescetto, H. A. A. Awan, M. Hinkkanen, G. Pellegrino, and R. Bojoi. Parameter identification and self-commissioning in ac motor drives: a technology status review. *IEEE Transactions on Power Electronics*, pages 1–1, 2018.

[13] A. Varatharajan, P. Pescetto, and G. Pellegrino. Injectionless sensorless control of synchronous reluctance machine for zero to low speeds region. In *2018 IEEE 9th International Symposium on Sensorless Control for Electrical Drives (SLED)*, pages 72–77, Sept 2018.

[14] P. Pescetto and G. Pellegrino. Automatic tuning for sensorless commissioning of synchronous reluctance machines augmented with high-frequency voltage injection. *IEEE Transactions on Industry Applications*, 54(5):4485–4493, Sept 2018.

[15] P. Pescetto, S. Ferrari, G. Pellegrino, E. Carpaneto, and Aldo Boglietti. Short-time transient thermal model identification of multiple three-phase machines. In *2018 IEEE Energy Conversion Congress and Exposition (ECCE)*, Oct 2018.

[16] G. Pellegrino. *The Rediscovery of Synchronous Reluctance and Ferrite Permanent Magnet Motors - Tutorial Course Notes*, chapter 4:

Identification of PM Synchronous Machines Parameters for Design and Control Purposes, page 77–107. Springer, 2016.

[17] A. Vagati, M. Pastorelli, and G. Franceschini. High-performance control of synchronous reluctance motors. *IEEE Transactions on Industry Applications*, 33(4):983–991, July 1997.

[18] A. Vagati, M. Pastorelli, G. Franceschini, and V. Drogoreanu. Flux-observer-based high-performance control of synchronous reluctance motors by including cross saturation. *IEEE Transactions on Industry Applications*, 35(3):597–605, May 1999.

[19] R. Morales-Caporal and M. Pacas. Encoderless predictive direct torque control for synchronous reluctance machines at very low and zero speed. *IEEE Transactions on Industrial Electronics*, 55(12):4408–4416, Dec 2008.

[20] S. Mariethoz, A. Domahidi, and M. Morari. Sensorless explicit model predictive control of permanent magnet synchronous motors. In *2009 IEEE International Electric Machines and Drives Conference*, pages 1250–1257, May 2009.

[21] M. Preindl and E. Schaltz. Sensorless model predictive direct current control using novel second-order pll observer for pmsm drive systems. *IEEE Transactions on Industrial Electronics*, 58(9):4087–4095, Sept 2011.

[22] B. Boazzo and G. Pellegrino. Predictive direct flux vector control of permanent magnet synchronous motor drives. In *2013 IEEE Energy Conversion Congress and Exposition*, pages 2086–2093, Sept 2013.

[23] M. Preindl and S. Bolognani. Model predictive direct torque control with finite control set for pmsm drive systems, part 1: Maximum torque per ampere operation. *IEEE Transactions on Industrial Informatics*, 9(4):1912–1921, Nov 2013.

[24] M. Preindl and S. Bolognani. Model predictive direct torque control with finite control set for pmsm drive systems, part 2: Field weakening operation. *IEEE Transactions on Industrial Informatics*, 9(2):648–657, May 2013.

[25] M. Bilewski, A. Fratta, L. Giordano, A. Vagati, and F. Villata. Control of high-performance interior permanent magnet synchronous drives.

IEEE Transactions on Industry Applications, 29(2):328–337, March 1993.

[26] G. Pellegrino, R. I. Bojoi, and P. Guglielmi. Unified direct-flux vector control for ac motor drives. *IEEE Transactions on Industry Applications*, 47(5):2093–2102, Sept 2011.

[27] G. Pellegrino, E. Armando, and P. Guglielmi. Direct-flux vector control of ipm motor drives in the maximum torque per voltage speed range. *IEEE Transactions on Industrial Electronics*, 59(10):3780–3788, Oct 2012.

[28] S. A. Odhano, A. Boglietti, R. Bojoi, and E. Armando. Unified direct-flux vector control of induction motor self-commissioning drive with analysis of parameter detuning effects. In *2013 IEEE Energy Conversion Congress and Exposition*, pages 2071–2078, Sept 2013.

[29] R. Bojoi, Z. Li, S. A. Odhano, G. Griva, and A. Tenconi. Unified direct-flux vector control of induction motor drives with maximum torque per ampere operation. In *2013 IEEE Energy Conversion Congress and Exposition*, pages 3888–3895, Sept 2013.

[30] G. Foo, S. Sayeef, and M. F. Rahman. Low-speed and standstill operation of a sensorless direct torque and flux controlled ipm synchronous motor drive. *IEEE Transactions on Energy Conversion*, 25(1):25–33, March 2010.

[31] P. Guglielmi, M. Pastorelli, G. Pellegrino, and A. Vagati. Position-sensorless control of permanent-magnet-assisted synchronous reluctance motor. *IEEE Transactions on Industry Applications*, 40(2):615–622, March 2004.

[32] P. Guglielmi, M. Pastorelli, and A. Vagati. Impact of cross-saturation in sensorless control of transverse-laminated synchronous reluctance motors. *IEEE Transactions on Industrial Electronics*, 53(2):429–439, April 2006.

[33] I. Boldea, M. C. Paicu, and G. Andreescu. Active flux concept for motion-sensorless unified ac drives. *IEEE Transactions on Power Electronics*, 23(5):2612–2618, Sept 2008.

[34] S. Agarliţă, M. Fătu, L. N. Tutelea, F. Blaabjerg, and I. Boldea. I-f starting and active flux based sensorless vector control of reluctance synchronous motors, with experiments. In *2010 12th International*

Conference on Optimization of Electrical and Electronic Equipment, pages 337–342, May 2010.

[35] M. Hinkkanen, S. E. Saarakkala, H. A. A. Awan, E. Mölsä, and T. Tuovinen. Observers for sensorless synchronous motor drives: Framework for design and analysis. *IEEE Transactions on Industry Applications*, 54(6):6090–6100, Nov 2018.

[36] A. Piippo and J. Luomi. Adaptive observer combined with hf signal injection for sensorless control of pmsm drives. In *IEEE International Conference on Electric Machines and Drives, 2005.*, pages 674–681, May 2005.

[37] T. Tuovinen and M. Hinkkanen. Adaptive full-order observer with high-frequency signal injection for synchronous reluctance motor drives. *IEEE Journal of Emerging and Selected Topics in Power Electronics*, 2(2):181–189, June 2014.

[38] E. Capecchi, P. Guglielmi, M. Pastorelli, and A. Vagati. Position-sensorless control of the transverse-laminated synchronous reluctance motor. *IEEE Transactions on Industry Applications*, 37(6):1768–1776, Nov 2001.

[39] IEEE Trial-Use Guide for Testing Permanent Magnet Machines. *IEEE Std 1812-2014*, pages 1–56, Feb 2015.

[40] E. Armando, R. I. Bojoi, P. Guglielmi, G. Pellegrino, and M. Pastorelli. Experimental identification of the magnetic model of synchronous machines. *IEEE Transactions on Industry Applications*, 49(5):2116–2125, Sept 2013.

[41] S. A. Odhano, R. Bojoi, M. Popescu, and A. Tenconi. Parameter identification and self-commissioning of ac permanent magnet machines - a review. In *2015 IEEE Workshop on Electrical Machines Design, Control and Diagnosis (WEMDCD)*, pages 195–203, March 2015.

[42] J. Holtz and Juntao Quan. Sensorless vector control of induction motors at very low speed using a nonlinear inverter model and parameter identification. *IEEE Transactions on Industry Applications*, 38(4):1087–1095, July 2002.

[43] G. Pellegrino, P. Guglielmi, E. Armando, and R. I. Bojoi. Self-commissioning algorithm for inverter nonlinearity compensation in sensorless induction motor drives. *IEEE Transactions on Industry Applications*, 46(4):1416–1424, July 2010.

[44] G. Pellegrino, R. I. Bojoi, P. Guglielmi, and F. Cupertino. Accurate inverter error compensation and related self-commissioning scheme in sensorless induction motor drives. *IEEE Transactions on Industry Applications*, 46(5):1970–1978, Sept 2010.

[45] I. R. Bojoi, E. Armando, G. Pellegrino, and S. G. Rosu. Self-commissioning of inverter nonlinear effects in ac drives. In *2012 IEEE International Energy Conference and Exhibition (ENERGYCON)*, pages 213–218, Sept 2012.

[46] Y. Zhao, W. Qiao, and L. Wu. Dead-time effect analysis and compensation for a sliding-mode position observer-based sensorless ipmsm control system. *IEEE Transactions on Industry Applications*, 51(3):2528–2535, May 2015.

[47] A. Gaeta, P. Zanchetta, F. Tinazzi, and M. Zigliotto. Advanced self-commissioning and feed-forward compensation of inverter nonlinearities. In *2015 IEEE International Conference on Industrial Technology (ICIT)*, pages 610–616, March 2015.

[48] R. Krishnan and F. C. Doran. Study of parameter sensitivity in high-performance inverter-fed induction motor drive systems. *IEEE Transactions on Industry Applications*, IA-23(4):623–635, July 1987.

[49] R. Krishnan and A. S. Bharadwaj. A review of parameter sensitivity and adaptation in indirect vector controlled induction motor drive systems. *IEEE Transactions on Power Electronics*, 6(4):695–703, Oct 1991.

[50] B. Robyns, P. A. Sente, H. A. Buyse, and F. Labrique. Influence of digital current control strategy on the sensitivity to electrical parameter uncertainties of induction motor indirect field-oriented control. *IEEE Transactions on Power Electronics*, 14(4):690–699, July 1999.

[51] M. Hinkkanen and J. Luomi. Parameter sensitivity of full-order flux observers for induction motors. *IEEE Transactions on Industry Applications*, 39(4):1127–1135, July 2003.

[52] B. Cheng and T. R. Tesch. Torque feedforward control technique for permanent-magnet synchronous motors. *IEEE Transactions on Industrial Electronics*, 57(3):969–974, March 2010.

[53] C. Lai, G. Feng, K. Mukherjee, and N. C. Kar. Investigations of the influence of pmsm parameter variations in optimal stator current design for torque ripple minimization. *IEEE Transactions on Energy Conversion*, 32(3):1052–1062, Sept 2017.

[54] V. . Leppanen and J. Luomi. Observer using low-frequency injection for sensorless induction motor control-parameter sensitivity analysis. *IEEE Transactions on Industrial Electronics*, 53(1):216–224, Feb 2006.

[55] N. Bianchi, E. Fornasiero, and S. Bolognani. Effect of stator and rotor saturation on sensorless rotor position detection. *IEEE Transactions on Industry Applications*, 49(3):1333–1342, May 2013.

[56] K. Lu, X. Lei, and F. Blaabjerg. Artificial inductance concept to compensate nonlinear inductance effects in the back emf-based sensorless control method for pmsm. *IEEE Transactions on Energy Conversion*, 28(3):593–600, Sept 2013.

[57] B. Chen, W. Yao, F. Chen, and Z. Lu. Parameter sensitivity in sensorless induction motor drives with the adaptive full-order observer. *IEEE Transactions on Industrial Electronics*, 62(7):4307–4318, July 2015.

[58] J. Kan, K. Zhang, and Z. Wang. Indirect vector control with simplified rotor resistance adaptation for induction machines. *IET Power Electronics*, 8(7):1284–1294, 2015.

[59] IEEE Draft Standard Test Procedure for Polyphase Induction Motors and Generators. *IEEE P112/D5, October 2015*, pages 1–110, Jan 2015.

[60] H. A. Toliyat, E. Levi, and M. Raina. A review of rfo induction motor parameter estimation techniques. *IEEE Transactions on Energy Conversion*, 18(2):271–283, June 2003.

[61] A. Tessarolo. Accurate computation of multiphase synchronous machine inductances based on winding function theory. *IEEE Transactions on Energy Conversion*, 27(4):895–904, Dec 2012.

[62] K. J. Meessen, P. Thelin, J. Soulard, and E. A. Lomonova. Inductance calculations of permanent-magnet synchronous machines including flux change and self- and cross-saturations. *IEEE Transactions on Magnetics*, 44(10):2324–2331, Oct 2008.

[63] Y. S. Chen, Z. Q. Zhu, and D. Howe. Calculation of d- and q-axis inductances of pm brushless ac machines accounting for skew. *IEEE Transactions on Magnetics*, 41(10):3940–3942, Oct 2005.

[64] E. S. Obe. Calculation of inductances and torque of an axially laminated synchronous reluctance motor. *IET Electric Power Applications*, 4(9):783–792, Nov 2010.

[65] T. Lubin, T. Hamiti, H. Razik, and A. Rezzoug. Comparison between finite-element analysis and winding function theory for inductances and torque calculation of a synchronous reluctance machine. *IEEE Transactions on Magnetics*, 43(8):3406–3410, Aug 2007.

[66] B. Stumberger, B. Kreca, and B. Hribernik. Determination of parameters of synchronous motor with permanent magnets from measurement of load conditions. *IEEE Transactions on Energy Conversion*, 14(4):1413–1416, Dec 1999.

[67] H. . Nee, L. Lefevre, P. Thelin, and J. Soulard. Determination of d and q reactances of permanent-magnet synchronous motors without measurements of the rotor position. *IEEE Transactions on Industry Applications*, 36(5):1330–1335, Sept 2000.

[68] A. Tenconi, M. Lazzari, F. Profumo, and A. Cavagnino. Axial flux interior pm synchronous motor: parameters identification and steady-state performance measurements. *IEEE Transactions on Industry Applications*, 36(6):1581–1588, Nov 2000.

[69] S. Yamamoto, T. Ara, S. Oda, and K. Matsuse. Prediction of starting performance of pm motors by dc decay testing method. *IEEE Transactions on Industry Applications*, 36(4):1053–1060, July 2000.

[70] T. Sun, S. Kwon, J. Lee, and J. Hong. An improved ac standstill method for testing inductances of interior pm synchronous motor considering cross-magnetizing effect. In *2009 IEEE Energy Conversion Congress and Exposition*, pages 2415–2422, Sept 2009.

[71] Y. Gao, R. Qu, Yu Chen, Jian Li, and Wei Xu. Review of off-line synchronous inductance measurement method for permanent magnet synchronous machines. In *2014 IEEE Conference and Expo Transportation Electrification Asia-Pacific (ITEC Asia-Pacific)*, pages 1–6, Aug 2014.

[72] R. Dutta and M. F. Rahman. A comparative analysis of two test methods of measuring lt;tex gt;*d* lt;/tex gt;- and lt;tex gt;*q* lt;/tex gt;-axes inductances of interior permanent-magnet machine. *IEEE Transactions on Magnetics*, 42(11):3712–3718, Nov 2006.

[73] B. Stumberger, G. Stumberger, D. Dolinar, A. Hamler, and M. Trlep. Evaluation of saturation and cross-magnetization effects in interior permanent-magnet synchronous motor. *IEEE Transactions on Industry Applications*, 39(5):1264–1271, Sept 2003.

[74] K. M. Rahman and S. Hiti. Identification of machine parameters of a synchronous motor. In *38th IAS Annual Meeting on Conference Record of the Industry Applications Conference, 2003.*, volume 1, pages 409–415 vol.1, Oct 2003.

[75] T. L. Vandoorn, F. M. De Belie, T. J. Vyncke, J. A. Melkebeek, and P. Lataire. Generation of multisinusoidal test signals for the identification of synchronous-machine parameters by using a voltage-source inverter. *IEEE Transactions on Industrial Electronics*, 57(1):430–439, Jan 2010.

[76] G. Pellegrino, B. Boazzo, and T. M. Jahns. Magnetic model self-identification for pm synchronous machine drives. *IEEE Transactions on Industry Applications*, 51(3):2246–2254, May 2015.

[77] K. Liu and Z. Q. Zhu. Position offset-based parameter estimation for permanent magnet synchronous machines under variable speed control. *IEEE Transactions on Power Electronics*, 30(6):3438–3446, June 2015.

[78] K. Liu, J. Feng, S. Guo, L. Xiao, and Z. Q. Zhu. Improved position offset based parameter determination of permanent magnet synchronous machines under different load conditions. *IET Electric Power Applications*, 11(4):603–612, 2017.

[79] K. Liu, J. Feng, S. Guo, L. Xiao, and Z. Zhu. Identification of flux linkage map of permanent magnet synchronous machines under uncertain circuit resistance and inverter nonlinearity. *IEEE Transactions on Industrial Informatics*, 14(2):556–568, Feb 2018.

[80] G. Wang, L. Qu, H. Zhan, J. Xu, L. Ding, G. Zhang, and D. Xu. Self-commissioning of permanent magnet synchronous machine drives at standstill considering inverter nonlinearities. *IEEE Transactions on Power Electronics*, 29(12):6615–6627, Dec 2014.

[81] S. A. Odhano, P. Giangrande, R. I. Bojoi, and C. Gerada. Self-commissioning of interior permanent- magnet synchronous motor drives with high-frequency current injection. *IEEE Transactions on Industry Applications*, 50(5):3295–3303, Sept 2014.

[82] M. Carraro, F. Tinazzi, and M. Zigliotto. Estimation of the direct-axis inductance in pm synchronous motor drives at standstill. In *2013 IEEE International Conference on Industrial Technology (ICIT)*, pages 313–318, Feb 2013.

[83] S. A. Odhano, R. Bojoi, Ş. G. Roşu, and A. Tenconi. Identification of the magnetic model of permanent-magnet synchronous machines using dc-biased low-frequency ac signal injection. *IEEE Transactions on Industry Applications*, 51(4):3208–3215, July 2015.

[84] M. M. Bech, J. H. Christensen, M. L. Weber, and N. H. Kristensen. An automatic parameter identification method for a pmsm drive with lc-filter. In *IECON 2016 - 42nd Annual Conference of the IEEE Industrial Electronics Society*, pages 2678–2683, Oct 2016.

[85] S. Yang and K. Lin. Automatic control loop tuning for permanent-magnet ac servo motor drives. *IEEE Transactions on Industrial Electronics*, 63(3):1499–1506, March 2016.

[86] L. Peretti, P. Sandulescu, and G. Zanuso. Self-commissioning of flux linkage curves of synchronous reluctance machines in quasi-standstill condition. *IET Electric Power Applications*, 9(9):642–651, 2015.

[87] G. Stumberger, T. Marcic, B. Stumberger, and D. Dolinar. Experimental method for determining magnetically nonlinear characteristics of electric machines with magnetically nonlinear and anisotropic iron core, damping windings, and permanent magnets. *IEEE Transactions on Magnetics*, 44(11):4341–4344, Nov 2008.

[88] N. Bedetti, S. Calligaro, and R. Petrella. Stand-still self-identification of flux characteristics for synchronous reluctance machines using novel saturation approximating function and multiple linear regression. *IEEE Transactions on Industry Applications*, 52(4):3083–3092, July 2016.

[89] Z. Qu, T. Tuovinen, and M. Hinkkanen. Inclusion of magnetic saturation in dynamic models of synchronous reluctance motors. In *2012 XXth International Conference on Electrical Machines*, pages 994–1000, Sept 2012.

[90] A. Accetta, M. Cirrincione, M. Pucci, and A. Sferlazza. A space-vector state dynamic model of the synchronous reluctance motor including self and cross-saturation effects and its parameters estimation. In *2018 IEEE Energy Conversion Congress and Exposition (ECCE)*, pages 4466–4472, Sep. 2018.

[91] J. Jacob, P. Kumar, S. Calligaro, and R. Petrella. Self-commissioning identification of permanent magnet flux-linkage magnitude in sensorless drives for pmsm at quasi stand-still. In *2018 IEEE 9th International Symposium on Sensorless Control for Electrical Drives (SLED)*, pages 144–149, Sept 2018.

[92] R. Antonello, L. Ortombina, F. Tinazzi, and M. Zigliotto. Online stator resistance tracking for reluctance and interior permanent magnet synchronous motors. *IEEE Transactions on Industry Applications*, 54(4):3405–3414, July 2018.

[93] A. Varatharajan, S. Cruz, H. Hadla, and F. Briz. Predictive torque control of synrm drives with online mtpa trajectory tracking and inductances estimation. In *2017 IEEE International Electric Machines and Drives Conference (IEMDC)*, pages 1–7, May 2017.

[94] N. Bedetti, S. Calligaro, and R. Petrella. Self-adaptation of mtpa tracking controller for ipmsm and synrm drives based on on-line estimation of loop gain. In *2017 IEEE Energy Conversion Congress and Exposition (ECCE)*, pages 1917–1924, Oct 2017.

[95] N. Bedetti, S. Calligaro, C. Olsen, and R. Petrella. Automatic mtpa tracking in ipmsm drives: Loop dynamics, design, and auto-tuning. *IEEE Transactions on Industry Applications*, 53(5):4547–4558, Sep. 2017.

[96] T. Sun, J. Wang, and M. Koc. Virtual signal injection-based direct flux vector control of ipmsm drives. *IEEE Transactions on Industrial Electronics*, 63(8):4773–4782, Aug 2016.

[97] C. Concari, G. Franceschini, and C. Tassoni. Induction drive health assessment in dsp-based self-commissioning procedures. *IEEE Transactions on Industrial Electronics*, 58(5):1490–1500, May 2011.

[98] Doo-Hee Jung and In-Joong Ha. An efficient method for identifying the initial position of a pmsm with an incremental encoder. *IEEE Transactions on Industrial Electronics*, 45(4):682–685, Aug 1998.

[99] M. Tursini, R. Petrella, and F. Parasiliti. Initial rotor position estimation method for pm motors. *IEEE Transactions on Industry Applications*, 39(6):1630–1640, Nov 2003.

[100] P. P. Acarnley and J. F. Watson. Review of position-sensorless operation of brushless permanent-magnet machines. *IEEE Transactions on Industrial Electronics*, 53(2):352–362, April 2006.

[101] J. Holtz. Acquisition of position error and magnet polarity for sensorless control of pm synchronous machines. *IEEE Transactions on Industry Applications*, 44(4):1172–1180, July 2008.

[102] S. Bolognani and M. Zigliotto. Self-commissioning compensation of inverter non-idealities for sensorless ac drives applications. In *2002 International Conference on Power Electronics, Machines and Drives (Conf. Publ. No. 487)*, pages 30–37, June 2002.

[103] F. Briz and M. W. Degner. Rotor position estimation. *IEEE Industrial Electronics Magazine*, 5(2):24–36, June 2011.

[104] Y. Yoon, S. Sul, S. Morimoto, and K. Ide. High-bandwidth sensorless algorithm for ac machines based on square-wave-type voltage injection. *IEEE Transactions on Industry Applications*, 47(3):1361–1370, May 2011.

[105] F. J. W. Barnard, W. T. Villet, and M. J. Kamper. Hybrid active-flux and arbitrary injection position sensorless control of reluctance synchronous machines. *IEEE Transactions on Industry Applications*, 51(5):3899–3906, Sept 2015.

[106] F. Tinazzi, P. Sandulescu, L. Peretti, and M. Zigliotto. On the true maximum efficiency operations of synchronous motor drives. In *2017 IEEE 12th International Conference on Power Electronics and Drive Systems (PEDS)*, pages 1,043–1,048, Dec 2017.

[107] S. Yamamoto, T. Ara, and K. Matsuse. A method to calculate transient characteristics of synchronous reluctance motors considering iron loss and cross-magnetic saturation. *IEEE Transactions on Industry Applications*, 43(1):47–56, Jan 2007.

[108] Andrzej W. Ordys. System identification, t. sodestrom and p. stoica. prentice-hall international, hemel hempstead, u.k. 1989, isbn 0138812365, xxiv + 612 pp., £47.00. *International Journal of Adaptive Control and Signal Processing*, 7(3):235–237, 1993.

[109] R. Bojoi, P. Guglielmi, and G. Pellegrino. Sensorless stator field-oriented control for low cost induction motor drives with wide field

weakening range. In *2008 IEEE Industry Applications Society Annual Meeting*, pages 1–7, Oct 2008.

[110] M. Hinkkanen and J. Luomi. Stabilization of regenerating-mode operation in sensorless induction motor drives by full-order flux observer design. *IEEE Transactions on Industrial Electronics*, 51(6):1318–1328, Dec 2004.

[111] L. A. Jones and J. H. Lang. A state observer for the permanent-magnet synchronous motor. *IEEE Transactions on Industrial Electronics*, 36(3):374–382, Aug 1989.

[112] R. D. Lorenz and K. W. Van Patten. High-resolution velocity estimation for all-digital, ac servo drives. *IEEE Transactions on Industry Applications*, 27(4):701–705, July 1991.

[113] M. J. Corley and R. D. Lorenz. Rotor position and velocity estimation for a permanent magnet synchronous machine at standstill and high speeds. In *IAS '96. Conference Record of the 1996 IEEE Industry Applications Conference Thirty-First IAS Annual Meeting*, volume 1, pages 36–41 vol.1, Oct 1996.

[114] M. J. Corley and R. D. Lorenz. Rotor position and velocity estimation for a salient-pole permanent magnet synchronous machine at standstill and high speeds. *IEEE Transactions on Industry Applications*, 34(4):784–789, July 1998.

[115] M. W. Degner and R. D. Lorenz. Using multiple saliencies for the estimation of flux, position, and velocity in ac machines. *IEEE Transactions on Industry Applications*, 34(5):1097–1104, Sept 1998.

[116] M. Fatu, R. Teodorescu, I. Boldea, G. Andreescu, and F. Blaabjerg. I-f starting method with smooth transition to emf based motion-sensorless vector control of pm synchronous motor/generator. In *2008 IEEE Power Electronics Specialists Conference*, pages 1481–1487, June 2008.

[117] L. I. Iepure, I. Boldea, and F. Blaabjerg. Hybrid i-f starting and observer-based sensorless control of single-phase bldc-pm motor drives. *IEEE Transactions on Industrial Electronics*, 59(9):3436–3444, Sept 2012.

[118] Z. Wang, K. Lu, and F. Blaabjerg. A simple startup strategy based on current regulation for back-emf-based sensorless control of pmsm. *IEEE Transactions on Power Electronics*, 27(8):3817–3825, Aug 2012.

[119] L. Ortombina, F. Tinazzi, and M. Zigliotto. An effective start-up algorithm for sensorless synchronous reluctance and ipm motor drives. In *2017 IEEE 12th International Conference on Power Electronics and Drive Systems (PEDS)*, pages 1,062–1,067, Dec 2017.

[120] L. G. Gonzalez, E. Figueres, G. Garcera, O. Carranza, and F. Gonzalez-Espin. Synchronization techniques comparison for sensorless control applied to wind energy conversion systems (wecs). In *2009 13th European Conference on Power Electronics and Applications*, pages 1–9, Sept 2009.

[121] Seog-Joo Kang, Jang-Mok Kim, and Seung-Ki Sul. Position sensorless control of synchronous reluctance motor using high frequency current injection. *IEEE Transactions on Energy Conversion*, 14(4):1271–1275, Dec 1999.

[122] S. Bolognani, S. Calligaro, R. Petrella, and M. Tursini. Sensorless control of ipm motors in the low-speed range and at standstill by hf injection and dft processing. *IEEE Transactions on Industry Applications*, 47(1):96–104, Jan 2011.

[123] X. Jin, R. Ni, W. Chen, F. Blaabjerg, and D. Xu. High-frequency voltage-injection methods and observer design for initial position detection of permanent magnet synchronous machines. *IEEE Transactions on Power Electronics*, 33(9):7971–7979, Sept 2018.

[124] J. M. Liu and Z. Q. Zhu. Novel sensorless control strategy with injection of high-frequency pulsating carrier signal into stationary reference frame. *IEEE Transactions on Industry Applications*, 50(4):2574–2583, July 2014.

[125] C. Hwang, Y. Lee, and S. Sul. Analysis on position estimation error in position-sensorless operation of ipmsm using pulsating square wave signal injection. *IEEE Transactions on Industry Applications*, 55(1):458–470, Jan 2019.

[126] D. Paulus, P. Landsmann, and R. Kennel. Sensorless field- oriented control for permanent magnet synchronous machines with an arbitrary injection scheme and direct angle calculation. In *2011 Symposium on Sensorless Control for Electrical Drives*, pages 41–46, Sept 2011.

[127] P. Landsmann, C. M. Hackl, and R. Kennel. Eliminating all machine parameters in encoderless predictive torque control without signal in-

jection. In *2011 IEEE International Electric Machines Drives Conference (IEMDC)*, pages 1259–1264, May 2011.

[128] C. Silva, G. M. Asher, and M. Sumner. Hybrid rotor position observer for wide speed-range sensorless pm motor drives including zero speed. *IEEE Transactions on Industrial Electronics*, 53(2):373–378, April 2006.

[129] O. Wallmark and L. Harnefors. Sensorless control of salient pmsm drives in the transition region. *IEEE Transactions on Industrial Electronics*, 53(4):1179–1187, June 2006.

[130] L. A. De S. Ribeiro, M. C. Harke, and R. D. Lorenz. Dynamic properties of back-emf based sensorless drives. In *Conference Record of the 2006 IEEE Industry Applications Conference Forty-First IAS Annual Meeting*, volume 4, pages 2026–2033, Oct 2006.

[131] W. T. Villet, M. J. Kamper, P. Landsmann, and R. Kennel. Evaluation of a simplified high frequency injection position sensorless control method for reluctance synchronous machine drives. In *6th IET International Conference on Power Electronics, Machines and Drives (PEMD 2012)*, pages 1–6, March 2012.

[132] P. Landsmann, R. Kennel, H. W. de Kock, and M. J. Kamper. Fundamental saliency based encoderless control for reluctance synchronous machines. In *The XIX International Conference on Electrical Machines - ICEM 2010*, pages 1–7, Sept 2010.

[133] W. T. Villet, M. J. Kamper, P. Landsmann, and R. Kennel. Hybrid position sensorless vector control of a reluctance synchronous machine through the entire speed range. In *2012 15th International Power Electronics and Motion Control Conference (EPE/PEMC)*, pages LS4b–1.1–1–LS4b–1.1–7, Sept 2012.

[134] Zhiqian Chen, M. Tomita, S. Doki, and S. Okuma. An extended electromotive force model for sensorless control of interior permanent-magnet synchronous motors. *IEEE Transactions on Industrial Electronics*, 50(2):288–295, April 2003.

[135] T. Ohnuma, S. Doki, and S. Okuma. Extended EMF Observer for Sensorless Control over a Wide Range of Speeds. *IEEJ Transactions on Industry Applications*, 131:208–218, 2011.

[136] K. UCHIDA T. Yokoama and H. KUBOTA. Position sensorless control for ipmsm based on extended emf and voltage injection synchronized with pulse-width modulation carrier. *Electrical Engineering in Japan*, 199(1):28–39, 2016.

[137] S. Ichikawa, M. Tomita, S. Doki, and S. Okuma. Sensorless control of synchronous reluctance motors based on extended emf models considering magnetic saturation with online parameter identification. *IEEE Transactions on Industry Applications*, 42(5):1264–1274, Sept 2006.

[138] Y. Yamamoto, Y. Higashi, H. Matsuno, and S. Ogasawara. Analysis of Unstable Regions in Vector-Controlled IPMSM Sensorless Control. *IEEJ Transactions on Industry Applications*, 127:1197–1204, 2007.

[139] S. Kondo, S. Doki, and M. Tomita. A study on position sensorless control without any q-axis inductance by using extended electromotive force with high frequency signal injection. In *2017 19th European Conference on Power Electronics and Applications (EPE'17 ECCE Europe)*, pages P.1–P.6, Sept 2017.

[140] S. Agarlita, I. Boldea, and F. Blaabjerg. High-frequency-injection-assisted active-flux-based sensorless vector control of reluctance synchronous motors, with experiments from zero speed. *IEEE Transactions on Industry Applications*, 48(6):1931–1939, Nov 2012.

[141] M. C. Paicu, I. Boldea, G. . Andreescu, and F. Blaabjerg. Very low speed performance of active flux based sensorless control: interior permanent magnet synchronous motor vector control versus direct torque and flux control. *IET Electric Power Applications*, 3(6):551–561, November 2009.

[142] A. Piippo, M. Hinkkanen, and J. Luomi. Adaptation of motor parameters in sensorless pmsm drives. *IEEE Transactions on Industry Applications*, 45(1):203–212, Jan 2009.

[143] T. Tuovinen and M. Hinkkanen. Signal-injection-assisted full-order observer with parameter adaptation for synchronous reluctance motor drives. *IEEE Transactions on Industry Applications*, 50(5):3392–3402, Sept 2014.

[144] H. A. A. Awan, T. Tuovinen, S. E. Saarakkala, and M. Hinkkanen. Discrete-time observer design for sensorless synchronous motor drives. *IEEE Transactions on Industry Applications*, 52(5):3968–3979, Sept 2016.

[145] L. Zhong, M. F. Rahman, W. Y. Hu, and K. W. Lim. Analysis of direct torque control in permanent magnet synchronous motor drives. *IEEE Transactions on Power Electronics*, 12(3):528–536, May 1997.

[146] G. Foo, S. Sayeef, and M. F. Rahman. Sensorless direct torque and flux control of an ipm synchronous motor at low speed and standstill. In *2008 13th International Power Electronics and Motion Control Conference*, pages 2269–2274, Sept 2008.

[147] I. Boldea, M. C. Paicu, G. Andreescu, and F. Blaabjerg. Active flux dtfc-svm sensorless control of ipmsm. *IEEE Transactions on Energy Conversion*, 24(2):314–322, June 2009.

[148] G. H. B. Foo and M. F. Rahman. Direct torque control of an ipm-synchronous motor drive at very low speed using a sliding-mode stator flux observer. *IEEE Transactions on Power Electronics*, 25(4):933–942, April 2010.

[149] G. Andreescu, C. I. Pitic, F. Blaabjerg, and I. Boldea. Combined flux observer with signal injection enhancement for wide speed range sensorless direct torque control of ipmsm drives. *IEEE Transactions on Energy Conversion*, 23(2):393–402, June 2008.

[150] D. Nguyen, R. Dutta, M. F. Rahman, and J. E. Fletcher. Performance of a sensorless controlled concentrated-wound interior permanent-magnet synchronous machine at low and zero speed. *IEEE Transactions on Industrial Electronics*, 63(4):2016–2026, April 2016.

[151] I. Boldea, C. I. Pitic, C. Lascu, G. . Andreescu, L. Tutelea, F. Blaabjerg, and P. Sandholdt. Dtfc-svm motion-sensorless control of a pm-assisted reluctance synchronous machine as starter-alternator for hybrid electric vehicles. *IEEE Transactions on Power Electronics*, 21(3):711–719, May 2006.

[152] E. Peralta-Sanchez, F. Al-rifai, and N. Schofield. Direct torque control of permanent magnet motors using a single current sensor. In *2009 IEEE International Electric Machines and Drives Conference*, pages 89–94, May 2009.

[153] Y. Zhao, W. Qiao, and L. Wu. An adaptive quasi-sliding-mode rotor position observer-based sensorless control for interior permanent magnet synchronous machines. *IEEE Transactions on Power Electronics*, 28(12):5618–5629, Dec 2013.

[154] Y. Zhao, W. Qiao, and L. Wu. Improved rotor position and speed estimators for sensorless control of interior permanent-magnet synchronous machines. *IEEE Journal of Emerging and Selected Topics in Power Electronics*, 2(3):627–639, Sept 2014.

[155] G. el Murr, D. Giaouris, and J. W. Finch. Universal pll strategy for sensorless speed and position estimation of pmsm. In *2008 IEEE Region 10 and the Third international Conference on Industrial and Information Systems*, pages 1–6, Dec 2008.

[156] L. Malesani, P. Mattavelli, and S. Buso. Robust dead-beat current control for pwm rectifiers and active filters. *IEEE Transactions on Industry Applications*, 35(3):613–620, May 1999.

[157] L. Rovere, A. Formentini, A. Gaeta, P. Zanchetta, and M. Marchesoni. Sensorless finite-control set model predictive control for ipmsm drives. *IEEE Transactions on Industrial Electronics*, 63(9):5921–5931, Sept 2016.

[158] C. Bian, S. Ren, and L. Ma. Sensorless dtc of super high-speed pmsm. In *2007 IEEE International Conference on Automation and Logistics*, pages 3060–3064, Aug 2007.

[159] A. Yousefi-Talouki and G. Pellegrino. Sensorless direct flux vector control of synchronous reluctance motor drives in a wide speed range including standstill. In *2016 XXII International Conference on Electrical Machines (ICEM)*, pages 1167–1173, Sept 2016.

[160] A. Consoli, F. Russo, G. Scarcella, and A. Testa. Low- and zero-speed sensorless control of synchronous reluctance motors. *IEEE Transactions on Industry Applications*, 35(5):1050–1057, Sep. 1999.

[161] N. Bianchi and S. Bolognani. Influence of rotor geometry of an ipm motor on sensorless control feasibility. *IEEE Transactions on Industry Applications*, 43(1):87–96, Jan 2007.

[162] J. A. Weimer. The role of electric machines and drives in the more electric aircraft. In *IEEE International Electric Machines and Drives Conference, 2003. IEMDC'03.*, volume 1, pages 11–15 vol.1, June 2003.

[163] C. R. Avery, S. G. Burrow, and P. H. Mellor. Electrical generation and distribution for the more electric aircraft. In *2007 42nd International Universities Power Engineering Conference*, pages 1007–1012, Sep. 2007.

[164] A. Boglietti, A. Cavagnino, A. Tenconi, S. Vaschetto, and P. di Torino. The safety critical electric machines and drives in the more electric aircraft: A survey. In *2009 35th Annual Conference of IEEE Industrial Electronics*, pages 2587–2594, Nov 2009.

[165] W. Cao, B. C. Mecrow, G. J. Atkinson, J. W. Bennett, and D. J. Atkinson. Overview of electric motor technologies used for more electric aircraft (mea). *IEEE Transactions on Industrial Electronics*, 59(9):3523–3531, Sep. 2012.

[166] E. Levi. Multiphase electric machines for variable-speed applications. *IEEE Transactions on Industrial Electronics*, 55(5):1893–1909, May 2008.

[167] M. Villani, M. Tursini, G. Fabri, and L. Castellini. Multi-phase fault tolerant drives for aircraft applications. In *Electrical Systems for Aircraft, Railway and Ship Propulsion*, pages 1–6, Oct 2010.

[168] R. Bojoi, M. G. Neacsu, and A. Tenconi. Analysis and survey of multiphase power electronic converter topologies for the more electric aircraft applications. In *International Symposium on Power Electronics Power Electronics, Electrical Drives, Automation and Motion*, pages 440–445, June 2012.

[169] P. H. Mellor, D. Roberts, and D. R. Turner. Lumped parameter thermal model for electrical machines of tefc design. *IEE Proceedings B - Electric Power Applications*, 138(5):205–218, Sep. 1991.

[170] A. Boglietti, A. Cavagnino, D. Staton, M. Shanel, M. Mueller, and C. Mejuto. Evolution and modern approaches for thermal analysis of electrical machines. *IEEE Transactions on Industrial Electronics*, 56(3):871–882, March 2009.

[171] A. Boglietti, A. Cavagnino, M. Lazzari, and M. Pastorelli. A simplified thermal model for variable-speed self-cooled industrial induction motor. *IEEE Transactions on Industry Applications*, 39(4):945–952, July 2003.

[172] W. Jiang and T. M. Jahns. Coupled electromagnetic–thermal analysis of electric machines including transient operation based on finite-element techniques. *IEEE Transactions on Industry Applications*, 51(2):1880–1889, March 2015.

[173] C. Kral, A. Haumer, and S. B. Lee. A practical thermal model for the estimation of permanent magnet and stator winding temperatures. *IEEE Transactions on Power Electronics*, 29(1):455–464, Jan 2014.

[174] Y. Bertin, E. Videcoq, S. Thieblin, and D. Petit. Thermal behavior of an electrical motor through a reduced model. *IEEE Transactions on Energy Conversion*, 15(2):129–134, June 2000.

[175] T. Huber, W. Peters, and J. Böcker. A low-order thermal model for monitoring critical temperatures in permanent magnet synchronous motors. In *7th IET International Conference on Power Electronics, Machines and Drives (PEMD 2014)*, pages 1–6, April 2014.

[176] A. Boglietti, E. Carpaneto, M. Cossale, and S. Vaschetto. Stator-winding thermal models for short-time thermal transients: Definition and validation. *IEEE Transactions on Industrial Electronics*, 63(5):2713–2721, May 2016.

[177] I. J. Perez-arriaga, G. C. Verghese, and F. C. Schweppe. Selective modal analysis with applications to electric power systems, part i: Heuristic introduction. *IEEE Transactions on Power Apparatus and Systems*, PAS-101(9):3117–3125, Sep. 1982.